The mDOM – a multi-PMT digital optical module for the IceCube-Gen2 neutrino telescope

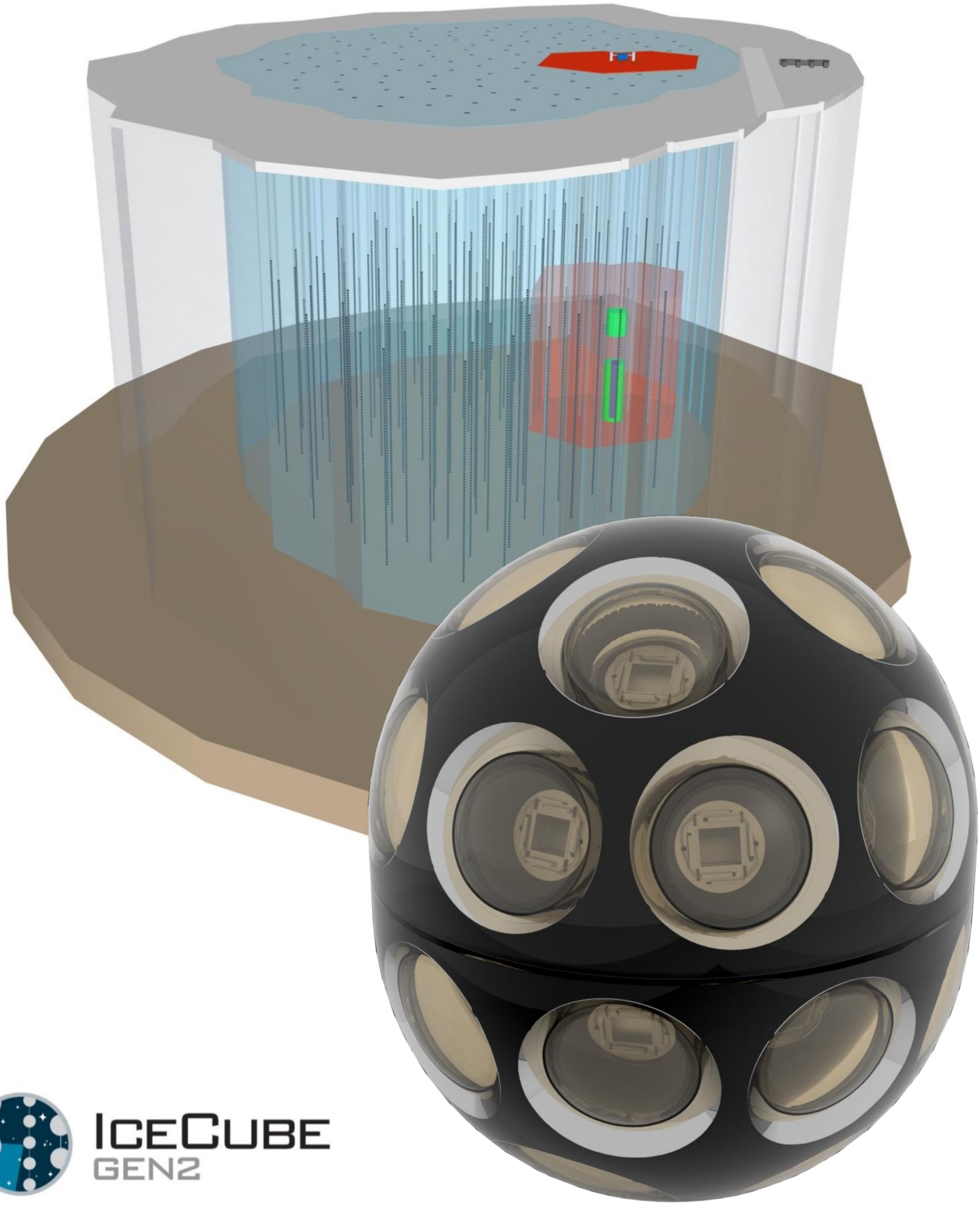

ICECUBE
GEN2

Title page features artist's impressions of IceCube-Gen2 (courtesy of the IceCube collaboration) and the mDOM (courtesy of the IceCube Münster group).

The mDOM – a multi-PMT digital optical module for the IceCube-Gen2 neutrino telescope

Der Naturwissenschaftlichen Fakultät
der Friedrich-Alexander-Universität Erlangen-Nürnberg
zur Erlangung des Doktorgrades Dr. rer. nat
vorgelegt von

Lew Classen
aus Nikolo-Pawlowskoje

Friedrich-Alexander-Universität
Erlangen-Nürnberg

ERLANGEN CENTRE
FOR ASTROPARTICLE
PHYSICS

Februar 2017

Als Dissertation genehmigt
von der Naturwissenschaftlichen Fakultät
der Friedrich-Alexander-Universität Erlangen-Nürnberg

Tag der mündlichen Prüfung:

- 21.06.2017

Vorsitzender des Promotionsorgans:

- Prof. Dr. Georg Kreimer

Gutachter:

- Prof. Dr. Alexander Kappes
- Prof. Dr. Christopher van Eldik

Überblick

Nach der erstmaligen Messung eines hochenergetischen astrophysikalischen Neutrinoflusses durch IceCube, wird momentan intensiv an den Planungen zur nächsten Generation eines Neutrino-Observatoriums am Südpol, IceCube-Gen2, gearbeitet. Dabei ist vorgesehen den Energiebereich nachweisbarer Neutrinos sowohl zu niedrigeren als auch zu höheren Energien hin gegenüber dem aktuellen IceCube Detektor zu erweitern.

Während die kompakte, dicht instrumentierte Niedrigenergiekomponente, unter anderem, zur Messung der Neutrinomassenhierarchie verwendet werden soll, wird die Suche nach Neutrinopunktquellen eine der Zielsetzungen der Hochenergiekomponente sein.

Eine wesentliche Steigerung der Sensitivität von IceCube-Gen2 wird dabei von neuen optischen Sensoren erwartet. Eines der vielversprechendsten Designs ist hierbei das sogenannte multi-PMT-Modul. Optische Module nach diesem Konstruktionsprinzip wurden erstmals im KM3NeT Detektor realisiert. Sie bestehen aus einer Anordnung mehrerer kleiner Photomultiplier innerhalb eines transparenten Druckkörpers, was, durch eine effektive Segmentierung der sensitiven Fläche, einige Vorteile gegenüber dem konventionellen Design mit einem großen PMT bietet, darunter eine vergrößerte effektive Fläche, eine gleichmäßige Raumwinkelabdeckung sowie intrinsische Richtungssensitivität und eine Erweiterung des dynamischen Signalbereichs.

Im Rahmen der vorliegenden Dissertation wurde die Entwicklung eines multi-PMT Digitalen Optischen Moduls (mDOM) für den Einsatz im IceCube-Gen2 Detektor aufgenommen, die nach derzeitigem Stand innerhalb eines Jahres in die Fertigstellung eines voll funktionsfähigen Prototyps münden wird. Die Arbeiten umfassten, neben Testreihen zur detaillierten Charakterisierung zentraler Hardware-Komponenten, sowohl Simulationsstudien zur Druckstabilität und Leistungsfähigkeit des Moduls, als auch Vorarbeiten für die Prototypkonstruktion.

Abstract

Inspired by the discovery of a comogenic high-energy neutrino flux in IceCube, plans are under way for the construction of new neutrino observatory at the South pole. This next-generation neutrino telescope, IceCube-Gen2, will expand the sensitivity range to lower as well as towards higher neutrino energies with respect to the currently operating IceCube detector.

While the compact and densely instrumented low-energy component will, amongst other questions, address neutrino mass hierarchy, the large-volume high-energy array primarily aims at the first detection of neutrino point sources.

A substantial increase of detector sensitivity is expected from the employment of novel optical sensors. One of the most auspicious of the new designs is based on the multi-PMT concept first introduced in the KM3NeT detector. As indicated by its name, a multi-PMT optical module houses, inside a transparent pressure vessel, an array of small-size PMTs. The effective segmentation of the sensitive area entails some attractive advantages compared to the conventional layout featuring a single large-area PMT. Most prominent among those advantages are an increased effective area uniformly covering the solid angle, an extended dynamic range, as well as intrinsic directional sensitivity of the module.

Within the scope of this thesis, the development of a dedicated multi-PMT Digital Optical Module for IceCube-Gen2 has been advanced from the original ideas to a stage where the realization of a first fully featured and working prototype is expected within a year. The reported work includes testing and detailed characterization of key hardware components, simulation studies concerning pressure stability and performance capabilities, as well as first steps towards the construction of a prototype of the novel module.

Contents

Preface

When Victor Hess boarded his baloon in the morning of August 7th, 1912, little did he know that this was not only the beginning of an experimental flight, but also of a journey that would last a century: The quest for the origins of the Cosmic Rays he was about to discover. Charged particles of the highest energies (up to $\sim 10^{21}\,\mathrm{eV}$) bombard Earth's atmosphere on a daily basis, but their sources and the mechanisms by which they gain their extreme energies are wrapped in mystery up to the current day. Being charged and, as a consequence, susceptible to magnetic fields they lose all information on the direction of their origin arriving at Earth. Leptonic as well as hadronic acceleration processes are considered, but unfortunately the most obvious messengers from possible sources, high energy photons, can not provide a final verdict.

It is this desperate situation that neutrinos, the tiniest and least interactive particles in the universe come to the rescue. The detection of neutrinos from the potential locations of these cosmic accelerators would be “smoking gun” signature, allowing to understand the underlying processes and hereby solve the long standing mystery. But their main advantage, being feebly interacting only, also makes neutrinos downright hard to detect.

The path towards the use of neutrinos as comic messengers was a hard and sturdy one. After a viable method was suggested, using natural aggregations of water as a detector volume, cosmic neutrinos still kept eluding the scientists. With time, it became clear that increasingly large volumes of water would have to be instrumented. Planning a km^3 sized neutrino telescope in the depths of the Pacific off the cost of Hawaii members of the DUMAND collaboration thought big, yet ultimately failed, as technical but also political difficulties stood in their way. But it was worth the effort: Since the finally successful first reconstruction of an up-going muon track, the unambiguous signature of a muon neutrino, in Lake Baikal the learning curve began to steepen. And it was in 2013, roughly a century after Hess' historic flight, that we were finally able to witness the detection of the first cosmogenic neutrinos in IceCube.

Ernie and Bert [1], later accompanied by roughly two-score of Muppets, opened the door and granted us a glimpse of the promised land. To walk, and explore, this land we are currently planning a new powerful telescope featuring roughly ten times the volume, and thus sensitivity of IceCube[1]. For the first time in history a neutrino detector will actually live up to the term “neutrino telescope”[2], indicating a device investigating distinct cosmic sources and not merely the flux of the messenger particles. Thus being the first of a new generation, the envisaged observatory was named IceCube-Gen2. With the construction of this discovery machine we will, at last, herald the advancing era of neutrino astronomy.

But great discoveries await not only on cosmic but also on sub-atomic scales: Neutrinos can not only be messengers from fascinating objects in deep space, but a fascinating field in their own right. Having been observed to engage is the mechanism of neutrino oscillation, they were unequivocally found to have mass. This property[3] was unasked for in the scope of the Standard Model of particle physics. And while sophisticated

---

[1] Which as of now is itself, with a volume of $\sim 1\,\mathrm{km}^3$, by far the largest neutrino detector in the world.

[2] Actually all neutrino telescopes so far have fallen short of fulfilling this claim, if not considering the singular detection of SN 1987A.

[3] Winning T. Kajita and A. B. McDonald the Nobel Prize in 2015.

detectors at CERN and elsewhere continue to search for physics beyond the Standard Model, neutrino oscillations are so far the only manifestation of such. After detailed investigation by dedicated experiments the oscillation parameters, as well as the absolute mass differences, are known. However the mass ordering, or as it has become known, the neutrino mass hierarchy, that is to say the actual sign of the differences, remains an open question. Even though being “only” a sign, this parameter is crucial for the interpretation of information obtained by other neutrino experiments and for constraining theoretical models aiming to explain the origin of mass itself in the leptonic sector. A possibility to access neutrino mass hierarchy is to study the differences in the oscillation probabilities of low energy atmospheric neutrinos and anti-neutrinos as they are affected differently when propagating through the interior of the Earth. Representing the low-energy part of the IceCube-Gen2 observatory, PINGU, the Precision IceCube Next-Generation Upgrade[1], will observe the feeble modulations of the atmospheric neutrino flux with the required precision.

But how to build such a detector? In theory the idea sounds rather simple: All one needs is a large volume of water, or say, a giant ice cube, instrumented by some sort of precision light sensors, forming a three-dimensional array, to capture the weak Cherenkov light signatures of the charged secondaries of the neutrinos. To make it work however is the hard thing. Keep in mind that it was hardware failures that stopped the ambitious DUMAND project in the first place. Tremendous amounts of research and work has since been dedicated to finding the best technical solutions and scientists had to go to the harshest locations in the world: the dark abyss of deep sea as well a the cold of Antarctica to look at the sky in a whole new light of neutrinos.

Until recently the optical modules, the eyes of the neutrino telescope, were in principle identical for all the detectors world-wide, consisting of a glass pressure vessel, housing a single large-area photomultiplier. The idea in IceCube-Gen2 is to not only enhance the volume or instrumentation density, depending on the sub-array, but also to employ novel optical sensor technology. One of these new sensors is the so-called multi-PMT optical module developed in the scope of this thesis. Implying an array of small-size PMTs inside a pressure vessel, rather than a single large one, the application of the multi-PMT concept will enhance the sensitivity of the newly planned telescope at its most basic unit, the individual optical module. And it is not only the mere sensitivity, in terms of effective area, that will be at least doubled with respect to the current baseline design and also distributed uniformly over the entire solid angle. Apart from that, the segmentation of sensitive area will add intrinsic directional sensitivity, enable digital photon counting, and enhance overall output linearity as well as performance uniformity on a module-by-module basis, which provides better agreement between simulation and reality. All these advantages will increase the sensitivity, precision and thus finally the discovery potential of the new detector infrastructure.

For centuries mankind has been looking at the sky. With each new messenger we gained in knowledge and understanding of the universe. No one knows what exactly lies ahead but the construction of the new neutrino observatory will be a first step towards a fascinating future. IceCube-Gen2 will not only explore the highest but also the lowest neutrino energies and, in both regimes, look where no neutrino telescope has looked before. I feel

---

[1] A densely instrumented small-volume array located inside the perimeter of the current IceCube detector.

honored to have the opportunity to add my humble contribution to this great collective endeavor.

The thesis at hand is structured as follows:

An overview of the basic concepts of neutrino (astro-) physics followed by the general layout and operation principles of neutrino telescopes, as well as an introduction to the functionality of photomultipliers and common techniques and definitions to assess their properties is given in the first part of the document.

The second part is concerned with the contributions by the author to the prototyping of the novel multi-PMT optical module for IceCube-Gen2. It includes PMT prototype characterization, as well as designing and testing of components, introducing experimental setups and respective results. Corresponding chapters are followed by an introduction to the optical module simulation tool developed in the scope of this thesis and its application in various studies of module properties, in particular comparing its expected performance to the respective properties of a single-PMT design.

The work is concluded by the introduction to two preliminary calibration studies and the path towards the construction of a first prototype.

Part I

Basics

1 Neutrino astrophysics

Extensive review articles on the topics of cosmic radiation and neutrino astrophysics can be found in [2], [3], and [4]. A compact introduction to cosmic rays is given in [5]. Being around for some decades, the subject is also covered by several textbooks such as [6].

1.1 Neutrino properties

Neutrinos are elementary particles that do not interact much with the rest of the universe. For means of illustration: billions of neutrinos will have passed through the reader by the end of this sentence, originating mostly from the sun, but also from cosmic rays, nuclear power plants and deep space (see section 1.2 for details), but only up to two neutrino-induced reactions are expected to happen inside the reader's body during lifetime. Even though they are the most abundant fermions in the universe, the existence of neutrinos only became apparent in 1930, when W. Pauli introduced them as an additional neutral particle into the mechanism of beta decay in his famous address to the *"Dear Radioactive Ladies and Gentlemen"* of Tübingen [1]:

$$ {}^{\mathrm{A}}_{\mathrm{Z}}\mathrm{X} \rightarrow {}^{\mathrm{A}}_{\mathrm{Z+1}}\mathrm{Y} + \mathrm{e}^- + \bar{\nu}_\mathrm{e} \tag{1.1} $$

It was an ad-hoc measure to explain the continuous energy spectrum of beta electrons without abandoning energy and momentum conservation on subatomic scale. Pauli himself expected the neutrino to be impossible to detect[2]. The reason for the neutrino's elusiveness is that it only engages in weak interactions (as well as in gravitational ones, which can be safely neglected in the scope of particle physics). In spite of the unfavorable prognosis by its "inventor", the neutrino was actually detected in 1956 by C. Cowan and F. Reines, observing the inverse beta decay of reactor electron anti-neutrinos [9, 10]. Today, neutrinos together with the electron, the muon, and the tauon (or simply tau) constitute the lepton class of the Standard Model of particle physics (illustrated in figure 1.1).

They come in three flavors, ν_e, ν_μ[3] and ν_τ[4], corresponding to their charged counterparts. While not required to have mass by the Standard Model, and for a long time assumed to be mass-less (which had the nice effect of simplifying theoretical calculations), neutrinos were finally found to have in fact small masses (below 2.2 eV in the case of the electron neutrino), when several "neutrino deficits" were explained by the mechanism of neutrino oscillations[5]. These oscillations occur due to the circumstance that, for neutrinos, the eigenstates of the free-particle Hamiltonian (which are associated with mass) are not

---

[1] Address to Group on Radioactivity of Tübingen, December 4, 1930 (unpublished). Regarding his idea premature, Pauli did not publish a final paper until 1934 [7].

[2] *"I have done a terrible thing: I have postulated a particle that cannot be detected."* W. Pauli, 1930 quoted from [8]

[3] Discovered in 1962 [12].

[4] Discovered in 2000 [13].

[5] The solar neutrino deficit emerged in 1968 when the measured flux of electron neutrinos from the Sun failed to match the predictions of the standard solar model roughly by a factor of three [14]. Another deficit, also known as "atmospheric neutrino anomaly", was found in the relative composition of atmospheric electron and muon neutrinos measured with Kamiokande [15], IMB [16] and other detectors,

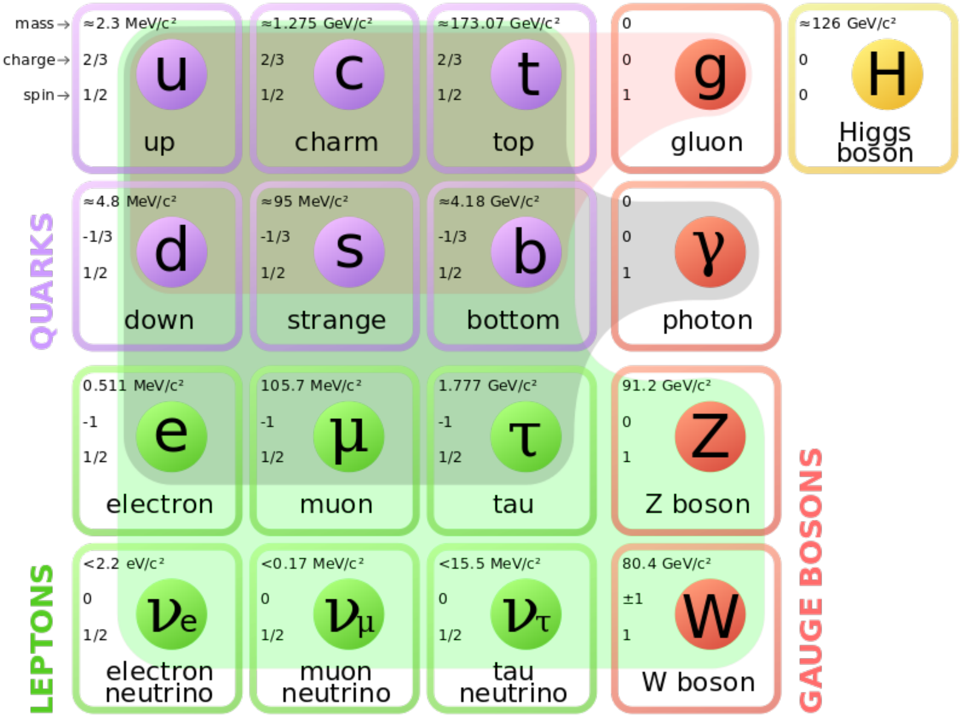

Figure 1.1: The Standard Model of elementary particles and force quanta (gauge bosons), featuring their main properties. Colored backgrounds connect quarks and leptons taking part in fundamental interactions (*red*: strong interaction, *blue*: electromagnetic interaction, *green*: weak interaction) to the respective mediators. Taken from [11].

identical to the eigenstates of the weak interaction, which define the flavor. In other words, neutrinos interact as either electron, muon, or tau neutrino (flavor eigenstates), but propagate as a superposition of the mass eigenstates ν_1, ν_2 and ν_3. Consequently a flavor eigenstate $|\nu_\alpha\rangle$ can be expressed as

$$|\nu_\alpha\rangle = \sum_{i=1}^{3} U_{\alpha i}\,|\nu_i\rangle \tag{1.2}$$

Both sets of eigenstates are connected (mixed) by a unitary matrix $U_{\alpha i}$, named “Pontecorvo–Maki–Nakagawa–Sakata matrix” (PMNS matrix) after the main contributors to the theory. This mixing can be parametrized as a rotation, using three angles (θ_{12}, θ_{23} and θ_{13}) and one phase δ_{CP}[1]. One possible representation of the PMNS matrix U_{PMNS} is

---

beginning in the mid-1980s. Around the turn of the millennium, the combined results of next-generation detectors Super-Kamiokande [17] and SNO [18] established neutrino flavor oscillations to be the explanation for these apparent deficits. For this discovery, which also implies that neutrinos (at least two of them) must have a non-zero mass, T. Kajita and A. McDonald were awarded the Nobel Prize in Physics in 2015.

[1] This is true assuming neutrinos are Dirac and not Majorana particles. If found to be non-zero, δ_{CP} introduces charge-parity violation in the lepton sector. Majorana particles would allow for two additional phases.

then given by:

$$\begin{pmatrix}\nu_e\\ \nu_\mu\\ \nu_\tau\end{pmatrix} = \overbrace{\underbrace{\begin{pmatrix}1 & 0 & 0\\ 0 & c_{23} & s_{23}\\ 0 & -s_{23} & c_{23}\end{pmatrix}}_{\text{atmospheric}} \underbrace{\begin{pmatrix}c_{13} & 0 & s_{13}e^{i\delta_{\mathrm{CP}}}\\ 0 & 1 & 0\\ -s_{13}e^{i\delta_{\mathrm{CP}}} & 0 & c_{13}\end{pmatrix}}_{\text{reactor}} \underbrace{\begin{pmatrix}c_{12} & s_{12} & 0\\ -s_{12} & c_{12} & 0\\ 0 & 0 & 1\end{pmatrix}}_{\text{solar}}}^{U_{\mathrm{PMNS}}} \cdot \begin{pmatrix}\nu_1\\ \nu_2\\ \nu_3\end{pmatrix} \tag{1.3}$$

with the abbreviations $c_{ij} = \cos\theta_{ij}$ and $s_{ij} = \sin\theta_{ij}$. Labels below the sub-matrices indicate the respective origins of neutrinos usually used to investigate experimentally the corresponding mixing angles.

Considering, for clarity of the argument, only two flavor mixing (e.g. mixing of electron and muon neutrinos by the solar sub-matrix with a single mixing angle θ_{12}) the probability $P(\nu_e \to \nu_\mu)$ to measure a muon neutrino at the distance L when an electron neutrino was emitted can be expressed as

$$P(\nu_e \to \nu_\mu) = \sin^2(2\theta_{12}) \cdot \sin^2 \frac{(m_1^2 - m_2^2)c^3 L}{4\hbar E} \tag{1.4}$$

where $\hbar$ is the reduced Planck constant, E is the neutrino energy and m_i^2 are the respective mass squares of the involved mass eigenstates. From the above equation it becomes obvious, that oscillations can only occur if neutrinos indeed feature a non-identical mass, resulting in at least two massive neutrinos in the three-flavor case. Another feature of neutrino oscillations reflected by the equation is its insensitivity to the sign of the mass difference term.

The above discussion applies to neutrino oscillations in vacuum. When however neutrinos travel through matter, for instance inside the Sun or crossing the Earth, the oscillation probabilities are modified. This so-called Mikheev-Smirnov-Wolfenstein (MSW) effect [19, 20] arises from the fact that, while muon and tau neutrinos travel through matter unaffected, electron neutrinos can weakly interact with contained electrons. Neutrino-electron interaction results in an additional effective mass term and the modification of the mixing angles depending on the electron density and the energy of the neutrinos. In addition, sharp variations of the electron density, as expected at Earth's mantle-core interface, give rise to "parametric enhancement" of oscillation probabilities based on resonances [21]. This effect has to be taken into account e.g. when analyzing solar neutrino fluxes or atmospheric neutrinos from below the horizon.

At present, the sines of the mixing angles and mass square differences have been measured with good precision by various experiments (see [25] and references therein). Nevertheless, several open questions remain, such as whether neutrinos are Dirac or Majorana particles, if there is charge parity violation, i. e. $\delta_{\mathrm{CP}} \neq 0$, or regarding the existence of additional sterile neutrino states. Another pressing question concerns the so-called mass hierarchy. While mass square differences of the neutrino mass eigenstates are known, their order in terms of absolute values can have different configurations (see figure 1.2 for illustration of alternatives). As it seems a "natural" choice to associate the lightest neutrino with the lightest charged lepton, the corresponding configuration ($m_1 < m_2 < m_3$) is called normal hierarchy[1]. Normal hierarchy is the case in the quark sector where (see figure 1.1)

---

[1] As discussed earlier, neutrino flavors are not directly associated with mass. It is therefore not really

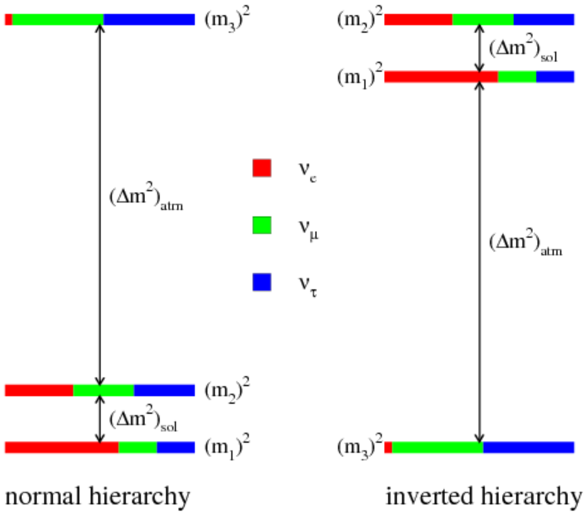

Figure 1.2: Sketch of the two considered alternatives for the neutrino mass hierarchy after the sign of $\Delta m^2_{12} \approx \Delta m^2_{\mathrm{sol}}$ the has been determined to be positive resulting in $m_1 < m_2$ [22]. The color coding indicates the fraction $|U_{\mathrm{PMNS}\,\alpha i}|^2$ of each distinct flavor ν_α, $\alpha \in \{\mathrm{e}, \mu, \tau\}$, contained in each mass eigenstate ν_i, $i \in \{1, 2, 3\}$. Taken from [23].

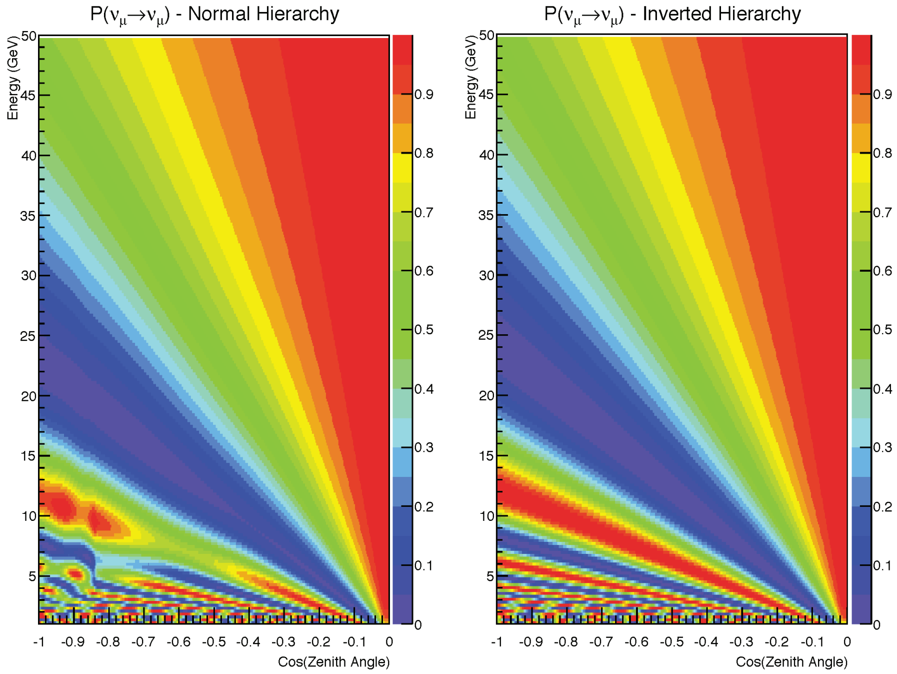

Figure 1.3: Muon neutrino survival probability after traveling through the earth, binned in both neutrino energy and cosine of the zenith angle. (A path directly through the center of the Earth corresponds to $\cos\theta = -1$.) The survival probabilities for antineutrinos in a given hierarchy are essentially the same as those for neutrinos under the opposite hierarchy. Taken from [24].

both, lighter and heavier members of each family increase in mass simultaneously, but it is not a priori clear that leptons follow the same pattern. Plans to determine the hierarchy experimentally aim at precise measurements of oscillation probability modifications by the MSW effect which is sensitive to the order of masses. This way the order of m_1 and m_2 was established to be $m_1 < m_2$ from the oscillation of solar neutrinos [22]. An example of the oscillation signature of the two hierarchies is shown in figure 1.3. Any detector featuring appropriate energy and directional precision and sensitivity to resolve the structures of the shown oscillograms is, in principle, able to determine the hierarchy. This goal is currently pursued by several scientific collaborations around the globe. Among them are underground Cherenkov detectors like Hyper-Kamiokande [26], as well as the low-energy neutrino telescopes PINGU and ORCA, discussed in more detail in sections 2.2.2 and 2.4.

Beyond being itself an important still free parameter of the Standard Model, it turns out that the mass ordering of neutrinos has deep connections to other physics topics: Determination of the neutrino mass hierarchy will allow to rule out the corresponding class of theoretical models, dealing with the unification of elementary forces and the development of the early universe, predicting the wrong mass hierarchy. It will also entail a better understanding of interaction processes taking place inside a supernova. Furthermore, the hierarchy is important for determining whether neutrinos are Majorana particles, being their own anti-particle, which would be itself a discovery of profound significance. Finally knowing the neutrino mass hierarchy would facilitate measurements of the charge parity violating phase and also allow to investigate differences in the oscillation behavior of neutrinos and anti-neutrinos, which in their turn have implications for the long-standing question of matter-antimatter asymmetry [26].

Apart from being an object of basic research in particle physics, their low interaction rates[1] make neutrinos ideal astrophysical messengers which allow to probe dense environments, such as the interior of the sun, accretion discs or dust clouds. While photons can be absorbed or scattered in the interstellar medium and charged particles lose directional information due to deflection by magnetic fields, neutrinos are able to travel long distances virtually unaffected, pointing back to their sources. Of course, the low interaction probability has an important drawback: In the same manner as they travel the universe, neutrinos cross a detector without leaving a trace. Sophisticated indirect techniques, discussed in more detail in chapter 2, had to be developed in order to be able to see the universe in the new “light” of neutrinos.

1.2 Neutrino sources

Neutrinos present on Earth originate from a variety of sources (see figure 1.4 for the energy spectrum of different source populations). Among them, sorted by energy of the produced neutrinos in ascending order, are

---

applicable to define a mass of e.g. an electron neutrino. The argument for the “normality” of this hierarchy is based on the fact that, as shown in figure 1.2, each mass eigenstate has one dominant flavor component.

[1] The cross-section $\sigma_{\nu p}$ for neutrino-proton interactions scales like $\sim E_\nu \cdot 10^{-38}\,\mathrm{cm}^2$ with neutrino energy E_ν [27]. For a more detailed presentation of cross-sections relevant for neutrino telescopes see figure 2.2.

- **relic neutrinos**: Featuring the lowest energies, between μeV and meV, primordial cosmological neutrinos are relics of the Big Bang, emitted two seconds after the event[1]. Although they are expected to outnumber by far neutrinos from any other source, practicable ideas to measure these neutrinos are only beginning to be developed, due to the extremely small interaction cross-section [28].

- natural **radioactive decays**: Neutrinos originating in $\beta^{\pm}$ decays of radioactive isotopes (see equation 1.1), such as ^{40}K, feature energies on the scale of a few MeV. These neutrinos are produced in the entire environment containing traces of radioactive materials. So-called "geo-neutrinos" produced in decays taking place deep inside the Earth have also been recently reported [29].

- **nuclear reactors**: Unstable intermediate products of induced nuclear fissions, responsible for generating the thermal power of the reactor, undergo a series of β^{-} decays until they reach a stable configuration. Thus, atomic power plants shine brightly in the "light" of low-MeV electron anti-neutrinos. This flux can be used e.g. to set up particle physics experiments, as done in the past by Cowan [9] and Reines [10] or more recently by several collaborations, such as RENO [30], Daya Bay [31] or DoubleCHOOZ [32], or monitor reaction rates in the scope of non-proliferation agreements [33].

- the **Sun**: Apart from the relic flux mentioned above, our central star is the most yielding source of neutrinos reaching Earth. Solar neutrinos, featuring typical energies from keV up to some ten MeV, are "by-products" of the fusion of hydrogen into helium that powers the Sun's energy output. The net reaction can be written as

  $$4\,{}^{1}_{1}\mathrm{H} \rightarrow {}^{4}_{2}\mathrm{He} + 2\,\mathrm{e}^{+} + 2\,\nu_{\mathrm{e}} \tag{1.5}$$

  while eventually it takes place via several intermediate stages and catalysts with the exact mechanism (either pp-chain or CNO cycle) strongly depending on the temperature and pressure in the center of the star [34].

- **core-collapse supernovae**: When a massive star (10 – 25 solar masses) has reached the end of its lifetime and no more energy can be gained from nuclear fusion (with the nuclear binding energy decreasing once iron is reached) it will collapse due to the lack of radiation pressure needed to counter-balance gravitation. The infalling outer layers of the star will compress the core resulting in the formation of a compact massive object (either a neutron star or a black hole, depending on the mass of the progenitor). Reflection of the shock wave at the massive core leads to a severe explosion making the star shine as bright as a whole galaxy for a short time. During the collapse of the core, neutrinos (typical energies MeV – GeV) are produced in the inverse beta decay (neutronization of the matter) which leave the star some hours before the final explosion. Most of the gravitational energy of the collapse is actually released in the form of neutrino emission. Neutrinos from the supernova **SN1987A** in the Large Magellanic Cloud have been recorded by three detectors around the world[2] making it the second extraterrestrial source[3] of neutrinos to be observed, after the Sun [37].

---

[1] Their spectrum fits that of a black body at 1.9 Kelvin making them the leptonic version of the 2.7 Kelvin microwave background.

[2] Kamiokande in Japan [35], IMB in the USA [36] (both water Cherenkov detectors) and the Baksan scintillation detector in the Soviet Union.

[3] Neutrino astronomy has thus already become reality in the MeV energy range, albeit, as of now with only two sources.

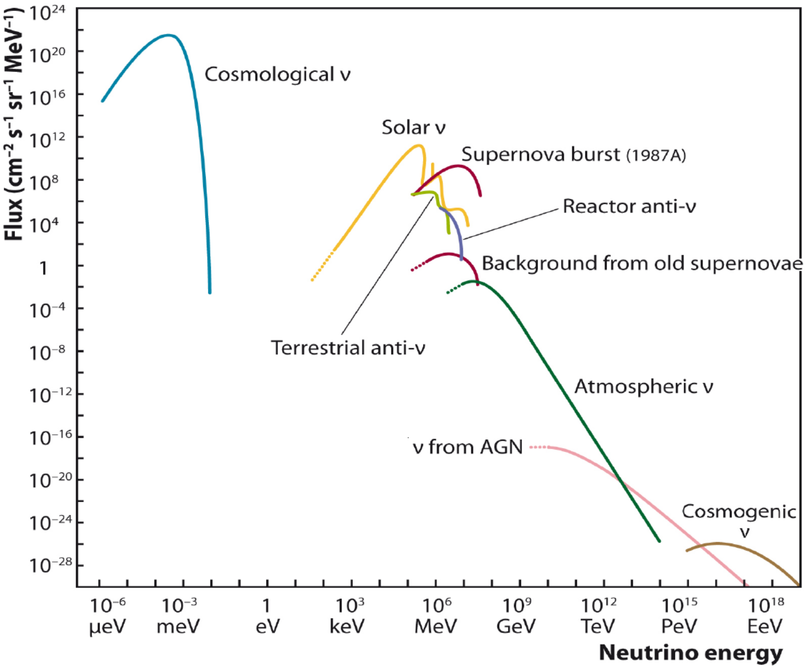

Figure 1.4: Overview of measured and expected neutrino fluxes shown for various sources, natural and artificial. Further information on selected sources is given in the text. The energy range from keV to several GeV is covered by underground detectors. The high energy region beginning from several ten GeV, comprising neutrinos of atmospheric and cosmic origin, is targeted by large volume neutrino telescopes presented in sections 2 and 2.4. Figure taken from [27].

- **Earth's atmosphere**, as well as
- **deep space**

Not included in the above compilation are potential neutrinos from the interaction of dark matter as their production mechanisms and energies are strongly model-dependent. Neutrinos from the two latter sources, which are, or will be in the near future, addressed by large volume neutrino telescopes (see sections 2.2 and 2.4 for details), are directly or indirectly linked to **cosmic rays**. The following sections will therefore introduce cosmic radiation and shed some light on the nature of its relation to the high energy neutrino flux on Earth.

1.3 Cosmic rays

Although the Earth is a target to millions of charged cosmic particles on a daily basis, it took till 1912 until people became aware of it: After the discovery of ionizing radiation by the end of the 19th century V. F. Hess soared up to a height of 5350 meters above sea level using a balloon in order to test a then widely accepted theory assuming radioactive decays inside the crust of the Earth to be the only origin of the natural background radiation. The unexpectedly observed increase of the flux of ionizing radiation with height was correctly interpreted by Hess as being a sign of *"a strongly penetrating radiation entering* *our atmosphere from above"* [38]. In the course of roughly one century since this discovery the knowledge on the cosmic rays has increased considerably. For some decades, prior to the construction of powerful accelerators, cosmic radiation continued to provide a natural laboratory for high energy particle physics [39]. Numerous results such as the discovery of the muon in 1936 [40] trace back to cosmic ray experiments.

Today, the energy spectrum and **chemical composition** are known to great detail: With the relative abundances being almost independent of energy[1], the charged primary cosmic rays[2] consist of roughly [25, 4]

- 79% **protons**,
- 8% **α particles**,
- few % **heavier nuclei**, e.g. iron,
- and traces of **electrons**, **positrons**, and **anti-protons**.

The **energy spectrum** was explored spanning several orders of magnitude up to 10^{21} eV. Over a large range of energies the all-particle flux follows a simple broken power-law

$$\frac{dN}{dE} \propto E^{-n} \tag{1.6}$$

(see figure 1.6, left) with an exponent of $n \approx 2.7$ which changes its value in the region of approximately between 10^{15} eV and 10^{16} eV to ~ 3. This softening of the spectrum is usually referred to as the **knee**[3]. The feature is widely accepted to be due to different sources of particles above and below the knee. Radiation above the knee (lower energies) is assumed to originate mostly in galactic supernovae, whereas the more energetic particles below are likely produced in other galactic sources gradually running out of power, with increasingly extra-galactic contributions (see section 1.5 for details). Another feature, a hardening of the spectrum back to $\sim E^{-2.7}$ around $10^{18.5}$ eV named **"ankle"**, potentially marks the transition to a further, purely extra-galactic, source population as at these energies all known galactic sources reach their acceleration limit and the gyro-radius of the particles exceeds the size of the Milky Way. For further details on the flux and its features, see a dedicated review in [25].

At even higher energies ($> 10^{19}$ eV) the spectrum is expected to decline sharply due to the onset of the GZK effect leading to the so-called **GZK cutoff**. This effect, named after K.

---

[1] There is indication of the abundance of heavier elements increasing with energy. Also, the cosmic ray composition at the highest energies is still under debate, with protons and iron nuclei being proposed as alternative major constituents.

[2] In the scope of this work all particles arriving the edge of the atmosphere will be considered primaries while the constituents of the resulting air showers are named secondary. An alternative naming convention (used e.g. by the Particle Data Group [25]) reserves the primary tag for the initially accelerated particles with all particles produced in interactions of these primaries, be it in space or on Earth, referred to as secondaries.

Also the term "cosmic rays" itself can be ambiguous: In some conventions it is used with an extended meaning, comprising gamma photons and neutrinos in addition to charged particles. In this work it will refer to the charged component only.

[3] A second knee-like feature observed at roughly $8 \cdot 10^{16}$ eV is explained by a possible transition to heavier primaries [41].

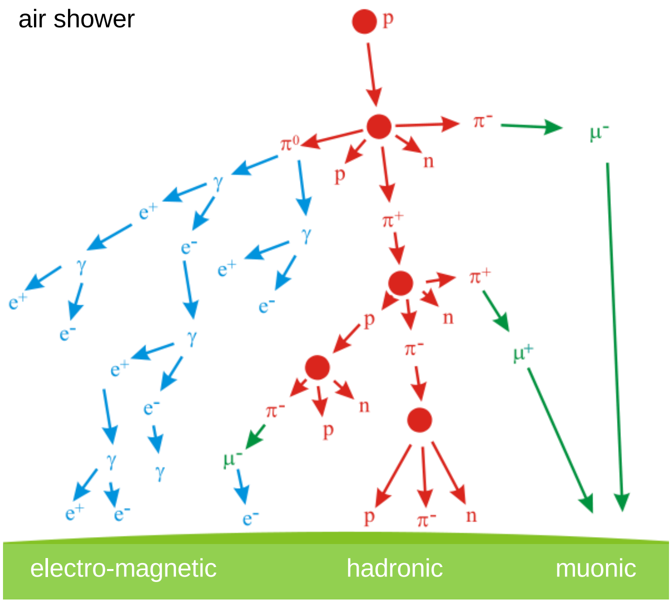

Figure 1.5: Schematic sketch of processes leading to the development of air showers induced by primary cosmic rays in the atmosphere. Depending on the involved particles and processes the shower can be subdivided into an electromagnetic (*blue*), a hadronic (*red*) and a muonic component (*green*). Figure taken from [51], modified.

Greisen, G. T. Zatsepin, and V. A. Kuz'min who first predicted it in 1966 [42, 43], describes the interaction of protons with the photons of the cosmic microwave background forming Δ^+ resonances. This process only occurs at proton[1] energies exceeding $\sim 6 \cdot 10^{19}$ eV. Strongly increasing the interaction cross-section it effectively limits the range of the high energetic protons to roughly 60 Mpc. After a period of debate and controversial results [44, 45], the existence of the GZK cutoff was confirmed unambiguously in 2010 by the Pierre-Auger Observatory [46, 47, 48]. The Δ^+ particles formed in the interaction predominantly decay into nucleons and pions, referred to as photopion generation, producing neutrinos and gamma photons in their final states:

$$\begin{aligned} p + \gamma \rightarrow \Delta^+ &\rightarrow p + \pi^0 \\ \pi^0 &\rightarrow \gamma + \gamma \end{aligned} \tag{1.7}$$

$$\begin{aligned} p + \gamma \rightarrow \Delta^+ &\rightarrow n + \pi^+ \\ \pi^+ &\rightarrow \mu^+ + \nu_\mu \\ \mu^+ &\rightarrow \mathrm{e}^+ + \nu_\mathrm{e} + \bar{\nu}_\mu \end{aligned} \tag{1.8}$$

These **GZK neutrinos** [49], featuring energies from 10^{16} eV to 10^{18} eV [50], are subject to observations by neutrino telescopes. They are part of the deep space neutrino population mentioned in the previous section, identified “cosmogenic neutrinos” in figure 1.4.

1.4 Atmospheric neutrinos

When an air molecule in the upper atmosphere is hit by highly energetic cosmic rays it will give rise to a particle cascade, referred to as **“air shower”**. In a rather complicated (and still not understood in full detail) sequence of hadronic, electromagnetic, and weak interactions, depending on the kind of incident and target particles but also on environmental

---

[1] Heavier nuclei can additionally lose energy via photo-desintegration.

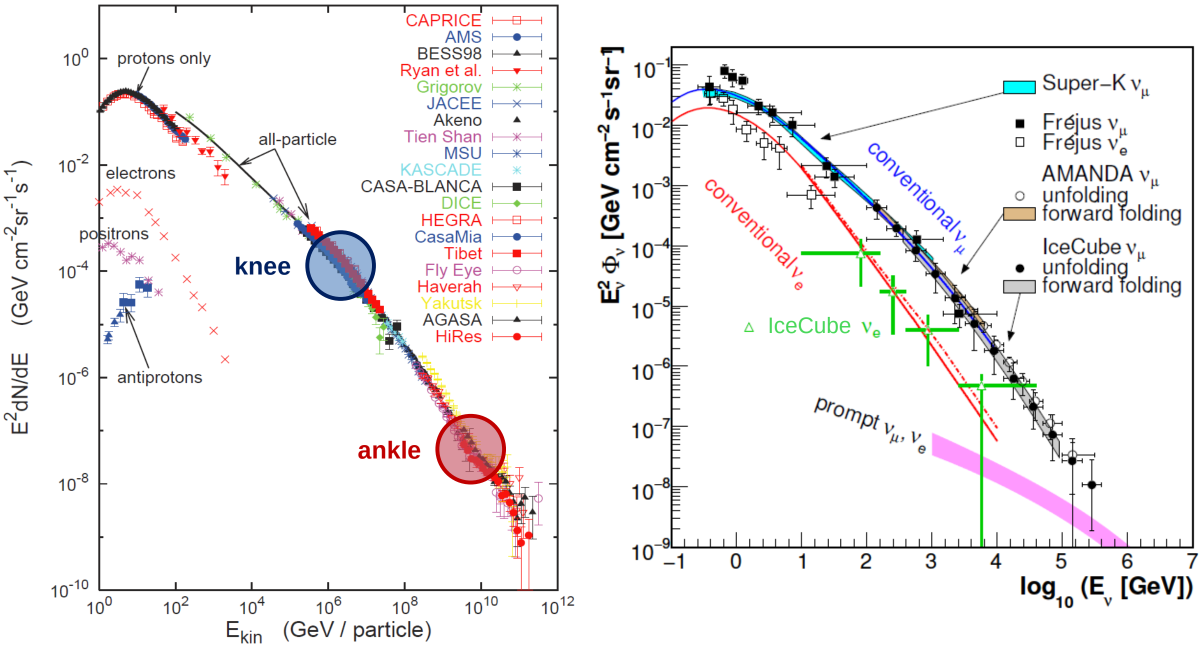

Figure 1.6: **Left**: All particle spectrum of the charged cosmic radiation. Figure taken from [5], modified. **Right**: Theoretical predictions and measurements of the energy spectrum of atmospheric neutrinos featuring the conventional and prompt components of the flux. Taken from [52], modified.

parameters such as humidity and air pressure, the energy of the primary is used to create huge numbers (of the order of millions) of a variety of (mostly exotic and short-lived) particles and distributed among them. These cascades constitute the natural atmospheric particle lab mentioned earlier. The shower has a hadronic core, emitting electromagnetic sub-showers, generated mostly in the decays of neutral pions ($\pi^0 \to \gamma + \gamma$). The resulting electrons/positrons account for the majority of the charged particles in the shower, outnumbering (by an order of magnitude) the muons, produced by decaying charged mesons (e.g. charged pions as given by equations 1.9 and 1.10). At ground level the “foot-prints” of air showers cover vast areas and can be measured by extended detector arrays, such as the Pierre Auger Observatory [46].

The **atmospheric neutrinos** emerging from air showers are mostly liberated in the decays of unstable intermediate particles (such as kaons and pions). The main reaction for their production is charged pion decay:

$$\pi^+ \to \mu^+ + \nu_\mu \to \mathrm{e}^+ + \nu_\mathrm{e} + \bar{\nu}_\mu + \nu_\mu \tag{1.9}$$

$$\pi^- \to \mu^- + \bar{\nu}_\mu \to \mathrm{e}^- + \bar{\nu}_\mathrm{e} + \nu_\mu + \bar{\nu}_\mu \tag{1.10}$$

This process results in the so-called **conventional** atmospheric neutrino spectrum (see figure 1.6, right) with a flavor ratio of

$$\nu_\mathrm{e} : \nu_\mu : \nu_\tau = 1 : 2 : 0 \tag{1.11}$$

not making the distinction between neutrinos and anti-neutrinos, which is indeed not possible in a neutrino telescope (see chapter 2).

The energy spectrum of the pions and muons is proportional to that of the cosmic primaries, i.e. approximately following $E^{-2.7}$, as is the spectrum of the atmospheric neutrinos over a wide energy range[1]. Figure 1.6 illustrates well this circumstance. With increasing neutrino energies however, a deviation of the power law occurs. This is caused by highly energetic secondary muons not decaying in-flight but, due to increasing time dilatation, reaching Earth's surface where they quickly lose energy via electromagnetic interactions or induce showers of low-energy particles instead of transferring the full extent of available energy to neutrinos. It results in a suppression roughly following $1/E$, leading to an effective softening of the spectrum.

There is also expected to be a harder, so far unresolved, component of **"prompt"** neutrinos (see figure 1.6, right), produced by very short-lived charm and bottom secondaries which, even with time dilatation at work, decay "promptly", i.e. without any prior energy loss due to interactions with the surrounding particles. As a consequence, their energy spectrum is directly proportional to that of the primary cosmic radiation ($\sim E^{-2.7}$). Although featuring a smaller scaling factor with respect to the conventional flux, the prompt component is expected to dominate the overall spectrum of atmospheric neutrinos starting from energies above $\sim 10^6$ GeV, where the conventional flux is increasingly depleted [53].

While being a non-reducible background for high-energy neutrino telescopes, atmospheric neutrinos will be a valuable tool to assess the neutrino mass hierarchy (see section 1.1) and to perform Earth tomography.

1.5 Cosmic neutrinos and the origin of cosmic rays

With roughly one hundred years passed after the initial discovery, one of the most fundamental questions concerning cosmic rays yet remains open. It is not clear where and by means of which non-thermal processes the particles gain their enormous energies. Having traveled the interstellar space, the charged particles that arrive at Earth lose any information on the direction of their origin due to deflection by magnetic fields. Bottom-up as well as top-down scenarios have been proposed to account for their existence.

In **top-down** scenarios cosmic rays are assumed to be decay products of ultra-heavy primordial particles or topological defects, such as cosmic strings [54, 55]. These models were strongly disfavored by the first generation of neutrino telescopes [55] as well as by results obtained from large area surface arrays [56].

Today, **bottom-up** mechanisms, where low-energetic particles are gradually accelerated to the observable high energies, appear more promising. Several locations, galactic as well as outside our galaxy, have been suggested for this acceleration to happen. Among them are [3, 4][2]

- **SuperNova Remnants** (SNRs): In addition to the neutrinos mentioned in section 1.2, the detonation of a supernova ejects large amounts of matter at high speeds. Also

---

[1] Neglecting small amounts of energy lost by pions and muons in the atmosphere prior to neutrino production by such mechanisms as scattering, ionization, Bremsstrahlung, or Cherenkov radiation

[2] See also references therein.

the initial particle acceleration can not reach cosmic ray energies, the shock front, developing when the ejecta collide with the interstellar medium can do the trick (see discussion below). Intense gamma radiation from the remnant continues to transfer energy to the shell for some time. In fact, supernova remnants are widely believed to be the main galactic source for the low-energy cosmic rays, in particular in the region above the knee[1] [4].

- **pulsars**: In principle a subclass of the above-mentioned SNRs, pulsars are fast rotating neutron stars featuring strong magnetic fields emitting synchrotron radiation along the field axis. If the magnetic field is off-axis with respect to the rotation of the star, and the emission cone happens to graze the Earth, the object is observable as a periodic source of radio and/or gamma radiation (lighthouse effect). Inside the emission region particles are accelerated to relativistic energies in addition giving rise to shocks [4, 57].
- **micro-quasars** are another potential galactic source of cosmic rays. They are binary systems comprising a neutron star or stellar black hole and an ordinary star, usually in its giant phase. Stable mass overflow from the stellar to the compact companion leads to the formation of an accretion disk and powers relativistic particle jets perpendicular to it. These jets provide a potential environment for cosmic ray acceleration [4, 57].
- **Active Galactic Nuclei** (AGN) are rotating super-massive black holes (up 10^9 solar masses) residing in the center of a galaxy surrounded by an accretion disc and a dust torus. Their "activity" lies in the accretion of matter from the surrounding disc powering two relativistic jets ejected perpendicular to the disc plane. These jets feature knots and hot spots, observable due to their radio emission, which are expected to represent shock environments where particles can be accelerated to high energies.

  AGNs are able to emit photons of various energies, with the disc shining in the optical region and the jets emitting radio and gamma rays. The actually observable spectra are strongly dependent on the angle between the line of sight and the jet axis[2]. Various astronomical phenomena, such as Seyfert galaxies, radio galaxies, quasars, blazars, and BL Lac objects, originally classified by their spectral features and variability, have been recognized to be active galactic nuclei seen under different angles [3].
- **Gamma Ray Bursts** (GRB) are transient phenomena featuring typical lifetimes from milliseconds to several minutes. During this short period of time they emit an intense flux of gamma rays, outshining all other sources in the sky. Their isotropic distribution across the solid angle suggests an extra-galactic origin. Core-collapse supernovae of very massive stars (also called hypernovae) and mergers of compact object[3] binaries are assumed to be accountable for the observed energy output. Both scenarios include the formation of a temporary relativistic jet which, if directed at Earth, is observable as a GRB. Currently, the so-called fireball model, featuring shock creation due to the collision of spherical shells ejected at relativistic velocities is assumed to be the mechanism behind the observed flares [3].

---

[1] Comparison between the power needed to create the observed energy density of cosmic radiation in the galaxy $P_{\mathrm{CR}} \approx 3 \cdot 10^{33}\,\mathrm{W}$ and the total power budget of galactic supernovae $P_{\mathrm{SN}} \approx 3 \cdot 10^{35}\,\mathrm{W}$ results in an energy transfer featuring an efficiency as low as 1% needed to be able to account for particle acceleration. This is regarded as circumstantial "evidence" for supernovae being sources of cosmic radiation [4].

[2] As e.g. the dust torus can block light from the disc and gamma rays are collimated along the jet.

[3] Which can be neutron stars or stellar black holes.

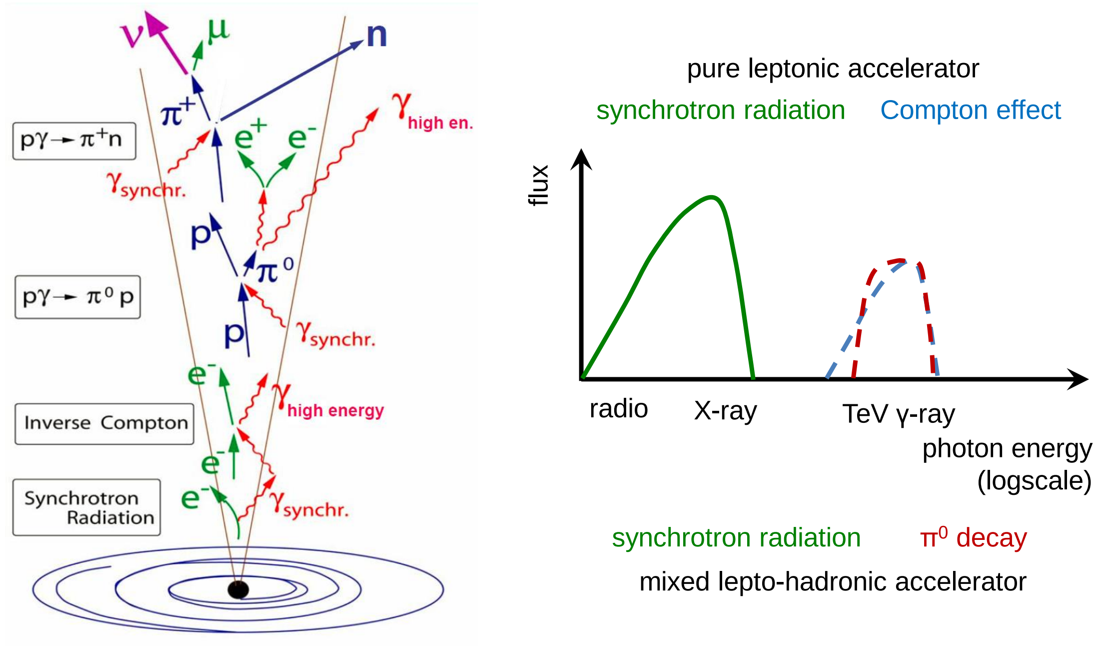

Figure 1.7: **Right**: Mixed leptonic and hadronic acceleration inside a jet with interaction processes potentially taking place. Shown is the case of strong magnetic fields, where only neutral particles can escape the production region. In this scenario, cosmic ray protons are secondaries of primary neutrons [4]. **Right**: Qualitative photon spectrum resulting from a purely leptonic accelerator compared with a mixed lepto-hadronic scenario. The high energy peak is degenerated between the two mechanisms, making it hard to distinguish the models based on photon observation only. Sketch based on plots in [59].

- **starburst galaxies** exhibit an unusually high rate of star formation, as well as of supernova explosions. The superposition of mass ejections by these violent events, together with stellar winds from massive stars, are expected to create collective shock fronts powerful enough to accelerate particles to cosmic ray energies, in particular in the dense central region of these galaxies. The observations of synchrotron radiation in the radio regime and of TeV gamma rays from these regions imply the existence of relativistic electrons [58]. Assuming that protons are accelerated along with these electrons, starburst galaxies are potential candidates for cosmic ray accelerators. Depending on core densities however, these protons may not escape, but give rise to a flux of high energy neutrinos created in proton-proton or proton-gamma interactions (similar to those occurring in the atmosphere, discussed in section 1.4) [3].

A common feature of the above-mentioned locations is the conversion of vast amounts of (in most cases gravitational) energy into kinetic energy of ejected particles and radiation by means of compact massive objects. When these ejecta, being either spherical or focused into a relativistic jet, collide among themselves or with the interstellar medium, shock fronts appear which, in conjunction with magnetic fields, are potentially able to accelerate charged particles to the observed energies. The mechanism of choice is the so-called first-order[1] **Fermi acceleration** [60]. It effectively transfers kinetic energy of the moving plasma to a charged particle through multiple scattering across the shock front region.

---

[1] The order refers to the power-law relation between the maximum achievable particle energy and the velocity of the shock front (see equation 1.12).

Magnetic inhomogeneities on both sides of the front are needed to provide elastic backscattering of the particle without energy loss. For each shock front transition, the particle will gain energy until finally leaving the region. This process can accelerate particles up to a maximum energy of

$$E_{\mathrm{max}} \propto Q \cdot V_{\mathrm{shock}} \cdot B \cdot L \tag{1.12}$$

where Q is the charge of the scattered particle, V_{shock} the velocity of the shock wave, B the magnetic field strength in the acceleration region and L the size of this region [4, 61, 62, 63]. Detailed calculations[1] of the resulting energy spectrum result in a power-law

$$\frac{dN}{dE} \propto E^{-n} \tag{1.13}$$

with a spectral index n varying between 2.0 and 2.3 depending on the particular model. The discrepancy between this original spectrum and the softer $\sim E^{-2.7}$ observed at Earth is due to modulations of the flux during propagation, in particular the leakage of high energy particles from the galaxy [2].

Results from gamma and radio astronomy lead to the conclusion that such acceleration indeed takes place in the case of electrons (**leptonic model**). In the presence of strong magnetic fields, highly energetic electrons get trapped emitting synchrotron radiation. The synchrotron photons can in addition undergo inverse Compton scattering off the electron population ending up at higher energies. This latter process is called synchrotron self-Compton. However, leptonic models offer no explanation for the origin of cosmic ray protons as a mechanism to efficiently transfer energy from accelerated electrons to protons remains unknown.

It is not clear whether also a direct acceleration of protons (**hadronic model**) is taking place. If protons, or even heavier nuclei, are in fact accelerated in those sources, they have to cross through areas of relatively high matter and radiation densities. In so doing they engage in processes similar to those occurring in air shower formation (see section 1.4). The accelerated protons interact with ambient photons (leading to e.g. Δ^+ resonance formation, see equation 1.7) or nucleons N as

$$p + N \to \pi + X, \qquad \pi \in \{\pi^+, \pi^0, \pi^-\} \tag{1.14}$$

producing, in addition to a hadronic component X, neutral and charged pions π which promptly decay releasing electrons, gamma photons, and neutrinos (see equations 1.9 and 1.10). Figure 1.7 (left) shows such a potential hadronic accelerator, together with interactions taking place. In contrast to the electrons, neutrinos and photons are able to leave their region of origin. While the photons give rise to the characteristic peak shown in figure 1.7 (right), the energy spectrum of the neutrinos is expected, as discussed in the case of atmospheric neutrinos in section 1.4, to closely follow the original proton spectrum, i.e. a $\sim E^{-2}$ power-law. The original flavor composition $\nu_{\mathrm{e}} : \nu_\mu : \nu_\tau = 1 : 2 : 0$ will however have changed to $1 : 1 : 1$ when arriving at Earth, due to neutrino oscillations. Predictions of the scaling factor between the fluxes of accelerated hadrons and neutrinos depend on model assumptions concerning the exact processes involved in neutrino production. A

---

[1] Simple calculations result in a E^{-2} power-law.

model-independent[1] upper limit on the flux of astrophysical neutrinos associated with primary cosmic rays can be derived from the observable flux of cosmic radiation to be

$$E_\nu^2 \cdot \Phi(E_\nu) < 2 \cdot 10^{-8} \, \frac{\mathrm{GeV}}{\mathrm{cm}^2 \, \mathrm{s} \, \mathrm{sr}} \tag{1.15}$$

for all relevant neutrino energies, referred to as the **Waxmann-Bachall flux** [65].

As of now, the potential cosmic ray sources discussed above have been observed in the light of radio and gamma photons. A qualitative sketch of obtained spectra is shown in figure 1.7, right. The observable spectral features, usually two pronounced peaks at different energies, can be explained assuming leptonic processes only, but allowing for hadronic contributions so that no indisputable statement on the nature of the underlying acceleration can be made. For instance, the gamma spectra of blazar jets (see AGNs) agree well with a purely leptonic acceleration scenario as a synchrotron as well as a Compton peak can be resolved. Small inconsistencies in the amplitude relation as well as in the peak evolution with time, observed in some blazars, might indicate hadronic contributions from pion decay[2].

The detection of neutrinos from the regions in question would be a **"smoking gun"** signature, an unambiguous indication for the presence of hadronic acceleration, and solve the long-standing question on the sources of Cosmic Rays [4].

Beginning in 2013, 37 neutrinos featuring reconstructed energies between 30 TeV and 2 PeV were registered in the IceCube neutrino telescope [1, 66] (see also section 2.2.3). At these high energies the softer flux of atmospheric (conventional as well as prompt) neutrinos is strongly suppressed. This allows to reject an atmospheric origin of the observed neutrinos at 5.7σ [67] making them the first neutrinos of undoubtedly astrophysical origin[3]. The measured spectrum, also statistics are still very low, fits best a $E^{-2.2}$ power-law, with a flux per flavor of $E_\nu^2 \cdot \Phi(E_\nu) = 0.95 \pm 0.3 \cdot 10^{-8}\,\mathrm{GeV}\,\mathrm{cm}^{-2}\,\mathrm{s}^{-1}\,\mathrm{sr}^{-1}$, which matches the order of magnitude of the Waxmann-Bachall upper limit discussed above (see equation 1.15), actually surpassing it. However it can be argued (see [68]) that the original bound is too restrictive, and it is more realistic to expect $1 \sim 5 \cdot 10^{-8}\,\mathrm{GeV}\,\mathrm{cm}^{-2}\,\mathrm{s}^{-1}\,\mathrm{sr}^{-1}$. This relatively high flux, at the upper end of initial expectations, indicates a high level of hadronic activity in the universe. The search for point sources has begun.

---

[1] Although the term "model-independent" is used referring to these calculations, they actually are based on three assumptions:

- neutrons can escape freely from the source (as shown in figure 1.7, left),
- magnetic fields do not modulate the flux of cosmic rays,
- the primary injection spectrum is $\propto E^{-2}$.

As the second prerequisite is only true for very high energy cosmic ray particles, the bound is derived from measurements in the $> 10^{18}$ eV energy region only. Losening some of the assumptions can result in considerably higher neutrino fluxes [64].

[2] The amplitude of the high-energy peak is degenerate, with both Compton scattering and pion decay producing photons of comparable energy.

[3] Apart from solar neutrinos and those registered from SN1987A.

2 Large volume neutrino telescopes

To explore the origins of the highly energetic cosmic rays using neutrinos, target volumes of the order of cubic kilometers are needed. First ideas to construct such large detector infrastructures trace back to a proposal by M. Markov made in 1960 [69, 70]. After initial drawbacks in the attempt to build the DUMAND experiment off the coast of Hawaii (see section 2.2), several such detectors, so-called neutrino telescopes, have been constructed and operated successfully, beginning in the 1990s. The hitherto gained results led, among other things, to a better mapping and understanding of the atmospheric neutrino spectrum as well as upper limits on exotic physics processes such as dark matter annihilation. 2013 saw the first detection of neutrinos originating beyond the Solar system by IceCube (see section 2.2.3). With the construction of larger volume next-generation neutrino telescopes, able due to improved statistics to trace back potential point-sources of the discovered flux, begins the era of neutrino astronomy.

2.1 Operation principles

The detection of neutrinos in neutrino telescopes is carried out indirectly via charged secondary particles produced in neutrino interactions with the detector medium. Due to the tiny interaction cross-sections of high-energy neutrinos, volumes in the range of cubic kilometers have to be instrumented to obtain a measurable flux [4, 69, 71]. In contrast to low-energy experiments, like Kamiokande [72], consisting of huge water tanks housed in underground cavities, it is not feasible to construct an artificial volume of appropriate size. Therefore natural accumulations of water (liquid or solid) are used as targets, such as glaciers or the deep sea. Inside the detector volume charged secondaries, due to their high energies, give rise to so-called Cherenkov radiation. The total light yield and the arrival times of Cherenkov photons enable conclusions concerning the direction and energy of the initial neutrino.

2.1.1 Neutrino interactions

Depending on their flavor and energy neutrinos will engage in either the **neutral current**[1] (NC) or in the **charged current**[2] (CC) branch of the weak interaction inside the target medium. The reaction partner of the neutrino further adds to the variety of possible final states.

At neutrino energies usually addressed by large volume neutrino telescopes, above some 10 GeV, interactions are dominated by **deep inelastic scattering** at nucleons in matter, or rather at their constituent quarks, described by

$$\overset{(-)}{\nu_l} + N \rightarrow l^{\mp} + X \quad \text{(CC)} \qquad \text{or} \qquad \overset{(-)}{\nu_l} + N \rightarrow \overset{(-)}{\nu_l} + X \quad \text{(NC)} \tag{2.1}$$

where $l \in \{\mathrm{e}, \mu, \tau\}$, N can be either a proton or a neutron and X denotes one or more

---

[1] Exchange of a Z^0 boson.

[2] Exchange of a W^+ or W^- boson.

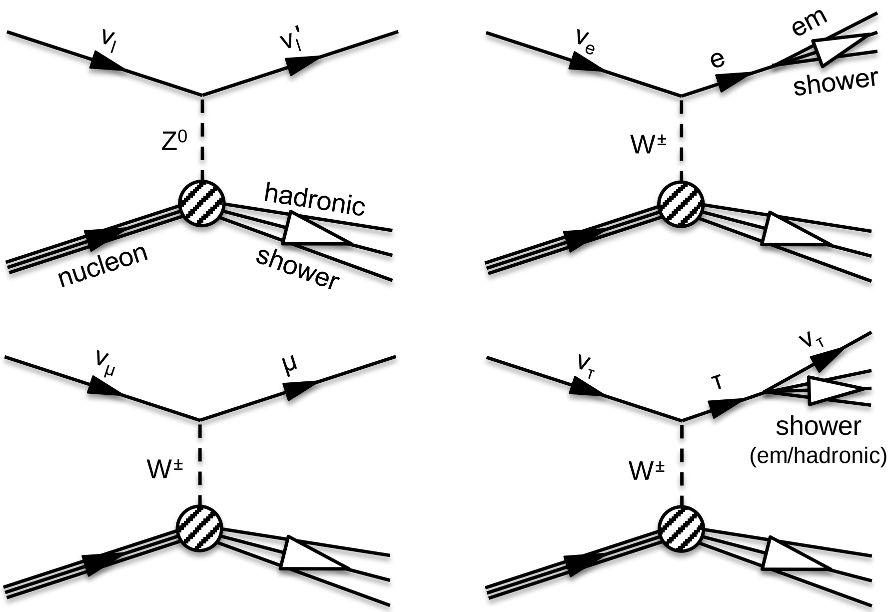

Figure 2.1: Schematic Feynman diagrams for the deep inelastic scattering of neutrinos at GeV energies off nucleons in matter (see equation 2.1). **Top left** subfigure shows the NC process entered by all neutrino flavors ν_l, $l \in \{e, \mu, \tau\}$. Remaining subfigures feature CC interactions for individual flavors (**top right**: ν_e, **bottom left**: ν_μ). For the τ neutrino only the channel resulting in a “double bang” event signature is presented (**bottom right**). Shown for neutrino interactions, the diagrams are equally valid for the respective anti-neutrinos (after reversion of lepton directions).

hadronic particles (potentially an entire hadronic cascade) [4]. See figure 2.1 for corresponding Feynman diagrams.

Currently planned low-energy arrays, such as ORCA (see section 2.2.2) or PINGU (see section 2.4), will extend the detectable spectrum to energies as low as few GeV. In this regime additional processes become relevant: In the case of **quasi-elastic scattering**, occurring at rather low energies up to $\sim 10\,\mathrm{GeV}$, the neutrino scatters off an entire nucleon, removing it (possibly together with other nucleons) from the core. The free nucleon(s) will then propagate through the surrounding medium until the full dissipation of their energy.

In the energy range between approximately 1 GeV and 3 GeV **resonance production** is the dominant interaction. In this process the neutrino excites a target nucleon into short-lived baryonic resonances (such as Δ^+). These resonances subsequently decay producing various hadrons, among them nucleons and pions. Figure 2.2 presents the energy dependence of the total (anti-)neutrino-nucleon charged current cross-section, featuring individual contributions by the above-mentioned processes.

More important from an experimentalist's point of view however, are the distinguishable signatures produced in the detector by these interactions. Events can be classified using three groups:

- **Track**: Muons (or ultra-high energy taus) crossing the detector travel long distances

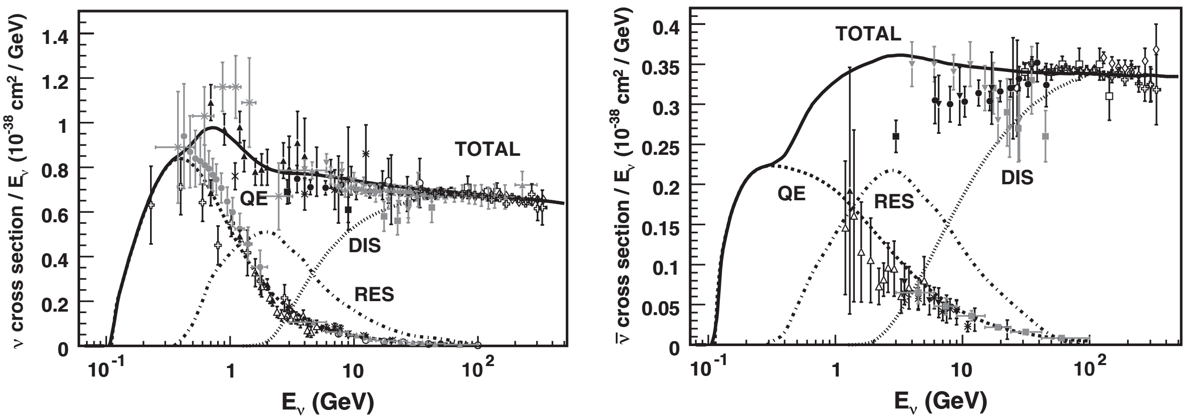

Figure 2.2: Energy dependence of the total cross-section of the charged current interaction of neutrinos (**left**) and anti-neutrinos (right) with an (isoscalar) nucleon $N_{\mathrm{iso}} = (p+n)/2$, divided by the lepton energy. The plot features contributions from quasi-elastic scattering (QE), resonance production (RES), and deep inelastic scattering (DIS). Plots taken from [73].

unaffected, emitting Cherenkov radiation along straight tracks. The elongated pattern of light deposition (see figure 2.3, right) allows for a precise directional reconstruction. Only lower limits on the particle energy can be derived though, as the track is usually not contained within the instrumented volume. If stemming from a neutrino charged current interaction the parent particle of the muon is a muon neutrino (see figure 2.1, bottm left). In the energy range addressed by neutrino telescopes the muons direction does not deviate much from the direction of the primary neutrino, making the underlying production mechanism the **"golden channel"** of neutrino astronomy looking for point sources.

- **Shower**: Near-spherical event signatures, resembling point sources, with a maximum of photon production in the center and virtually no elongation (see figure 2.3, left) are referred to as showers. Directional information is very poor but the energy of the original neutrino can be well reconstructed from the total light deposition, in particular if the event is fully contained in the detector. Uncertainties arise however, due to the unknown fraction of energy carried away from the vertex by (anti-) neutrinos. Two different processed can give rise to a shower pattern: In the **electromagnetic** case, an electron or positron, produced by a corresponding neutrino (or anti-neutrino) in a CC interaction, results in a shower signature as the charged lepton, due to a large interaction cross-section, only travels short distances in the detector medium depositing its energy in a relatively small volume. figure 2.1 (top right) shows the corresponding Feynman diagram. Furthermore, all neutrino flavors are able to induce a **hadronic** cascade via the neutral current, which also becomes manifest in a shower signature (see figure 2.1, top left).

- **Double Bang**: The so-called double bang is a unique signature of a high-energy τ neutrino. The incoming neutrino, via charged current weak interaction, produces a tauon in the detector volume which, after a short distance, in its turn decays weakly into a muon or electron/positron accompanied by the corresponding neutrinos and anti-neutrinos (this case is illustrated in figure 2.1, bottom right) or via the strong

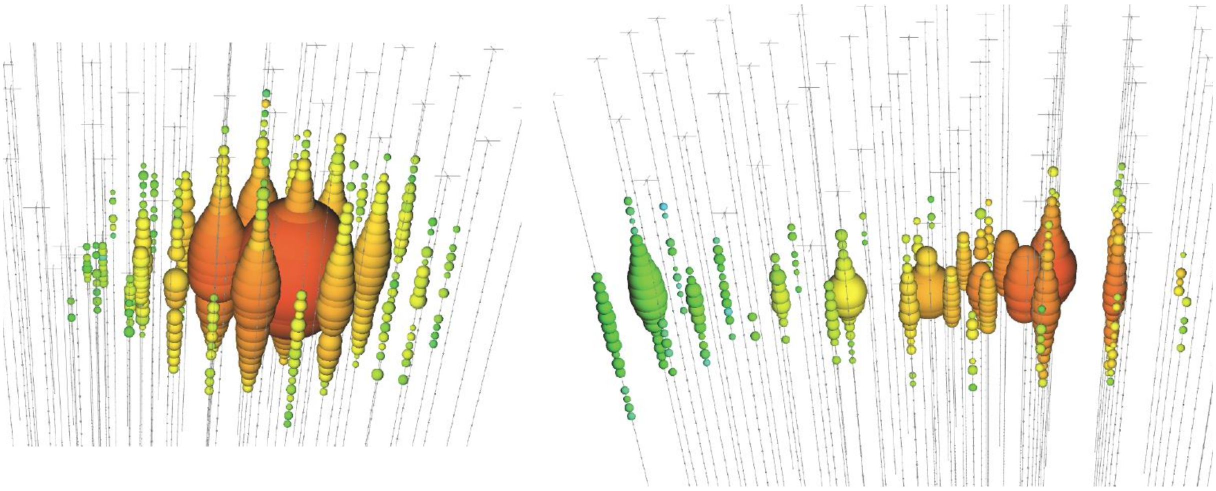

Figure 2.3: Light deposition patterns of showers/cascades (**left**) and track events (**right**) inside a volume instrumented with photon sensors (optical modules). Each module is shown as a sphere, whose size scales with the amount of recorded photons. The color coding illustrates the arrival time of the light, ranging from red (early hits) to blue (later hits). Figures taken from `https://icecube.wisc.edu/masterclass/neutrinos`.

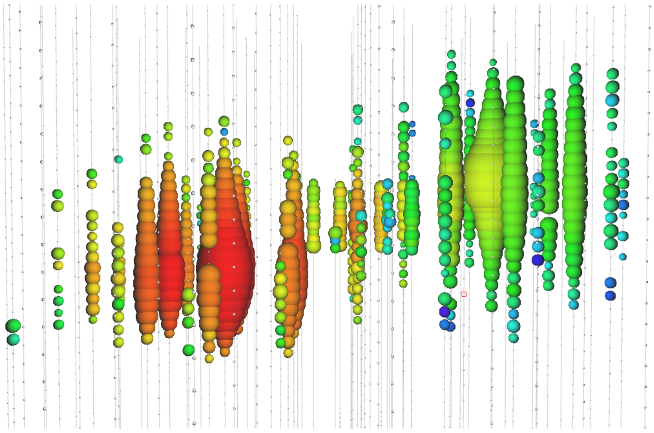

Figure 2.4: Double bang event signature as expected from the interaction of τ neutrinos. The plot is based on simulated data as such events have not been observed up to date. Color and size coding analogous to figure 2.3. Taken from `https://icecube.wisc.edu/masterclass/neutrinos`.

force producing neutral and/or charged pions in various combinations, together with a τ neutrino. While the (anti-) neutrinos leave the detector without further interaction, the pions and electrons/positrons give rise to a hadronic or electromagnetic cascade, respectively. As the τ itself hardly deposits any energy, two distinct "bangs", spatially separated showers, can be observed, as illustrated in figure 2.4. Potentially produced muons do not contribute to the characteristic double bang pattern, producing tracks as described above.

All charged current neutrino interactions are in addition accompanied by a, more or less pronounced, hadronic cascade stemming from the debris of the nucleonic reaction partner as shown in figure 2.1. Although only neutrinos are mentioned in the above statements, these are equally true for their antiparticles. Neutrino telescopes are not able to distinguish between neutrinos and anti-neutrinos.

2.1.2 Cherenkov medium

A charged particle crossing a transparent dielectric excites the medium, inducing temporary dipoles. During de-excitation of these dipoles electromagnetic fields are created which, at sub-luminal velocities, interfere destructively without net radiation output. If however, the charged particle travels the medium faster than the local (phase) speed of light, the so-called **Cherenkov effect**[1] occurs. The elementary waves of the decaying dipoles overlap constructively, hereby causing the charged particle to radiate photons in a cone along its trajectory. An illustration is shown in figure 2.5. The spectral distribution of the light emitted by singly charged particle as well as the amount of energy radiated per unit length is approximated by the original Frank-Tamm formula (neglecting quantum mechanic corrections and using Gaussian units) [75]:

$$\frac{dE}{dx} = \frac{e^2}{c^2} \int \left(1 - \frac{1}{\beta^2 n(\omega)^2}\right) \omega d\omega \tag{2.2}$$

where ω is the angular frequency, $\beta = V_{\text{charge}}/c$ is the particle speed relative to the vacuum speed of light c, n the refractive index of the medium and e the charge quantum. Applying the substitutions

$$d\omega = -\frac{2\pi c}{\lambda^2} d\lambda, \qquad dE = \frac{hc}{\lambda} dN_\gamma, \qquad \text{and} \qquad \alpha = \frac{2\pi e^2}{hc} \tag{2.3}$$

where λ is the wavelength and N_γ the number of the emitted photons, h is Planck's constant, and α the fine structure constant, equation 2.2 can alternatively be expressed as

$$\frac{d^2 N_\gamma}{dx d\lambda} = \frac{2\pi\alpha}{\lambda^2} \cdot \left(1 - \frac{1}{\beta^2 n(\lambda)^2}\right) \tag{2.4}$$

Assuming a constant refraction index of $n \approx 1.33$ (which is a good approximation for the case of visible light in deep sea water) it is possible to calculate the amount of photons N_γ emitted inside the wavelength range defined by λ_1 and λ_2 by a particle traveling the distance Δx using

$$N_\gamma = -2\pi\alpha \left(1 - \frac{1}{\beta^2 n^2}\right) \cdot \left[\frac{1}{\lambda}\right]_{\lambda_1}^{\lambda_2} \cdot \Delta x \tag{2.5}$$

A muon, traveling with almost the vacuum speed of light, thus emits roughly 400 photons per centimeter at wavelengths ranging from 300 nm to 700 nm.

The opening angle θ_{C} of the emission cone, characteristic for the medium and the energy/velocity V_{charge} of the charged particle, is given by :

$$\cos\theta_{\mathrm{C}} = \frac{c/n}{V_{\text{charge}}} = \frac{1}{n\beta} \tag{2.6}$$

using the above defined variable conventions. The expression only produces valid results for speeds above the Cherenkov threshold of c/n. Insertion of $n = 1.35$, characteristic for water, and $\beta \approx 1$ for a highly relativistic particle results in a Cherenkov angle of approximately 42°.

---

[1] Sometimes also referred to as "Vavilov-Cherenkov effect". Named after P.A. Cherenkov who discovered it being a PhD student supervised by S.I. Vavilov in 1934 [74]. A theory of the effect was developed by I.M. Frank and I.Y. Tamm in 1937 [75].

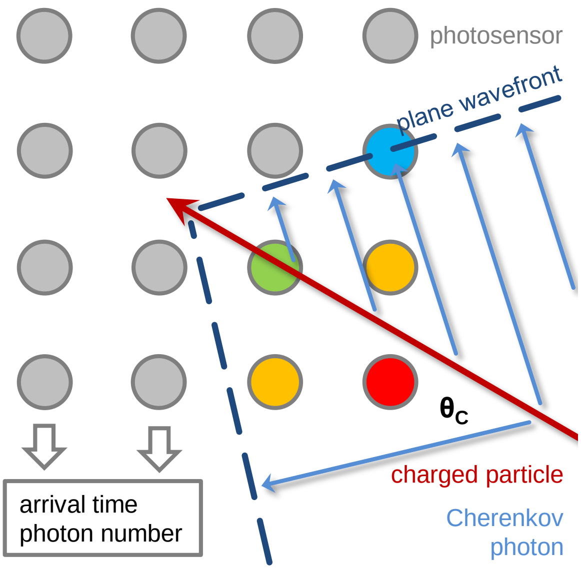

Figure 2.5: Operation principle of large volume Cherenkov detectors: A charged particle at super-luminal speed emitting photons under the characteristic Cherekov angle θ_C, forming conical plane waves, enters a volume instrumented with photosensors. The sensors record the number of incident photons[a] as well as their respective arrival times (rainbow color-coded where *red* corresponds to "early" and *blue* to "late"). Idealized case omitting dispersion and absorption.

---

[a] As discussed in section 3.1, only a fraction of the photons arriving at the PMT, usually lower than $\sim 25\,\%$ in the case of bialkali photocathodes, are actually detected.

Important for physics applications is not only the emitted Cherenkov spectrum, but its convolution with the transmission of the utilized medium. In the case of liquid water, for example, it results in a spectral maximum at a wavelength of 470 nanometers while in ice no absorption of the ultraviolet fraction takes place.

In order to be able to draw conclusions on the primary neutrino, exact knowledge of the arrival time and the total amount of Cherenkov photons is crucial. In practice, the light is collected by photomultiplier tubes (PMTs), ultra-sensitive detectors able to measure low light intensities down to single photon level with a timing resolution in the nanosecond range[2] (see section 3 for a detailed introduction of the devices and their properties). Via spatial triangulation it is then possible to locate the origin of the Cherenkov light and reconstruct the position of a track or shower as well as its temporal evolution (direction of travel). The number of registered photons allows conclusions concerning the energy deposited by the charged particle inside the target volume and in consequence an estimation of the energy of the original neutrino.

However, the successful reconstruction of direction and energy information not only requires efficient sensors but also detailed knowledge on the propagation of light in the target medium. Two main effects affect the photon propagation: **absorption** and **scattering**. The number N_dir of "direct" (meaning unscattered and unabsorbed) photons, decreases exponentially as a function of the distance d from the source

$$N_\mathrm{dir}(d) = N_\mathrm{emit} \cdot e^{-d/L_\mathrm{a} - d/L_\mathrm{s}} \tag{2.7}$$

with L_a and L_s denoting the effective absorption and scattering lengths, respectively, and N_emit being the number of initially emitted photons.

Depending on the medium, various underlying physical processes will contribute to absorption and scattering. In practice, their characteristic effective quantities are measured

---

[2] This level of timing precision is necessary as e.g. a position uncertainty of $\Delta t \sim 1\,\mathrm{m}$ for a source moving at a velocity close to the speed of light transforms, via $\Delta t \approx \Delta s/c$, to a time difference of $\Delta t \sim 3.5\,\mathrm{ns}$.

in-situ using dedicated devices as is the effective scattering function $\chi(\theta, \lambda)$, which quantifies the fraction of photons with wavelength λ scattered under an angle θ. Figures 2.6, 2.7, and 2.8 present results of such measurements performed for different target materials. While absorption merely reduces the total amount of detectable light, scattering effectively delays the propagation of photons between their origin and the point of detection and therefore deteriorates timing information of the event. Consequently, both effects put constraints on the achievable quality of event reconstruction: energy and directional reconstruction both benefit from increased statistics, corresponding to a large number of arriving photons whereas precise timing is important for the reconstruction of the position and direction of an event [4, 76].

For the operation of a neutrino telescope good knowledge of the optical properties of the medium and of the expected backgrounds is crucial. Three potential media are, in principle, available for the construction of neutrino telescopes, each coming with unique advantages and drawbacks. A short overview of the maximum effective values of absorption and scattering length for the respective media is given in table 2.1.

- **Glacial ice**: Natural deep glacier ice provides a medium featuring very low optical background due to the lack of bio-luminescence and a low rate of radioactive decays due to the age of the material. Low ambient temperatures are also advantageous decreasing background from the intrinsic dark rate of PMTs (see section 3.8). For illustration purposes: A ten-inch tube of the IceCube experiment in Antarctica (see section 2.2.3) detects noise at a rate of $\sim 0.5\,\text{kHz}$, whereas $20 - 40\,\text{kHz}$ are measured by similar PMTs operated in the Mediterranean [4]. Hit selection thus benefits from lower contamination of the hit patterns from particle interactions with random noise hits compared to the case in sea or lake water. Compared to water, deep ice in general features larger absorption lengths but shorter scattering lengths. A typical value of the effective scattering length, averaged over measurements in Antarctica at depths between 1500 and 2000 meters, was found to be 20 meters [77]. In the clearest ice region the effective scattering length ranges up to 50 meters and the absorption length to 230 meters for blue light [4]. Another feature is the transparency to photons in the ultra-violet region. This results in a higher net Cherenkov light yield due to the $1/\lambda^2$ dependence of the flux (see equation 2.4). An undesired property of the ice is the dependency of optical parameters on position as well as on photon direction: Strong density variations of dust grains inside the ice, forming non-horizontal layers, result in a pronounced depth dependence of absorptivity and effective scattering coefficient shown in figure 2.6 [4, 77]. In addition, a directional dependence of optical parameters was found. This peculiarity was traced back to a predominant orientation of elongated dust particles leading to an angular dependent cross-section. The orientation correlates with the direction of ice flow of the Antarctic glacier [24, 78] Additional inevitable anisotropies arise from refreezing of the boreholes needed to inject instrumentation into the ice and potential pollution during the drilling process.

- **Marine water**: Water in the deep sea features stronger absorption in comparison to ice in particular in the ultraviolet range, but weaker scattering. Spectral behavior of the optical parameters is shown in figure 2.7. Main contributions to background light originate from deep-sea wildlife and the radioactive decay of ^{40}K. In the Mediterranean

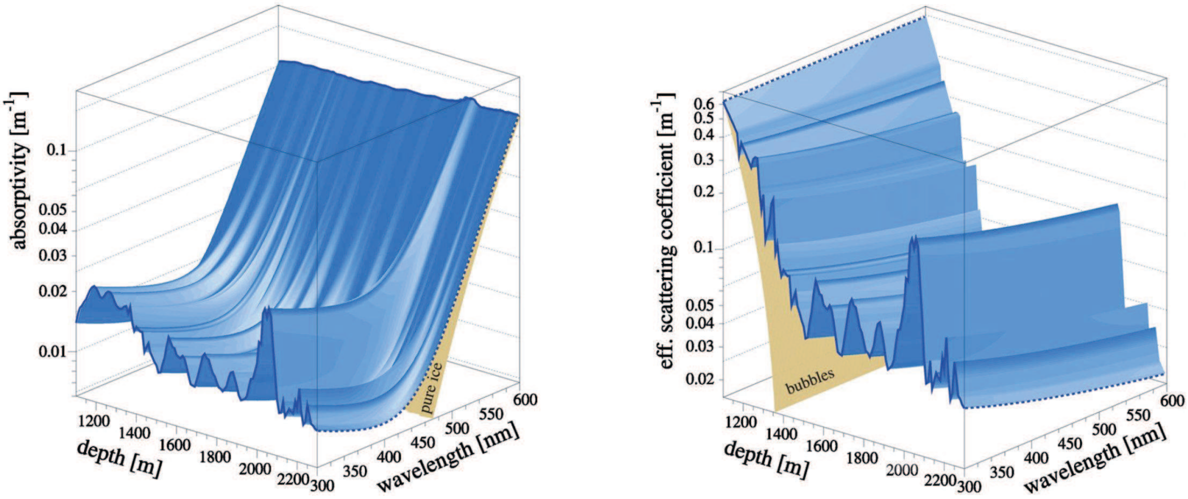

Figure 2.6: Deep ice optical properties shown as a function of photon wavelength and depth. **Left**: Measured asorptivity (*blue*). Behavior expected from pure ice marked in *khaki*. **Right**: Scattering coefficient (*blue*) with the contribution of enclosed air bubbles present at shallow depths (*khaki*). Taken from [77].

the bio-luminescence trigger rate of the ANTARES detector[1] exhibits second-scale bursts in the MHz region superimposed on a slowly varying baseline of typically some 10 kHz to a few 100 kHz. Efficient data taking is possible up to baseline rates of 200 kHz [4]. The level of bio-luminescence varies in the course of the year. The yearly light maximum at the ANTARES site (off the French coast near the city of Toulon) e.g. correlates with the Alpine snow melt which, after a time offset, leads to an increase of food abundance in the deep sea supplied by the river Rhône.

- **Fresh water**: As a medium for neutrino telescopes, fresh water enables the utilization of less chemically resistant materials for modules and cabling, e.g. stainless steel in stead of titan, due to the absence of dissolved salts. For the same reason, the background from radioactive isotopes such as ^{40}K included in those salts is also strongly reduced. However bio-luminescence is an issue. Long term measurements of optical properties performed in lake Baikal found 20 to 24 meters for the absorption length and 30 to 50 meters for the scattering length to be characteristic values inside the "transparency window" (480 – 500 nm). See figure 2.8 for detailed spectra. Seasonal variation of the absorption length was determined to be below 20% with respect to the characteristic range, whereas the scattering can increase by an order of magnitude [80, 76]. Over long operation periods modulation of the acceptance of optical sensors by sedimentation and fouling have to be taken into account.

A medium-independent background is given by the flux of atmospheric muons and neutrinos[2]. In order to reduce it, neutrino telescopes are constructed at great depths, shielded

---

[1] See section 2.2.2.

[2] This is of course only true in case of neutrino telescopes aiming at high-energy astrophysical neutrinos. Currently planned low-energy detectors, such as PINGU and ORCA (see sections 2.4 and 2.2.2

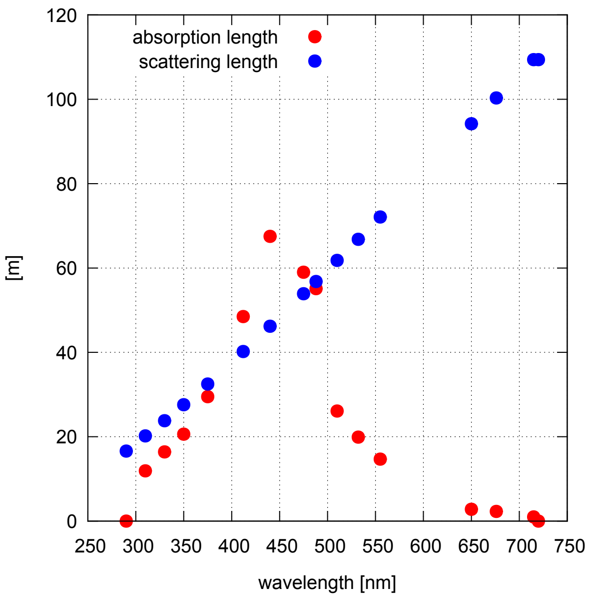

Figure 2.7: Absorption and scattering length of sea water at the ANTARES site as a function of wavelength. Compiled from data retrieved from [79].

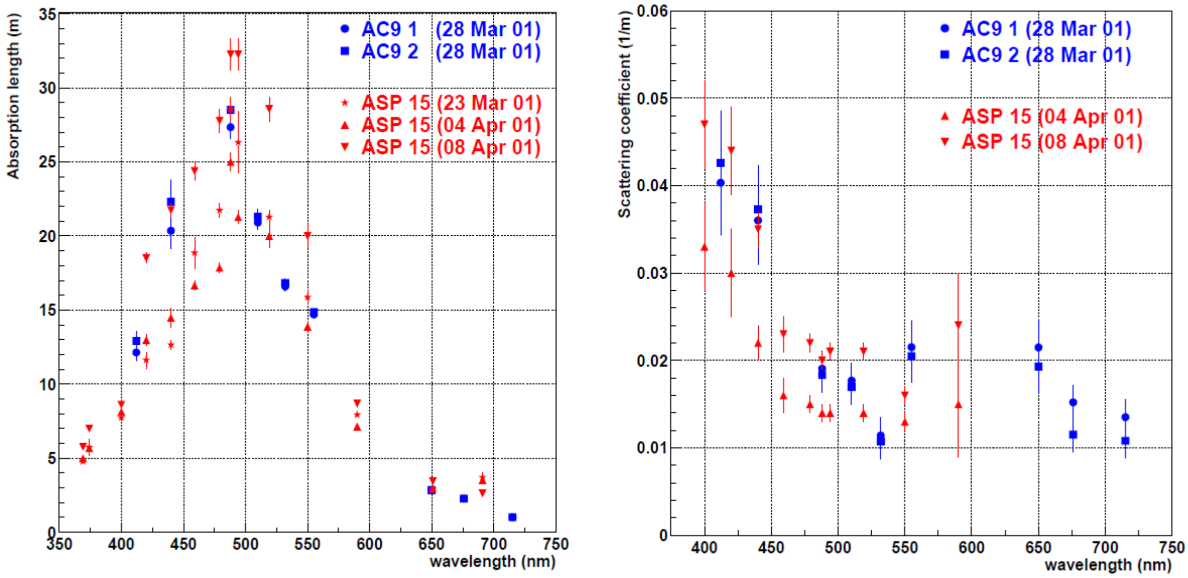

Figure 2.8: Wavelength dependence of absorption length and the scattering coefficient of the fresh water of lake Baikal. Measurements were performed at a depth of 1000 meters using two independent devices (AC9 and ASP15). Plots taken from [80].

Site	**depth** [km]	L_a [m]	L_s [m]
Lake Baikal	1	22	150 – 400
Deep sea	$>$ 1.5 km	40 – 70	200 – 400
Antarctica	$>$ 2.2 km	150	40

Table 2.1: Summary of effective values of absorption length L_a and scattering length L_s for deep Antarctic ice, deep sea water, and fresh water in lake Baikal. Taken from [4]. The values present an idealized case as shown for their respective maximum wavelength. Ranges are due to seasonal and/or site variations. Antarctic values are averages.

by extensive layers of water or ice. In spite of these shielding efforts, atmospheric muons outnumber the neutrino flux by a factor of $\sim 10^6$. Therefore, in the classical neutrino telescope concept the PMTs are oriented downwards using the Earth as an additional muon shield. As a consequence the detector's sensitivity is limited to tracks originating below the horizon (usually dubbed "up-going tracks"). Down-going tracks are in general rejected as background. In a more sophisticated approach, used e.g. in the HESE[1] analysis of IceCube data (see [1] for details), the outermost layer of the detector is used as a veto to select events having their origin inside the detector. This technique enables efficient suppression of atmospheric muons simultaneously expanding the field of view to the upper hemisphere.

The geometrical arrangement of optical modules defines the fiducial volume as well as the energy and directional resolution of the telescope. Signatures of high-energy neutrinos are in general very extended, resulting in the necessity of a large instrumented volume in order to collect a representative fraction of the totally produced light which is used to estimate the initial energy of the primary neutrino and to reconstruct its direction. The respective distances between the modules can be relatively large. By contrast, a dense instrumentation is needed for the study of low-energy neutrinos to be able to resolve the the more delicate photon deposition patterns with adequate accuracy.

2.2 Current neutrino telescopes

All current neutrino telescopes are based on the principles introduced in the previous section. A typical neutrino telescope consists of a three-dimensional array of light sensors, so-called optical modules, inside a natural target medium[2]. In the classic approach, the centerpiece of an optical module is a single photomultiplier tube featuring a large effective area. In addition it can, if applicable contain digital read-out electronics and further auxiliary devices. PMT and electronics are protected against ambient pressure by a glass pressure vessel. The individual module data is extracted (e.g. by wires or optical fibers) and collected centrally for storage and analysis. A first attempt to build a detector based on these construction principles was made by the **DUMAND**[3] project, an international collaboration active from 1976 till 1996. The aim was to construct a multi-km^3 detector at a depth of 4800 meters in the Pacific ocean off the coast of Hawaii [69]. See figure 2.9 for an impression of the planned layout. The project was eventually abandoned, having failed to resolve technical difficulties arising in particular from the harsh environment of deep sea salt water [4]. The gained knowledge and expertise[4] however paved the way for the successful construction of several neutrino telescopes around the globe [81].

---

respectively), will use atmospheric neutrinos to study their properties.

[1] High-Energy Starting Events

[2] Being abundant on Earth and transparent to optical photons, water, liquid or solid, is the medium of choice.

[3] Deep Underwater Muon and Neutrino Detector

[4] It is worth mentioning that several novel design concepts being put into effect now, such as utilization of several PMTs or wavelength-shifting elements [69] inside an optical module (see section 2.4), were actually already conceived and partially applied by members of the former DUMAND collaboration.

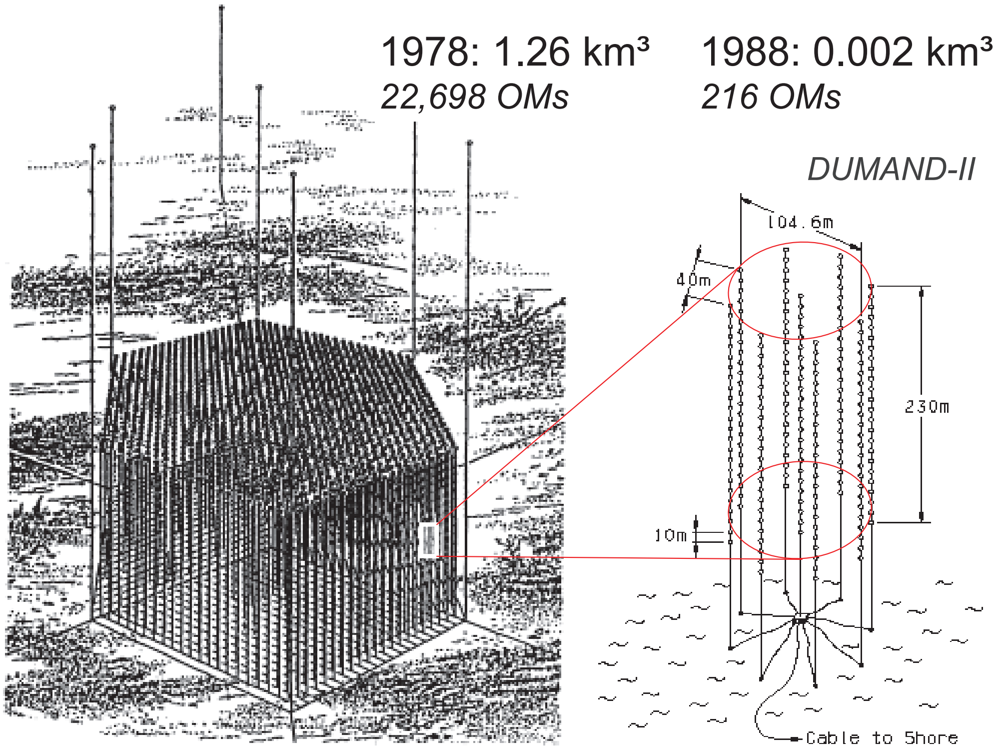

Figure 2.9: Impressions of the DUMAND neutrino telescope concepts at different stages of planning. The initial proposal for a cubic kilometer-sized detector (**left**) had to be scaled down due to technical and financial problems. Figure taken from [4].

2.2.1 Baikal neutrino telescopes

The **Baikal detector**[1] was the first successfully built neutrino telescope [83]. Located at the bottom of lake Baikal in eastern Siberia, it has been continuously taking data since 1993. In the current configuration the detector consists of an array of eight lines, anchored at the seabed and held in an upright position by underwater buoys, carrying 24 optical modules each at a depth of 1100 meters. In addition four prototype lines have been installed increasing the fiducial volume of the detector and testing technology for a future extension [84]. Positions of the optical modules are monitored using a sonar triangulation system. The original optical modules comprise custom developed QUASAR-370 hybrid PMTs[2], while a future extension will use conventional Hamamatsu R7081HQE enhanced quantum efficiency tubes. [85, 82]. The small module spacing leads to a comparably low energy threshold of about 15 GeV [4]. The original detector was able to make the very first underwater neutrino detection [86] but also to investigate the atmospheric muon flux, set competitive limits on baryon decay, dark matter annihilation in the center of the Earth and the Sun, and the flux of magnetic monopoles [4, 76].

---

[1] The official name of the final, post-1998 installation, is actually “NT-200”, which stands for “Neutrino Telescope” and the approximate number of installed optical modules [82].

[2] In hybrid PMTs, first developed by Philips as type XP2600 for the DUMAND project, photoelectrons emitted from the photocathode do not enter a dynode system but are accelerated and focused onto a scintillator using very high voltages (25 kV in the case of the QUASAR-370). The produced scintillation light is then detected using a small standard PMT. Such devices feature good timing and superior charge resolution but are costly and require two individual high voltage supplies [82].

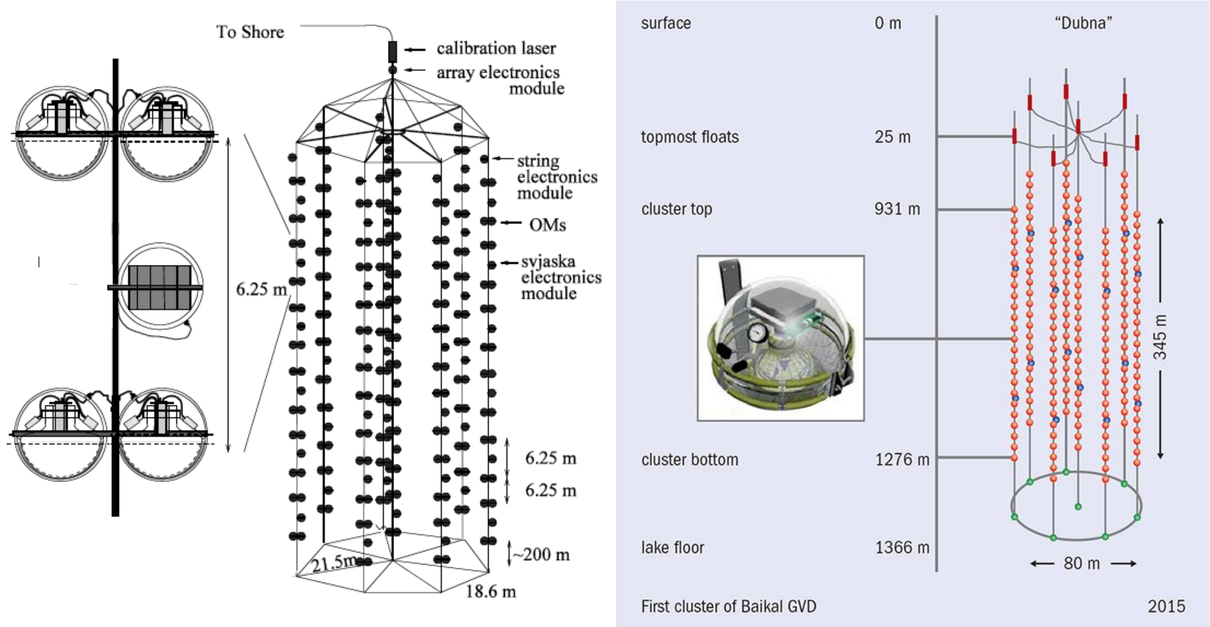

Figure 2.10: **Left**: Lake Baikal neutrino telescope in the NT-200 configuration together with *svjaska*, a four-module bundle sharing front-end electronics (inside a dedicated pressure vessel) which is the elementary cell of the array. Taken from [76]. **Right**: A cluster of the next-generation detector Baikal-GVD. Subplot features the new single-PMT optical module. Figure taken from [87].

From a technical point of view, the location allows for a relatively comfortable deployment and maintenance of the instrumentation. The lines are lowered into the water through holes in the ice layer during winter time. Compared to marine locations the main disadvantage of lake Baikal is the relatively shallow depth, resulting in a higher background rate by atmospheric muons.

At present, an upgrade of the detector facilities is under construction. The Baikal Gigaton Volume Detector (**Baikal-GVD**), also dubbed NT-1000, in its final configuration will feature a volume of approximately one cubic kilometer equipped with 2304 optical modules mounted on 96 strings at a vertical distance of 15 meters. A first eight-string cluster, named "Dubna" (see figure 2.10), has been deployed in April 2015. When completed, the telescope will comprise twelve such clusters covering a total ground area of approximately $2\,\mathrm{km}^2$ in a triangular grid at a next-neighbor distance of 300 meters. The geometrical layout is optimized to provide an effective shower detection volume of about 0.1–$0.7\,\mathrm{km}^3$ above 30 TeV shower energy and an effective area for muon tracks rising asymptotically from $0.1\,\mathrm{km}^2$ for 3 TeV muons to $0.8\,\mathrm{km}^2$ [76, 87].

The extension is aiming at mapping the high-energy neutrino sky in the Southern hemisphere including the region of the Galactic Center. A further topic will be the indirect search for dark matter via WIMP annihilation neutrinos produced in the Sun or in the center of the Earth. GVD will also search for exotic particles such as magnetic monopoles, Q-balls, or nuclearites [76, 88, 89].

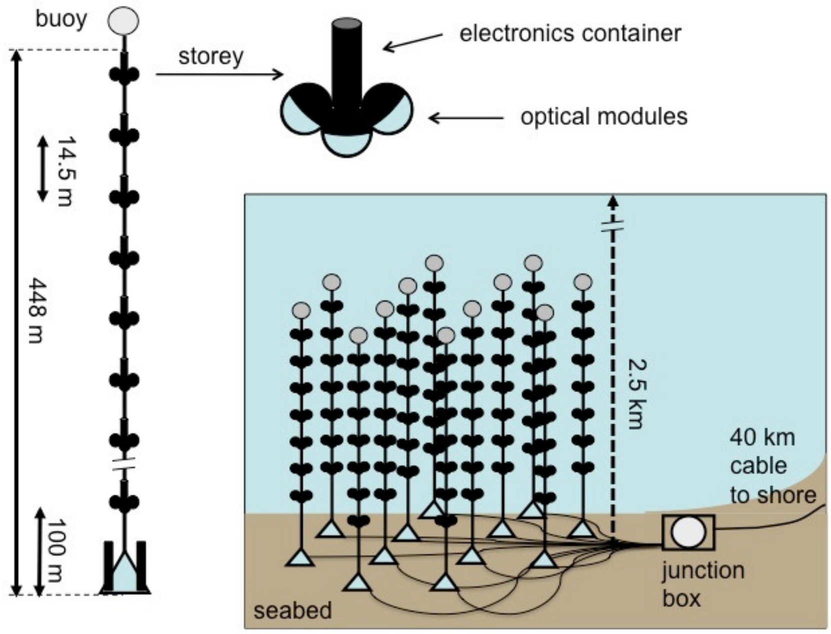

Figure 2.11: Schematic of the ANTARES neutrino detector infrastructure featuring main components and dimensions. Taken from [98].

2.2.2 ANTARES & KM3NeT

Design studies for the **ANTARES** (Astronomy with a Neutrino Telescope and Abyss environmental RESearch) detector began in the 1990s [90, 91]. Originally starting out as a purely French project, ANTARES became an international collaboration developing, and by 2008 actually deploying, a neutrino detector in the Mediterranean sea in parallel to independent efforts by NESTOR[1] (Greece) and NEMO[2] (Italy). Eventually, these groups joined together to form a consortium, and later a single international collaboration, bundling resources towards the construction of a next-generation km^3-scale telescope. ANTARES is located at a depth of 2475 meters, 40 kilometers off the French coast near the city of Toulon. It consists of twelve strings à 25 so-called stories with each story housing three optical modules. The individual strings are moored 60 to 70 meters apart. Similarly to the above mentioned Baikal detector, an ANTARES optical module features a single ten-inch PMT (Hamamatsu R7081-20) including its read-out electronics inside a 17-inch glass sphere. A µ-metal cage shields the photomultiplier against the magnetic field[3] of the Earth [96]. Additional electronics are housed inside a Titanium cylinder (one per story). The digitized single module hits are transmitted to the shore station via optical fibers without any in-situ data reduction, referred to as “all-data-to-shore” principle [97]. In total, a volume of $\sim 0.1\,\mathrm{km}^3$ has been equipped with instruments [91]. An illustration of the mechanical layout is given in figure 2.11. Due to the dynamic deep-sea environment the geometry of the array is subject to constant change[4] resulting in the

---

[1] Neutrino Extended Submarine Telescope with Oceanographic Research [92, 93]

[2] NEutrino Mediterranean Observatory [94, 95]

[3] See section 3.5 for the impact of external magnetic fields on PMT performance.

[4] The detector’s behavior is similar to that of sea grass in current.

need of real-time monitoring by means of an acoustic positioning system and compasses inside the stories [99]. In parallel, the acoustic devices are used for feasibility studies for potential future acoustic neutrino detectors[1].

Primary physics goals of the experiment were the search for astrophysical neutrinos in the TeV-to-PeV energy range from the Southern hemisphere, multi-messenger analyses, as well as for neutrinos from exotic physical processes, such as dark matter annihilation. It was able to measure the diffuse neutrino flux in its field of view, independently confirm the oscillation of atmospheric neutrinos, and set competitive upper limits on point sources and the WIMP annihilation cross-section [101].

Beyond that, being the first operational detector in salt water, thus demonstrating the feasibility of deep-sea neutrino telescopes, ANTARES also embodies a first step towards the **KM3NeT** neutrino telescope [102, 103, 104]. This new detector is currently in construction phase. After the deployment of first "pre-production" devices (PPM-DOM[2] and PPM-DU[3]) provided a proof of concept, the first finalized string (DU-2) was installed in December 2015. Upon completion KM3NeT will span over three sites[4] in the Mediterranean sea with each sub-detector having a multi-km^3 volume. As in envisaged IceCube upgrades (see section 2.2.3), it is planned to extend the spectrum of detectable neutrinos towards high as well as low energies with respect to ANTARES. The low-energy extension named **ORCA** (Oscillation Research with Cosmics in the Abyss) is expected to consist of one so-called "building block" corresponding to 115 instrumentation strings with 18 modules per string featuring a vertical distance of nine meters and a mean inter-string separation of 20 meters, located at the French site [104]. For the high-energy extension, called **ARCA** (Astroparticle Research with Cosmics in the Abyss), two larger volumes, near France as well as at the Italian site off Sicily, will be equipped with a sparse instrumentation (one building blocks at each site with 18 modules per string, a module-to-module distance of 36 meters, and approximately 95 meters between the strings) [104]. The Greek site near Pylos is reserved for potential future extensions. Among the physics goals of the experiment are the determination of the neutrino mass hierarchy (see section 1.1) for ORCA and the search for point sources of the ultra-high energetic neutrinos discovered by IceCube in 2013 (ARCA).

A hardware novelty of the KM3NeT detector is the layout of its optical modules. It has done pioneering work introducing the "multi-PMT" concept in the form of a highly integrated module comprising 31 three-inch PMTs with their respective high-voltage supplies, read-out electronics, as well as acoustic positioning and optical calibration devices inside one 17-inch spherical pressure vessel [107, 104]. Some of the drives for the development were the reduction of costs lowering the amount of titanium needed compared to the ANTARES story, increased reliability due to the use of less risky under-water connectors, and the minimization of drag. For more detailed information on the module, which also was the starting point for the module subject of this thesis, see section 4.

---

[1] These efforts feature under the label of the AMADEUS project (ANTARES Modules for the Acoustic Detection Under the Sea) [100]

[2] Pre-Production Model - Digital Optical Module: A single multi-PMT module installed at the instrumentation line of ANTARES [105].

[3] Pre-Production Model - Detection Unit: A stand-alone prototype string carrying three optical modules [106].

[4] In detail, these are Toulon (France, depth 2450 m), Capo Passero (Italy, depth 3500 m) and Pylos (Greece, depth 4000 m). The segmentation of the infrastructure is primarily a result of optimization for access to regional funding.

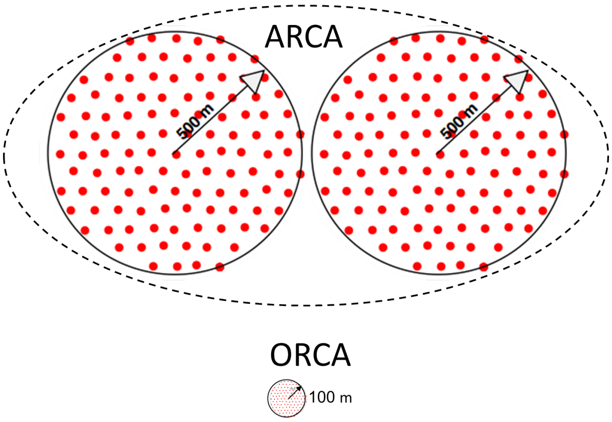

Figure 2.12: Footprints and dimensions of the high-energy (ARCA) and low-energy (ORCA) sub-detectors of the KM3NeT project. Red dots mark the positions of vertical instrument strings (detection units). Taken from `http://www.km3net.org/news.php`.

Figure 2.13: KM3NeT multi-PMT digital optical module mounted between two dyneema ropes and connected to an electro-optical cable via a break-out box. Shown is the final configuration before deployment. Photo taken from [104].

2.2.3 IceCube

With a target volume of roughly one cubic kilometer, **IceCube** is currently the largest existing neutrino telescope in the world [71, 108]. It is located at the South Pole 2450 meters below the surface using the natural Antarctic ice shield as a medium for neutrino detection. Based on pioneering work by the **AMANDA**[1] detector (active from 1996 to 2008) it reached its full extent by the end of 2010 with data taking starting from 2005 on, using sub-arrays. In its final configuration (IceCube 86) the detector features 86 vertical strings, with a length of 1 km, distributed over an area of one square kilometer holding a total of 5160 optical modules. An optical module[2] consists of a 13-inch glass sphere equipped with one conventional ten-inch PMT (type R7081-02 by Hamamatsu) [111] and digital read-out devices [112]. With a vertical module separation of 17 meters and an inter-string distance of 125 meters IceCube aims at the study of neutrinos in the energy range between 100 GeV and $\sim$ PeV. A schematic overview of the IceCube detector infrastructure at the South Pole is shown in figure 2.14.

In order to expand the spectrum of detectable neutrinos in the low-energy regime, six additional strings corresponding to 300 additional modules featuring R7081-MOD enhanced quantum efficiency phototubes[3] (horizontal string separation 72 m, vertical module distance 7 m) were deployed in the central region of the array in 2010. This sub-detector, named **DeepCore**, uses the rest of the IceCube array as a veto enabling the detection of neutrinos down to energies as low as $\sim$ 10 GeV from the entire sky [71, 113, 114, 108].

---

[1] Antarctic Muon And Neutrino Detection Array [109, 110]

[2] For details on optical module components see section 4.1.

[3] Resulting in an overall module sensitivity improvement of 30% to 40% with respect to a standard IceCube DOM[113].

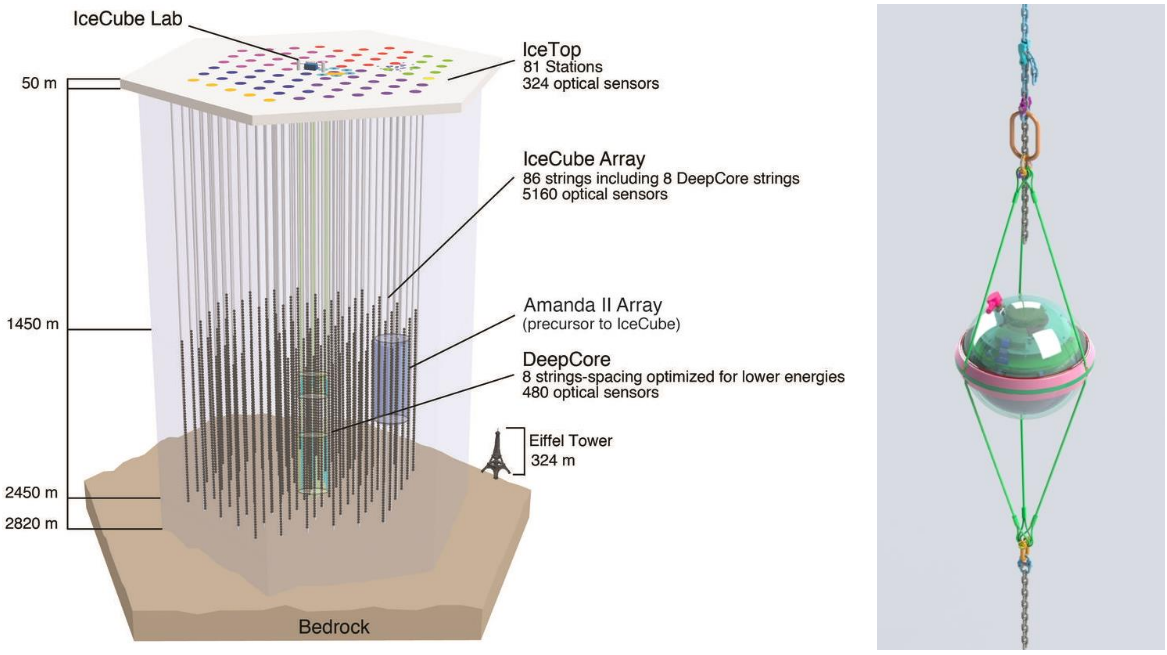

Figure 2.14: **Left**: Layout of the IceCube detector infrastructure at the South Pole. Colors group strings deployed in one construction season. The Eiffel tower is shown to scale for comparison. **Right**: IceCube digital optical module inside mechanical mounting structure of a string. Read-out cable not shown. For details on optical module components and readout see figures 4.3 and 4.4, respectively.
Drawings taken from `https://gallery.icecube.wisc.edu/internal/` and modified.

In addition, an array of 81 ice tanks each equipped with two optical modules, called **IceTop**, is located at the surface above IceCube. IceTop can be operated as an independent air shower detector for cosmic rays in the 300 TeV to 1 EeV energy range, simultaneously providing IceCube with a veto against atmospheric muons [4, 115].

Initial physics goals of IceCube were searches for high-energy neutrinos from transient sources (e.g. gamma ray bursts), point sources of ultra-high energy neutrinos, exotic particles (like WIMPs and magnetic monopoles) and monitoring the Galaxy for MeV neutrinos from supernovae [116]. The greatest break-through[1] so far, was achieved in 2013 with the first detection of neutrinos of cosmic origin [1, 66]. As of now, 37 neutrino candidates featuring energies[2] between 30 TeV and 2 PeV were registered. The measured flux matches best an $E^{2.2}$ energy spectrum in agreement with Waxmann-Bachall predictions. An atmospheric origin of the observed neutrinos could be rejected at 5.7σ [67]. Although their currently found angular distribution is consistent with isotropy, the diffuse flux allows to constraint the source density to $\lesssim 10^{-7}\,\mathrm{Mpc}^{-3}$ for constant output or $\lesssim 10^{-8}\,\mathrm{Mpc}^{-3}\mathrm{yr}^{-1}$ in the case of fast transient sources (burst duration below 100 s) [117]. This discovery represents one of the major motivations for the construction of next-generation detectors with multitudes of the IceCube target volume opening the window for actual neutrino astronomy.

---

[1] Awarded the "Breakthrough of the Year 2013" by *Physics World*.

[2] Stated values refer to the energy actually deposited in the detector. In particular in the case of muon track events leaving the array (see section 2.1.1) the total energy of the initial neutrino can be significantly larger.

2.3 Towards a Global Neutrino Network

With the Global Neutrino Network (**GNN**) a framework has been initiated in 2014 aiming at a closer collaboration between the existing neutrino telescope projects. Goals of the GNN include the coordination of alert and multi-messenger policies, the exchange and mutual cross-checks of software, creating a common software pool, establishing a common legacy of public documents, developing standards for data representation, cross-checks of results with different systematics, and in general promoting the exchange ans interaction between its members by e.g. organizing joint scientific meetings.

Joined, as of now, by all major players in the community, namely the ANTARES and KM3NeT collaboration as well as the Baikal collaboration and IceCube collaboration, intends to pave the way towards a unified global neutrino observatory [118].

2.4 IceCube-Gen2: A vision for the future

From a historic point of view, the main motivation for neutrino telescopes was the still unresolved question of the origin of cosmic rays. Construction of larger detectors is the next logical step to take, following the “first light” by IceCube. The relatively strong diffuse flux of high-energy neutrinos indicates a strong activity of hadronic accelerators. One of the main goals of a next generation of neutrino telescopes, featuring instrumented volumes larger than 10 km^3, will be the identification of point sources and the detection of GZK neutrinos. Furthermore, the opportunity for multi-messenger astronomy arises from the cooperation with future gamma ray and gravitational wave detectors.

Alongside the above-mentioned KM3NeT project in the Mediterranean, extensions of the Antarctic neutrino telescope infrastructure are currently envisaged, subsumed under the label of **IceCube-Gen2** [119] (see figure 2.15). The high-energy section of IceCube-Gen2 [120], sometimes dubbed **IceCube HEA** (for High-Energy Array), will comprise up to ~ 15000 optical modules (roughly tripling the number used in the currently operated array). Due to the high energy of the targeted neutrinos however ($E_\nu \gtrsim 50\,\text{TeV}$), these can be distributed more sparsely, resulting in a total volume larger than $10\,\text{km}^3$, corresponding to an increase by a factor of ten with respect to the original IceCube volume. The average string-to-string distance is supposed to be around 240 meters. Enhancing the volume will not only improve statistics but also result in an angular resolution for muon tracks of well below 0.5° due to a longer lever arm. Main physics topics to be addressed by the high-energy section of IceCube-Gen2 are the detailed investigation of the so-called “IceCube flux”[1] (e.g. energy spectrum, flavor composition) as well as the search for possible point-sources of these neutrinos and hereby for potential origins of the charged high-energy cosmic ray particles. In addition, the science program includes the detection of GZK neutrinos and the definite identification of τ neutrinos in the detector. Another goal is the measurement of neutrino interaction cross-sections at energies beyond $100\,\text{TeV}$ which are inaccessible to accelerator experiments. In cooperation with a next generation of detectors for high-energy gammas and gravitational waves, as well as future optical telescopes, IceCube-Gen2 will contribute to the realization of multi-messenger astronomy,

---

[1] See section 2.2.3.

but also probe areas opaque for photons. Last but not least, there is potential to find new and unexpected physics.

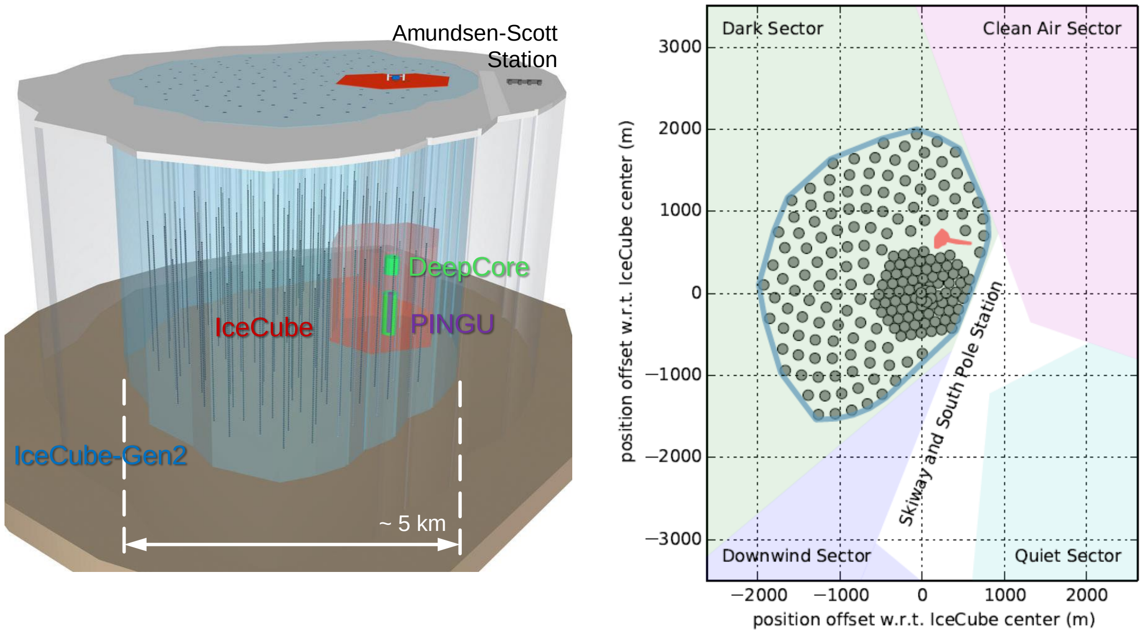

Figure 2.15: **Left**: Impression of the future IceCube-Gen2 neutrino telescope, featuring the high-energy array (*blue*) and PINGU (*violet*) as well as the currently existing detectors IceCube (*red*) and DeeCore (*green*). The Amundsen-Scott South Pole Station shown in *grey*. Figure retrieved from `https://gallery.icecube.wisc.edu/internal/` and modified. **Right**: Footprint of the benchmark design of IceCube-Gen2 adding a total of 120 strings to the existing IceCube array. Taken from [119].

Besides HEA, IceCube-Gen2 will include an dense array for the detection of low-energy neutrinos. Named **PINGU**, which stands for Precision IceCube Next Generation Upgrade, this detector will be realized by the deployment of 26 additional stings in the central region of IceCube inside the DeepCore sub-volume [24, 119]. Current design studies favor a horizontal string distance of 20 meters. The vertical instrument density will also be increased keeping 60 modules per string but reducing the vertical distance to five meters. In this configuration PINGU is optimized for neutrino energies between 5 GeV and 15 MeV. The physics case includes the determination of the neutrino mass hierarchy (see section 1.1) from the observation of matter dependent oscillation of atmospheric neutrinos as well as the verification of corresponding oscillation parameters.

An expansion of the IceTop surface detector array is also considered in the scope of IceCube-Gen2 [119].

Based on the demonstrated high reliability of the IceCube optical module (only 1.6% loss during installation, 0.4% of outage within five years of operation, as of now. The estimated 15-year survival probability[1] is 94%. [71]) a slightly modernized version of the module is considered the baseline technology for the Gen2 array. Outdated respectively

---

[1] The “15-year survival probability” is a figure used to rate devices for space applications, such as satellites. 90% is considered an acceptable value.

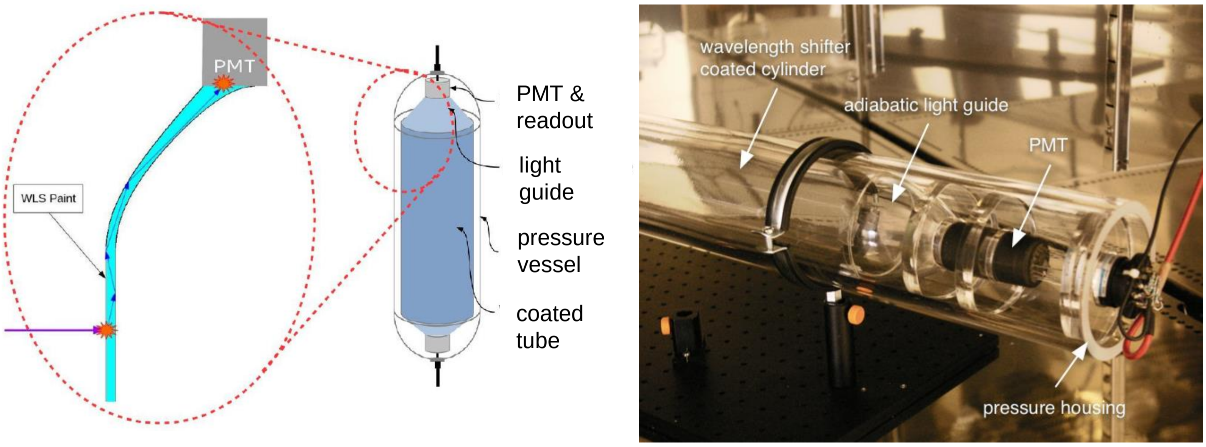

Figure 2.16: **Left**: Light detection principle of the Wavelegth-shifting Optical Module (WOM). **Right**: Module prototype featuring main components.
Figures taken from [121], modified.

electronic components will be replaced by a new design while at the same time keeping the well-proven mechanical parts, such as the pressure vessel, cabling, and the PMT [24, 119].

Alongside the baseline design there are plans to increase the yield of the detector utilizing novel optical technology. Design goals driving the new developments are the reclaiming of the ultra-violet fraction of the Cherenkov radiation, the introduction of intrinsic directional sensitivity, and a general increase of the effective area of the module. At present three alternative module concepts are under development:

- **WOM** (Wavelength-shifting Optical Module): The WOM project aims at increasing the module effective area introducing sensitivity to UV photons. As mentioned in section 2.1.2, UV sensitivity is of no importance in water neutrino telescopes due to strong absorption by the medium whereas ice is UV transparent. Due to the $1/\lambda^2$ dependence of the Cherenkov spectrum (see section 2.1.2, in particular equation 2.4), increasing the UV acceptance has a strong impact on the photon yield resulting in a larger effective area of the module. In order to meet this goal the pressure vessel of the WOM will mostly be made of UV-transparent quartz glass which also features low radioactivity to take full advantage of the low-background environment in the deep ice (see figure 2.16). Inside the optical module the ultraviolet photons hit a plastic (currently PMMA) cylinder coated in a wavelength shifting agent. The paint converts the UV photons to visible light which, if emitted inside the cylinder material, will propagate trapped by total internal reflection. At both ends of the cylinder, adiabatic concentrators are located which focus the light onto the actual sensors, two low-noise two-inch PMTs producing a digital output signal [121].

  While the main advantage of the approach is a significant increase of the effective area, it comes at the cost of limited time resolution, caused by the re-emission time of optical photons by the wavelength-shifter. A further problem are the higher costs for quartz pressure vessels compared to standard boro-silicate glass.

- **DEgg**: Main goal of the DEgg layout is an increased sensitive area per module. In addition, based on the lessons from the HESE analysis [1, 66, 67] (see also section 2.1.2)

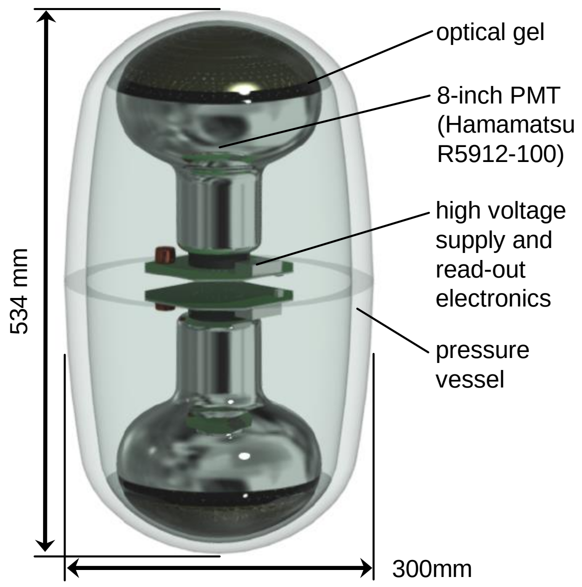

Figure 2.17: Dimensions and main components of the dual-PMT optical module (DEgg). Taken from [122], modified.

it adds sensitivity to light from the upper hemisphere. For this purpose the DEgg (see figure 2.17) features two eight-inch PMTs, with mounted read-out electronics, oriented back-to-back along the vertical axis of the module. In addition, the quantum efficiency (see section 3.1) of the used PMTs will be enhanced compared to the IceCube standard model. A further increase of the effective area is to be gained from a reduced wall thickness of the pressure vessel in front of the photocathode area of the PMTs. Therefore a roughly elliptical custom bipartite pressure vessel produced from borosilicate has been developed featuring a variable wall thickness with the maximum at the joint of the two segments [122].

- **mDOM**: The mDOM (multi-PMT Digital Optical Module) is an optical module based on the KM3NeT layout featuring an array of three-inch PMTs inside a near-spherical pressure vessel. The development and testing of mDOM components is the subject of this work. A detailed introduction of the new module is given in the dedicated chapter 4.

For most recent developments in the project, as well as future perspectives, see chapter 12.

3 Photomultiplier tubes

Photomultiplier tubes (PMTs) are powerful devices for light detection. Starting with signals at single photon level, they cover a dynamic range up to several thousand photons per pulse, featuring output linearity and precise timing. Since their first introduction, back in the 1930s, they continue being the workhorse detection devices for tasks such as scintillation counting, gamma ray astronomy or neutrino detection. The operation method of a PMT is based on the conversion of photons to electrons via photoeffect and the subsequent multiplication of the produced electrons. The output is a charge or voltage signal measurable with devices such as amperemeters, pulse-height analyzers or oscilloscopes. A schematic drawing of a PMT is shown in figure 3.1, featuring the main components of the tube and main processes contibuting to photon detection: photoconversion at the cathode and electron multiplication at the dynodes.

The constituents of PMT and their operation principles are described in this section, together with their influence on major output properties.

3.1 Photocathode

The photocathode is a thin semi-transparent layer on the inside of the entrance window of the tube[1] with the ability of emitting electrons when hit by photons. It usually consists either of alkali metals (e.g. potassium and caesium in case of the widely used, so-called “bi-alkali” cathodes) evaporated on a layer of antimony or of doped crystalline semiconductors. In both cases the resulting cathode has semiconductor properties [123]. The conversion of photons into electrons is governed by the **photoeffect/photoemission**. According to a theoretical model described in [125], this process can be split into three discrete sub-processes illustrated in figure 3.2:

- **excitation** of an electron into the continuum by the absorbed photon inside the photocathode material

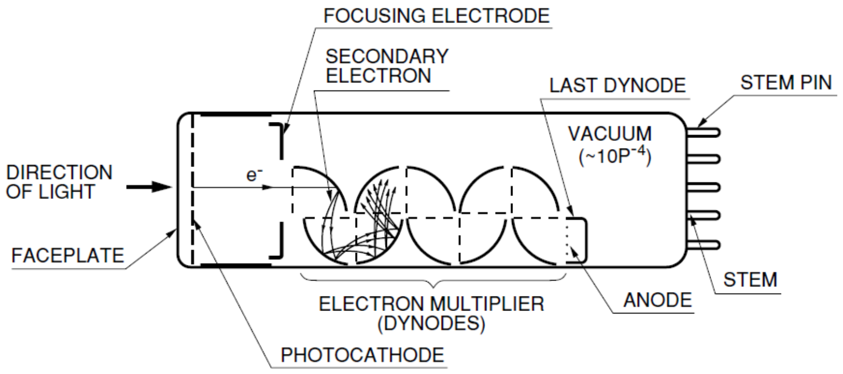

Figure 3.1: Schematic of a (head-on window type) PMT showing main constituents and the principle of photon detection. Figure taken from [123].

---

[1] Described here is the case of transmission mode photocathodes and frontal window PMTs as these are commonly used for neutrino telescopes. For alternative configurations see [123] or [124].

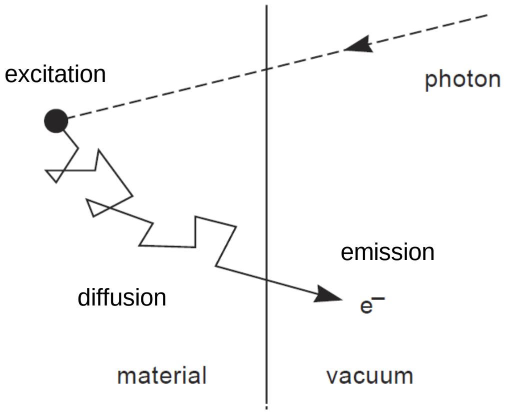

Figure 3.2: Photoemission of electrons from a material. The overall process is split into independent sub-processes (excitation, diffusion, and emission) as discussed in section 3.1. Taken from [124], modified.

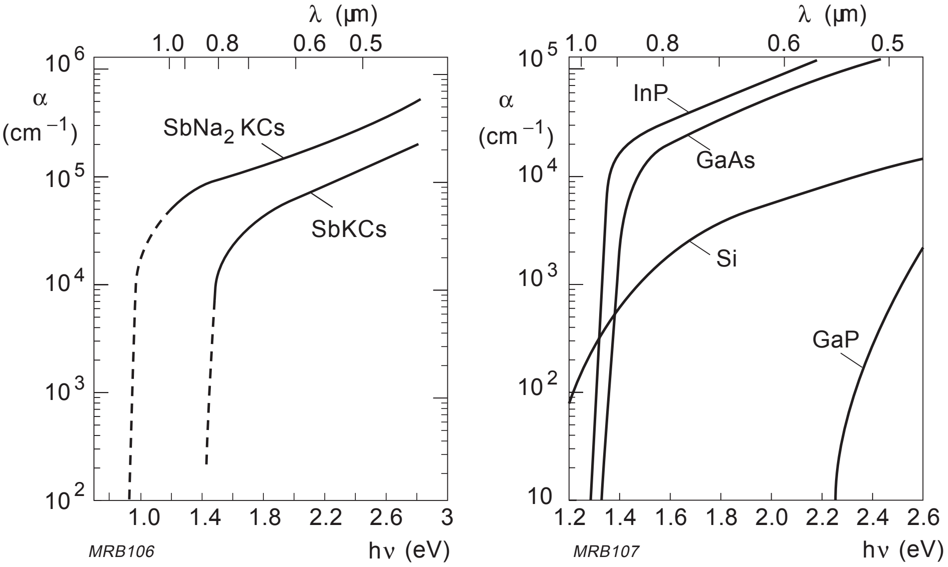

Figure 3.3: Absorption coefficients α for a selection of photocathode compositions as a function of photon energy $h\nu$ or wavelength λ. Cathodes based on SbKCs are usually referred to as "standard bialkali". Taken from [124].

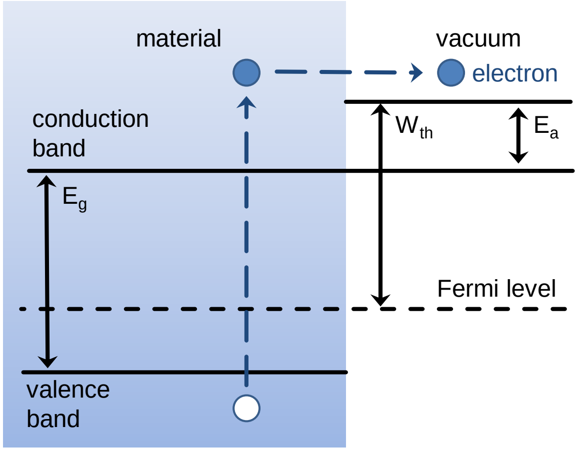

Figure 3.4: Band model of an alkali photocathode, featuring band gap E_{g}, electron affinity E_{a}, and work function W_{th}. The energy deposited by a photon has to be greater than the sum of E_{a} and W_{th} in order to emit a photo-electron into vacuum. Surface effects on the energy levels are not taken into account.

- **diffusion** of the electron through the material including energy loss
- **emission** of the electron in case it reaches the surface with enough energy to overcome the potential barrier

The discretization approach allows to derive the **quantum efficiency** QE of the process, defined as

$$QE = \frac{N_\mathrm{e}}{N_\gamma} \tag{3.1}$$

where N_γ and N_e are the respective mean numbers of photons reaching the photocathode and of emitted electrons, as a function of the probabilities of the underlying sub-processes:

$$QE(\lambda) = \big(1 - R(\lambda)\big) \cdot \frac{P_\mathrm{ex}(\lambda)}{\alpha(\lambda)} \cdot \frac{1}{1 + 1/\alpha(\lambda)L} \cdot P_\mathrm{surf} \tag{3.2}$$

where $R(\lambda)$ is the reflection coefficient at the cathode surface, $\alpha(\lambda)$ the absorption coefficient for optical photons inside the cathode material, $P_\mathrm{ex}(\lambda)$ the electron excitation probability, L the mean escape length of excited electrons, P_surf the probability to escape the surface and λ the wavelength of the incident light [123].

Due to the strong α-dependence, the long-wavelength cut-off of the quantum efficiency is determined by the drop of this coefficient. Absorption coefficient curves for different photocathode materials are presented in figure 3.3. A simplified, more intuitive way to derive the low-energy cut-off for alkali-based cathodes is the fact that, to be able to liberate an electron, the photon energy E_γ must exceed the combined band gap E_g and electron affinity E_a:

$$E_\gamma > E_\mathrm{g} + E_\mathrm{a} \tag{3.3}$$

This requirement is illustrated in the energy band model of figure 3.4. Further simplification (neglecting of the semiconductor properties) results in the possibility to connect the cut-off to the work function of the material ($E_\gamma > W_\mathrm{th}$). With typical work functions $W_\mathrm{th} \approx 2\,\mathrm{eV}$ alkali metals are intrinsically well suited for the detection of visible light[1].

At short wavelengths, corresponding to high photon energies, a drop in efficiency occurs due to decreasing transparency of the window glass in the ultraviolet region. The overall wavelength dependence of the quantum efficiency is shown in figure 3.5 for various window materials. The values can be influenced by the compositions of cathode and window, as well as by variation of their respective thicknesses. As in particular the cathode is typically a semi-transparent sub-micrometer layer, multiple reflections and interference effects have to be taken into account as discussed in [124].

It is also possible to quantify cathode efficiency in terms of radiant (or luminous) sensitivity, as often done by PMT manufacturers when stating PMT performance in test sheets. **Radiant sensitivity** is defined as the cathode photocurrent I_C divided by the spectral radiant flux $F_\mathrm{rad}(\lambda)$ evoking it:

$$S_\mathrm{rad}(\lambda) = \frac{I_\mathrm{C}}{F_\mathrm{rad}(\lambda)} \tag{3.4}$$

---

[1] Photocathodes based on original semiconductors, such as silicon, gallium or arsenic, need to undergo heavy doping and special surface treatment, resulting in negative electron affinity, to be able to detect visible light, For details, see [124].

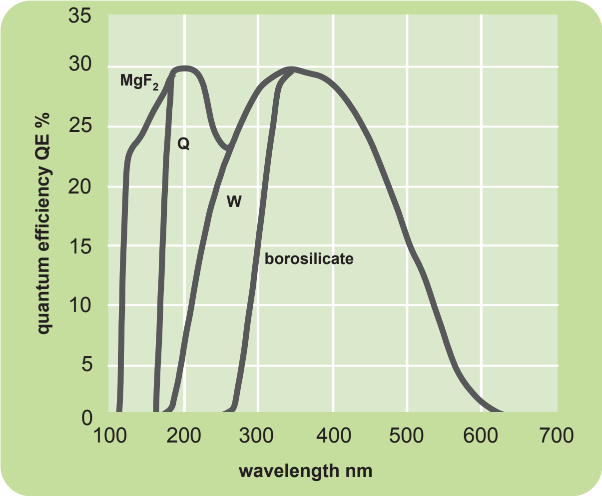

Figure 3.5: Dependence of the quantum efficiency of a PMT on the wavelength of the incident photons. Curves show the efficiency of a standard bialkali photocathode with different window materials. "Q" and "W" denote quartz glass and UV transparent glass, respectively. Taken from [126].

where λ is the photon wavelength. The relation between radiant sensitivity and quantum efficiency QE is given by

$$QE(\lambda) = \frac{hc}{\lambda e} S_{\mathrm{rad}}(\lambda) \tag{3.5}$$

with the Planck's constant h, speed of light c, and electron charge e [123].

The photoelectrons emitted from the cathode are accelerated by the electric field, which originates in a voltage applied between photocathode and first dynode, and fed into the electron multiplier system.

3.2 Electron multiplier

The electron multiplier of a PMT is responsible for the conversion of a single electron signal, produced by the photocathode, into a measurable charge pulse. It is comprised of an array of metal electrodes, so-called dynodes (e.g. made from AgMg, CuBe or NiAl [124]), coated with a material featuring a high secondary emission coefficient, usually doped semiconductors with negative apparent electron affinity. The amplification process is illustrated in figure 3.1. An electric field, produced by voltages applied between the dynodes, guides the electrons to the subsequent dynode, accelerating them along the way. For a more detailed description of the voltage supply system see section 3.4. **Secondary electron emission** occurs when a dynode is hit by electrons, multiplying their total number. The process can be described using three discrete steps – **excitation, diffusion** and **emission** – similar to the treatment of the photoeffect in section 3.1. The main excitation mechanism is the ionization of atoms at deep energy levels by primary electrons penetrating the dynode surface, followed by a series elastic and inelastic scattering interactions of secondary electrons. Up to 30 % of the primary electrons can be back-scattered without producing secondaries [124]. The approach results in the representation of secondary emission coefficient δ, which is the factor of multiplicity i.e. the fraction between the mean numbers of incoming and outgoing electrons (N_{in} and N_{out}), as a function of the primary electron energy E_{p} (which in its turn is a linear function of the inter-dynode voltage)

$$\delta = \frac{N_{\text{out}}}{N_{\text{in}}} = aE_{\text{p}}^{k} \tag{3.6}$$

where a is a constant. The exponent k, reflecting material and surface properties, usually varies between 0.7 and 0.8 [123]. This relation implies the possibility to exponentially increase the gain applying higher voltages. The equation holds true until δ reaches a maximum. For higher energies primary electrons are able to penetrate deeper into the material releasing secondaries which do not reach the surface. This causes the secondary emission coefficient to decrease with $\delta = aE_{\text{p}}^{1-k}$ setting an intrinsic limit to the achievable gain per dynode stage [124].

Based on the emission coefficient of the individual dynodes δ_i an expression can be derived for the **gain** G of the PMT which relates the mean number of electrons leaving the cathode N_{C} to the expected value of the number of electrons arriving at the anode N_{A}:

$$N_{\text{A}} = N_{\text{C}} \cdot G_{\text{DC}} = N_{\text{C}} \cdot C_0 \cdot G_{\text{pulse}} = N_{\text{C}} \cdot C_0 \cdot \prod_{i=1}^{n} g_i = N_{\text{C}} \cdot C_0 \cdot \prod_{i=1}^{n} c_i \delta_i \tag{3.7}$$

where n is the number of dynodes. The overall gain is the product of individual dynode gains g_i, which, in their turn, are comprised of dynode secondary emission coefficients δ_i and inter-dynode **collection efficiencies** c_i. In the convention applied, c_i denotes the probability that an electron emitted from dyonde i hits the subsequent dynode $i+1$, while C_0 is the probability of primary photo-electrons hitting the first dynode. Their values are smaller than one, but usually close to unity. Note that the definition of the PMT's gain depends on whether it is operated in current (G_{DC}) or pulse mode (G_{pulse})[1]. For further details on PMT operation modes see section 3.3. It is also possible to define a "global" collection efficiency for a PMT, usually abbreviated *CE*. Using this convention formula 3.7 becomes

$$N_{\text{A}} = N_{\text{C}} \cdot C_0 \prod_{i=1}^{n} c_i \cdot \prod_{i=1}^{n} \delta_i = N_{\text{C}} \cdot \mathit{CE} \cdot G_{\text{ideal}} \tag{3.8}$$

where $G_{\text{ideal}} = \prod_{i=1}^{n} \delta_i$ is an idealized gain neglecting electron losses in the dynode system.

A value close to unity is desired in particular for C_0 to minimize the spread of output amplitudes for repeated identical input. This can be achieved by additional focusing dynodes added between cathode and first dynode which optimize the shape of the electric field guiding the electrons or by increasing the area of the first dynode with respect to the cathode area. These measures also ensure that photoelectrons originating at different positions are equally well collected and fed into the dynode system decreasing variation of C_0 across the cathode and improving spacial/radial **output uniformity** [124]. A schematic example of a uniformity scan is shown in figure 3.6. Another goal achievable by optimization of the dynode structure is the minimization of timing **jitter** or **transit-time spread** (TTS). It is discussed in more detail in section 3.5.

---

[1] The difference in gain definition results from different measurement techniques: In current mode gain is measured as the ratio between cathode and anode current which includes influence of the collection efficiency C_0 between photocathode and first dynode. In pulse mode gain is derived from a charge spectrum dividing the position of the single photoelectron peak by the elementary charge (see also section 3.6). The latter approach does not include C_0 as it only influences the amplitude of the peak but not its position.

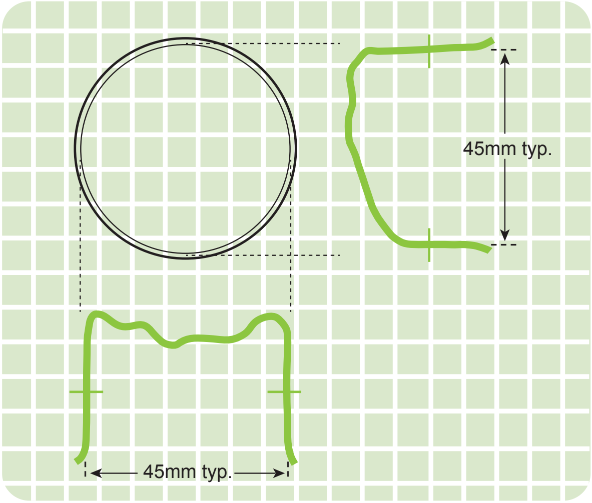

Figure 3.6: Qualitative sketch of output variations for identical input across the photocathode, measurable using a pencil light beam scanner. The shape is affected by the form factor of the entrance window as well as by the shape of the first dynode and reflective surfaces inside the PMT (see section 5.2). Taken from [126].

Figure 3.7: Equivalent circuitry for a PMT operated with positive supply voltage. Internal resistance and capacity of the tube are dubbed R_0 and C_0. R_L and C_L are properties of the read-out device. The signal $V(t)$ is measured in pulse mode. For the dependence of $V(t)$ on the highlighted circuit components see section 3.5. Taken from [126].

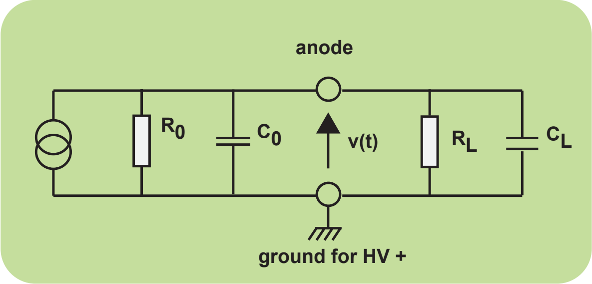

Performance of a PMT is also influenced by the geometrical layout of the dynodes and their arrangement. Current PMT prototypes for the KM3NeT project feature a so-called “linear focused” dynode structure optimized for output linearity and low TTS. The dynode structure is followed by the anode, where the produced electrons are collected and can be read out. Depending on the operation mode of the PMT (see section 3.3 for details) an incident photon results in a current or voltage pulse.

3.3 PMT operation modes

A PMT is per-se a time-variable charge/current source (see figure 3.7 for equivalent circuitry). Depending on the application in mind however, there are two different ways to read-out and process the signal:
If detected in **current** or **DC mode**, the electrons reaching the anode are directly fed into a current measuring device, such as a picoamperemeter. The total charge of all pulses arriving inside a certain time window is integrated resulting in a current value. As information on individual pulses is lost, current mode is usually used when vast numbers of photons and high pulse frequencies are expected. This situation is illustrated in figure 3.8,b.

In **pulse mode** the PMT output is first applied to a resistor (e.g. the internal resistor

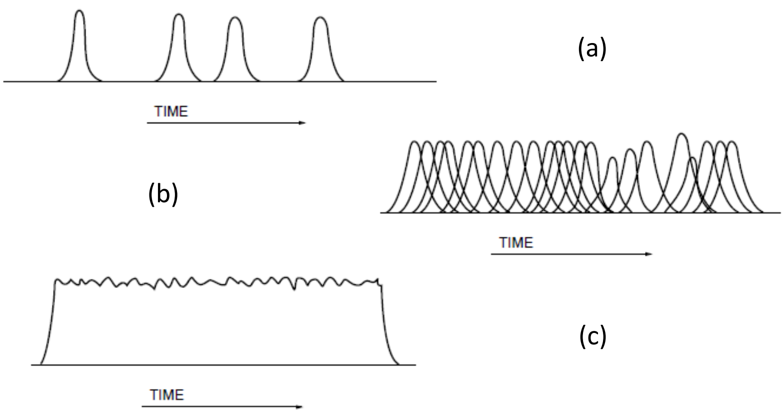

Figure 3.8: Sketch of possible PMT output. **a**: Sparse pulses measured in pulse mode, **b**: Overlapping pulses, **c**: Output measured in current mode. Figure taken from [127].

of an oscilloscope) and the resulting voltage pulse is measured. This approach enables investigation of the signal on individual pulse level. Besides counting the pulses, it is possible to explore their properties applying amplitude thresholds, deducing arrival time or integrating the charge of individual pulses. As a result, pulse mode read-out is especially useful for the detection of weak low-frequency signals or single photon counting. With increasing pulse frequency however, the intrinsic dead-time of the read-out device has to be taken into consideration as pulse counting will underestimate the real signal rate. A "natural" limit is reached when subsequent pulses start overlapping. At this point no additional information is to be gained from pulse mode and DC mode can be used (see figure 3.8).

In the scope of this work both modes were utilized to investigate PMT properties. As the goal of neutrino telescopes is to count and time-stamp photons arriving at the optical module, the installed PMTs are operated in pulse mode.

3.4 Voltage dividers

For the electron multiplication to take place, the photocathode and each subsequent dynode need to be at a positive potential with respect to the preceding stage. In the most simple case, this is usually achieved using a resistive voltage divider installed parallel to the dynodes. The total voltage provided to the PMT is thus subdivided according to

$$U_i = \frac{R_i}{\sum\limits_{j=1}^{n} R_j} \cdot U_{\mathrm{PMT}} \tag{3.9}$$

where R_i is the resistance connected between dynode i and $i+1$, U_i the according inter-dynode voltage and n the number of dynodes of the PMT. The total supplied voltage is dubbed U_{PMT}.

This approach leaves the user with two possible supply voltage configurations: A PMT can be operated either with its photocathode at negative high voltage (HV) and the anode at ground potential (**negative polarity**) or, in the case of **positive polarity**, the

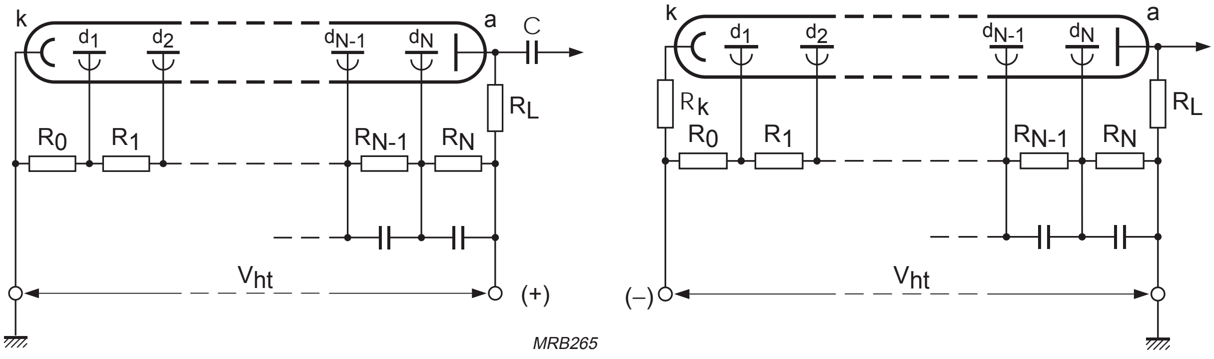

Figure 3.9: Schematic circuit diagrams of resistive voltage-dividers for positive (**left**) and negative supply voltage polarity (**right**). The shown circuits are designed for pulse mode applications. If a negatively-fed PMT is read out in DC mode the shown capacitors are omitted. R_0 to R_N are equal is DC mode, whereas in pulse mode higher resistances are used at the final dynode stages in order to improve output linearity [124].

cathode is grounded and the anode connected to positive high voltage. For a schematic circuit diagram of corresponding voltage dividers see figure 3.9. Both approaches come with their respective advantages and limitations: While the output of a PMT at negative polarity can be directly fed into read-out electronics, positive polarity demands galvanic separation of the anode (e.g. using a capacitor) which affects the quality of the output leading e.g. to potential drift of the baseline. This becomes problematic if the signal is to be examined applying an amplitude threshold. The choice of HV polarity also impacts on the readout modes available as DC mode is only possible in conjunction with negative high voltage. On the other hand however, a photocathode at high negative potential promotes increased and unstable dark rates. This effect is more pronounced if objects at ground potential are placed near the PMT, in particular near the photocathode area. Possible counter-measures are discussed in section 3.8. Apart from the general decision for one of the possible high-voltage polarities, the voltage divider itself can be object to fine-tuning in order to fit a specific task. The right choice of resistors is defined by the maximum expected anode current. Their values have to be chosen according to

$$I_{\mathrm{HV}} > f \cdot I_{\mathrm{A}} \tag{3.10}$$

where I_{HV} is the current flowing through the divider's resistor network. I_{A} represents the maximum anode current for DC operation or the mean anode current in case of pulse mode read-out. The factor f depends on the desired degree of **output linearity**. Values between 20 [123] and 100 [126] are suggested by manufacturers. Substantial deviation from linearity will occur if the anode current reaches $\sim 10\,\%$ of I_{HV} [123].

Capacitors inserted parallel to the last dynode stages in the pulse mode divider layout improve output linearity. In case of strong pulses arriving, these dynodes need to be able to emit large numbers of electrons which are then resupplied by the capacitors. Their capacitances C_i have to satisfy

$$C_i > \frac{\mathit{\Delta} Q_i / U_i}{\mathit{\Delta} U_i / U_i} \tag{3.11}$$

where $\mathit{\Delta} Q_i$ is the charge drawn from the capacitor to resupply the electrons emitted by

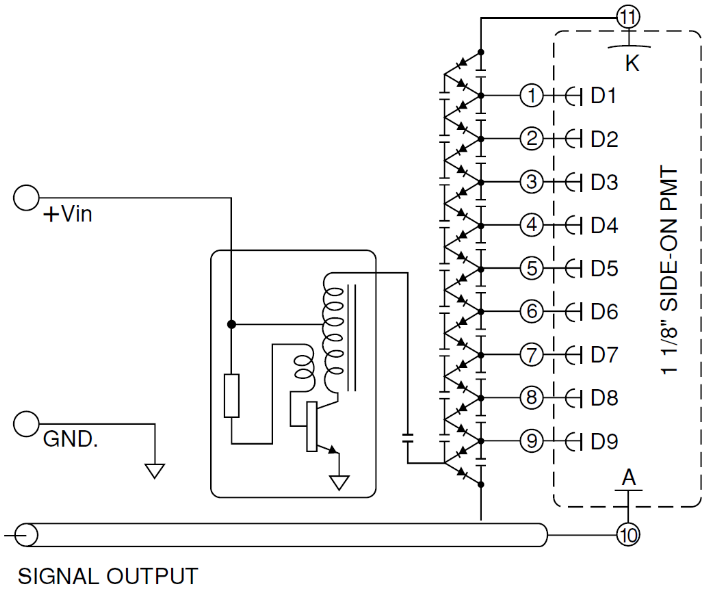

Figure 3.10: Basic Cockcroft-Walton voltage multiplier circuitry. The shown setup provides equal voltage increments to all dynode stages D_i. Amplitude of the required AC input is set by the reference voltage V_{in}. Figure taken from [123].

the i-th dynode, U_i is the inter-dynode voltage and $\Delta U_i/U_i$ is the maximum acceptable relative voltage drop during pulse amplification [126].
Deviation form linear behavior is also promoted by the so-called "space-charge effect". In case of high input intensity the released electrons form extended clusters making their way through the vacuum inside a PMT. If dense enough, these clusters distort the electric field in the area, superimposing their own electric fields. For instance, additionally arriving electrons will be repelled, and thus slowed down. To overcome this undesirable effect, larger values of resistance at the final dynode stages are used to increase the electric field strength between them.

Increasing resistance of the divider circuit to cope with high signal levels reaches a limit when the amount of power drawn becomes non-negligible. For application featuring a tight power budget, such as neutrino telescopes, it makes sense to use more complicated but power-saving active voltage supplies. In one such approach, the **Cockcroft-Walton voltage multiplier**, instead of resistors a series of diodes is connected to the dynode structure. Two neighboring diodes are in turn connected by capacitors. Driven by an AC source, featuring a peak-to-peak voltage V_{pp}, one such building block, or stage, provides a DC output, doubling the amplitude $V_{\mathrm{DC}} = 2V_{\mathrm{pp}}$. Adding stages to the chain results in further output increase by increments of V_{pp}. This circuitry, presented in figure 3.10, features lower power consumption (as current only occurs during reloading of the stages and no resistive elements are used) and better output linearity than a purely resistive device, due to the use of capacitors. As a (minor) drawback, inter-dynode voltages can only be integer multitudes of the basic increment [123].

This solution was applied in the PMT base design of KM3NeT, which is the basis for the mDOM base currently developed (see chapter 4).

3.5 Output pulse shape

If operated in pulse mode (see section 3.3), the response of a PMT to a short light pulse is a characteristic voltage peak (see figure 3.11) which can be examined e.g. by means of an oscilloscope. The pulse shape depends on light input parameters as well as on properties of the PMT and the device used for read-out. Resistors and capacitors highlighted in the schematic equivalent circuitry diagram (see figure 3.7) contribute to the pulse shape via the time constant τ of the combined circuitry of PMT and readout device as follows:

$$R = \frac{R_0 R_\mathrm{L}}{R_0 + R_\mathrm{L}} \tag{3.12}$$

$$C = C_0 + C_\mathrm{L} \tag{3.13}$$

$$\tau = RC \tag{3.14}$$

where R_0 and C_0 are qualities of the PMT while R_L and C_L denote load (i.e. readout) properties. The idealized **pulse shape** $U_\mathrm{pulse}(t)$ is then given by

$$U_\mathrm{pulse}(t) = \frac{N_\mathrm{phe} \cdot e \cdot G \cdot R}{\tau - \tau_\mathrm{s}} \cdot \left(e^{-t/\tau} - e^{-t/\tau_\mathrm{s}}\right) \tag{3.15}$$

where:

- N_phe is the number of photoelectrons produced by the light pulse at the cathode,
- e is the elementary charge,
- G represents the gain of the PMT, and
- τ_s the time constant of the light pulse, assuming exponential decay of the intensity.

In practice, the shape is characterized in terms of the rise time, transit-time spread and fall time of the pulse.

Rise time and **fall time** are defined as the time needed by the signal waveform to cross two subsequent amplitude thresholds during rise and drop-off. Usual choices are combinations of 10 % and 90 % or 20 % and 80 % of the maximum amplitude. In case of pulse mode voltage readout, the rise time is actually associated with a drop in voltage as the signal is negative.

The **jitter** or **transit-time spread** (TTS) is the variation of the time between production of a photoelectron and the arrival of the signal at the anode, dubbed transit time. This time varies due to different lengths of electron trajectories between cathode and anode (with the main contribution from the distance between cathode and first dynode) as well as due to different initial directions and velocities of primary and secondary electrons. Its distribution is roughly Gaussian. The TTS is usually quantified in terms of full-width-half-maximum or standard deviation of the transit time distribution. It introduces a lower limit to achievable signal timing precision and can be reduced by optimizing the electric field geometry and minimizing the path differences changing the cathode shape accordingly. As a result, PMTs featuring hemispherical entrance windows have usually

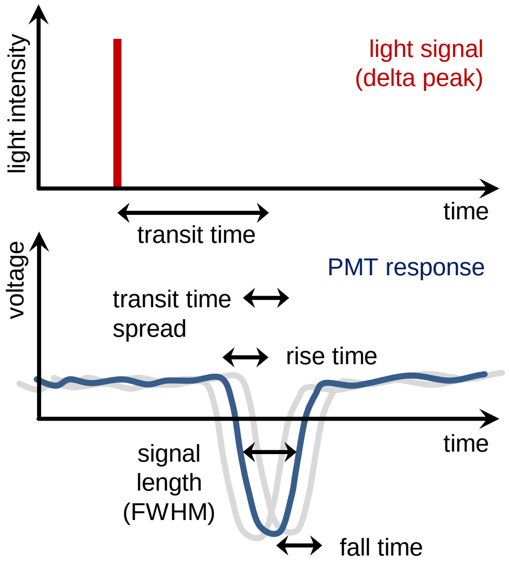

Figure 3.11: Schematic sketch of PMT voltage pulse invoked by a delta peaked light signal illustrating main timing properties.

superior timing compared to flat-window types. Timing also benefits from stronger electric fields i.e. higher supply voltage (variation approximately with $U_{\mathrm{PMT}}^{-1/2}$ [126]). Optimization has to be done keeping in mind increased dark count levels (see section 3.8). Improvement of timing can also be achieved by reducing the number of dynodes, which on the other hand reduces gain (see section 3.2), or a smaller diameter of the photocathode (trade-off against sensitive area). External magnetic and electric fields, strong enough to deflect electrons inside the PMT from their ideal trajectories, degrade timing precision [126].

3.6 Single photoelectron spectrum

If a PMT is operated in pulse mode, a charge spectrum of the signal can be acquired integrating the output voltage waveform. A similar distribution can be obtained sampling signal amplitudes. The principle is illustrated in figure 3.12. The integration window is set to a fixed width and positioned in time relative to the trigger. Triggering can either be done on the signal amplitude (self-trigger) or externally by the reference signal of a pulsed light source. In order to obtain a single photoelectron (SPE) spectrum, the light source is operated at a very low light output level of one photon per pulse and external triggering is used. In practice, with the light emission being a Poisson random process, the mean number of photons per pulse has to be substantially lower then one (e.g. 0.1) to reduce contamination by multi-photon events. The use of a fixed integration gate ensures purity of the signal with respect to pulsed background, such as afterpulses (see section 3.7). The SPE spectrum can be used do derive PMT properties, such as gain and peak to valley ratio. A quantitative sketch of the SPE spectrum (highlighting peak, valley and pedestal) is shown in the right part of figure 3.12. It consists of a convolution of near-Gaussian peaks. The most prominent peak (*red*) originates from the integration of the baseline and corresponds to the case of zero detected photoelectrons. Its position, marked by “0 phe” and dubbed “pedestal”, provides a natural origin for the charge axis, while its width is due to random noise and can be reduced using a low-noise setup. If the measurement is performed by means of an oscilloscope, the pedestal position reflects the

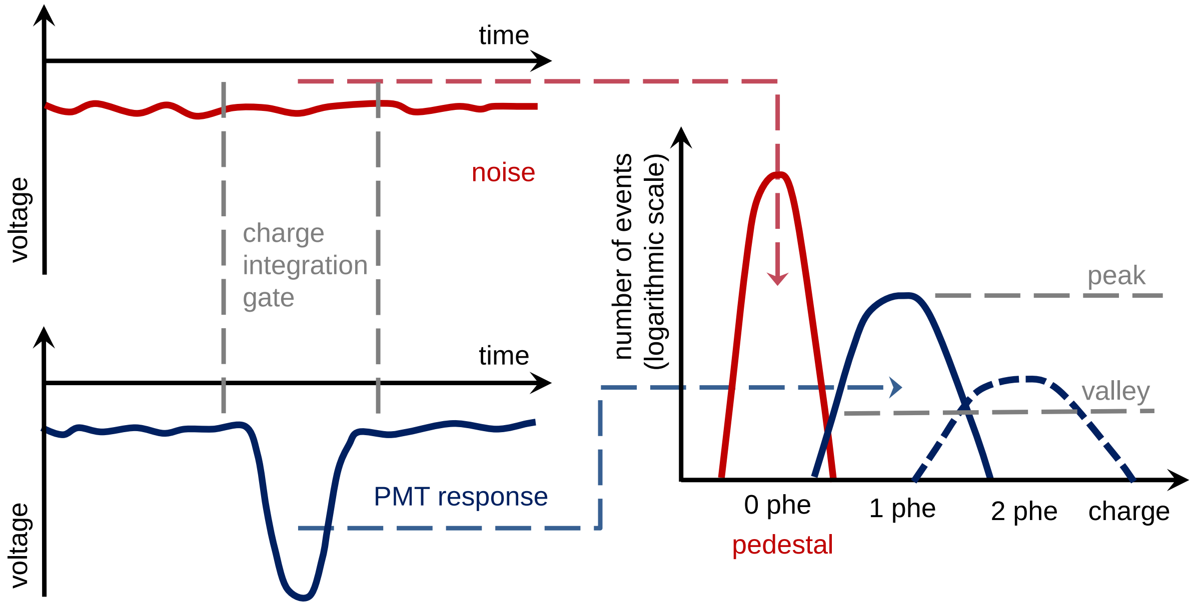

Figure 3.12: **Left:** Principle of charge spectrum acquisition from externally triggered voltage waveforms at low illumination level by a pulsed light source. The area between time axis and waveform enclosed by the integration gate represents the deposited charge used to construct the charge spectrum. **Right:** Qualitative sketch of resulting single photo-electron spectrum.

baseline shift relative to the true origin of the voltage axis. The *blue* peak with a centroid charge of "1 phe" is comprised of integrated single photoelectron pulses, whereas the *dashed blue* curve represents contamination by events where two electrons are emitted from the cathode. Increased light input leads to the emergence of additional multi-photoelectron peaks and the decrease and final disappearance of the pedestal peak. The widths of the photoelectron peaks are representations of gain (electron yield) variations of the electron multiplier system and provide a measure for the single photon resolution. The (pulse mode) gain[1] G_{pulse} of a PMT can be derived from the presented distribution as

$$\frac{Q_{1\text{phe}} - Q_{0\text{phe}}}{e} = \frac{Q_1}{e} = G_{\text{pulse}} \tag{3.16}$$

where $Q_{0\text{phe}}$ and $Q_{1\text{phe}}$ are the respective (charge) positions of the pedestal and SPE peak, Q_1 is the mean charge deposited at the anode by a single photoelectron event and e is the quantum charge. Modeling the underlying processes, as suggested in [128], results in an analytic description of charge spectra, outlined in the following paragraph.

Considering photon emission of the source (e.g. a pulsed LED) to be Poissonian and the conversion to a photoelectron to be a binary process results in a Poisson distribution for the number N of emitted electrons:

$$P(N,\mu) = \frac{\mu^N \cdot e^{-\mu}}{N!} \qquad \text{with} \qquad \mu = N_\gamma \cdot QE \cdot C_0 \tag{3.17}$$

where μ is the mean number of photoelectrons fed into the dynode system, QE the quantum efficiency of the cathode (see also section 3.1), C_0 the collection efficiency of

---

[1] For gain definitions see section 3.2.

the first dynode and N_γ the mean number of photons arriving at the photocathode. The amplification process inside the dynode structure (see also section 3.2) results, in the case of a large secondary emission coefficient of the first dynode (i.e. $\delta_1 > 4$) and assuming inter-dynode collection efficiencies close to unity, in a Gaussian distribution $G_1(q)$ for the charge output q evoked by one primary photoelectron:

$$G_1(q) = \frac{1}{\sigma_1\sqrt{2\pi}} \exp\left(-\frac{(q-Q_1)^2}{2\sigma_1^2}\right) \tag{3.18}$$

where Q_1 is the mean SPE output charge (see equation 3.16 for relation to SPE peak position and gain) and σ_1 is the corresponding standard deviation. The assumption of mutually independent amplification processes for individual photoelectrons (which is true for low rates) enables the expression of the multi-photoelectron case as a convolution of SPE events, resulting in the charge distribution $G_N(q)$ for N input electrons:

$$G_N(q) = \frac{1}{\sigma_1\sqrt{2\pi N}} \exp\left(-\frac{(q-NQ_1)^2}{2N\sigma_1^2}\right) \tag{3.19}$$

As no noise is included in this approach, the limit of $G_N(q)$ for $N \to 0$ results in a delta peaked pedestal at zero charge. An idealized PMT charge response $S_{\text{ideal}}(q)$ to N_γ incoming photons ($\mu \propto N_\gamma$, see equation 3.17) can then be obtained folding equations 3.17 and 3.19:

$$\begin{aligned} S_{\text{ideal}}(q) &= P(N,\mu) \otimes G_N(q) && (3.20)\\ &= \sum_{N=0}^{\infty} \frac{\mu^N \cdot e^{-\mu}}{N!} \cdot \frac{1}{\sigma_1\sqrt{2\pi N}} \exp\left(-\frac{(q-NQ_1)^2}{2N\sigma_1^2}\right) && (3.21) \end{aligned}$$

Incorporation of background processes and noise (for discussion of potential sources see sections 3.7 and 3.8) parametrized according to distribution $B(q)$

$$\begin{aligned} B(q) &= \frac{1-w}{\sigma_0\sqrt{2\pi}} \exp\left(-\frac{q^2}{2\sigma_0^2}\right) + w\theta(q)\alpha \cdot e^{-\alpha q} && (3.22)\\ &\approx \frac{1}{\sigma_0\sqrt{2\pi}} \exp\left(-\frac{(q-Q_0-Q_{\text{shift}})^2}{2\sigma_0^2}\right) && (3.23) \end{aligned}$$

where θ is a step function, σ_0 reflects non-zero pedestal width induced by low-amplitude continuous background, w is the probability for the occurrence of discrete background processes and α describes exponential decrease of discrete background probability with increasing amplitudes. Equation 3.23 is a low-noise approximation for $1/\alpha \ll Q_1$ where discrete processes contribute in the form of an effective pedestal shift $Q_{\text{shift}} = w/\alpha$ from its initial position Q_0. Convolution of equation 3.22 with the idealized PMT response (equation 3.20) yields an extensive expression for the realistic response charge distribution $S_{\text{real}}(q)$, whereas with the assumption of low noise and high values of μ (i.e. $\mu \geq 2$), it can be simplified to:

$$\begin{aligned} S_{\text{real}}(q) \approx &\left\{ \frac{1-w}{\sigma_0\sqrt{2\pi}} \exp\left(-\frac{(q-Q_0)^2}{2\sigma_0^2}\right) + w\theta(x-Q_0) \cdot \alpha \exp\left(-\alpha(x-Q_0)\right) \right\} e^{-\mu}\\ &+ \sum_{N=1}^{\infty} \frac{\mu^N e^{-\mu}}{N!} \cdot \frac{1}{\sigma_1\sqrt{2\pi N}} \cdot \exp\left(-\frac{(q-Q_0-Q_{\text{shift}}-NQ_1)^2}{2N\sigma_1^2}\right) && (3.24) \end{aligned}$$

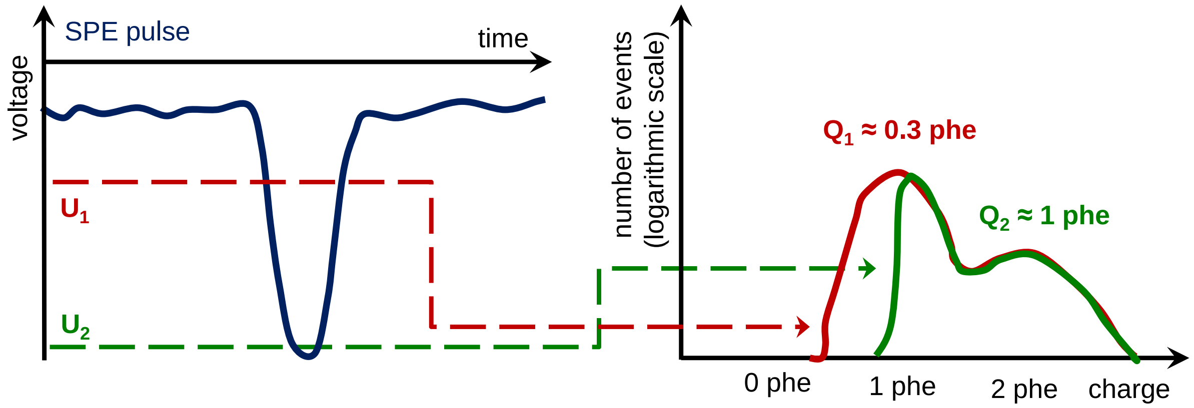

Figure 3.13: Expression of voltage amplitude thresholds in terms of integrated anode charge. The charge distribution is obtained integrating self-triggered waveforms. Triggering on amplitude thresholds (U_1 and U_2) results in characteristic cut-offs in the corresponding charge spectra (Q_1 and Q_2). Positions of the cut-offs define the threshold charge equivalent. The charge axis is scaled by multitudes of the mean SPE charge (see figure 3.12 for details).

The latter expression can be used to fit and characterize charge spectra. As for high pulse intensities the pedestal peak vanishes, and noise contributions become negligible, the resulting spectrum can be fitted using a single Gaussian curve.

A charge spectrum can further be used to assign charge equivalents to thresholds applied on the (voltage) amplitude of a pulse. The principle is explained and illustrated in figure 3.13. If the charge axis is scaled in number of photoelectrons, it provides a threshold value independent of knowledge of the PMT's gain and amplification of the readout device. This charge equivalent is in particular useful when comparing threshold-dependent PMT properties, such as the dark rate, measured with different setups.

3.7 Correlated pulsed background

Any pulses originating at the photocathode[1] can be, with their respective probabilities, replaced by early or delayed pulses, or succeeded by so-called afterpulses. This correlated background limits signal timing and photon counting performance in pulse mode applications and leads to artificially increased anode current if the PMT is operated in DC mode.

- **Early pulses** or pre-pulses occur if a photon crosses the photocathode without evoking an electron but produces an electron upon hitting the first dynode. This results in weak pulses (lacking the amplification of the first dynode) arriving at the anode earlier than the mean transit time. The magnitude of "earliness" is given by distance between

---

[1] These pulses include original signals produced by incoming photons, but can also be dark rate pulses or afterpulses

cathode and first dynode divided by the speed of light. Typical values are of the order of less than one to a few nanoseconds.

- **Late pulses** are produced by photoelectrons back-scattered from the first dynode without production of secondaries. These electrons are re-accelerated towards the first dynode by the electric field. If secondary electrons are produced upon the second impact, the resulting pulse is delayed with respect to the expected transit time. Typical delays are of the order of nanoseconds, with the actual values defined by the cathode-dynode spacing of the PMT (corresponding to half the available maximum electron travel distance) and the speed of the electrons depending on the acceleration and thus on the applied voltage. In case of short time offsets, late pulses will overlap with those "on-time" leading to a distortion of the falling edge of the waveform [129].
- **Afterpulses** are partially high-amplitude pulses arriving with a delay ranging from nanoseconds to several microseconds. The main mechanism for their production is the ionization of dynode adsorbents or residual gas atoms of the non-ideal vacuum of the PMT. While the emitted electrons will continue traveling towards the first dynode, the ionized atoms will be accelerated in the opposite direction and hit the photocathode. The impact of the energetic ions liberates several electrons resulting in retarded high-amplitude pulse. Bombardment by ions also leads to abrasion of the photocathode material. Exposure to helium, or other agents able of diffusion through the glass envelope of the PMT, leads to a dramatic increase of afterpulsing probability and results in a shortened lifetime of the PMT. Photons, produced during the amplification process, able to reach the photocathode also give rise to delayed correlated pulses (see "scintillation" in section 3.8).

The above-mentioned processes also occur at each stage of the dynode system where they do not produce individual pulses but contribute to the smearing in amplitude and time of the shape of the original pulse [123, 124, 130].

The signal contamination by correlated background is in particular undesirable in pulse mode applications. Its impact can be countered introducing dead-time after a primary signal in case of low count rates. Apart from improving PMT vacuum techniques, the afterpulsing probability can be decreased by lowering the voltage applied between cathode and first dynode thereby reducing ionization capability of the photoelectrons. A trade-off has to be made regarding collection efficiency and gain variation which both benefit from a high voltage.

3.8 Dark rate and dark current

Even in total absence of photons a PMT will produce a measurable signal as illustrated in figure 3.14. Depending on the manner of read-out, it will become manifest in "dark current" (in DC mode) or "dark rate" if the tube is operated in pulse mode. Several sources, discrete as well as continuous ones, contribute to the total amount of dark signals. The individual contributions and their dependence on (environmental) variables such as gain (related to high-voltage amplitude), ambient temperature, humidity or high-voltage polarity will be discussed in this section.

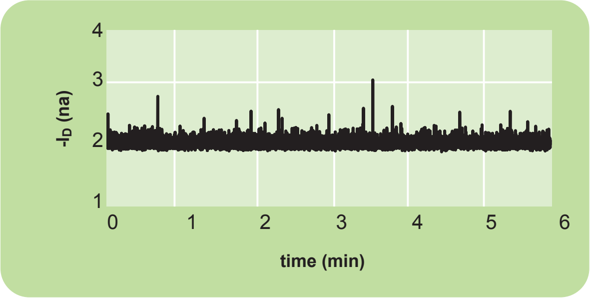

Figure 3.14: Dark current time trace of an type 9829B PMT by ET Enterprises. The curve features "spikes" form discrete dark rate sources superimposed on a baseline produced by leakage current. Taken from [126].

- **leakage current** is a continuous ohmic flow of charge onto the anode or the pin connected to it. Using Ohm's law with typical PMT input values ($R = 10^{12}\,\Omega$, $U_{\mathrm{PMT}} = 1000\,\mathrm{V}$) the intensity of leakage can roughly be estimated to be of the order of nanoamperes. As can be expected from Ohm's law, leakage current scales with applied voltage and has a very weak temperature dependence due to changing resistance. Originating either from internal components, other pins at the rear end of the PMT or from the glass envelope of the tube, it adds an offset to DC mode measurements. External factors increasing surface conductivity, such as humidity, grease or dust, enhance the amount of leakage. Being roughly constant with temperature, leakage current is the dominant dark current contribution in low-temperature applications [123, 124].

- **thermionic emission:** the main discrete component is thermionic emission of electrons from the photocathode (and to a smaller extent from the dynode coating). These electrons are collected by the dynode system producing regular output pulses. The emission is described by Richardson's law:

$$J = AT^2 e^{-\frac{W_{\mathrm{th}}}{kT}} \tag{3.25}$$

  in which $A \approx 6 \cdot 10^5\,\mathrm{Am^{-2}K^{-2}}$ is the Richardson constant, J represents the current density, W_{th} the work function, T the absolute temperature, and k is the Boltzmann constant. The work-function dependence implies that red/IR-sensitive PMTs suffer from increased dark count. The current induced by thermionic emission rises linearly with gain (and thus exponentially with PMT voltage) and has a strong dependence on ambient temperature which is illustrated in figure 3.15 for two different photocathode compositions. At room temperature, thermionic emission is the main source of dark rate. Significant reduction can be achieved by cooling the PMT[1]. Not reflected by equation 3.25 is the dependence of the emission on the photocathode area which is (to first order) expected to be linear [123, 124].

- **field emission**: (also known as cold emission) is emission of electrons from a material (in this case the electrodes of a PMT) induced by a strong electrostatic field. The emission is a form of quantum tunneling depending on the work function. In spite of

---

[1] Cooling also affects the spectral response curve shape of a PMT due to the temperature-dependence of the quantum efficiency and its gain via changing secondary emission coefficients. However, the drift is usually of the order some % for bi-alkali PMTs [124].

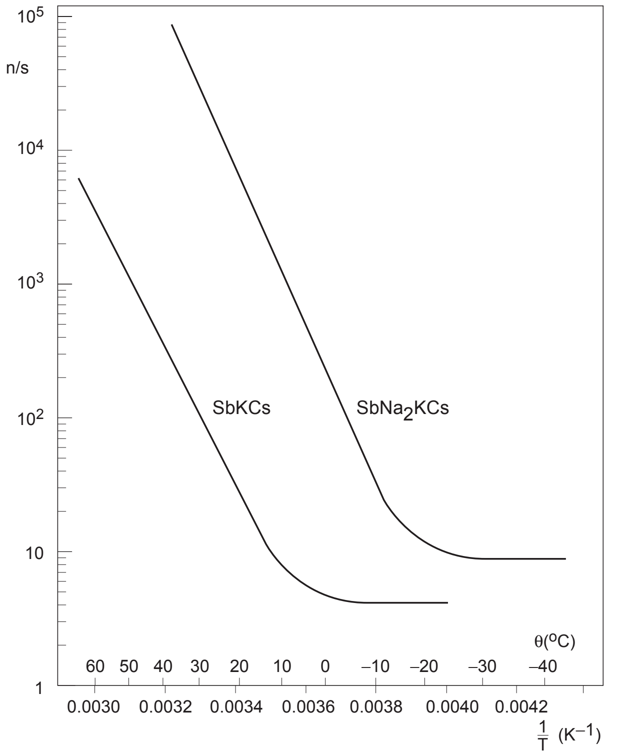

Figure 3.15: Number of dark pulses per second as a function of temperature, shown for different photocathode compositions. Figure from [124].

the electric fields inside a PMT being rather weak, this form of emission takes place due to roughness of the electrode surfaces. The escaped electrons can hit other electrodes or the inner surface of the glass envelope giving rise to scintillation light which can reach the cathode and produce pulses. Field emission non-linearly depends on the applied voltage. Rising steeper with voltage than the gain of the PMT it limits the maximum gain achievable with a fixed number of dynodes [124] (see figure 3.17).

- **background radiation**: The decay of radioactive isotopes (predominantly ^{40}K) included mostly in the glass contributes to the descrete dark rate. The emitted ionizing particles can either hit the photocathode or, if featuring energies above the Cherenkov threshold in glass, give rise to Cherenkov photons. Decays taking place ouside the tube (e.g. in air or inside the glass of a pressure vessel) further contribute to the rate. Another source of natural background radiation are high energy myons form cosmic ray air showers. Passing the PMT they produce numerous Cherenkov and scintillation photons leading to high amplitude pulses [123].

- **scintillation**: Apart from the charged particles already mentioned above, electrons deviating from their paths and escaping the multiplier system can hit the inside of the glass tube or parts of the dynonde support structure. Usually below the Cherenkov threshold, they produce scintillation light that can reach the cathode [123].

- **excitation** (of residual gas, cathode and dynode material): Exposure to powerful light sources (e.g. daylight) leads to excitation of particles inside the constituents of the PMT, mainly inside the photocathode and the glass envelope. The photons emitted during their de-excitation result in strongly enhanced dark count rates immediately after powering up the PMT. Unlike the rate from above-mentioned sources this fraction of the dark rate is temporary. It declines with operation time and disappears after a period ranging from minutes to days depending on the PMT type, initial exposure and supply voltage polarity [124].

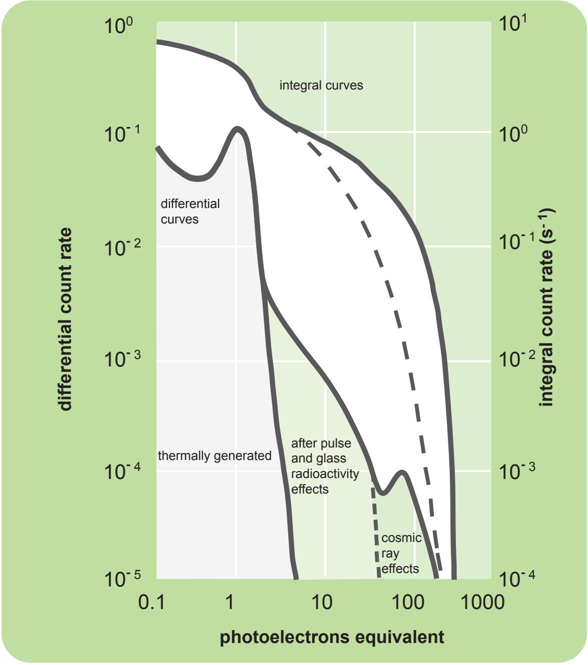

Figure 3.16: Amplitude spectrum of dark rate pulses with respective sources. Taken from [126].

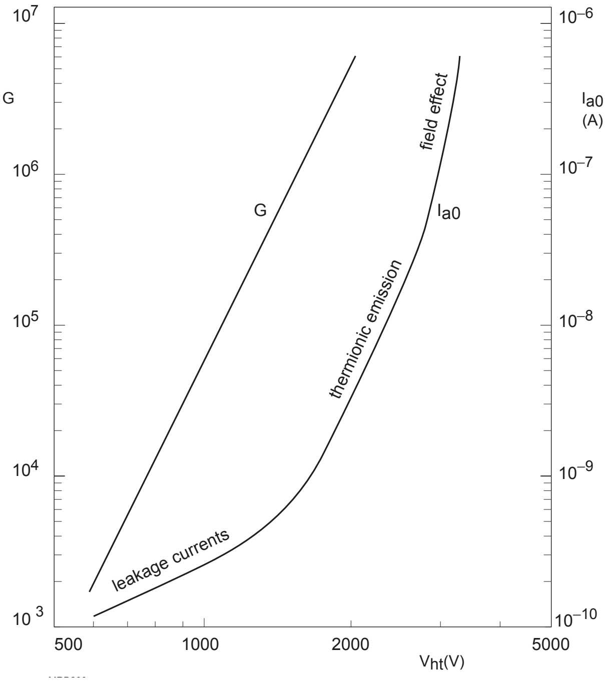

Figure 3.17: Dependence of main dark current and rate sources on voltage supplied to the PMT. Figure taken from [124].

The amplitude of dark rate pulses strongly varies, depending on the nature of their origin. An amplitude spectrum, with the sources denoted, is shown in figure 3.16. Scintillation, discussed above as one of the sources for dark rate, can also be induced by electric fields. Field gradients with respect to the photocathode potential are particularly problematic. Objects at a different potential situated outside the PMT near the cathode will promote scintillation from stray electrons inside the glass envelope leading to unstable and erratic behavior of the dark rate. Consequently, PMTs operated with negative supply voltage polarity are stronger affected by this effect as any object at ground potential (e.g. PMT housing or support structures) will enhance dark rate. With the photocathode grounded this problem can be eliminated [123, 124]. If positive voltage polarity is not an option, precautions have to be taken to insulate the PMT, in particular the photocathode, electrically from its surroundings. Another measure proposed by the manufacturers is the coating of the PMT surface with an electrically conductive material connected to photocathode potential in order to prevent field gradients inside the glass. On top of the coating, a layer of insulator is applied [123, 127]. The principle is illustrated in figure 3.18. The idea behind this approach (dubbed “HA coating” by Hamamatsu, but also available from other manufacturers) is to prevent stray electrons escaped from the electron multiplier system from being attracted to and hitting the inner surface of the glass envelope thus preventing the emission of scintillation light.

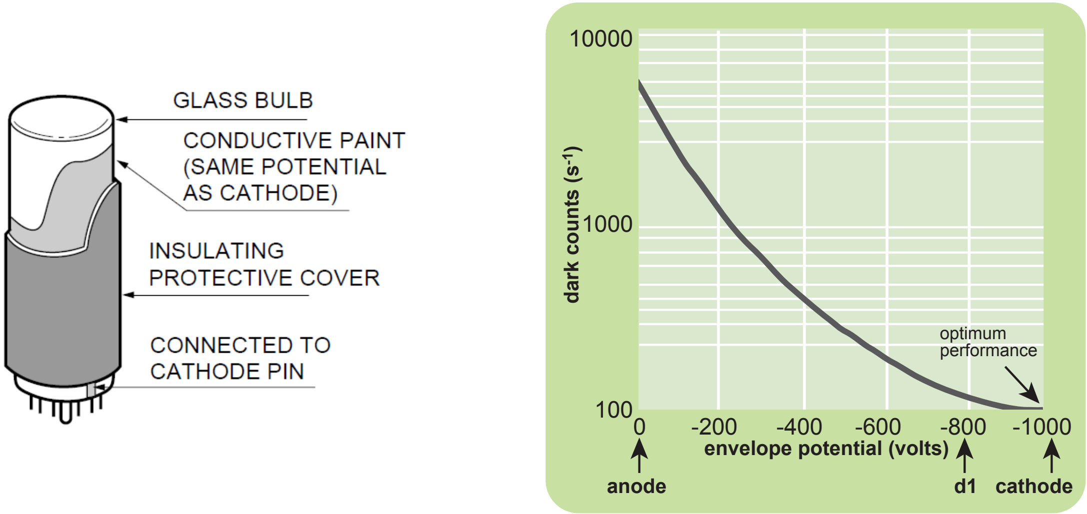

Figure 3.18: Dark rate reduction measures: **Left**: Sketch of "HA coating" as suggested by Hamamatsu to improve dark rate stability for negatively-fed PMTs. Taken from [127]. **Left**: Impact of the electric potential of a conductive PMT housing on the dark rate. Figure taken from [126].

Part II

The mDOM: A multi-PMT optical module for IceCube-Gen2

4 Concept introduction

As introduced in chapter 2, the optical modules of all currently operative neutrino telescopes[1] feature a single large PMT inside a spherical pressure vessel. Depending on the respective implementation, the vessel in addition houses read-out or digitization electronics. Based on the initial idea by S. O. Flyckt, an alternative, multi-PMT, concept[2] was first adopted and realized in the framework of the KM3NeT project (see section 2.2.2). In an optical module based on this layout the pressure vessel houses an array of several small-size PMTs, as well as auxiliary devices. The resulting segmentation of the sensitive area features several attractive advantages compared to the conventional single-PMT concept:

- **Increase of photocathode area**: The photocathode area of ten 3-inch PMTs roughly corresponds to that of one 10-inch tube. Thus a multi-PMT module containing several tens of 3-inch PMTs is equivalent to several conventional IceCube optical modules.
- **Superior photon counting**: The total number of deposited photoelectrons can be more directly derived from the number of hit PMTs compared to the extraction from a multi-photoelectron signal waveform.
- **Improved angular acceptance**: With the distribution of the photocathode area across the total solid angle, a near homogeneous 4π coverage can be achieved.
- **Extension of dynamic range**: Cathode segmentation also benefits the overall dynamic range of the module, as multiple photons arriving at the same time are more likely to hit different PMTs. Assuming comparable dynamic ranges of small and large PMTs, the collective range is extended by a factor given by the number of small PMTs facing one direction (roughly 10 in the case of the mDOM).
- **Intrinsic directional sensitivity**: The orientation of the hit PMT, in combination with its well-known angular acceptance, carries information on the direction of the incoming photon that can be used in event reconstruction.
- **Local coincidences**: Uncorrelated single-hit noise, such as dark rate (see section 3.8), can be suppressed using coincidences between individual PMT of one module.

The hardware functionality and physics capability of the multi-PMT concept have in the meantime been demonstrated in-situ with the deployment and operation of KM3NeT prototypes in the Mediterranean [105]. Due to the development of suitable three-inch PMTs by several manufacturers, originally done for the KM3NeT project, these devices are meanwhile available at moderate prices resulting in the “price per photocathode area” for a multi-PMT module being comparable to, or lower than, the value in the case of the conventional layout. As a consequence, the above-mentioned advantages come at no additional cost.

---

[1] Excluding KM3NeT, being under construction.

[2] This notion refers to the idea of placing a large number of small-diameter (three-inch) PMTs inside a single spherical pressure vessel [131]. It is predated by the so-called “quasi-spherical module”, a bundle of eight individually-housed PMTs – technically as well a multi-PMT design – which was proposed for DUMAND [69], and later realized in the NEVOD neutrino detector [132].

These advantages make the multi-PMT approach a promising concept for the currently planned IceCube-Gen2 neutrino observatory (see section 2.4). While the high-energy array can above all benefit from the increased effective area per module, the additional information on the direction of incident photons will be applicable in the densely instrumented volume of the low-energy PINGU detector[1].

4.1 General design considerations

The initial impetus for the work reported in this thesis was the idea to transfer these attractive features to a future Antarctic detector. The natural starting point for this endeavor was the multi-PMT module, under active development in the KM3NeT collaboration since 2008.

In its current, supposedly final[2], configuration the **KM3NeT module** features 31 three-inch PMTs housed inside a 17-inch borosilicate glass sphere for pressure protection (see figure 4.1 for details). This pressure vessel, a standard commercial product available from several manufacturers, such as Nautilus Marine Services or Teledyne Benthos, is rated to tolerate hydrostatic pressures up to 670 bar, making it perfectly suited for the utilization in the project at a maximum depth of 3500 meters[3]. As mentioned earlier, corresponding three-inch PMTs are available from several manufacturers. Optical coupling of the PMTs to the inner surface of the glass is achieved by means of a vulcanizing two-component silicon-based gel. To enhance their effective area, the PMTs are equipped with a conical highly reflective device. Both PMTs and reflectors are mounted on a plastic holding structure. A dedicated low-power active base has been developed in Nikhef including a Cockcroft-Walton high-voltage supply[4] and active read-out electronics. On-base readout consists of a signal pre-amplifier and a tunable single-stage discriminator, usually operated at a threshold of ~ 0.3 photoelectrons. Signals from individual PMTs are transmitted to the so-called Central Logic Board, featuring an FPGA[5] comprising individual TDCs[6] for each PMT channel, to be time-stamped and sent ashore via optical fiber cables. A custom version of the White Rabbit ethernet protocol has been designed for this purpose [133]. The modules are held in position by titanium harnesses attached to two vertical Dyneema ropes. Glass fibers and power supply are bundled in an oil-filled cable, meandering along the string between the ropes. This so-called Vertical Electro-Optical Cable contains one optical fiber per module on a string, together with copper wires for power transmission ($U_{\mathrm{DC}} = 400\,\mathrm{V}$). A converter mounted on the module is used to provide the 12 V needed for DOM electronics. In addition, the module houses a fast LED pulser, a compass, a tilt-meter, and a piezo acoustic sensor for calibration purposes. The overall power consumption of a module amounts to 7 W [104].

Development of a **multi-PMT module for IceCube** extensions began in 2012, initially

---

[1] Due to strong scattering in ice, photons tend to lose directional information with increasing path lengths, so that sparse arrays might not be able to take full advantage of the module's directionality.

[2] Discussed here is the early-2017 design.

[3] At the ARCA site off the coast of Sicily.

[4] For general details of this layout see section 3.4. The actual devices used in KM3NeT and the mDOM are presented in chapter 7.

[5] Field-Programmable Gate Array

[6] Time-to-Digital Converter

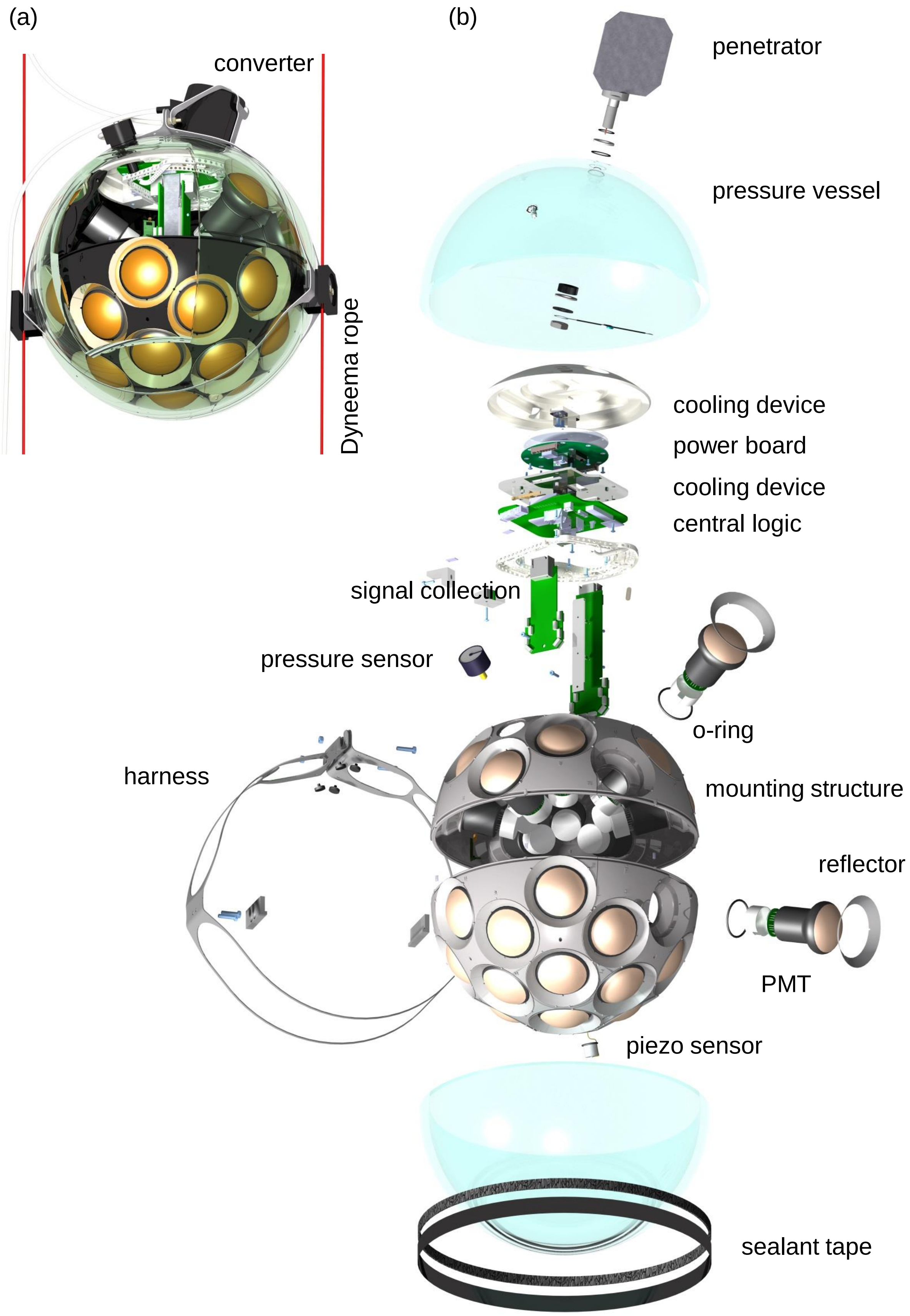

Figure 4.1: KM3NeT multi-PMT optical module: Artist's impression (a) and exploded view (b) featuring main components. Figures courtesy of the KM3NeT collaboration. Taken from `https://www.km3net.org/news-media/album-optical-module/`, modified.

as a “spin-off” of the KM3NeT project. At that point, the KM3NeT design was not yet finalized and both projects evolved in parallel. Some of the work reported in this thesis therefore had a “multi-use” character, in particular the characterization of PMT prototypes (see chapters 5 and 6) and passive optical components (see chapter 9).

Unfortunately introducing the multi-PMT concept to IceCube-Gen2 is not as easy as placing the available KM3NeT module into the glacier. The deep-ice environment at the South Pole imposes a number of specific conditions the module has to meet:

- The boreholes, needed to install the instrument strings of IceCube, were produced using a custom-developed hot-water drill. The intention to keep the well-proven drilling technique of the original detector, **limits the diameter** of any future module to **$\sim$ 13 − 14 inch** . Larger diameters are also a cost issue, as, given the depth of the boreholes of $\sim 2500\,\mathrm{m}$, roughly $70\,\mathrm{m}^3$ of ice have to be melted for each additional inch[1].
- Due to the temperature gradient of the glacier (the deeper, the “warmer”, see figure 4.2) the water column refreezes first at the top. Subsequent freezing of the remaining volume results in a pronounced pressure excess. While the hydrostatic pressure is below 300 bar, peak pressures measured during IceCube deployment, were found to be as high as $\sim 10,000\,\mathrm{psi}$, corresponding to $\sim 690\,\mathrm{bar}$. As a consequence the module is required to withstand **pressures up to 700 bar** [2] [108].
- **Temperature rating** of all module components, active and passive, has to ensure stable and reliable operation at **~ -30°C**, as well as allow storage at ambient temperatures as low as **~ -70°C** [78].
- Unlike water, ice is transparent to **ultra-violet light**, which is also more abundant in the spectrum of Cherenkov radiation, as discussed in section 2.1.2. Harvesting these extra photons was considered beneficial.

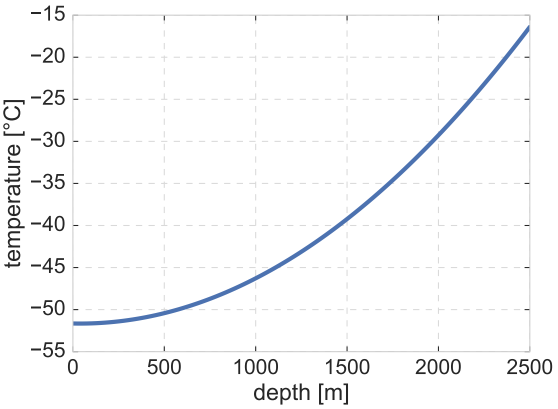

Figure 4.2: Temperature profile of Antarctic ice at the IceCube location. Function taken from [78].

Last, but definitively not least, the envisaged new module had to be compatible with the infrastructure available at pole and fit into the planned IceCube-Gen2 data acquisition framework. This framework is an update of the original IceCube layout, intended to

---

[1] Compared to the borehole volume of $215\,\mathrm{m}^3$ this is an increase of $\sim 30\%$.

[2] This value corresponds to the pressure rating of the original IceCube vessels. As no module failure occurred during refreezing it was decided to stick with this specification.

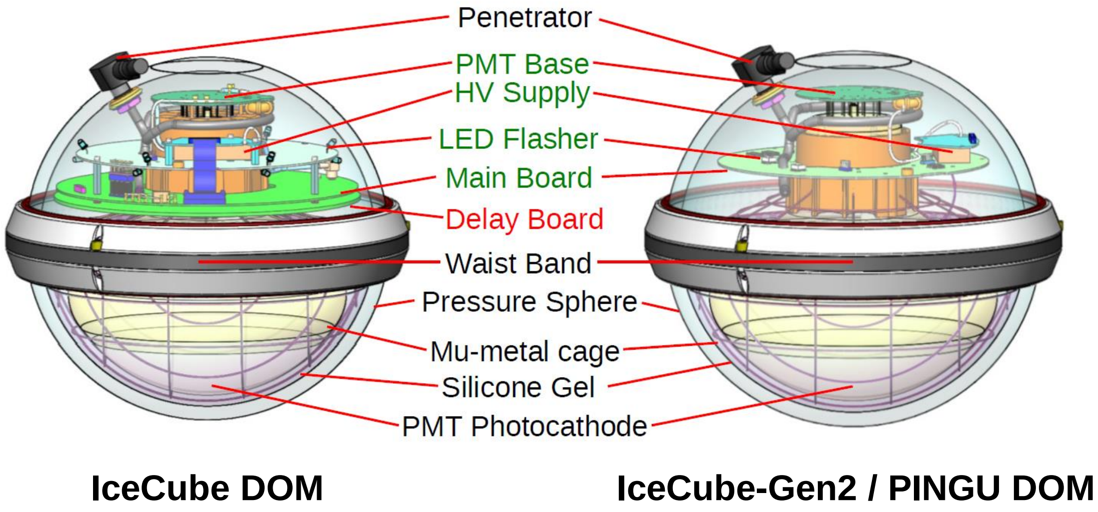

Figure 4.3: Optical module of IceCube and DeepCore (**left**) in comparison to the baseline single-PMT IceCube-Gen2 DOM (**right**). *Black* labels identify identical components while *green* elements are being redesigned. *Red* denotes discarded parts. Taken from [134], modified.

house baseline Gen2-DOMs, which are in turn updated versions of the initial single-PMT module of IceCube (see also section 2.4).

In the IceCube approach [108], power supply and communication is done via twisted pair copper cables[1]. Several DOMs share one cable pair, with the final Gen2 number still needing to be defined. In the case of the densely instrumented low-energy part of IceCube-Gen2 (PINGU) four to up to eight modules per pair are under discussion. Each wire pair also provides DC power, which is transformed to the necessary values by a low-power (125 mW) DC-DC converter inside the DOM. A comparison between the original IceCube module layout and the considered single-PMT IceCube-Gen2 module, highlighting the changes, is shown in figure 4.3. The main idea behind those changes was to keep reliable components and most of the functionality, but replace outdated or obsolete electronics. A block diagram of the corresponding Gen2 DAQ layout is presented in figure 4.4. The pre-amplified and shaped (broadened in time) signal will be processed by a single, commercially available, 250 MHz 14-bit differential ADC[2]. This device is controlled and read-out by an FPGA mounted on a system-on-chip[3], which is the centerpiece of the in-DOM DAQ system. Triggered pulses are unfolded by a deconvolution algorithm by a virtual processor implemented in the FPGA: Fitting single photoelctron templates to the waveforms, this algorithm will extract arrival time and (charge) amplitude. In this approach only two values are needed to characterize an individual signal, resulting in a substantial gain in memory and reduction of bandwidth demand approximately by a factor of ten. All triggered waveforms are continuously sent to the so-called string hub

---

[1] This design choice dates back to the days of AMANDA (see section 2.2.3) when problems occurred in test strings equipped with optical fibers.

[2] Texas Instruments ADS4149

[3] A SoCKit by Terasic Inc., featuring an Altera Cyclone V SX-series FPGA.

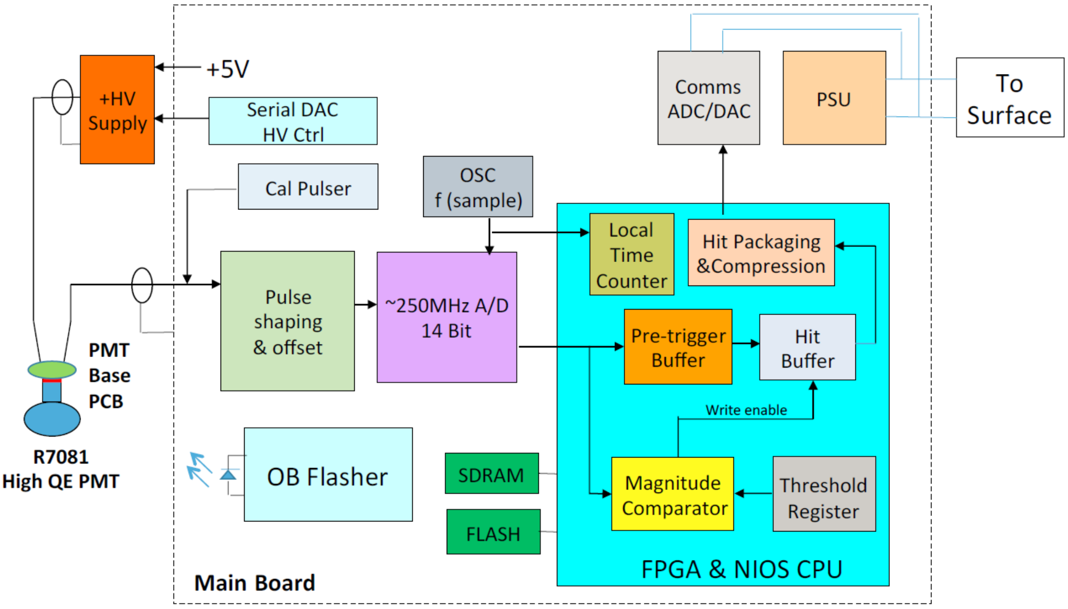

Figure 4.4: Functional block diagram of data acquisition electronics in the planned IceCube-Gen2 module. Figure taken from [24].

at the surface[1]. Multi-photon signals too complicated to be fitted by a the template are planned to be fully digitized and stored for offline processing alongside the unfolded data[2]. As firmware and software of this system are currently under development they may still be subject to changes.

The modules will also feature LED flashers with adjustable output for calibration and potentially also house cameras for the monitoring of optical properties of the ice [24, 119].

These design choices result in additional essential demands which need to be met by the mDOM:

- The use of a supply voltage of 96 V[3], in combination with the voltage drop along the copper wires and the minimum voltage of 42 V required by the DC-DC converter, limits the power budget available per wire pair to 9.4 W. Depending on the final number of optical modules per, envisaged to be between two and four in case of the mDOM, this constraint results in 4.7 W to 2.4 W available per module [24].
- Use of copper wire pairs for data transfer and communication limits the available bandwidth to ∼ 1Mbit/s per pair.
- DAQ hardware and data formats must comply with the standards lined out above. In particular it makes sense to implement readout using the same core components of the main board, including the FPGA.

---

[1] Unlike the case in the original IceCube DAQ, no local coincidences are implemented, to reduce the amount of data. This limit was lifted due to advances in computer technology.

[2] Though meaning larger bandwidth demand, the approach is not anticipated to exceed the limits as corresponding events are expected to occur rarely.

[3] Chosen not for physics but for safety reasons.

The hardware and electronics for the mDOM developed along these guidelines are presented in the following sections.

4.2 Mechanical design

From a mechanical layout point of view, most important among the above-mentioned constraints is the limited diameter in combination with (almost) fixed PMT dimensions (see chapter 5). Impossibility to use the 17-inch sphere of KM3NeT and the fact that a standard IceCube 13-inch vessel does not provide the space sufficient to house a number of PMTs (together with associated electronics) large enough to provide satisfactory homogeneous covering of the solid angle, as well as a substantial increase of the overall sensitive area, resulted in the conception of a cylindrical pressure housing. Based on finite-element simulations[1] as well as consulting and negotiations with a potential manufacturer (Nautilus GmbH) a bipartite pressure vessel was designed. Each part of this vessel consisted of a 13-inch cylinder terminated on one end by a hemisphere. A corresponding structure to support the PMTs, together with reflectors and auxiliary equipment, such as calibration devices, inside the module was also designed to be produced from polyamide using laser sintering. More details on this development are presented in section 8.2. In this initial cylindrical configuration the mDOM provided space for 42 three-inch PMTs, roughly quadrupling the sensitive area of the module with respect to the single-PMT baseline design[2] [135]. Unfortunately, the initial approach also came with some drawbacks:

- First production tests by Nautilus revealed problems concerning the precision of the vessel diameter originated in the molding process[3]. Thus, while two arbitrary hemispheres can be connected to form a vessel, this could not be achieved for the cylinders.
- To still enable coupling between two semi-vessels, the manufacturer introduced stainless steel flanges glued to the outer rim of the cylinders. Although providing heat conduction, and thus being a natural location to mount central electronics, these metal parts also drastically increased the mass of the module to $\gtrsim 60\,\mathrm{kg}$, not including the internal components.
- Due to the utilization of (individually fitted) flanges, and in opposition to initial cost estimates, the mass production price did not drop below a value of several thousand Euros per vessel.

Based on negative feedback from the collaboration concerning the handling during deployment, and the unresolved cost issues, it was decided to redesign the module.

A new degree of freedom was given by the loosening of the diameter constraint: While initially a value of $\sim 13\,\mathrm{in}$ was considered a fixed upper limit, it was pointed out by col-

---

[1] Find a more detailed account of these efforts in section 8.1.

[2] In case of the need to further increase the sensitivity per module, it was planned to add cylindrical segments in the center, housing additional 15 to 20 PMTs each. These open cylindrical segments would be produced e.g. from semi-cylindrical ones by removing the hemisphere.

[3] Unlike spheres which maintain their shape once detached from the casting mold, cylinders slide along the mold when taken out. This contact with the mold of the still viscous glass results in (uncontrolled) deformation.

laborators, that a small-scale increase was achievable given the available drilling devices. The new solution, found in the trade-off between increasing the number of PMTs and decreasing the diameter and consulting the manufacturer, is closer to a sphere: While increasing the outer diameter of the vessel to 356 mm ($\simeq$ 14 in), the cylindrical central section was replaced by a cone (wall inclination angle of 2.8°, see figure 8.7) to facilitate production and reduced to a height of 27.5 mm to maintain pressure stability[1]. Given the dimensions of currently available three-inch tubes, each hemisphere is able to house twelve PMTs. Not suffering from the precision limitations of the initial design, vessels featuring the current layout are now available at prices comparable to those of standard spheres.

In this configuration, which is now the baseline design and will be used for a first module prototype, presented in figure 4.5, the mDOM features a total of 24 PMTs housed inside the newly designed pressure vessel. While the R12199-02 (HA) PMT by Hamamatsu is the default tube for prototyping, the use of alternative three-inch models, available from several manufacturers, is also considered, and might be beneficial to enhance module performance[2].

As in all optical modules currently in use, coupling of the PMTs to the inner surface of the glass will be achieved by means of a silicon-based gel. As of now, the KM3NeT choice, Wacker 612 A/B, is considered the baseline, but dedicated test series are needed comparing it to other products, in particular concerning low temperature behavior[3].

As in KM3NeT, the effective area of the PMTs will be enhanced using conical reflectors produced from coated aluminum sheets[4]. Details concerning the optical properties of these devices are presented in section 9.2, while section 10.4.1 deals with a simulation study of the optimum opening angle. Being conductive objects at floating electrical potential the reflectors can also have an impact on the dark rate behavior of the PMTs (see section 3.8 for potential mechanisms). A corresponding investigation can be found in section 6.6.3.

The polyamide holding structure, supporting PMTs and reflectors, has been redesigned to fit the new vessel layout, as well as to improve electrical insulation of the PMTs. Details on the design process and main considerations are depicted in section 8.2. It is planned to locate main readout electronics in the conical part, i.e. the center of the module. Power supply and communication will be connected via a penetrator, adopted from the current IceCube model, located in the upper hemispherical section. Front-end readout includes a low-power active PMT base, adapted from the KM3NeT design. An conceptional overview of the mDOM readout is given in the following section while details on base development and performance are located in chapter 7. A stainless steel harness to mount the module on the instrumentation string is under development. It will be based on the more delicate KM3NeT layout (see figure 4.1) in order to minimize shadowing of PMTs.

Keeping in mind the optical properties of the ice, it makes sense to provide UV sensitivity of the module (as e.g. done by colleagues developing the WOM, see section 2.4). The obvious approach of using quartz glass for the pressure vessel as well as the PMT envelope

---

[1] See section 8.1.3 for a discussion of the pressure rating.

[2] In particular, the three-inch tube offered by ET Enterprises (9320KFL) features a larger photocathode. Further information on properties of available PMTs can be found in chapter 5.

[3] According to the manufacturer, the Wacker gel will crystallize below $\sim -50°$C [136, 137].

[4] In addition, alternatives, such as adhesive reflective foils are under investigation.

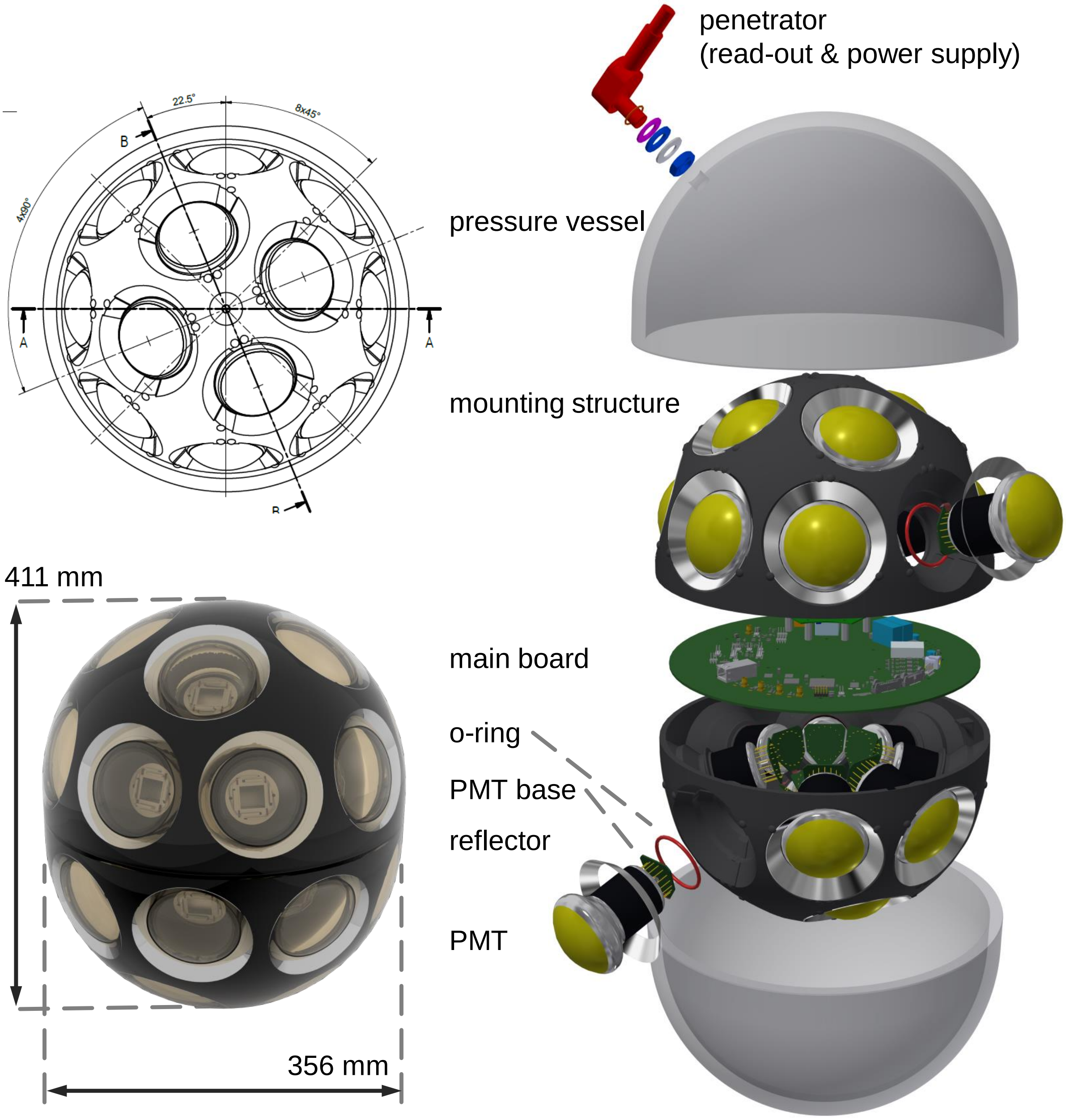

Figure 4.5: Current mDOM layout: Top view technical drawing (**top left**), artistic rendering (**bottom left**), featuring main dimensions, and explosion view of the module, highlighting main components (**right**). Shown is the default configuration based on the Hamamatsu R12199-02 PMT. Figures courtesy of the IceCube Münster group.

was rejected for cost reasons[1]. However there are possibilities to (slightly) enhance the transparency of borosilicate glass in the ultra-violet region. Corresponding investigations are presented in section 9.1.

A comprehensive account of the current status of the project, as well as the next steps towards the production of a first fully functional prototype, is given in the dedicated chapter 11.

4.3 Data acquisition

As introduced in section 4.1, a major difference between the designs of KM3NeT and IceCube-Gen2 is the read-out and signal processing. In the **KM3NeT** approach the current pulse produced by the PMT is converted to a single time-stamped time-over-threshold signal (ToT). The obvious advantage of this approach is the high rate of data compression: Instead of a potentially large number of data points, only the arrival time and the duration of the event need to be transferred to shore. It also eliminates the need for a complicated digitizer and allows to keep power budget low. The utilized preamplifier also reshapes the signal, stretching it, allowing for slower components.

These advantages come at the cost of the loss of information on the signal shape and amplitude. Having ToT information only, makes it, in particular for larger signal amplitudes, hard to reconstruct the number of incident photons. This is countered by carefully calibrating the base output (ToT vs. number of photo-electrons), but due to the used signal shaper the relation is a logarithm, sloping off for signals exceeding ~ 60 photo-electrons [138]. Also, several single photons arriving with timing offsets on the order of some nanoseconds will produce one long ToT, emulating a signal amplitude much larger than the cumulative number of photons, potentially complicating event reconstruction. However, this “feature” is not considered a problem by the KM3NeT collaboration: Due to the feeble scattering in sea water the first photons of an event will arrive virtually unscattered, bearing precise timing information, which, if available, is far more crucial to the precision of event reconstruction than the exact amplitude distribution[2].

Not having this luxury in ice (see section 2.1.2 for a comparison of ice and water properties), the existing **IceCube** detector has been additionally relying on signal shape for event reconstruction [108]. Data rate is equally reduced using a deconvolution approach, which, similar to the ToT procedure, defines a pulse by only two values (arrival time and reconstructed amplitude), but needs in-DOM computing power for deconvolution.

In the case of the **mDOM** it was decided to extract more information from a pulse than the mere time-over-threshold, but yet to refrain from resource-intensive full deconvolution. Base-borne front-end readout electronics are based on an enhanced KM3NeT layout: The high voltage is generated in-situ by a Cockcroft-Walton cascade adopted from the original design (see chapter 7 for details). For the digitization of the analog pulse produced by the PMT, two solutions, varying in achievable precision and level of integration, are currently

---

[1] The main cost-drivers here are the higher molding temperatures, requiring more robust equipment.

[2] So large is the importance of the first photons arrival time, that in fact as of now, KM3NeT modules are read out in a “digital” mode, taking the number of hit PMTs for signal amplitude and neglecting their respective ToT values.

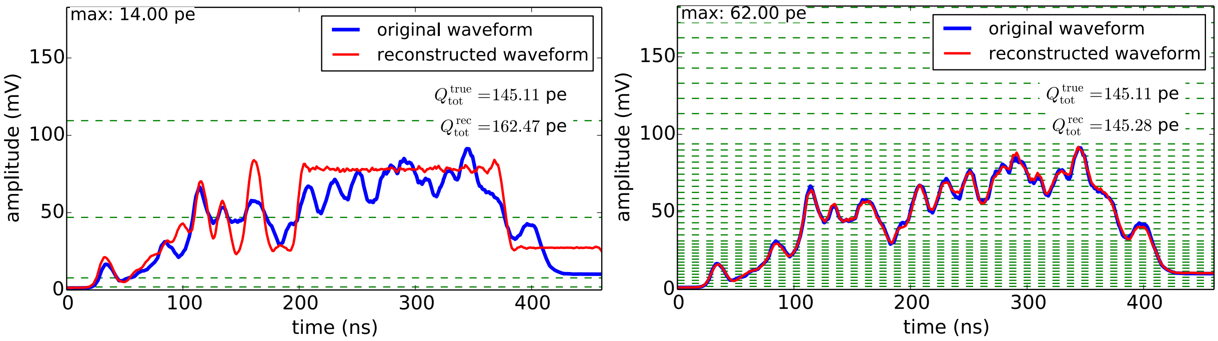

Figure 4.6: Impact of the choice of threshold levels on the precision of event waveform reconstruction, comparing a four-comparator setup corresponding to the baseline mDOM design (**left**) to the more ambitious read-out scheme using a 63-level ASIC (**right**). Final threshold levels are subject to change after optimization. Plots courtesy of the IceCube Münster group.

under development:

- In the **baseline concept**, the waveform is split after pre-amplification and passed to **four** base-borne **discriminators** with independently adjustable thresholds. The (analog) time-over-threshold signals from each discriminator and PMT are routed via single-ended circuit board tracks.[1] to a single FPGA on the main board, clocked at 150 MHz, where the leading and trailing edge times for each channel are determined. Parallel processing allows an effective sampling of each channel at a rate of 600 MHz. As two channels are employed in digitizing data from the lowest threshold, the resulting effective sampling is 1.2 GHz at this level. The information finally available on each pulse amounts to four time-stamped ToT values. To speed up and simplify development, the circuitry will be constructed form **discrete parts**, rather than embedded in an ASIC[2]. This design will be used in the first prototypes, and serve as a fall-back solution. The baseline layout is currently developed at DESY.

- In a more ambitious approach, under development by colleagues from the Institute for Electronics Engineering at the University of Erlangen, the analog pulse is fed into a custom on-base **ASIC**, which comprises **63 comparators**[3], featuring level precision of 200 µV and a maximum amplitude of ~ 2 V. The ASIC also contains a $2^N - 1$ to N encoder which reduces the data to a 6-bit output word. As in the baseline design the output is time stamped in a central FPGA. In the ASIC scheme, the larger number of thresholds allows for a detailed sampling even of complex waveforms. The higher level of integration also reduces power consumption. Total power budget of the mDOM is targeted to be below 3 W.

A simulation set up in the IceCube Münster group (see figure 4.6) clearly indicates that the employment of the 63-level scheme allows reliable reconstruction even of complicated waveforms. A more detailed study is currently the subject of a Master's thesis in Münster.

---

[1] Used to reduce power consumption.

[2] Application-Specific Integrated Circuit

[3] The individual comparator levels can be freely adjusted prior to chip production, allowing to optimize the spacing as illustrated in figure 4.6.

Contribution of the author to mDOM base development was of a consulting kind, e.g. to formulating the design goals. It was also my responsibility to test the base prototype and evaluate its performance. Results of this evaluation are presented in chapter 7.

5 PMT characteristics

The multi-PMT module project, initiated by members of the KM3NeT collaboration, relies heavily on the availability of small, fast, cost effective, and mass producible tubes. At the moment of the initial proposition of the novel approach, corresponding PMTs were available from **Photonis Technologies S.A.S.**[1]. Original quality requirements for three-inch PMTs, formulated in the conceptual and technical design reports of KM3NeT [102, 103], very much reflect the properties of model **XP53B20** tubes available at the time of writing of the reports. After Photonis ceased PMT production, several manufacturers, namely **Hamamatsu Photonics K.K.**, **ET Enterprises Ltd.**[2], **MELZ FEU Ltd.**, and later **HZC Photonics Ltd.**, initiated the development of corresponding three-inch tubes, based in part on medical application models from their respective assortments.

Being the active elements of an optical module for the detection of the Cherenkov radiation, the characteristics of the PMT determine (and limit) the principal performance of a neutrino telescope: Uncertainties in the measurement of the timing of detected photons affect the track reconstruction, while uncertainties on the charge reconstruction affect mainly the evaluation of the energy of the charged particle that originated the Cherenkov radiation. Any PMT noise pulse that is not related to incoming Cherenkov radiation also affects the efficiency in track reconstruction.

5.1 Characterization campaign for KM3NeT

In a joint effort newly available three-inch PMT prototypes were characterized and tested for compliance with the KM3NeT requirements by groups in Amsterdam (Nikhef), Erlangen (ECAP) and Catania (INFN). The measured properties were the foundation for communication with the manufactures concerning the iterative refinement of existing tubes as well as for the development of new types, and also for the formulation of tighter constraints on tube quality.

The main **quality benchmarks**[3] are listed in the table 5.1. Quantum efficiency is specified for two wavelengths, corresponding approximately to the position of bialkali peak efficiency[4] and the maximum of the Cherenkov-weighted water transparency spectrum (470 nm).

In the scope of a service task to the collaboration the author contributed to the characterization efforts taking place in Erlangen. Several prototypes have been subjected to extensive scrutinizing using a set of standardized tests. Test setups and procedures will be introduced in the scope of the current chapter. The intermediate and final results

---

[1] Which was convenient, as S. O. Flyckt who had the initial idea, was a Photonis engineer.

[2] Referred to as “ET Enterprises” or “ETEL” in the text.

[3] Based on simulations of the respective impact of the PMT property on detector performance (such as precision of energy and angular reconstruction).

[4] Values for 390 nm and 404 nm are encountered in corresponding KM3NeT publications, e.g. [139]. While the lower value roughly corresponds to the location of maximum quantum efficiency, the latter was chosen to coincide with the wavelength of the blue radiant sensitivity index, which is a standard parameter employed in PMT characterization by the manufactures [123]. As discussed in section 3.1, it can be translated to a quantum efficiency, allowing for a cross-check of manufacturer specifications.

presented are based on measurements by the author, but also by J. Reubelt, O. Kalekin and several (student) assistants.

The experimental approaches used to assess particular PMT properties are presented in subsequent sections, followed by a summary of the results for each of the prototypes under investigation while the author participated in the testing campaign. With new models being developed by the companies, PMT testing and characterization has continued since.

quantum efficiency[a] (390-404 nm)	$\sim 27\,\%$	**supply voltage**[b]	$900 - 1400\,\mathrm{V}$
quantum efficiency (470 nm)	$\sim 20\,\%$	**dark rate** (at 20°C)	$0.2 - 1.5\,\mathrm{kHz}$
transit time spread[c] (FWHM)	$< 5\,\mathrm{ns}$	**peak to valley ratio**	2.5
pre-pulsing	$< 1\%$	**delayed pulsing**	$< 3.5\%$
early afterpulsing	$< 2\%$	**late afterpulsing**	$< 10\%$
effective diameter	$\gtrsim 76\,\mathrm{mm}$	**inhomogeneity**	$\sim 10\%$

---

[a] The lower value marks the location of maximum quantum efficiency. The latter corresponds to the peak transmission wavelength of the filter used to measure the blue radiant sensitivity index, a standard parameter in PMT characterization by the manufactures [123]. As discussed in section 3.1, it can be translated to a quantum efficiency value.

[b] Upper voltage limit defined by the performance of the Cockcroft-Walton circuitry of the active PMT base [140].

[c] The TTS criterion was specified in order not to corrupt the overall timing precision of muon reconstruction [103].

Table 5.1: Typical performance of three-inch PMTs used for KM3NeT multi-PMT optical modules (compiled from the evolution of quality requirements in [103, 104, 107, 139].). Dark rate is specified for a threshold of ~ 0.3 photoelectrons at room temperature. Pulsing properties are given as occurence probabilities. Inhomogeneity benchmark refers to the photocathode response.

5.1.1 Gain

The gain of the PMT prototypes was assessed in pulse mode (see section 3.2 for the relation between operation mode and gain definition). Positioned in a light-tight environment, the entrance window of the PMT was illuminated homogeneously at a single photoelectron level[5] (achieved setting the average light yield to ~ 0.1 photoelectrons per pulse) using a sub-nanosecond pulsed LED[6] in combination with a PicoQuant PDL 800-B picosecond pulsed LED driver [142]. The LED's output was transferred into the interior of the box by means of a glass fiber, terminated by a diffusor which was positioned at a distance of one meter relative to the PMT, in order to provide homogeneous illumination of the cathode. A schematic block diagram of the experimental setup is presented in figure 5.1. The light pulses, usually generated at a repetition frequency of 1 kHz, feature a centroid wavelength of $\lambda = 460 \pm 10\,\mathrm{nm}$. Typical pulse widths achievable with the setup (given as values of the FWHM), range from 800 ps to 900 ps, defining the timing precision[7]. Before

---

[5] The principles of the acquisition of charge spectra, as well as related technical terms, such as quantification of illumination levels in "photoelectrons", are explained in detail in section 3.6.

[6] A generator-driven PLS 450 by PicoQuant [141].

[7] Not relevant to the gain measurement, the timing precision is nevertheless important as the same setup was used to measure the transit time spread, presented in section 5.1.2.

further processing, the output signal of the PMT was pre-amplified by a factor of 10, using a dedicated NIM[1] module[2]. The original current pulse was converted into a voltage waveform by an internal load resistor ($R = 50\,\Omega$) and recorded by means of a digital oscilloscope[3] externally triggered by a reference signal from the LED driver. Sampling rate varied between one and 2.5 Gigasamples per second. The achieved timing precision made it possible to use the same waveforms for time resolution analyses (see section 5.1.2). A single-photoelectron charge spectrum was obtained from the stored waveforms and fitted using a convolution of several Gaussians to derive the gain from the relative positions of pedestal and single photoelectron peak using equation 3.16 (for details of the procedure, see section 3.6 and the references therein).

Gain values were typically determined for PMT voltages ranging from 1000 V to 1400 V. Usually inside an interval of ±100 V around the nominal voltage provided by the manufacturer corresponding to a gain of $3 \cdot 10^6$ [4]. Determination of the so-called gain slope[5] was used to derive the exact voltage, at a precision of 1 V, corresponding to the nominal gain in pulsed mode. This voltage was then used for the assessment of further PMT parameters. As in the final use case in the KM3NeT module, voltage polarity was negative.

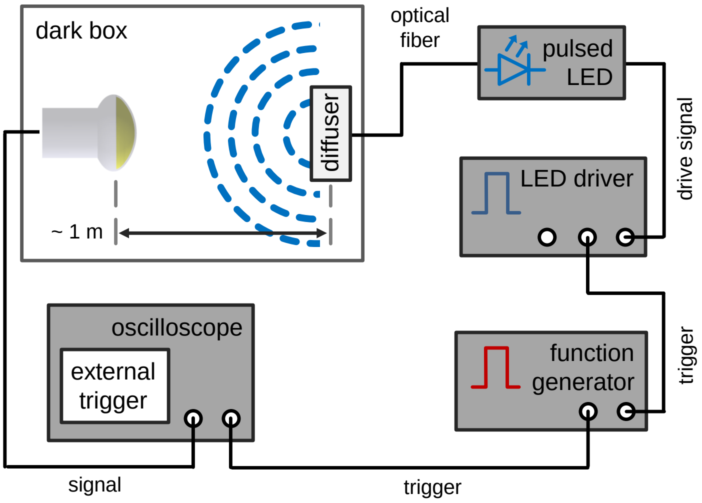

Figure 5.1: Principle of externally triggered waveform capture in pulse mode. The setup was used to measure gain, transit time spread as well as afterpulsing probability. PMT high voltage supply and output pre-amplifier omitted.

5.1.2 Transit time spread

A measure of the timing precision achievable by a PMT is given by the transit time spread (TTS) of the signal, see section 3.5 for further information on this PMT characteristic. The measurement of the TTS relied on the same raw data (oscilloscope-acquired voltage signal waveforms, produced illuminating the PMT with a precise pulsed light source) as the measurement of single photoelectron gain[6] The single photoelectron charge distribu-

---

[1] Nuclear Instrumentation Module

[2] Model 612A amplifier by LeCroy.

[3] LeCroy waveRunner 6100

[4] Initially the value was $5 \cdot 10^6$. It was changed in the course of active base development.

[5] The linear slope of the gain as a function of supply voltage, if plotted on a logarithmic scale.

[6] Find the experimental setup and data taking technique described in section 5.1.1.

tion, derived from recorded signal waveforms, was used to define a voltage amplitude threshold corresponding to a ~ 0.3 photoelectron input level[1]. Applying the threshold to the waveforms resulted in a distribution of signal arrival times featuring a characteristic main peak. The TTS was quantified in terms of the FWHM of this feature. An alternative measure of the timing was achieved fitting the peak with a Gaussian function and retrieving the standard deviation σ. Both figures of merit are connected via

$$TTS = 2\sqrt{2 \cdot \ln 2} \cdot \sigma \tag{5.1}$$

The non-zero duration of the light source pulse ($t_{\text{pulse}} = 800\,\text{ps}$) was taken into account using

$$TTS_{\text{PMT}} = \sqrt{TTS^2 - t_{\text{pulse}}^2} \tag{5.2}$$

to derive the actual timing property TTS_{PMT} of the PMT. Given typical values, the relative impact of the correction was however limited to $\lesssim 2\%$.

The TTS criterion for PMTs was specified in order not to corrupt the overall timing precision of muon reconstruction. Intrinsic uncertainties originate in the maximum achievable precision of module positioning (approximately 20 cm to 40 cm , corresponding to 1 to 2 nanoseconds in timing uncertainty) as well as in dispersion of the Cherenkov light in water. For a traveling distance of $\sim$ 50 meters, considered a typical value in KM3NeT, timing uncertainty amounts to $\sim 2\,\text{ns}$. As a result, the time resolution of PMTs is demanded to be below two nanoseconds, if given in terms of the standard deviation. Assuming a Gaussian distribution of the arrival times, this translates to a FWHM of $\approx 4.6\,\text{ns}$ [103].

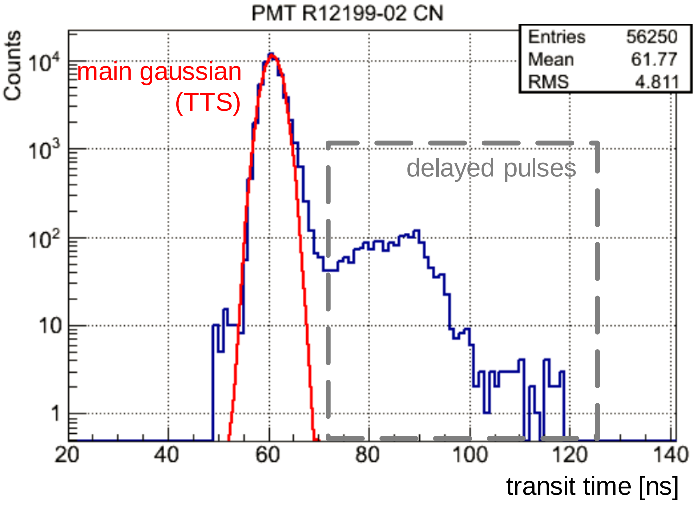

Figure 5.2: Typical transit time spectrum of a Hamamatsu R12199-02 PMT, featuring main parameters for the derivation of the transit-time spread and delayed pulsing probability. The shown absolute values, defined by the pulse position in the data-acquisition window of the oscilloscope, do not represent an actual property of the tested PMT.

5.1.3 Correlated background probability

As introduced in more detail in section 3.7, the "usual" PMT signal can, with some probability, be replaced by so-called early or delayed pulses or be succeeded by afterpulses, each featuring characteristic time intervals. In the case of the tested three-inch prototypes,

---

[1] This approach is explained in more detail in section 3.6

pre-pulses typically arrive ~ 10 ns prior to the expectation, while delayed pulses are off by 10 to 60 nanoseconds. Afterpulses consist of two sub-groups, with early afterpulses featuring delays of 10-100 ns and the late fraction occurring after 100 ns to 10 µs [139].

The probability of **early and delayed pulses** was estimated from the transit-time distribution as the fraction of the respective numbers of events and the total number of recorded pulses.

To assess **after-pulsing**, dedicated long-duration (5µs) single-photoelectron waveforms[1] were recorded. For a corresponding test setup see figure 5.3. In the first step of data analysis the leading pulse is identified and its charge determined. If it is found to exceed 1.7 photoelectrons[2], the waveform is vetoed and excluded. Otherwise the waveform is scanned for further pulses. As the first ~ 100 nanoseconds after the primary pulse are the domain of early afterpulses, the scan for late afterpulses started 100 ns after the initial event. The afterpulsing probability was derived as the the fraction between the total numbers of detected afterpulses and the non-vetoed events.

In the setup used in Catania the fraction of afterpulses was calculated by means of dedicated electronics, acquiring signals succeeding the main pulses in a time range from 10 ns up to 10 µs.

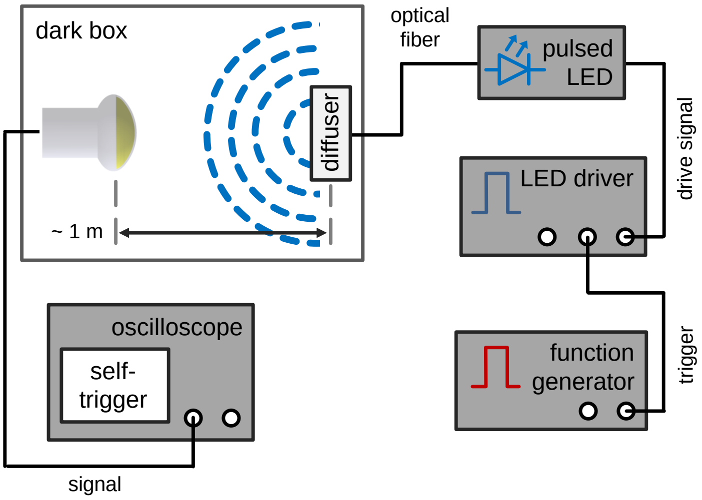

Figure 5.3: Principle of self-triggered pulse mode measurements. In the featured configuration it was used to assess after-pulsing probability. PMT high voltage supply and output pre-amplifier not shown.

5.1.4 Dark rate

All signals produced by a PMT in the absence of incident photons[3] are subsumed under the terms "dark rate/count" (in pulse mode) or "dark current" (in current mode). An extensive introduction to the main sources and the underlying physical processes is given in section 3.8.

---

[1] Either externally triggered using low-level illumination, or self-triggered e.g. on dark rate pulses.

[2] This threshold was chosen in order to ensure a pure single-photoelectron sample of the leading pulses, as for larger values 2 ph.e. pulses begin to dominate.

[3] Referring to "external" photons, i.e. not including those produced in background processes, such as radioactive decays, inside the PMT itself.

The determination of the dark count (and the after-pulsing behavior) was scheduled after the measurements of gain and time resolution. Consequently, the PMTs were typically kept in a light-isolated environment for one to three days before being tested (at minimum for 12 hours). This period of time was considered sufficient for contributions from de-excitation of residual gas ions to settle. The supplied voltages ranged from 1000 V to 1400 V, with the particular value corresponding to a gain of $3 \cdot 10^6$ (earlier $5 \cdot 10^6$) established in the earlier gain measurement. Throughout the characterization campaign negative voltage polarity was used. The tests were carried out at "room temperature", approximately corresponding to 20°C, without dedicated control or logging of environment variables, such as temperature and humidity.

In the initial approach the amplified (by a factor of 10) pulse mode output of the PMT was passed to a discriminator, generating a logical NIM signal whenever the voltage exceeded a threshold of 30 mV (which is the minimum threshold setting available with the device). This fixed value roughly corresponded to ~ 0.3 photoelectrons in case of a gain of $5 \cdot 10^6$ and to 0.5 to 0.8 photoelectrons when PMTs were operated at the later standard gain of $3 \cdot 10^6$. The mean dark pulse rate was retrieved from the number of pulses counted by a TTL[1] counter[2] in a certain time interval, usually of the order of 100 seconds, determined by means of a hand-held stopwatch. For typically expected rates (of the order of 1 kHz [3]) this archaic approach ensures a relative precision of $< 1\%$, deemed sufficient for mass testing.

5.1.5 Quantum efficiency

To measure the quantum efficiency a PMT operated in DC/current mode is placed in a light tight box. A potential difference roughly corresponding to the typical voltage increment between the photocathode and the first dynode[4] in normal operation at the nominal gain (either $5 \cdot 10^6$ or $3 \cdot 10^6$), is established between the cathode and the short-cut dynode system. In this configuration the photocurrent produced at the cathode can be accessed directly. Due to the resulting lack of amplification the read-out is performed by means of a picoampere meter[5] connected to the dynode system. Light provided by a xenon lamp[6] is guided through a remote controllable monochromator[7], allowing to select a narrow wavelength segment (width of $\lesssim 2$ nm) from the original xenon spectrum, to the photocathode of a PMT. A filter wheel is mounted at the output of the monochromator. It allows e.g. the insertion of neutral density filters, adjusting light intensity in order to avoid saturation effects of the cathode material. Saturation was found to occur when

---

[1] Transistor-Transistor Logic

[2] Type 775 by Ortec. The NIM output signal was processed using a NIM-TTL converter prior to counting.

[3] The fact that the unit "Hz" is, strictly speaking, only applicable in case of periodic signals and "s^{-1}" is more appropriate speaking of the dark rate of a PMT is known to the author. However, for the sake of consistency with the jargon established in both the KM3NeT and IceCube collaborations, it will be used in the scope of this work.

[4] −360 V in the case of type R6233-01MOD and R12199-02

[5] Keithley model 487 [143].

[6] A LOT QuantumDesign LSH 102 lamp equipped with a LSB 511 xenon bulb.

[7] MSH 301 by LOT QuantumDesign.

the "current density"[1], drawn from the cathode, surpassed a threshold of $\sim 10\,\mathrm{nA/cm^2}$. The initially mounted color bandpass filters used to suppress stray light in the wavelength interval between 280 nm and 340 nm fell out of use after the source of the leakage was found and fixed. A calibrated photodiode[2], its quantum efficiency tabulated as a function of wavelength, was used as a reference detector. From the respective photocurrents exhibited by the diode I_{diode} and the tested PMT I_{PMT}, when exposed to light (in a wavelength range $\lambda \in [280\,\mathrm{nm}; 700\,\mathrm{nm}]$) the quantum efficiency spectrum of the PMT $QE_{\mathrm{PMT}}(\lambda)$ can be derived from the known efficiency of the photodiode $QE_{\mathrm{diode}}(\lambda)$ using

$$QE_{\mathrm{PMT}}(\lambda) = \frac{I_{\mathrm{PMT}}(\lambda)}{I_{\mathrm{diode}}(\lambda)} \cdot QE_{\mathrm{diode}}(\lambda) \tag{5.3}$$

after both current values have been corrected for dark current contributions[3]. The relation relies on the photon flux encountered by both devices to be identical[4]. This condition is satisfied on the one hand by the long baseline of the monochromator, resulting in a low-divergence parallel light beam, which also loosens constraints on precise positioning of diode and PMT. On the other hand, the impact of the slow drift of the xenon lamp, affecting the output intensity as well as its spectral shape, is reduced by performing the reference measurement close in time to the PMT measurement. A schematic overview of the experimental setup is given in figure 5.4.

According to earlier analyses, this technique leads to typical measurement uncertainties in the PMT's quantum efficiency of the order of one percentage point, corresponding to a relative error of $\sim 5\%$. For detailed information concerning the test bench setup and a discussion of the achievable precision, see [145, 146, 147, 148].

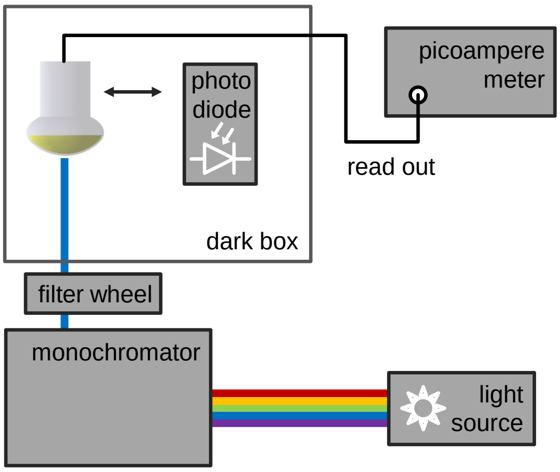

Figure 5.4: Schematic of quantum efficiency characterization setup. For reference measurements PMT and photodiode are switched. Monochromator, filter wheel and picoampere meter are remotely controlled by a PC (not shown).

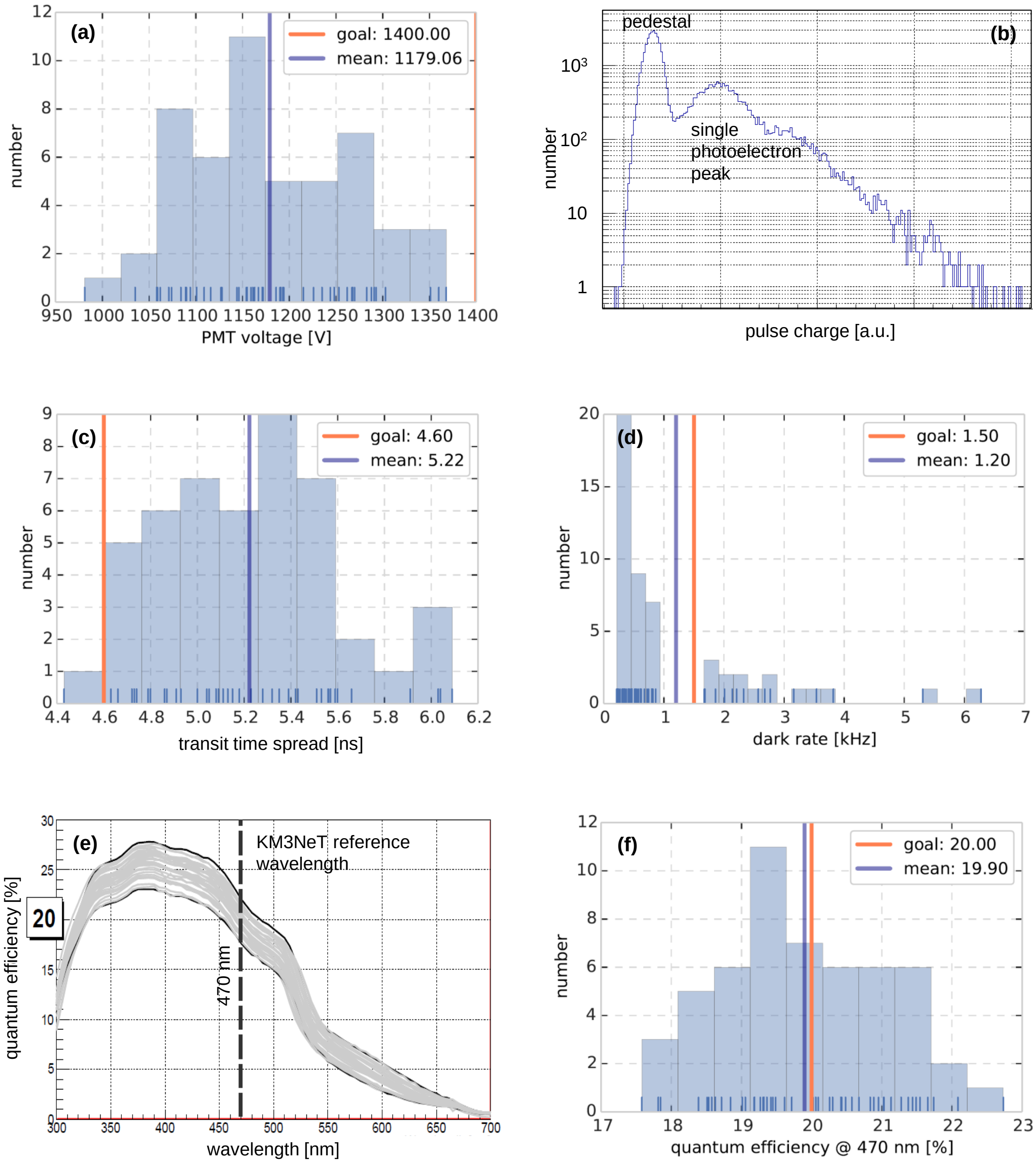

Figure 5.5: Overview of test results for the Hamamatsu R6233-01MOD three-inch prototype. Presented are distributions of nominal[a] PMT voltage (a), transit-time spread[b] (c) and dark rate (d), quantum efficiency spectra[c] (e) for all PMTs under investigation, as well as the respective values at the reference wavelength of 470 nm (f). Tics inside histograms indicate values of individual PMTs. KM3NeT quality criteria, valid at the time of testing, marked in *orange*, average values in *blue*. A typical charge distribution (b) demonstrates a peak-to-valley ratio, exceeding the demanded minimum of 3. Figures (b) and (c) taken from [149], modified. Remaining figures are based on KM3NeT internal report data and must be considered preliminary. A comprehensive paper on KM3NeT prototype testing is in preparation.

---

[a] Needed to achieve the KM3NeT standard gain of $5 \cdot 10^6$.

[b] Given in terms of the full-width-half-maximum of the main peak of the transit-time distribution.

[c] Highlighting the quality requirements.

5.1.6 Hamamatsu R6233-01MOD

A total of 53 tubes were delivered by the manufacturer to be tested in Erlangen. Some of the requirements were met by the prototypes, with the transit time spread being the main remaining issue [149].

- All PMTs were found to achieve a gain of $5 \cdot 10^6$ if supplied with voltages ranging from 1000 V to 1400 V, with none of the tubes exceeding the quality cut of 1400 V.
- Operated at a gain of $5 \cdot 10^6$, five tubes (corresponding to 9.4% of the sample) exhibited a dark rate exceeding the initially required maximum of 3 kHz, whereas a the majority (68.%) was found to also comply with the more restrictive 1.5 kHz introduced later.
- The quantum efficiency features the typical spectra of bialkali photocathodes. At the reference wavelength of 470 nm the values scattered around the average of 19.9%. The requirement of $QE(470\,\mathrm{nm}) \geq 20\%$ was met by 47% of the sample.
- With 5.2 ns the average transit-time spread exceeded the limit. Only one of the tested tubes was found in compliance with the KM3NeT requirement of < 4.6 ns, effective at the time of the measurement.

Summary plots of the obtained results are presented in figure 5.5. Based on these results it was decided to communicate the need for a better tube to the manufacturer. The observed poor TTS-performance was attributed to the box-type dynode structure inherited from the original model R6233 (see section 3.2 for details). The newly designed model R12199-02 consequently features the superior “linear-focused” electron multiplier.

5.1.7 Hamamatsu R12199-02

PMTs of type R12199-02 first became available from Hamamatsu in early 2012. By mid-2013, a total number of 203 PMTs had been characterized in test facilities in Erlangen (158 specimen), Amsterdam (30 specimen) and Catania (22 specimen). Some of the tubes were also tested in all sites to provide cross-calibration. Overviews of the cumulative results[1] are presented in figure 5.6 and table 5.2. The investigated parameters were, by and large, found to comply with the KM3NeT requirements. Although the dark pulse rate distribution featured a large-value tail, with 18% of the tested sample exceeding the condition of < 2 kHz, and some PMTs exhibited a larger than required probability for spurious pulsing, the discussed PMT type was agreed upon to be used in the majority of the KM3NeT modules [139]. This decision was in part driven by the large production capacity of the manufacturer.

---

[1] The term current density is used in this context to denote the photocurrent produced by a photocathode when a part of its area is illuminated.

[2] Type S6337-01 by Hamamatsu [144].

[3] Via subtraction of a value interpolated between dark current measurements taken before and after the actual PMT test.

[4] $N_\gamma = \mathit{const.}$ and $N_\gamma \cdot QE = N_\mathrm{e} \propto I \Rightarrow QE/I = \mathit{const.}$

[1] Not all PMTs were tested for all parameters, while the results from cross-tested tubes are treated in the plots as individual measurements.

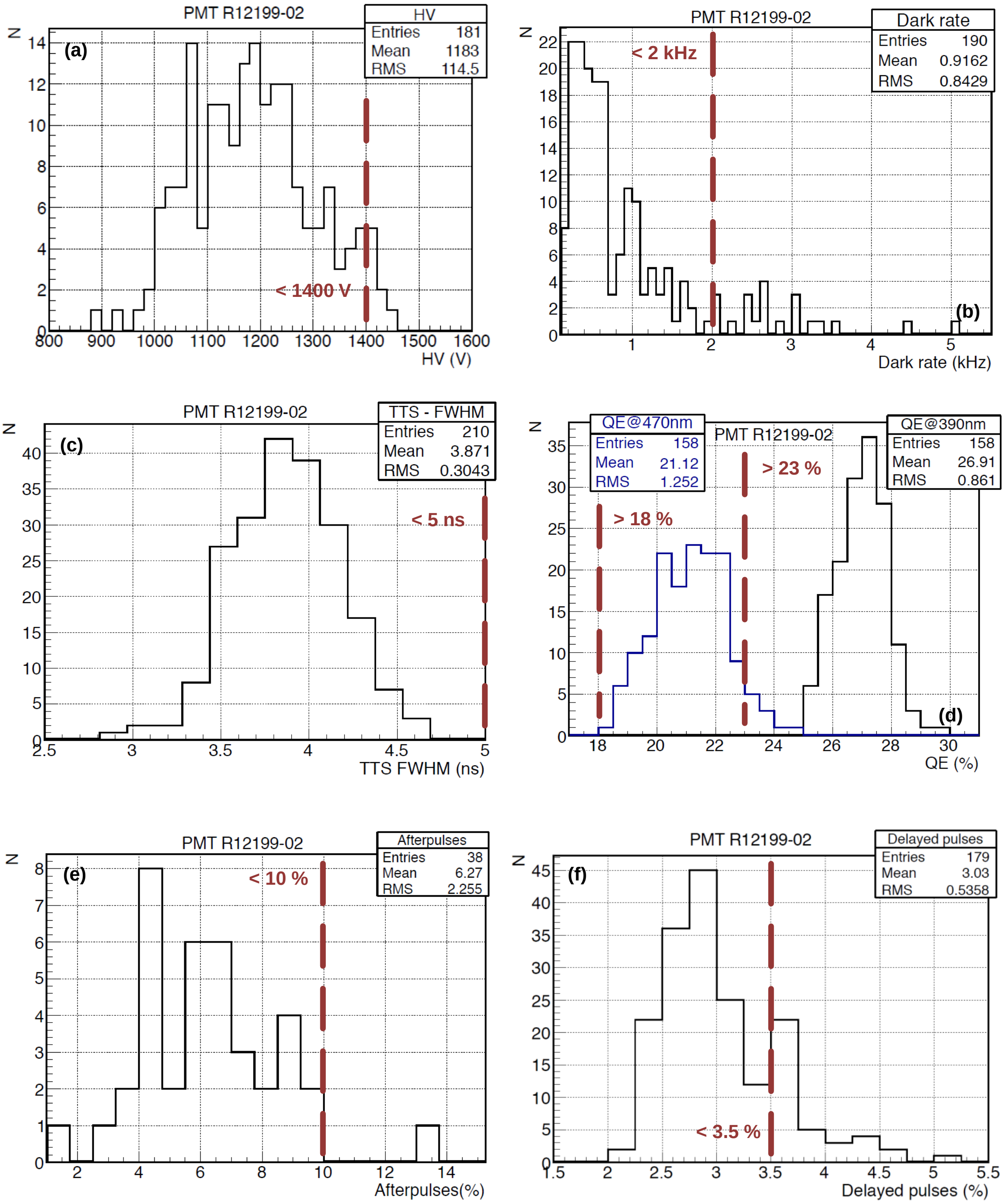

Figure 5.6: Characterization results for the Hamamatsu R12199-02 three-inch PMT. Featuring distributions of nominal[a] PMT voltage (a), dark rate (b), transit-time spread[b] (c), quantum efficiencies at reference wavelengths (d) as well as the occurrence ratios of afterpulses (e) and delayed pulses (f). Dashed *red* lines indicate the corresponding KM3NeT quality requirements in effect at the time of the measurements (see also table 5.1). Figures taken and modified from [139] and internal KM3NeT reports. The plots must be considered preliminary. A comprehensive paper on KM3NeT prototype testing is in preparation.

---

[a] Needed to achieve the KM3NeT standard gain of $5 \cdot 10^6$.

[b] Given in terms of the full-width-half-maximum of the main peak of the transit-time distribution.

parameter	**minimum**	**maximum**	**mean**
nominal voltage (181)	900 V	1450 V	1183 V
quantum efficiency (390 nm) (158)	25%	30%	27%
quantum efficiency (470 nm) (158)	18%	25%	21%
transit time spread (FWHM) (210)	2.8 ns	4.7 ns	3.9 ns
dark rate (190)	200 Hz	5000 Hz	916 Hz
early pulsing (20)	0.01%	0.8%	0.16%
delayed pulsing (179)	2%	5%	3%
early afterpulsing (38)	2%	13%	6.3%

Table 5.2: Test result summary for Hamamatsu R12199-02. Sample size for the test of a particular parameter is indicated by numbers in brackets. For details on parameter definition see table 5.1.

5.1.8 Alternative PMTs

In order not to depend on a single manufacturer[1], three-inch PMT prototypes were also acquired from alternative sources. Three different PMT types were provided for testing by **ET Enterprises Ltd.**:

- 104 specimen of type D783KFLA and
- ten D793KFLA tubes, both featuring an outside diameter of 77 mm, as well as
- twelve large-area (diameter of 86 mm) D792KFLA PMTs.

Further, seven 76 mm PMTs of type XP53 were delivered by **HZC**.

The KM3NeT group at Nikhef (Amsterdam) performed tests of the gain, transit-time spread (TTS), dark rate, and fraction of spurious pulses for all tubes. The ECAP group in Erlangen contributed measurements of the quantum efficiency as well as cross-checks on other properties for selected PMTs.

- 80% of the ETEL PMTs of types D783KFLA and D793KFLA, and 100% of D792KFLA were found to meet **nominal voltage** specifications. All HZC tubes needed voltages larger than 1300 V (1400 V) to reach a gain of $3 \cdot 10^6$ ($5 \cdot 10^6$).
- 96% of D783KFLA PMTs had **dark rates** below 2 kHz. The dark rates of types D792KFLA and D793KFLA were found to be below 0.5 kHz and 1 kHz, respectively.

  In case of the tested HZC PMTs, dark rates ranged between 1.6 kHz and 3.3 kHz, with three PMTs ($\sim$ 43%) exceeding the limit of 2 kHz.
- The **transit-time spread** was found to comply with specifications for all tested tubes.
- The probability for **delayed pulses** was below the limit for all investigated models.

---

[1] In particular after the experience made with Photonis.

- Concerning the probability for late **afterpulses**, 28% of the tested D783KFLA PMTs, 33% of type D793KFLA and all XP53 tubes exceeded the specified value of 10%. Only 1 of the 8 measured D792KFLA PMTs has a percentage of late afterpulses slightly above the specifications.
- All PMTs from both manufacturers met the KM3NeT specifications concerning **quantum efficiency**.

The PMTs delivered by ET enterprises did comply with (almost) all specifications and found eligible for KM3NeT module production. The large-area model D792KFLA was determined to be the most favorable one.

Type XP53 by HZC were (in the then-current configuration) was discarded, violating quality parameters concerning supply voltage and afterpulsing [150].

5.1.9 Current status and further development

Development of appropriate three-inch PMTs continued. Prototypes by three manufacturers, namely

- **MELZ FEU "project KM3NeT"**, with a diameter of 85 mm,
- **ETEL 9320KFL**, featuring a diameter of 87 mm, as well as
- two model by **HZC**, **XP72B80** (76 mm) and **XP82B20** (85 mm)

are currently undergoing extensive scrutinizing by KM3NeT collaborators. Even though the testing is still work in progress at the time of writing of this thesis, in particular the ETEL model appears very promising, exhibiting equal or superior performance with respect to the R12199-02 by Hamamatsu. Due to its strongly increased photocathode area, it was also included in the Geant4 simulation of the mDOM, alongside the Hamamatsu PMT, in order to evaluate the impact on module performance (see section 10.2).

5.2 Response uniformity

All PMT characteristics introduced in the previous section are measured either homogeneously illuminating the entire photocathode or, in the case of quantum efficiency, a central region featuring an area of $\sim 1\,\mathrm{cm}^2$. This approach corresponds to an effective averaging of the investigated property over the illuminated area. However, PMT output is in general known to be a (non-constant) function of position (and also the angle) of the incident light. An illustration of this behavior can e.g. be found in figure 3.6. In manufacturer handbooks [123, 124, 126] the deviation from uniformity[1] is usually attributed the following effects:

---

[1] Usually illustrated by the results of linear scans (horizontal or vertical) across the entrance window of a PMT.

- inferior **photoelectron collection** efficiency at large cathode radii, due to a non-homogeneous electric field between cathode and first dynode,

- larger effective **cathode material thickness** for photons impinging at large radii, with respect to the center, resulting in an effective sensitivity increase [151],

- increased **reflective losses** at larger distances from the PMT center due to the curvature of the glass, resulting in effectively increased incidence angles, as well as a

- deterioration of response uniformity with increasing photon wavelengths, caused by a stronger impact of **photocathode surface conditions** on the quantum efficiency in the long-wavelength regime.

The uniformity of the (anode) output, although specified in (some versions of) the KM3NeT requirements to be only tolerable if below 10%, is (usually) not systematically investigated by the collaboration for all PMT prototypes.

The motivation for a more detailed investigation of response uniformity in the scope of this work was the desire to:

- check the most current PMT prototypes, namely models R12199-02 by Hamamatsu and 9320KFL by ETEL, for compliance with the KM3NeT **uniformity benchmark**,

- derive an **effective diameter**[1] for these tubes, and compare its deviation from the geometrical for different models.

- investigate the **impact of reflectors** in detail, and also

- get a better understanding of the **physical mechanisms** responsible for the non-homogeneity.

Furthermore, detailed knowledge of the response uniformity of a PMT, together with that of the angular acceptance discussed in section 9.2.2, provide valuable **input for simulations** of the optical module. For instance, in case of the mDOM simulation efforts by the author, presented in detail in chapter 10, non-homogeneous response is not included in the model of the PMTs. All photons are collected equally with no dependence on their impact position or angle, an approach in need of verification and understanding of its intrinsic limits.

A more sophisticated approach to PMT simulation was taken by C. Hugon (INFN Genoa), modeling a semi-transparent cathode for the KM3NeT module [152, 153] (based on findings by [151]). It can as well benefit from experimental verification.

Setup conception, data taking and analysis were done in cooperation with J. Reubelt (ECAP Erlangen).

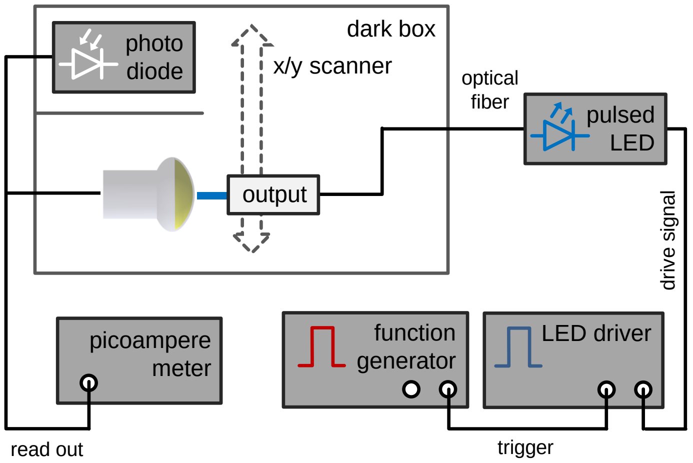

Figure 5.7: Output uniformity scan setup. The depicted reference photodiode was only utilized in the quantum efficiency scan (see section 5.2.2). For details on mounted fiber output devices see figure 5.8 and discussion in text.

Scanner setup

A pulsed diode[1], introduced in the scope of gain and TTS characterization (see sections 5.1.1 and 5.1.2), was utilized in the experiment. The incident light intensity is adjusted via the pulse frequency, as well as by changing its "tune", a (log-scale) variable affecting pulse length and amplitude (see also section 7.2). The output light was fed via optical fiber into a dark box where the PMT to be examined, was mounted as a fixed target, with its symmetry axis parallel to the beam direction. The emitting end of the fiber was mounted on a custom-made x/y scanner (see figure 5.7). Driven by high-precision remote-controlled[2] stepping motors, the setup allowed to scan the cathode in vertical and horizontal directions with steps well below 1 mm and a positioning precision in the µm regime. Due to the hemispherical shape of the PMT's entrance window this setup results in a vertical incidence of the light in the center, while the incidence angle increases with the radial position (eventually reaching 90 degrees at the very edge of the tube).

To produce a small diameter pencil beam, different approaches were investigated, also presented schematically in figure 5.8:

- A **black tube**, featuring a diameter of 1.0 mm and length of 1 cm, mounted on a fiber[3] of the same diameter. Limiting the initial dispersion of the fiber output light field, the use of a tube still resulted in a rather disperse beam resulting in a spot diameter varying, due to the curvature of the PMT entrance window, between ~ 1.4 mm at the center and ~ 12.2 mm at the outer perimeter of the PMT[4]. Distance between tube

---

[1] This feature is also specified in some versions of the KM3NeT quality parameters. The value tends to increase with the commercial availability of new tubes and is currently at 76 mm. In case of the Hamamatsu R12199-02 had been previously measured by means of a linear scan at ECAP by J. Reubelt [139]

[1] A generator-driven PLS 450 by PicoQuant featuring a pulse length of $t_{\text{pulse}} \approx 800$ ps and a centroid wavelength of ≈ 460 nm.

[2] Using Python scripts.

[3] Actually intended for data transport.

[4] These values were retrieved analytically assuming simple geometrical optics and cross-checked with measurement of the actual light spot with a high-precision ruler. However the actual measurement was deemed to be not overly precise as the determination of the light spot boundary was done relying on the observer's eyes.

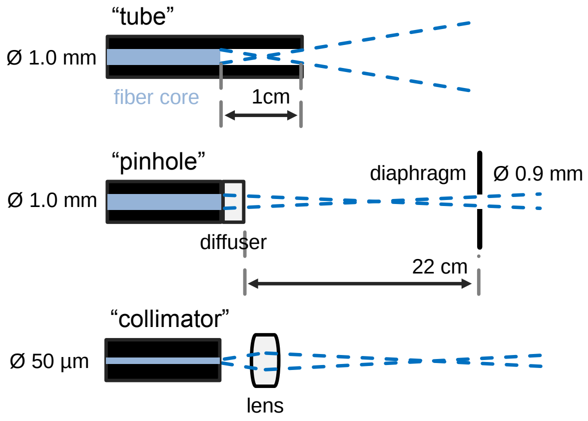

Figure 5.8: Fiber terminators employed in the output uniformity study. Featuring main components, dimensions, and qualitative impression of achievable beam diameters (not to scale).

output and PMT surface was set to $\sim 2\,\mathrm{mm}$ to prevent collisions.

- A **camera obscura** style setup, featuring a pinhole (diameter[1] 0.9 mm), located at a distance of 22 cm from (the same) fiber. This approach resulted in an effective selecting of a narrow beam from the diffuse far-field of the fiber output. The device allowed for a close-to-parallel beam featuring diameters of $\sim 0.9\,\mathrm{mm}$ and $\sim 1.1\,\mathrm{mm}$ at the central and peripheral positions, respectively. A disadvantage was the low efficiency as most of the produced light was lost, requiring to operate the light source at the upper limit of its specifications.
- A dedicated thin multi-mode optical fiber featuring a diameter of 50 µm and a numerical aperture of 0.22 equipped with a **lens collimator**[2]. Although not producing a perfectly parallel beam[3] this approach resulted in a beam diameter below 0.8 mm throughout the relevant distance range (at moderate light source output level).

The uniformity measurement using the discussed scanner setup was found to be very time consuming. A full scan of a reflector-equipped PMT featuring a step size of 1 mm occupied ~ 30 hours.

PMT output was characterized in terms of anode response and quantum efficiency. These independent measurements are discussed in the following sections.

5.2.1 Anode response

Experimental setup

Readout of the PMTs, operated at the nominal gain of $3 \cdot 10^6$ with negative high voltage supplied by a resistive base, was done in **current mode** using a picoampere meter. Typical illumination levels corresponded to $\lesssim 10$ photoelectrons, i.e. were well below the occurrence of saturation[4]. At this output level, dark rate contribution was found to be

---

[1] The diameter was chosen to prevent cathode saturation as well as a non-negligible impact of diffraction.

[2] Model 60FC-SMA-0-A7.5-01 by Schäfter+Kirchhoff.

[3] Only achievable in combination with a single-mode fiber.

[4] Referring to "local" cathode saturation, expected at photocurrent densities larger than $\sim 10\,\mathrm{nA\,cm^{-2}}$ (the value was well below $0.5\,\mathrm{nA\,cm^{-2}}$ in the presented measurements) as well as the deviation form

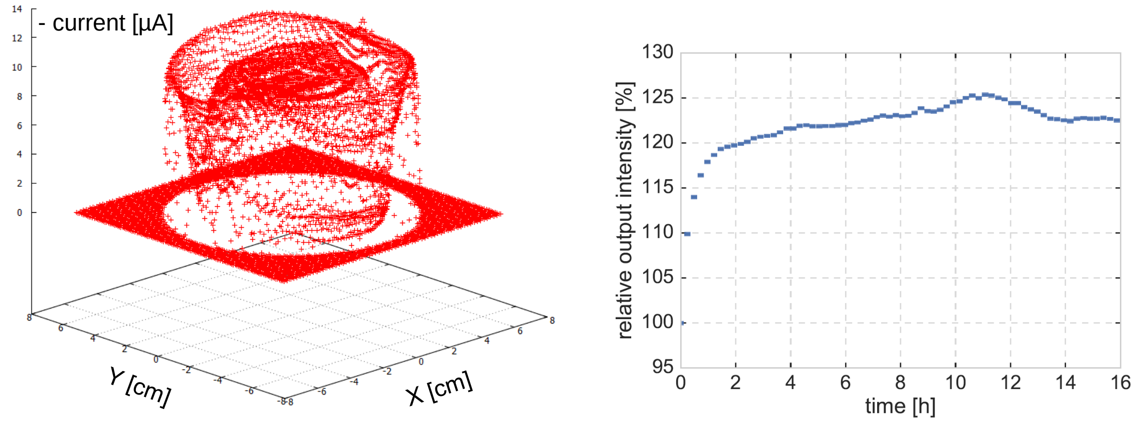

Figure 5.9: Illustration of data processing for response uniformity. **Left**: Example raw scan data (reflector-equipped Hamamatsu R12199-02 PMT). Notable is the central rectangular structure, reflecting the position of the first dynode. **Right**: Corresponding reference measurement of the light source output. Values are normalized to the first datapoint. Errorbars indicate (negligible) standard errors.

on a ‰-scale and could safely be neglected. For each position current measurement was performed 30 times to derive an average and a standard error.

In the course of setup development, the output of the utilized light source was found to be unstable, varying substantially (up to $\sim 70\%$, in the most extreme of the observed cases) during the long operation time of a scan. This behavior was monitored taking a reference measurement in the center of the PMT after each horizontal slice of the scan. Using a time-interpolation $I_{\mathrm{ref}}(t)$ of this reference value, the final relative local sensitivity $I_{\mathrm{rel}}(x, y)$ (relative to the sensitivity of the PMT's center) was derived from the time-stamped raw data $I(x, y, t)$ as

$$I_{\mathrm{rel}}(x,y) = \frac{I_{\mathrm{corr}}(x,y)}{I_{\mathrm{corr}}(0,0)}, \qquad I_{\mathrm{corr}}(x,y) = \frac{I(x,y,t) \cdot I_{\mathrm{ref}}(t)}{I_{\mathrm{ref}}(0)} \tag{5.4}$$

Examples of typical raw data, as well as the corresponding data monitoring the light source output level, are presented in figure 5.9.

Consideration of the (relative) standard errors of the reference current, which where found to be 0.4‰ in the maximum case, allowed to safely neglect them in further data processing. The precision of the results discussed below is considered to be dominated by the (unknown) systematics of positioning and pointing of the PMTs.

Results

Scan results presented in figures 5.10 and 5.13 show clear indication that the anode response is very sensitive to the internal structure of the PMT. Its shape is modulated by

---

linearity of the anode output at $\sim$ 500 photoelectrons (see section 7.2). The small scale of deviations between scans using different beam diameters can be considered an experimental confirmation of this claim.

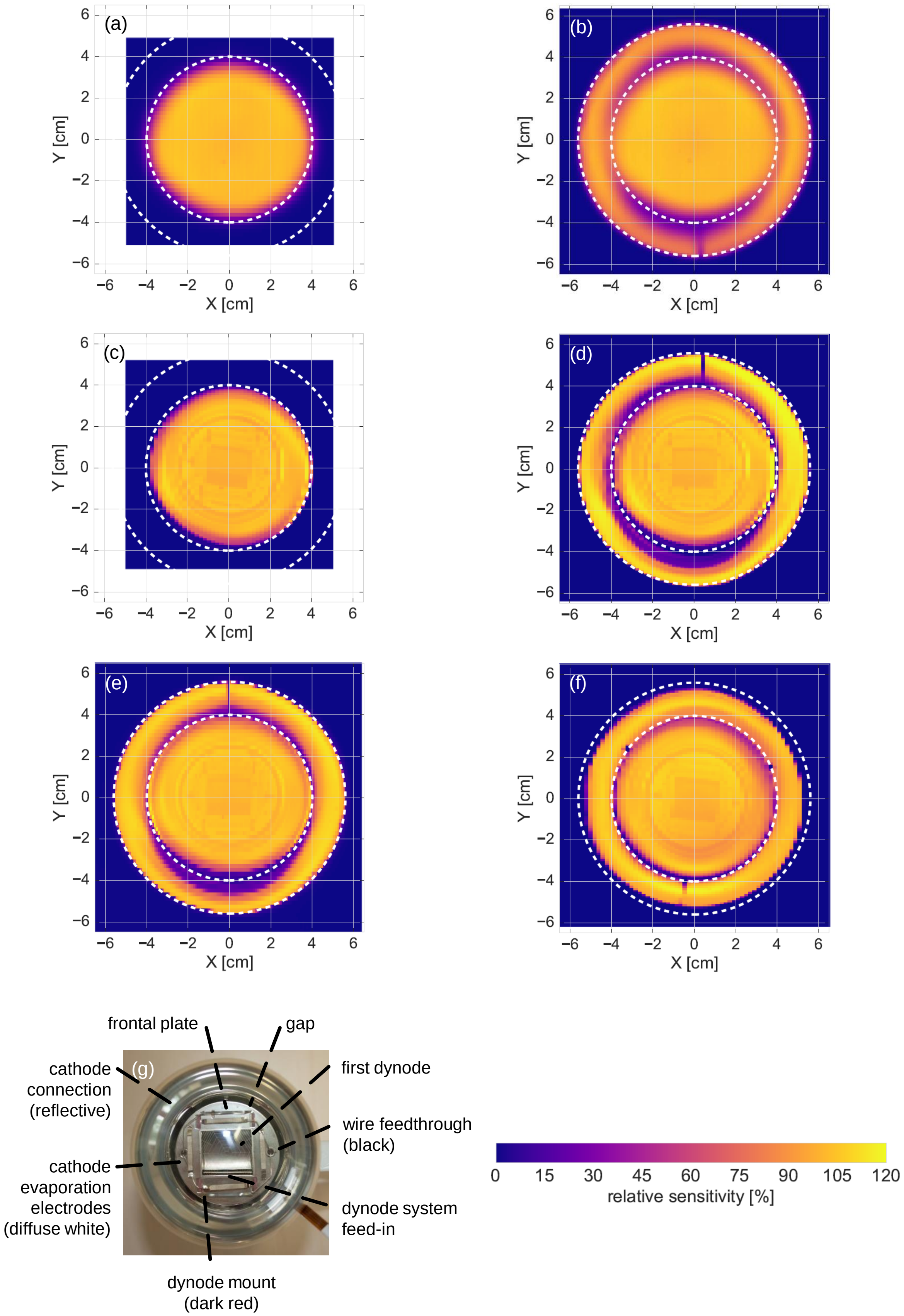

Figure 5.10: Anode response scan results for Hamamatsu R12199-02. Turn page for details.

Figure 5.10: Anode response scan results for the Hamamatsu R12199-02 PMT. Subfigures (a) to (f) show the relative anode sensitivity in different configurations: Figures (a) and (b) feature scans of the bare and reflector-equipped[a] PMT using the “tube” output, while corresponding scans performed with a collimator are presented in (c) and (d). Figure (e) features a reflector-equipped PMT scanned using a pinhole output. A (collimator) scan of a PMT equipped with a KM3NeT reflector is shown in (f). See text (and figure 5.8) for details on the different light guide outputs. Values are normalized to the center of the PMT. A photo of the tested PMT type is presented in subfigure (g), featuring prominent hardware components impacting the sensitivity results. The mechanism of the impact is discussed in the text. *Dashed* circles feature radii of 4 cm and 5.6 cm, corresponding to the actual dimensions of the PMT and the custom mDOM reflector, respectively[b].

---

[a] In this case the custom-made mDOM reflector was used, which later was found to be too large (see discussion in text).

[b] For means of relative comparison, the circles shown in figure 5.13 feature identical radii.

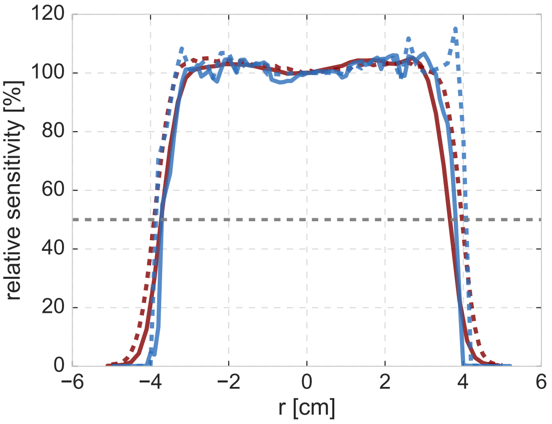

Figure 5.11: Linear scans of Hamamatsu R12199-02. Results are given in terms of anode sensitivity relative to the center. Presented are slices from the full x-y scans in figure 5.10 used to derive effective diameters (*red*: large light spot, setup (a); *blue* small light spot, setup (c)). See table 5.3 for results. *Solid* lines mark vertical slices, while horizontal scans feature *dashed* ones. The 50% level is emphasized by a *dashed gray* line.

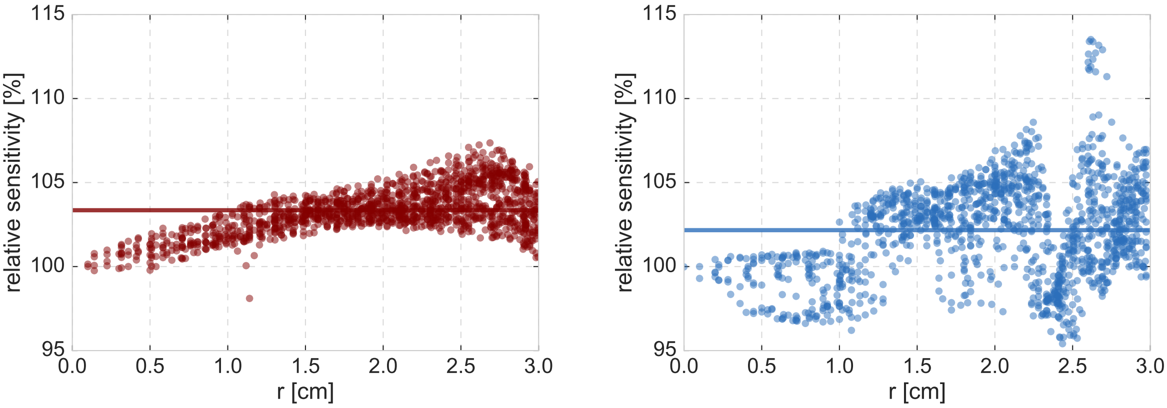

Figure 5.12: Anode response uniformity Hamamatsu R12199-02: **Left**: Measurement performed using a tubed large diameter fiber. **Right**: Collimator-teminated fiber measurement. Datapoints were mapped on center distances r. For corresponding uniformity heatmaps see figures 5.10 (a) and (c). Derived uniformity parameters are presented in table 5.4

reflection and scattering of photons, which have initially passed the photocathode without electron production, from internal components. These photons thus get a second (in some cases even a third) chance to hit the cathode and liberate electrons. The scans clearly feature the metallic cone, used to electrically contact the photocathode, the circular mounting structure of the dynode system and its rectangular entrance window. In particular in the case of the Hamamatsu PMT, it is also possible to deduce the curvature of the first dynode. Even small features, namely two electrodes used to initially create the cathode by evaporation, the holes for the corresponding wiring, and the small gap between the dynode shield and the inner surface of the glass envelope (Hamamatsu PMT) or the gap in the cathode connection (ETEL PMT) are resolved by the scans. As expected, the level of details visible in the scan results strongly depended on the spot diameter: While the above discussion applies to the scans using a collimator-terminated fiber, those structures were mostly averaged/smoothed out in the large diameter data. Results obtained using the pinhole setup were found to be comparable to those of collimator-terminated fiber, indicating a similar beam diameter, thus confirming the initial considerations.

In case of the scans of reflector-equipped tubes, linear structures and "holes" in the reflector area indicate the positions of the metal sheet joint and mounting holes in case of the KM3NeT reflector. The strong impact of reflector curvature is also noteworthy, resulting in a non-uniformity of the sensitivity in the reflector area, particularly in the case of the Hamamatsu PMT, when comparing the custom-made hand-bent mDOM reflector (figure 5.10 (d)) to the professionally produced reflector of KM3NeT (figure 5.10 (f)).

A general left-right and top-bottom asymmetry of the sensitivity was observed in several scans and could be either attributed to misalignment of the PMTs or an actual non-uniformity in PMT performance. The reason for the peculiar behavior of setup (d) in the ETEL results (figure 5.13) is not clear. Unfortunately the PMT became unavailable soon after completion of the test, preventing a follow-up of the results.

Effective diameters were derived from the anode response scan data in three ways:

- From the full width at 50% of the central sensitivity value, using horizontal and vertical slices,
- integrating the relative sensitivity along the (same) slices, as well as
- integrating the entire relative sensitivity map,

with the latter approach considered to be most reliable. A summary of the results, obtained for different setups[1] is presented in table 5.3. Noteworthy is the good match between results obtained from scans of the same tube using different beam diameters, which was expected as the use of a larger beam (ideally) results in an effective smearing of the sensitivity, without affecting its integral.

The effective area relation[2] between ETEL and Hamamatsu PMTs from the scan data was found to be 1.18, with the difference to the value expected from the outer diameters

---

[1] As measurements of the bare ETEL PMT suffered from a pronounced asymmetry of the response, the central region of a reflector-equipped PMT scan (figure 5.13 (f)) was used as a substitute. The large light spot scan was discarded from the analysis for the same reasons.

[2] Comparing collimator scan data of the Hamamatsu tube to the pinhole scan of the ETEL model.

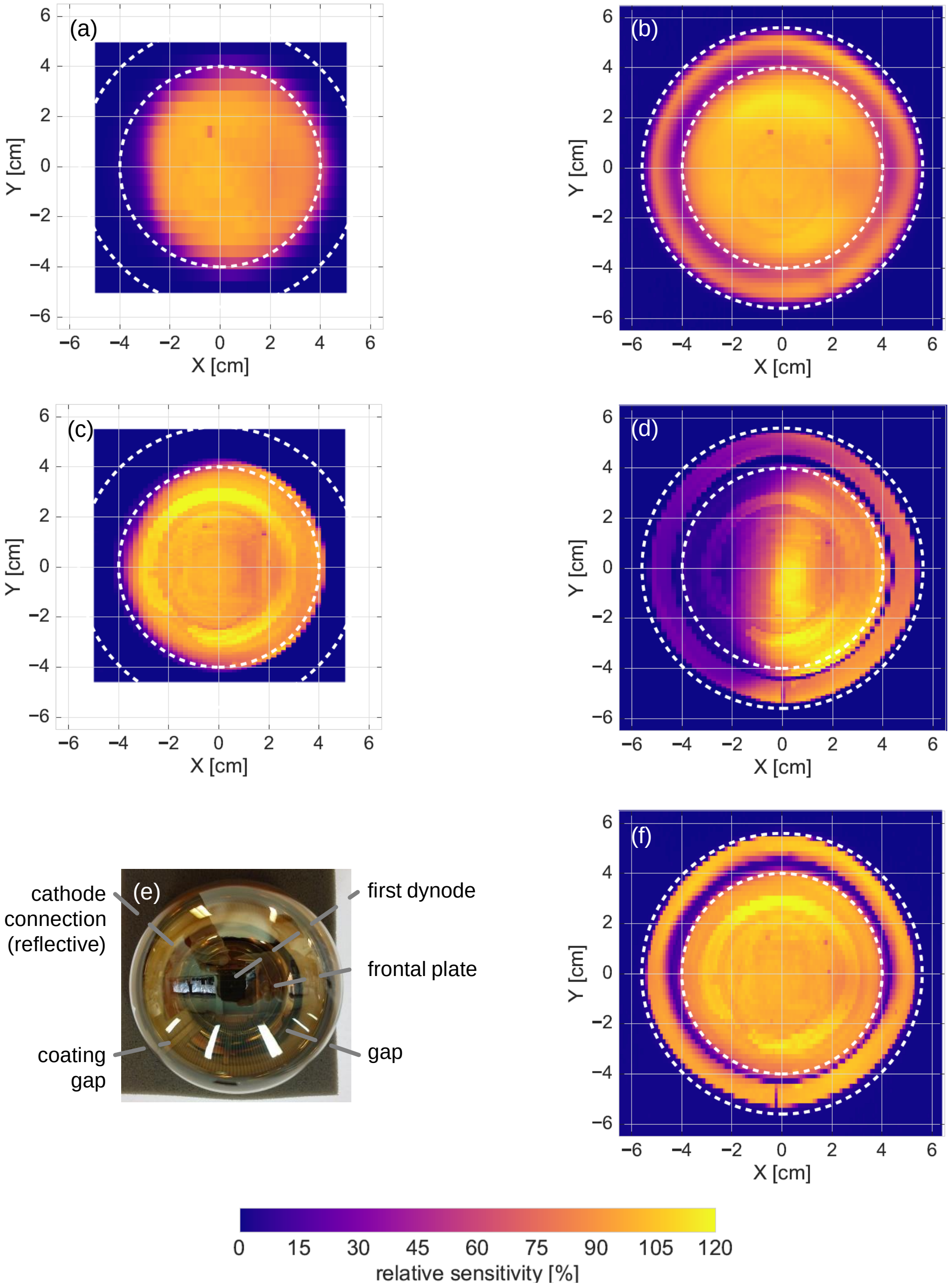

Figure 5.13: Anode response scan results for PMT 9320KFL by ET enterprises. Subfigures (a) and (b) feature scans of the bare and reflector-equipped PMT using a "tubed" fiber, while corresponding scans performed with a collimator are presented in (c) and (d). Figure (f) features a reflector-equipped PMT scanned using a pinhole output. Details on the different light guide output options are given in the text and illustrated in figure 5.8. Sensitivities are normalized to the central position on the PMT. A photo of the PMT under investigation is presented in subfigure (e), with prominent hardware components impacting the sensitivity results highlighted. The mechanism of the impact is discussed in the text. For means of relative comparison, *dashed* circles, featuring radii of 4 cm and 5.6 cm, indicate the dimensions of the Hamamatsu PMT and the corresponding custom mDOM reflector, respectively (see figure 5.10).

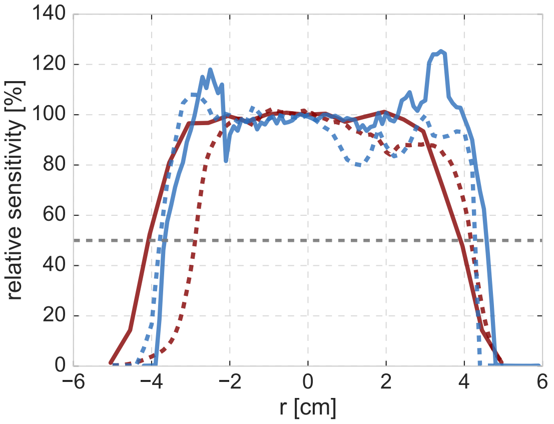

Figure 5.14: Linear relative anode sensitivity scans for ETEL 9320KFL, selected from x-y scans of the PMT input window presented in figure 5.13, utilized in the derivation of the effective PMT diameter (see table 5.3 for an overview of the results). For details on nomenclature see figure 5.11. Due to obvious issues with the data obtained using the "tube" fiber termination (*red* curves) it was excluded not used to determine the effective diameter.

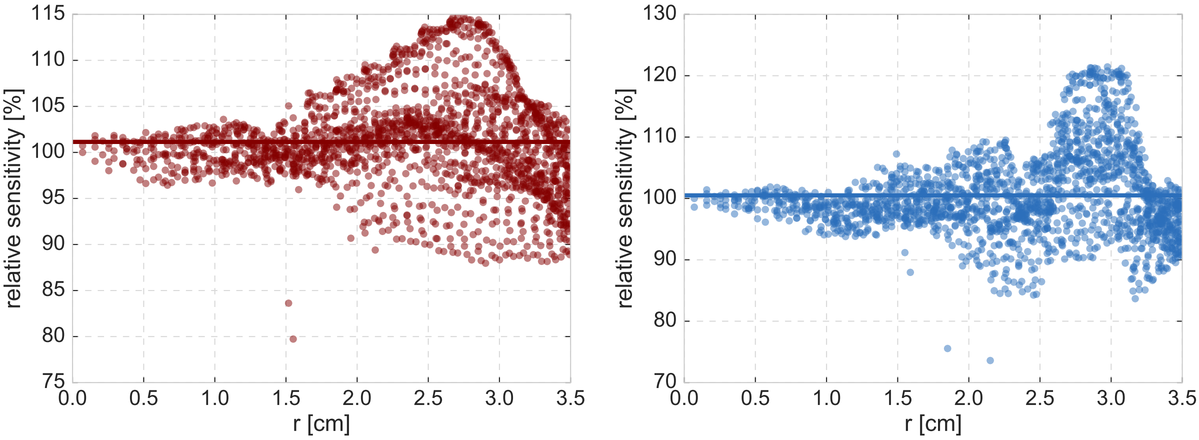

Figure 5.15: Anode response uniformity ETEL 9320KFL **Left**: Measurement performed using a tubed large diameter fiber. **Right**: Collimator-teminated fiber measurement. Datapoints were mapped on center distances r. For uniformity heatmaps see figures 5.13 (a) and (c). Derived uniformity parameters are presented in table 5.4

		linear slice				total surface	
		50% center value		weighted average		integration	
PMT type	fiber output	$\boldsymbol{d}_\mathrm{v}$ [cm]	$\boldsymbol{d}_\mathrm{h}$ [cm]	$\boldsymbol{d}_\mathrm{v}$ [cm]	$\boldsymbol{d}_\mathrm{h}$ [cm]	$\boldsymbol{d}$ [cm]	$\boldsymbol{A}$ [cm^2]
Hamamatsu	tube (a)	7.4	7.9	7.5	8.1	7.8	47.3
R12199-02	coll. (c)	**7.5**	**7.9**	**7.5**	**8.0**	**7.7**	**46.4**
ETEL	coll. (c)	8.2	8.1	8.2	7.6	8.0	50.8
9320KFL	pinhole (f)	**8.4**	**8.1**	**8.5**	**7.9**	**8.3**	**54.6**

Table 5.3: Effective PMT diameters d_i derived from anode uniformity scans. Indices v and h refer to vertical and horizontal slices, respectively. In case of the full surface average also the total effective area A is presented. Different fiber outputs were used, with “tube” referring to black plastic tube, “pinhole” to the camera obscura device, and “coll.”/“collimator” to the lens collimator, as introduced in more detail in the text. Characters in brackets refer to subplots of figures 5.10 (Hamamatsu) or 5.13 (ETEL), depending on the PMT model. Results deemed most reliable are set in bold font. Found to be on the sub-percentage level statistical uncertainties are omitted.

(and respective production margins) as provided by the manufacturers (see figures 10.9 and 10.10) of 1.17 ± 0.03 below 1%. The good agreement with the purely geometrical relation, indicates a comparable “sensitivity density” for both PMTs. This would not be the case if one of the tubes featured e.g. strong variations of the response.

The obtained data set also allowed to derive effective areas for reflector-equipped PMTs in order to assess the gain in sensitivity in case of frontal illumination by a plane wavefront. Values were derived integrating anode output scans. Results for applicable configurations[1] are presented in table 5.5. The values agree well with results from angular acceptance measurements discussed in detail in section 9.2.2.

As it was not clearly specified[2] how to interpret the KM3NeT homogeneity requirement of $< 10\%$, to assess **response uniformity**, different figures of merit, comparing standard deviation and maximum occurring differences[3], to the average relative sensitivity, as well as sensitivity at the center of the PMT, were derived from the central region of the PMT, featuring a radius of 3.0 cm. In case of the larger ETEL tube a radius of 3.5 cm was also considered. Results are summarized in table 5.4. This approach, based on the mapping of all data points on their respective distance to the center of the PMT (see figures 5.12 and 5.15), relied on the knowledge of the position of this center. As the tubes were not precisely centered in the scanner setup, it had to be deduced based on the data. This was done “by hand”, as respective centers of first dynode, front plane, as well as the outer perimeters of PMT and reflector, did not line up. All in all, the anode response of the investigated PMTs was deemed satisfyingly uniform, with the Hamamatsu PMT featuring the more uniform output compared to the ETEL model (a factor of ~ 2 was found between the respective uniformity parameters for both tubes).

The anode scan results also allowed to check the output of the **Geant4 simulation** developed in the scope of this thesis. A corresponding cross-check is presented in a

---

[1] Again, the inferior quality of the data on the ETEL tube prevented some scans from being usable.

[2] Also, a “standard reference beam diameter”, defining the amount of “smoothing” of the curve, was not specified.

[3] After exclusion of outliers.

PMT type	fiber output	measure of anode response uniformity [%]			
		$\boldsymbol{\sigma/\mu}$	$\boldsymbol{\Delta_{\mathrm{max}}/\mu}$	$\boldsymbol{\Delta_{\mathrm{max}\,\mu}/\mu}$	$\boldsymbol{\Delta_{\mathrm{max}\,c}/c}$
Hamamatsu R12199-02	tube (a)	1.3	9.0	5.1	7.4
	collimator (c)	**2.8**	**17.7**	**11.1**	**13.5**
ETEL 9320KFL	pinhole (f)	**6.4** (6.8)	**36.8** (38.11)	**20.6** (21.0)	**21.6** (21.6)

Table 5.4: Uniformity of the anode response of both tested PMT types. As no "canonic" figure of merit is defined by the KM3NeT collaboration, different measures of uniformity are given. Standard deviation and average of the relative response distribution are referred to by σ and μ. Δ_{max}, $\Delta_{\mathrm{max}\,\mu}$, and $\Delta_{\mathrm{max}\,c}$ indicate the largest difference occuring between two datapoints, the largest deviation from the mean value, and the largest deviation from the sensitivity at the center of the PMT, respectively. The results are based on radii smaller than 3.0 cm, in case of the larger ETEL PMT results for the central 3.5 cm are given in brackets. Obvious outliers were excluded from the sample prior to processing. For fiber output nomenclature see figure 5.8. Bold font marks the results considered most reliable (see discussion in text).

PMT type	setup, fiber output	$\boldsymbol{A}$ [cm^2]	**gain** [%]
Hamamatsu R12199-02	b, tube	85.6	80.9 [a]
	e, collimator	86.5	86.5 [c]
	f, collimator	82.2	77.3 [c]
ETEL 9320KFL	f, pinhole	79.7	46.0 [f][a]

---

[a] Due to the in general poor quality of most ETEL measurents, the gain was derived comparing the overall effective area to the integral of a central region representing bare PMT data.

Table 5.5: Effective areas for reflector-equipped PMTs. Values were derived integrating anode output scans. In case of the Hamamatsu PMT values are given for a dedicated mDOM reflector (setup (b) and (e)) as well as the current KM3NeT model (setup (f)). For an overview setup and fiber output nomenclature see figures 5.12 and 5.15 as well as the discussion in text. The reflector gain was derived from comparison to setups in square brackets.

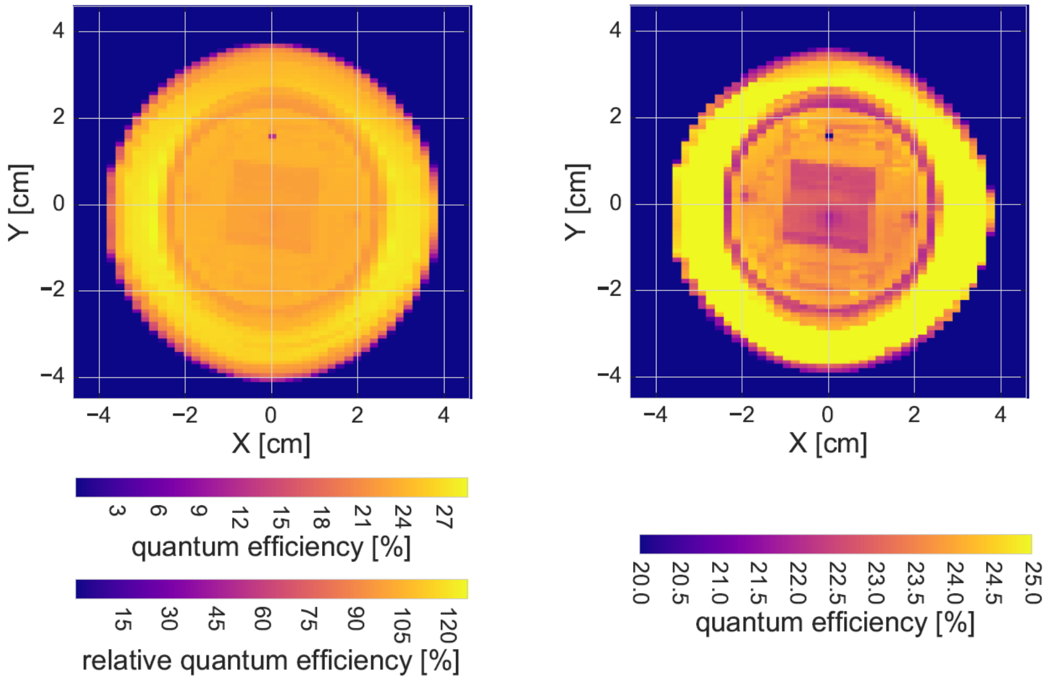

Figure 5.16: Quantum efficiency uniformity scan of Hamamatsu R12199-02. The quantum efficiency is given in terms of its absolute magnitude, as well as normalized to the values at the center of the cathode (**left**). In the **right** subfigure the range is adapted highlighting the structures observable in the data.

dedicated section 10.3.1.

5.2.2 Quantum efficiency

As introduced above, in the standard PMT characterization approach, the quantum efficiency is measured (as a function of the incident photon wavelength) illuminating the central region, effectively averaging the parameter over an area of $\sim 1\,\mathrm{cm}^2$ (see section 5.1.5).

As the specimen of the ETEL PMT had in the meantime become unavailable, the quantum efficiency was measured for the Hamamatsu PMT, only. Earlier (horizontal) scans[1], of this model carried out by J. Reubelt, indicated an increase of the quantum efficiency in a concentric region at large center distances, before a final drop-off at the perimeter. This behavior was interpreted as being due to reflections of light at surfaces inside the PMT (see also discussion of anode response results above, as well as the following section).

---

[1] Using a beam diameter of 1.3 mm and rotating the PMT, corresponding to spacial sampling of $\sim 5\,\mathrm{mm}$ [154].

Experimental setup

The scans of anode response and quantum efficiency (cathode response) shared the light source and scanner, introduced above. For the quantum efficiency, only the more precise collimator-terminated fiber was used.

During the measurement the PMT was operated in **current mode** with its dynode system cut short. As discussed in section 5.1.5, the voltage applied between the cathode and the dynode system corresponded to the typical voltage increment ($\sim 300\,\mathrm{V}$) occurring between cathode and first dynode in normal operation to reproduce the electric field configuration. Read-out of the tube was done using a picoampere meter.

To derive the absolute quantum efficiency, a calibrated photodiode was used (in analogy to the standard characterization technique). This device, located in the dark environment close to the PMT in the scanner's range, was also a means to monitor the time variation of the LED output. The photodiode current was recorded after the completion of each horizontal slice and interpolated in time to be applied to respective scan positions.

The final result for the quantum efficiency of the PMT at a given position $QE_{\mathrm{PMT}}(x,y)$ is then obtained from the relation

$$QE_{\mathrm{PMT}}(x,y) = -\frac{I_{\mathrm{PMT}}(x,y,t) - I_{\mathrm{dark\,PMT}}(t) - I_{\mathrm{dark\,diode}}(t)}{I_{\mathrm{diode}}(t) - I_{\mathrm{dark\,PMT}}(t) - I_{\mathrm{dark\,diode}}(t)} \cdot QE_{\mathrm{diode}} \tag{5.5}$$

where $I_{\mathrm{PMT}}(x,y,t)$ is the PMT current, $I_{\mathrm{diode}}(t)$ is the photocurrent obtained by the diode, and QE_{diode} is its known quantum efficiency. Time dependence is shown explicitly as it was used to assign reference measurements to pixels of the scan. The leading minus accounts for the different signs of PMT and diode currents.

Typical relative quantum efficiency uncertainties were found[1] to be $\sim 0.5\%$, with the absolute value of the errors never exceeding 0.02%. Thus being negligible, these small errors, already including uncertainties caused by the interpolations involved in data analysis, were omitted from the result plots. The uncertainty of the obtained values is believed to be dominated by systematic effects, such as positioning and pointing of the PMT.

Results

As observed in the case of anode response, as well as in earlier scans, the **quantum efficiency** is not flat across the photocathode. Even though, contributions from e.g. reflection losses at the air-to-glass boundary and increasing cathode thickness are expected, the observable overall behavior appears to be dominated by reflection and/or scattering of non-converted photons at the inner structure as discussed in the previous section, with the impact of the reflective cathode connection being most prominent (see figure 5.16). The latter effect was found to be more pronounced comparing to the anode response scan (see also figure 5.17, left). This can be attributed to the collection efficiency of the PMT (see section 3.1 for details and relation properties such as quantum efficiency and detection efficiency) as, roughly speaking, the quantum efficiency reflects the amount of produced photoelectrons, while the anode response relates only to the fraction accepted by the electron multiplier system (see also discussion below).

---

[1] Using Gaussian propagation of statistic standard errors.

		measure of quantum efficiency uniformity [%]			
PMT type	r_{uni} [cm]	$\boldsymbol{\sigma/\mu}$	$\boldsymbol{\Delta_{\max}/\mu}$	$\boldsymbol{\Delta_{\max\,\mu}/\mu}$	$\boldsymbol{\Delta_{\max\,c}/c}$
Hamamatsu	3.0	5.6	29.0	20.5	26.8
R12199-02	3.5	6.9	28.2	17.1	26.8

Table 5.6: Quantum efficiency uniformity of a R12199-02 PMT. Details on the figures of merit are introduced in table 5.4. The radius of the central region used to derive the properties is referred to as r_{uni}.

This exact shape of the quantum efficiency, featuring inhomogeneities up to $\sim 27\%$ (referring to the maximum deviation from the central value, see figure 5.17, left, and table 5.6), is important regarding individual photons arriving at certain positions on the PMT, but is smeared out when large amounts of light, such as a plane wave front, are considered. Results indicate that assuming universal validity of the quantum efficiency retrieved in the center will underestimate the actual property[1] of the PMT. If however, interested in the "pure" quantum efficiency as a property of the cathode material (defined in section 3.1 as the conversion probability from photon to electron) a good approximation is given by the values at positions where no reflection and scattering can occur, such as the gap between the electron multiplier and the inner surface of the glass envelope. In case of the investigated PMT the efficiency in these particular regions did not deviate significantly from the central value[2], which can be considered an argument in favor of the standard characterization procedure (see figure 5.16, right).

With information on anode response and quantum efficiency of a PMT it is, in principle, possible to derive also its **collection efficiency**. The available relative detection efficiency (identical to the relative anode response) allows the determination of a relative value for this property[3]. The relative collection efficiency CE_{rel} was deduced using vertical and horizontal central slices from the scans of relative anode response DE_{rel} and relative quantum efficiency QE_{rel} as

$$CE_{\mathrm{rel}} = \frac{QE_{\mathrm{rel}}}{DE_{\mathrm{rel}}} \tag{5.6}$$

Results are presented in figure 5.17. For the central region, featuring radii below 3 cm, the collection efficiency is rather constant, at least in case of the vertical slice, dropping off at larger distances from the center. This trend is to be expected from a homogeneous electric field deteriorating at large center distances. However, the result has to be taken with a grain of salt, as the measurements of quantum and detection efficiencies were not done with the PMT in an exactly identical position, with individual positioning and inclination of the PMT introducing different systematics. Those are deemed accountable for the peculiar trend of the collection efficiency obtained from horizontal slice data.

---

[1] Nevertheless, the standard characterization technique of measuring in the center is a good approach, in particular for mass tests, as it does not rely on precision of mounting or light spot positioning, as long as the spot stays in the inner square.

[2] This however, could be an effect of the beam diameter being comparable to the size of the gap. Usage of a finer light spot might lead to a different result.

[3] The measurement of the absolute detection efficiency at a single position (e.g. the center) would then allow to get immediately the full distribution.

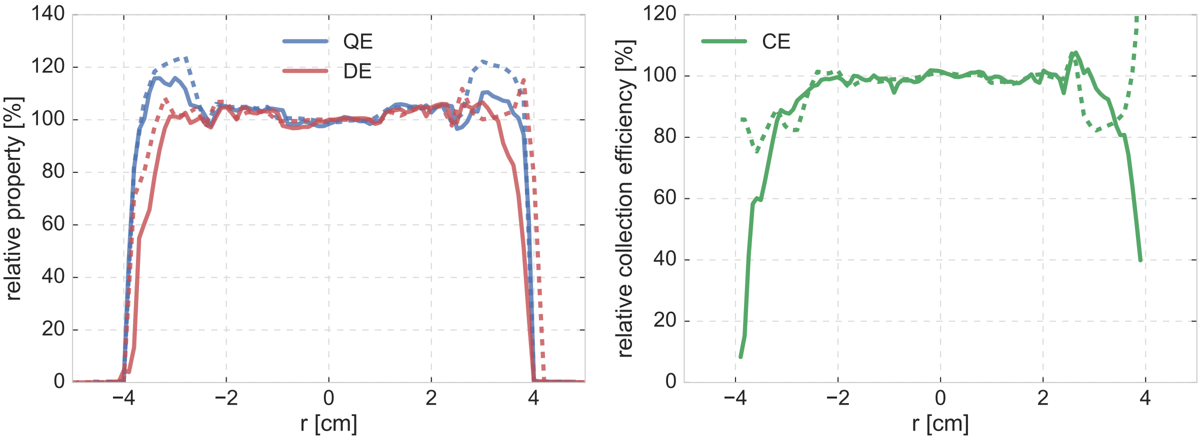

Figure 5.17: Derivation of the relative collection efficiency CE for a Hamamatsu R12199-02 PMT from linear slices extracted from the scans of its relative detection efficiency DE (*red*, proportional to the anode response) and the quantum efficiency QE (*blue*). *Dashed* lines mark horizontal while *solid* lines indicate vertical slices.

5.2.3 Transit time

The x/y scanner also allowed to assess the behavior of the signal transit time. As introduced in the discussion of PMT functionality principles (see section 3.5), the transit time is expected to be a function of the position of photon incidence on the cathode, increasing, in general, with distance from the PMT center. This effect is responsible for the transit-time spread, defining the timing precision of the device.

The setup to assess the local dependence of the transit time included the fast pulsed light source and a collimator-terminated optical fiber. Scans were performed horizontally across the cathode[1]. As introduced in the dedicated gain and TTS characterization sections (5.1.1 and 5.1.2, respectively), the PMTs were read out storing (and analyzing off-line) externally triggered pulse waveforms by means of a digital oscilloscope. The light source was operated at an output level of ~ 0.5 photoelectrons per pulse. Individual transit times were determined applying a ~ 0.3 photoelectron threshold to the stored waveforms. The mean transit time was then derived from the resulting distribution fitting the position of the main (quasi-Gaussian) peak, as indicated in figure 5.2, with the fit covariance matrix providing corresponding uncertainties. The scans were performed on one PMT specimen of types R12199-02 (Hamamatsu) and 9320KFL (ET Enterprises), each.

The signal amplitude, in terms of the mean number of photoelectrons liberated per pulse (see section 3.6 for a detailed explanation of the data processing), was also derived from the waveforms. Mainly, this was done in order to determine a potential center correction for the transit time measurement. Although being less detailed than the scan data presented in the previous sections, due to lack of automation, it agrees with those in terms of the general trend (see figure 5.18, left).

The resulting transit time curves for both PMTs, presented in figure 5.18 (right), feature the expected shape. Furthermore, the data allows to derive the transit-time spread from

---

[1] Not having being automatized, as of now, data taking in pulse mode is a manual, time-consuming, process. Upon successful automation, it might the topic will be revisited in terms of a full surface scan.

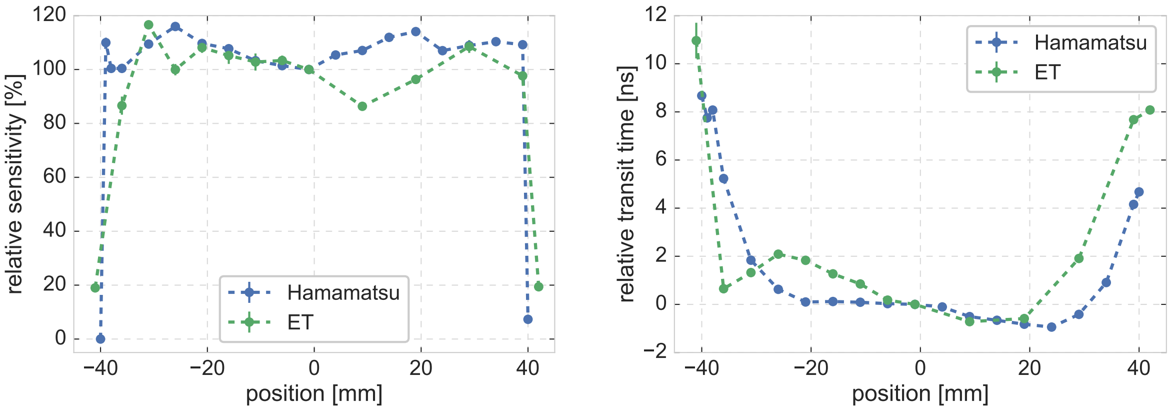

Figure 5.18: **Left**: Relative anode response derived in pulse mode. The results were normalized to the central value. **Right**: Transit time as a function of (radial) position, given relative to the central value. Errorbars indicate fitting uncertainties.

a (weighted) radial integration[1] as follows:

$$\bar{t}_{\text{trans}} = \frac{1}{N}\int t_{\text{trans}}(r)\cdot DE(r)\cdot r\,dr, \quad N = \int r\,dr \tag{5.7}$$

$$TTS = \sqrt{\frac{1}{N}\int (t_{\text{trans}}(r) - \bar{t}_{\text{trans}})^2\cdot DE(r)\cdot r\,dr} \tag{5.8}$$

where $DE(r)$ is the respective anode output relative to the central value, taking the role of the relative detection efficiency.

Neglecting the rather small uncertainties (see figure 5.18), the integration including radii[2] up to 39 mm, results in values of 1.6 ns in case of the Hamamatsu PMT and and 1.1 ns for the ETEL tube, well in agreement with those measured in the standard full illumination approach, introduced in section 5.1.2. Being measured using the same PMT, the Hamamatsu result can also be compared, and found consistent, with the values presented in section 5.3 (figure 5.21) which were obtained using the full illumination approach.

Upon definition of dedicated IceCube-Gen2 requirements, concerning the timing precision of the mDOM, this data[3] can be used to revisit the optimization of the opening angle of the reflectors, introduced in section 10.4.1.

5.2.4 Summary and outlook

In the scope of the work, object of the current section, a viable procedure was found to assess PMT response uniformity in detail. The measurements yielded some insight in the

---

[1] Unlike in the full illumination approach, the value derived by this method does not require correction for the timing uncertainty of the light source output.

[2] Choice was made based on the data quality. At larger radii the identification of the main peak of the transit-time distribution was problematic.

[3] Or rather a more detailed scan of the transit time, possible once the data taking process in pulse mode has been fully automatized.

degree of non-uniformity as well as its reasons. In addition, the results of the detection efficiency and quantum efficiency scans provided a benchmark to test simulations, such as the Geant4 mDOM model by the author (see section 10.3.1) and the sophisticated KM3NeT simulation by C. Hugon [152, 152], who was also supplied with the results.

Yet, there was also found to be room for improvement of the experimental approach. Potential improvements include:

- utilization of a **$x/y/z$ scanner**, allowing for a constant distance between light source and PMT surface, following the curvature of the entrance window, to ensure uniformity of light spot at all positions,
- use of different **photon wavelengths** to study their impact,
- measurement under variable photon **incidence angles** (ideally allowing to retrieve the response at each position under all possible angles),
- introduction of **absolute calibration**[1] to additionally derive the actual values of detection and collection efficiencies,
- improvement of angular and spacial **mounting precision**, as well as
- the employment of **low-noise steppers**[2].

As mentioned earlier, the discussed experimental setup was of temporary nature and had to be dismantled, as core components were used in other setups or were only borrowed from other institutes[3]. Consequently, not all identified issues[4] could be addressed. The main factors limiting the informative value of the results, were positioning and pointing of PMT, including the exact knowledge of the PMT center location.

Due to its rather long duration this detailed approach is unfortunately not suited for mass tests. If yet interesting for larger tube quantities, the uniformity of PMT properties could be assessed using a mask (center only vs. full illumination) or a well-calibrated multi-spot LED array[5].

Furthermore, the obtained results did motivate an even more detailed study. The work, including the construction of a high-precision $x/y/z$ scanner, presented in figure 5.19, as well as the investigation of the dependence of the quantum efficiency on position, angle and wavelength of the incident light, is presently ongoing in Münster in the scope of a Master's thesis co-supervised by the author [156].

---

[1] This could either be done using a calibrated reference PMT or by means of a photodiode, if the light intensity and protecting the investigated PMT by e.g. neutral density filters.

[2] Due to noise production the currently used stepping motors needed to be switched off during PMT current acquisition. As the holding torque of the stepper is strongly reduced when powered down, the position of the carriage can, in principle, change due to its weight. Employment of low-noise devices will thus improve the achievable positioning precision. Even though positioning precision had no discernible impact on the presented measurements, it might become important after elimination of other uncertainty contributions.

[3] Special thanks F. Uhlig, M. Pfaffinger (PANDA group, ECAP, FAU) and M. Sondermann (Chair of Experimental Optics, FAU) for their generosity.

[4] For instance, the sensitivity drop in the ETEL PMT measurement with the collimator-equipped fiber. Or whether the observed asymmetries are real properties of the PMTs or mere artifacts of poor positioning.

[5] As was done e.g. by the GRAPES-3 collaboration [155].

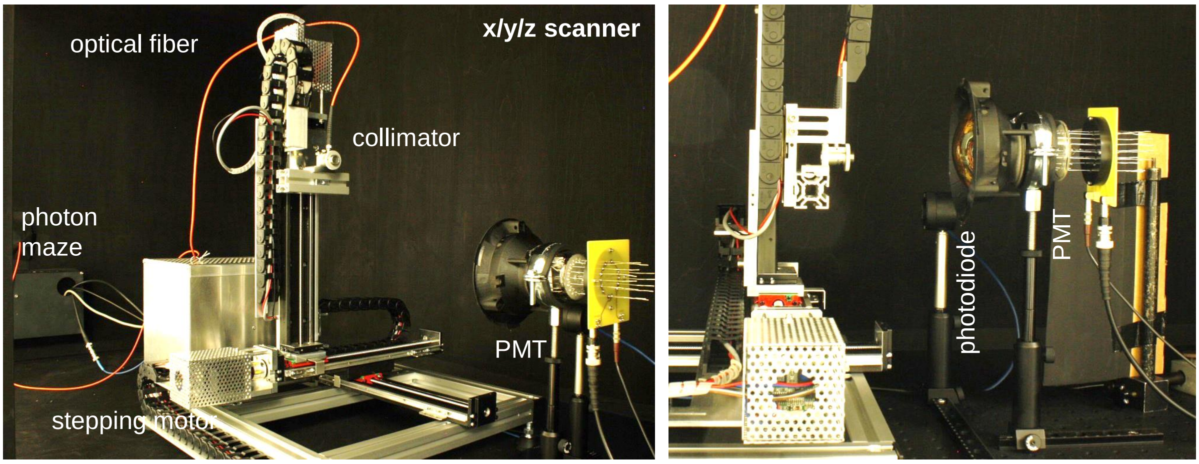

Figure 5.19: Newly constructed precision $x/y/z$ scanner for detailed PMT characterization in Münster, featuring main components. Pictures courtesy of the IceCube Münster group.

5.3 Low temperature performance

As PMTs are to be used in the ice of Antarctica, their performance at low temperatures is of utmost interest. A low-temperature setup was developed in the wake of a detailed dark rate characterization, which is discussed in detail in section 6.4. Modifications, namely the addition of a diffusor-terminated optical fiber guiding the output of the fast-pulsed LED source into the aluminum box located inside the climate chamber[1], allowed to also use it to assess other key PMT properties, that is to say gain, transit-time spread, as well as the afterpulsing probability, as a function of temperature. The respective measurement techniques were identical to those introduced in the corresponding subsections of the general KM3NeT PMT characterization (section 5.1).

A specimen[2] of the R12199-02 HA PMT by Hamamatsu was tested. The PMT was supplied with negative high voltage using a passive resistor base. Illumination was at a level of ~ 0.1 photoelectrons per pulse for the measurements of gain and TTS, while ~ 0.8 in case of afterpulsing. A low-noise amplifier[3] featuring a gain of ~ 10 was used to pre-amplify the signals[4]. The tests were performed at ambient temperatures[5] ranging from 18°C to -45°C.

In general, the tested tube complied with the above-introduced (KM3NeT) quality parameters (see table 5.1) throughout the examined temperature range. At the nominal **supply voltage** ($U_{\mathrm{PMT}} = -910\,\mathrm{V}$), specified by the manufacturer to provide a gain of $3 \cdot 10^6$, the PMT actually exhibited a gain of $4.1 \cdot 10^6$ (see figure 5.20, left). While **afterpulsing probability** and the **transit-time spread** were not significantly affected by cooling, as shown in figures 5.22 and 5.21, respectively, the **gain** was found to rise

---

[1] Resulting effectively in a temperature-controlled version of the setup presented in figure 5.1.

[2] Due to the slowness of the cooling process and pulse-mode data processing, as well as the limited space inside the climate chamber, no mass tests, comparable to the KM3NeT campaign, have been conducted so far. The ongoing construction of large-volume, low-temperature test facility by the IceCube group in Aachen (based on a refrigerated truck container) might change that in the near future.

[3] Type ZX60-43+ by Mini-Circuits [157]

[4] Actual amplifier gain was determined to be 13.2 ± 0.1.

[5] The actual PMT temperature was estimated by a sensor attached to the metallic PMT mount.

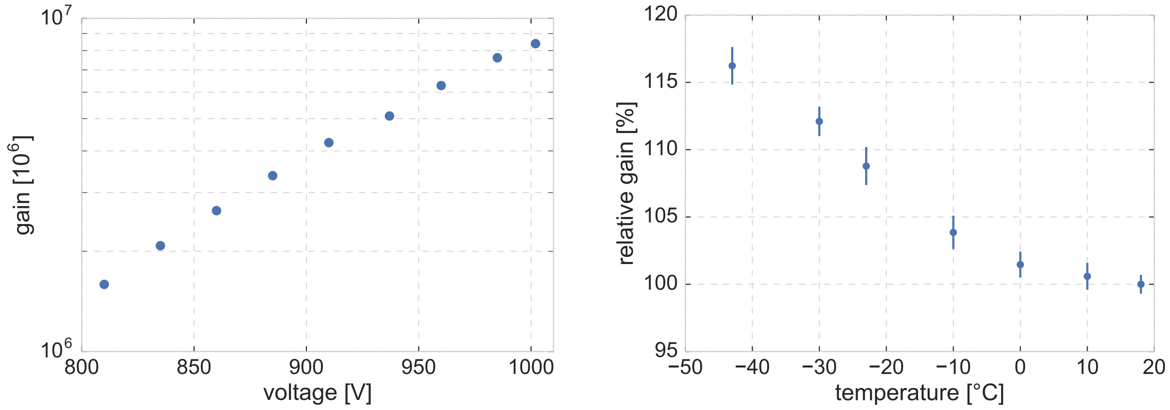

Figure 5.20: **Left**: PMT gain as function of the supply voltage. Uncertainties are smaller than data point markers. **Rigth**: Relative gain as a function of temperature, using the room temperature (18°) value as reference. Errorbars represent fit uncertainties.

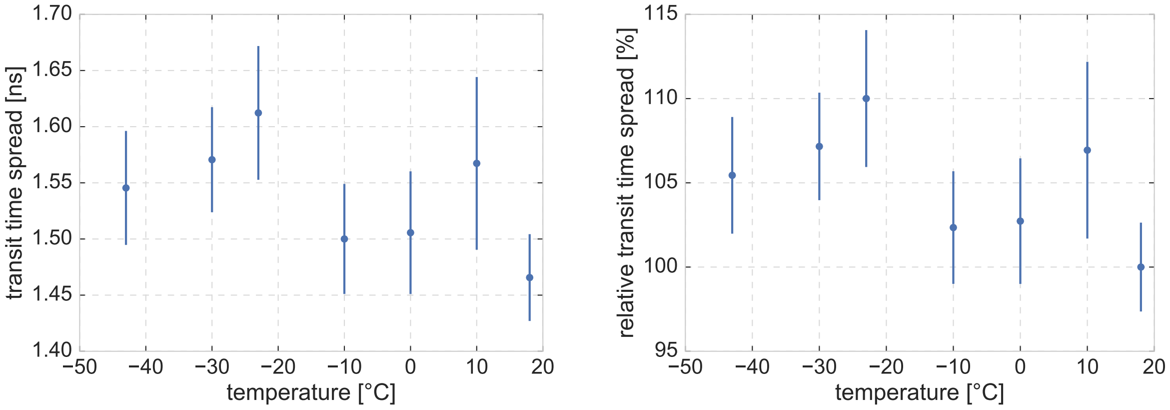

Figure 5.21: Transit-time spread as a function of temperature, presented in terms of the absolute values (**left**) as well as relative to the room temperature result (**right**). Errors were derived form a fit of the main peak position of the transit time distribution using a Gaussian (see figure 5.2).

with decreasing temperature, reaching, at the lowest measured temperature (−43°C), an increase of $\sim$ 15% compared to the room temperature value. A plot of this behavior is presented in figure 5.20 (right). Consequently, the observed rise in **dark rate**, reported in detail in a dedicated chapter (section 6.5, see in particular figure 6.10), can, at least in part, be attributed to this feature, effectively lowering the amplitude applied threshold. The actual extent of the impact of temperature-induced gain variation on the dark rate is discussed in more detail in the dedicated section 6.5.

Consultation of literature suggests that a gain variation with temperature is to be expected for bialkali PMTs, with some ambiguity, however, concerning the trend: On the one hand, cooling is argued to enhance quantum efficiency[1] via suppression of optical phonon generation in the bulk cathode material, thus increasing the probability to emit

---

[1] A property not measured independently in the scope of the low temperature study.

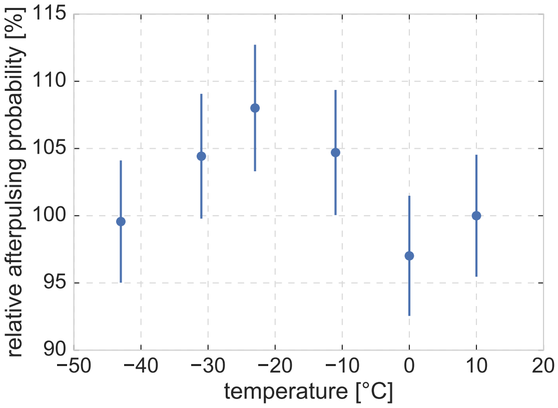

Figure 5.22: Afterpulsing probability as a function of temperature. Values are normalized to the probability measured at 10°C. Errorbars indicate statistical uncertainties (based on $\sqrt{N}$ errors).

Figure 5.23: Temperature dependence of the output amplitude. Results are normalized to the value measured at 10°C. Errorbars indicate fitting uncertainties. The outlier data point at room temperature is considered an effect of the light source not having reached its temperature regime of stable operation.

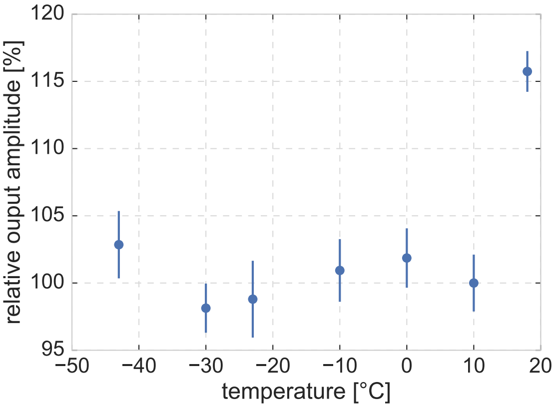

photoelectrons, as well as the secondary emission coefficients of the dynodes, directly linked to the gain (see section 3.2), predicting an increase [158]. On the other hand however, a drop of the gain at low temperatures is reported [159], attributed to changes of resistance (of the cathode material as well as the dynodes) which, modifying the electric field configuration, deteriorate the collection efficiencies[1] between the dynodes, also linked to the gain via equation 3.7. Notably, an increase of the dark rate at low temperatures, following an initial decrease, is reported in both cases.

An idea on the (collective) temperature variability of quantum and collection efficiencies can be obtained examining the PMT's output amplitude in terms of the mean number of photoelectrons per pulse, presented in figure 5.23. Derived from a fit of the charge distribution independently of the gain (as introduced in section 3.6), this parameter is a function of the quantum efficiency, the collection efficiency (of the first dynode) as well as the intensity of the input light. No significant temperature dependence could be observed[2].

Even though further measurements, including a quantum efficiency characterization at low-temperatures, will be beneficial for a better understanding of the involved mech-

---

[1] This mechanism is also supposed to impair output linearity, which was not investigated in the current study.

[2] Of course, the possibility remains that an increase of quantum efficiency is exactly compensated by a simultaneous decrease of the collection efficiency. Also the light source output is not exactly stable in time, as introduced the previous chapters (see figure 5.9).

anisms, no “show-stoppers” were found concerning low-temperature operability of the tested PMT type.

5.4 PMT choice for the mDOM

As the multi-PMT module development for IceCube-Gen2 began as a spin-off of the KM3NeT effort, the three-inch PMTs developed for the Mediterranean are also natural candidates for the mDOM project. In particular since the characteristics of these tubes are compatible with key PMT properties found suitable for the construction of IceCube[1] (see [111] for properties of the IceCube PMT). Original IceCube-Gen2 quality requirements have yet to be defined, however.

In the current stage of the project the Hamamatsu R12199-02 (in a HA-insulated version, see section 3.8) is considered the PMT of choice for the upcoming prototype construction, having been shown to perform in compliance with the quality specifications not only at room temperature but also in realistic operation conditions.

Tubes by alternative manufacturers, such as the type 9320KFL by ET Enterprises, will be further investigated and potentially used in later versions of the optical module. Featuring larger photocathode areas their employment will allow for a substantial enhancement of module sensitivity, as demonstrated in section 10.4.2.

---

[1] Although, having different sizes the PMTs are not directly comparable.

6 Dark rate investigations

In absence of bio-luminescence, as well as of radioactive decays from potassium isotopes, in the ancient glacial ice of Antarctica, the optical module itself is the main source of background. Knowledge of the dark rate is therefore important to estimate the overall background rate and potentially search for counter-measures. The dark rate of PMTs inside an optical module is expected to increase with respect to a bare PMT, mainly due to additional radioactive decays in glass and gel of the module. Secondary particles of these decays give rise to optical photons due to

- **Cherenkov radiation** emitted by charged secondaries and
- **scintillation** in the glass,

as presented in more detail in section 3.8. The use of reflectors, effectively being conductive objects at floating potential, was also expected to further increase the rate.

Any attempt to quantify the overall effect, as well as the contributions from individual module components, relies strongly on the precise knowledge of the baseline, i.e. the dark rate exhibited by a single bare PMT. Apart from being of interest in its own right, e.g. concerning the appropriate settling time before current-mode measurements, the investigation of the temporal development of the dark rate was (originally) motivated by the search for the dark rate baseline.

The desire to know the dark rate behavior in realistic conditions, comparable to the final situation in ice, also demanded measurements at ambient temperatures as low as $-50°$C.

Findings concerning the dark rate are presented in this chapter, alongside with resulting design decisions concerning the layout of the mDOM. The corresponding measurements were carried out by the author, but also by M. Ivren and J. Bloms, in the scope of their respective Bachelor's theses [160, 161].

6.1 General experimental setup

As mentioned earlier (see section 5.1.4), the "canonical" approach to dark rate, in the scope of PMT characterization for the KM3NeT neutrino telescope, was to manually record the number of pulses per time period exceeding a certain amplitude threshold (usually ~ 0.3 photoelectrons) after a settling time in a dark environment of one to several days.

This technique is naturally not a viable solution for long-term monitoring of the dark rate behavior lasting for days (or longer). Measurements were therefore performed by means of a remote-controlled digital oscilloscope[1]. The dark rate was retrieved using the "trigger-time" function[2] of the oscilloscope in conjunction with the "hold-off" option to delay signal acquisition by a preset number of triggers. Average trigger time $\Delta t_{\mathrm{trig}}(t)$ and the number of triggered events $N_{\mathrm{hold-off}}$ were recorded automatically and stored together

---

[1] Model LeCroy waverunner 6100. Same device used to record waveforms for gain and timing precision measurements of PMT prototypes.

[2] This function returns the time difference between the current and the last triggering.

with the time of acquisition t, allowing to calculate the mean dark pulse frequency $f_{\mathrm{dark}}(t)$ as

$$f_{\mathrm{dark}}(t) = \frac{N_{\mathrm{hold-off}}}{\Delta t_{\mathrm{trig}}(t)} \tag{6.1}$$

Assuming a Gaussian distribution of the measured quantity[1] the statistical uncertainty of the derived dark rate was given by

$$\Delta f_{\mathrm{dark}}(t) = \left| \frac{N_{\mathrm{hold-off}}}{(\Delta t_{\mathrm{trig}}(t))^2} \right| \cdot \frac{\sigma_t}{\sqrt{N_{\mathrm{seeps}}}} \tag{6.2}$$

where σ_t is the standard deviation of the trigger time distribution and N_{seeps} the number of measurements per datapoint.

The validity of this approach was tested using a function generator. With e.g. $N_{\mathrm{hold-off}}$ set to 1000 it was able to reliably reproduce frequencies up to several ten kHz, with discrepancies between set and measured frequency below the 1% level, before starting to be affected by oscilloscope dead-time from data acquisition and processing. Given the fact that the PMTs were optimized to comply with $f_{\mathrm{dark}} < 3\,\mathrm{kHz}$[2] and later $f_{\mathrm{dark}} < 1.5\,\mathrm{kHz}$ (see section 5.1.4), this precision and dynamic range were deemed sufficient for the task.

Being the default tube for mDOM construction, and abundantly available at ECAP, PMTs of the type R12199-02 by Hamamatsu were used in the investigation. All measurements were done in a dark, light-isolated environment. As in the standard approach, the trigger threshold was set to ~ 0.3 photoelectrons (if not stated otherwise). PMTs were operated in pulse mode with the applied voltage corresponding to a gain of $3 \cdot 10^6$. Negative as well as positive polarity of the supply voltage were tested[3]. Durations of the measurements ranged from some hours to several weeks.

6.2 Initial observations

Defining a baseline dark rate proved to be a complex (and time consuming) task. First, the starting value and decay rate were different for the tested specimen, as well as for the same PMT when repeating the measurement. This behavior can however be traced back to differences in initial exposure to light, which could not be reproduced from run to run. After the initial exponential drop of the rate, taking from hours to days and associated with the de-excitation of residual gas taking place (see e.g. figure 6.5), the tested PMTs exhibited a variety of behaviors: Having stabilized at a particular low value, the dark rate rose again, at different rates (for an example see figure 6.1). This rise would then in some cases result in subsequent stabilization at a new (higher) level, but still comparable to the initial baseline. In other cases however, the rising dark rate reached values ranging from several kHz to some ten kHz, exceeding by far the required performance. The dark rate then either stabilized at a very high level of some (tens of) kHz or declined rapidly

---

[1] Which was verified examining the distribution of the trigger times.

[2] It is known to the author that the unit "Hz" is, strictly speaking, only applicable in case of periodic signals and "s^{-1}" is more appropriate referring to the dark rate of a PMT. However it will be used in the scope of this work for the sake of consistency with the jargon established in both the KM3NeT and IceCube collaborations.

[3] The anticipated impact of the choice of polarity is discussed in sections 3.4 and 3.7.

again. In some runs several cycles of increase and subsequent decline could be observed. These combinations of increase and decline were interpreted as a sign of static electricity, with charge accumulating until reaching a maximum value resulting in a break-down.

The particular time development of the dark rate was found to be not reproducible, with the same PMT exhibiting a different combination of the above-mentioned features on each test run. Similar observations were also made by KM3NeT colleagues at Naples investigating the dark rate behavior of the same PMT prototypes [162].

Consultation of literature shows, that an increased and also unstable dark rate are actually to be expected if a PMT is operated with negative high voltage polarity (see section 3.4, and references therein), which was used due to an earlier design decision by KM3NeT. At the time of the measurements the development of a corresponding active Cockcroft-Walton base (see section 7) was finalized and could not been altered.

Poor control of environmental variables is also expected to account for a part of the erratic behavior of the dark rate, in particular for the non-reproducibility of measurements: Neither the temperature nor the humidity of the lab were controlled or tracked during the tests. Changes in both variables are in principle able to affect the dark rate of a PMT (see section 3.8).

From these, rather inconclusive, initial measurements, as well as from literature, the following conclusions were drawn concerning the further developments of dark rate test beds as well as the mDOM:

- Negative PMT voltage is in general a bad choice if high dark rates are an issue.
- If used nevertheless, dedicated measures have to be taken to control the rates.
- A well-controlled environment is needed for reliable baseline determination.

The measurements covered in the following sections were set up along these directives.

6.3 Reduction measures

Upon discovery of the erratic dark rate behavior of the PMT prototypes, a natural next step was the investigation of possible sources, generation mechanisms, as well as, most important from a practical point of view, measures to prevent or reduce the effect. Corresponding measurements were performed by the author, and later M. Ivren in Erlangen [160] as well as by KM3NeT collaborators from Naples [162].

Several potential influences, such as charge build-up at the glass surface or the induction of noise by strong electromagnetic fields (e.g. from the ECAP particle accelerator located close to the lab or strong radio emitters at the Italian site) have been discussed with colleagues and experts from the manufacturers.

While the underlying physics still remain a matter of debate[1], measures were found ex-

---

[1] The physics explanation in the paper based on the Naples results [162] had to remain vague as no comprehensive consensus could be established on the mechanism. Concerning literature the situation is similar, as discussed in section 3.8.

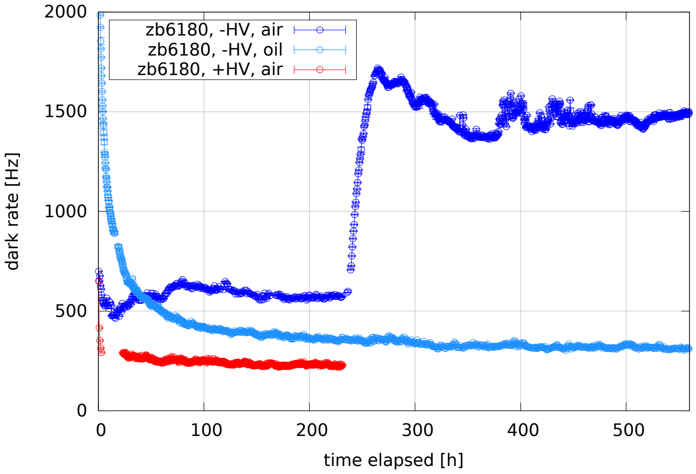

Figure 6.1: Overview of the effect of different measures to reduce and stabilize the dark rate. The same PMT was tested in air and silicon oil supplied with negative voltage, as well as positively fed in air. The plot shows a general behavior representative for all tested tubes. Also note the slower decline of the initial rate in the silicone oil measurement, which was a typical feature. Errorbars represent statistical uncertainties. As no environmental data was logged in the initial setup, it is not possible to exclude that some of the variation is actually caused by temperature change (see e.g. figure 6.9).

perimentally to stabilize and reduce the dark rate.

6.3.1 Insulation

Literature, although being not overly precise on the topic, suggests a beneficial influence of insulation on dark rate stability. A similar conclusion was drawn by the Naples KM3NeT group engaged in dark rate measurements. A general stabilization and reduction was observed by our colleagues if the cylindrical part of the PMT was covered with (several layers) of insulating tape. Attempts to reproduce[1] the Italian results at the Erlangen site however failed to exhibit a clear behavior.

The only clear and reproducible effect was found when the frontal part of the PMTs was immersed into silicon oil [163]. Originally intended to emulate optical gel due to identical optical properties, the oil, as the gel, also features good electric insulation. After the decrease of the initial, excitation-induced, high value, PMTs immersed in oil showed an extraordinarily stable dark rates over long periods of time[2].

In parallel, the Naples group found the coating of PMTs with so-called “tropicalized var-

---

[1] After consultations inside the Erlangen hardware group, build-up of static electricity at the outer glass surface was considered to best explain the observable behavior of repeatedly slowly increasing and promptly decaying dark rate. Insulation of parts of the surface was believed to prevent charge accumulation. As an improvement of pure insulation emerged the idea to add an conductive layer connected to ground potential between glass and insulation in order to allow the charge to dissipate. This attempt failed to produce the desired result but, showing increased erratic behavior, verified unequivocally the literature warning against bringing objects at ground potential close to, or in contact with, a negatively fed PMT, in particular its photocathode.

[2] The initial rate drop was slower however, when compared to bare PMTs.

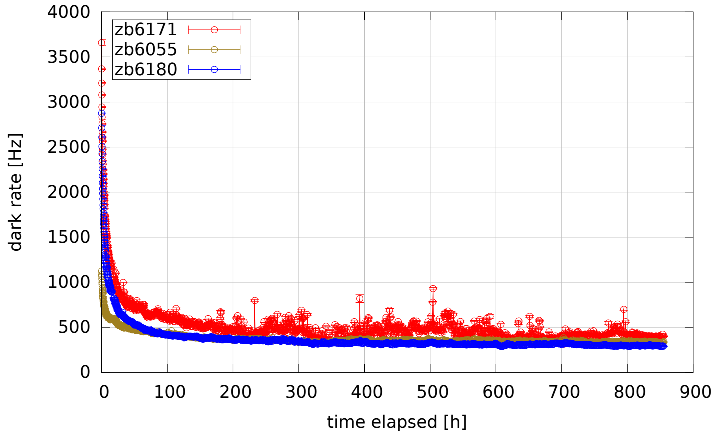

Figure 6.2: Long-term dark rate measurements of PMTs insulated with silicon oil. Labels refer to the respective serial numbers of the tested tubes. Errorbars represent statistical uncertainties. All PMTs were operated at individual (negative) voltage levels providing a gain of $\sim 5 \cdot 10^6$.

nish" [164], an insulating agent used to seal e.g. computer boards intended for application in humid environments, and originally applied to the active base of the PMTs, to be very effective in terms of rate stabilization. Their approach, which by now has been adopted as standard procedure in the production of KM3NeT optical modules, consists in the immersion of the PMT, which has been equipped with a base prior to the coating, into solved varnish up to the rim of the photocathode, leaving a sub-millimeter layer after drying of the agent.

6.3.2 Positive voltage polarity

A passive, resistor-based base was constructed to supply Hamamatu R12199-02 PMTs with positive high voltage, based on the rationales introduced in section 3.4. Galvanic separation, needed in this approach, was done using capacitors. The circuitry layout, together with a picture of the actual device, is shown in figure 6.3. General tests of base functionality showed the expected performance, with the waveforms not deviating from those exhibited by a negative polarity base, showing in particular no discernible distortion by the chosen capacitors. Dark rate levels proved stable, in line with expectations. A typical example of dark rate time development of the same PMT supplied with negative and positive voltage is given in figure 6.5. Nevertheless, upon discussion with the engineers in charge of read-out electronics development, the positive high-voltage option was discarded from the implementation in the mDOM. This decision was driven by problems experienced by the developers of the original IceCube module, which uses a positively-fed PMT, with controlling the droop of the signal baseline caused by the coils used for galvanic decoupling[1].

As PMTs fed with positive supply voltage are in addition supposed to be immune to electric field distortion by objects featuring non-cathode potential in close proximity to it, this configuration appears to be the best choice for the testing of DOM materials for radioactivity affecting the dark rate[2].

---

[1] General information on potential PMT base designs, together with their respective advantages and difficulties, can be found in section 3.4.

[2] This was not done so far, due to the concentration on the impact of low temperatures for which the current positive base is not usable based on the limited temperature rating of the employed decoupling capacitors of −25°C, whereas negative base components are rated for −55°C. A corresponding study is currently ongoing in Münster in the scope of a Master's thesis [165].

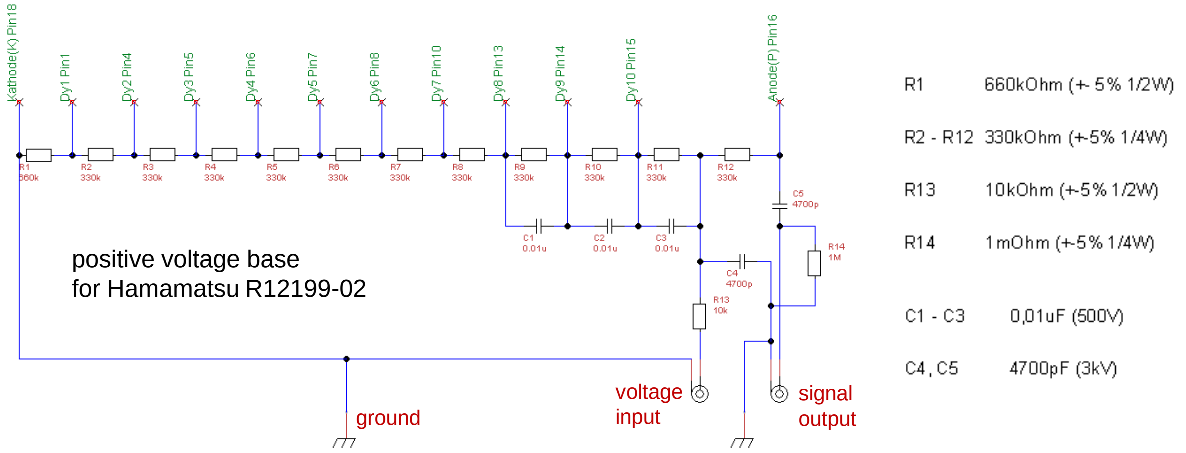

Figure 6.3: Circuitry of the positive supply voltage base produced for dark rate characterization. For the actual device see figure 6.4.

Figure 6.4: Resistive positive supply voltage base. The device was produced based on the circuitry presented in figure 6.3. Note the characteristic large capacitor used for the decoupling of the output.

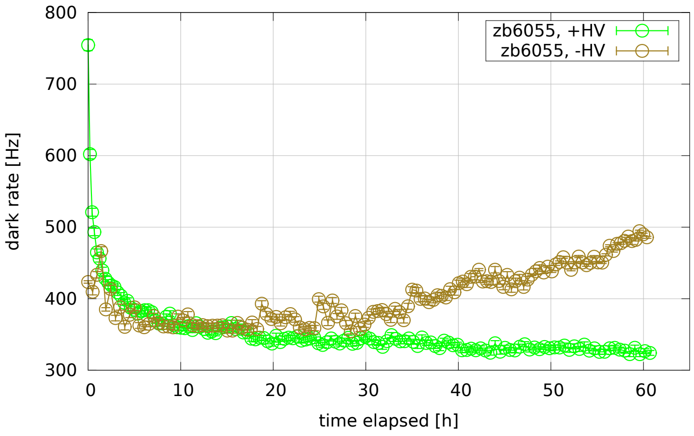

Figure 6.5: Impact of supply voltage polarity on long-term dark rate stability. Label refers to the serial number of the tested PMT. Errorbars represent statistical uncertainties.

6.3.3 HA coating

The problem of dark rate stability of negatively-fed PMTs has also been addressed by PMT manufacturers. As introduced earlier in section 3.8, a common measure is the coating of the tube with electrically conductive paint, usually containing graphite, connected to the electrical potential of the photocathode (see figure 3.18). Two specimen of the correspondingly upgraded type R12199-02 HA by Hamamatsu have been acquired for testing.

As long-term stability measurements gave promising results, and negative voltage supply being the option favored for mDOM development, these PMTs were used in subsequent investigations of the impact of low temperatures and module components, presented in sections 6.5 and 6.6, respectively.

6.4 Controlled environment

The availability of a climate chamber[1] allowed to perform measurements with good knowledge of environment variables. It features a volume of approximately $0.5\,\mathrm{m}^3$ with the temperature adjustable to values ranging from −73°C to 175°C. The device is remote-controllable and enables the definition of temperature time-profiles. Humidity control is however not included, which was deemed problematic, as potentially allowing condensation on the PMT during cooling.

First preliminary measurements placing a PMT inside a lightproof wooden box, filled with silica granulate to absorb humidity, showed an achievable relative air humidity well below $\sim 10\%$ rH, along with the expected substantial decrease of the dark rate with temperature. No effect of the silica on the dark rate was observed[2]. The tests also showed that a tight wooden box is very good at retaining initial heat, resulting in the temperature measured inside the box following the preset chamber temperature with a retardation of several hours.

Based on this experience, a new box, fitting the interior of the climate chamber, was designed: The new layout, based on a commercially available aluminum container, was optimized for heat transfer (see figure 6.6). In addition to having an intrinsically superior heat conductivity due to its wall material, the box features "photon-mazes" instead of the usual cable ports, used in the initial design. This term is used here to refer to an, otherwise light-tight, box with entrance and exit holes featuring internal barriers to prevent the direct passage of light. Only photons scattered and/or reflected multiple times are able to reach the opposite opening. To increase absorption, the inner surfaces of the mazes, as well as all internal surfaces of the box, were lined with a matte black material. The choice of a matte-colored, rough-surface lining (such as black neoprene) also helps suppressing reflection in favor of scattering, resulting in effectively extended photon path lengths, thus additionally increasing the probability of absorption. Cables are guided around the light barriers, making the box a flexible multi-purpose device with no need to initially know all cable standards to be potentially used and install corresponding connectors, and

---

[1] Model 1007C by TestEquity LLC [166]

[2] Indicating no substantial radioactive contamination and making it safe to use in the setup.

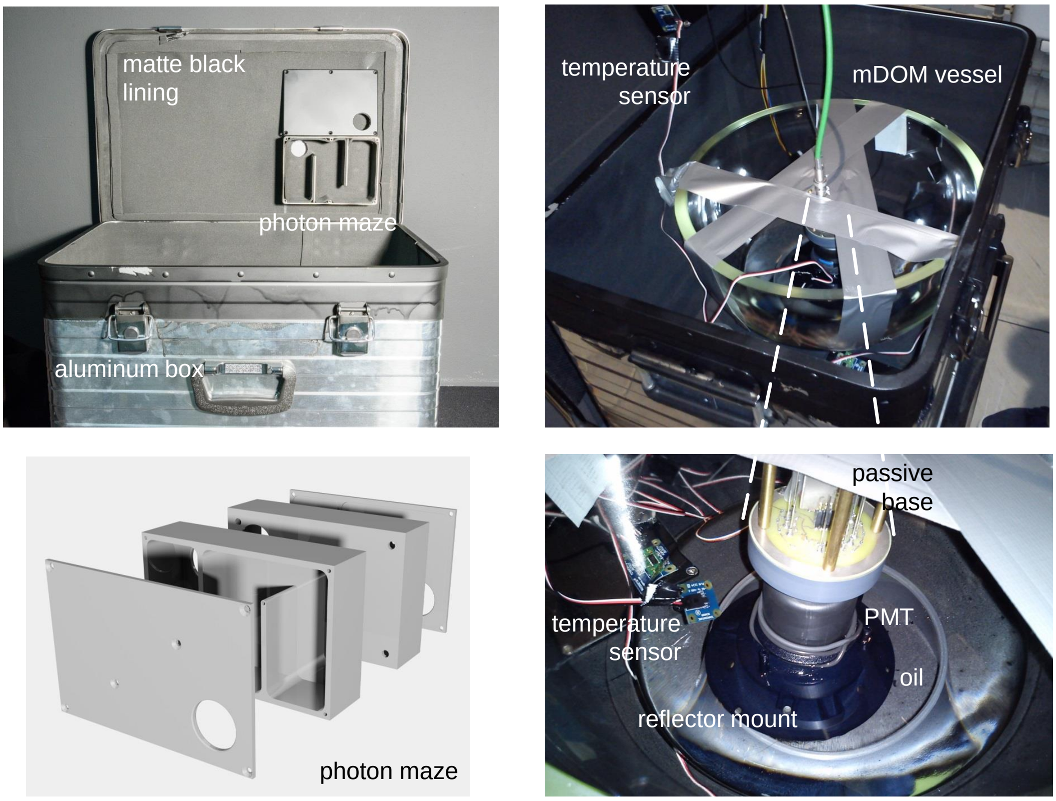

Figure 6.6: Details of the controlled-environment setup for long-term dark rate measurements. To investigate temperature effects, the depicted aluminum box was placed into a climate chamber. The exploded view depicts a more advanced version of the photon maze, produced from anodized aluminum. Figures on the right feature the configuration used to assess the impact of reflector and glass vessel.

enabling the unproblematic utilization of optical fibers. In addition, exchange of air is possible between box and environment. Such mazes were installed in the lower as well as in the upper part of the container, providing the possibility for effective heat removal by air circulation due to convection. In order to monitor and log environmental data, the interior of the container was equipped with four temperature sensors (featuring a resolution of 0.2°C and typical errors of ±0.5°C [167]) as well as a device to measure relative air humidity (to 0.4% rH with typical uncertainties of ±3% rH [168]). The devices are remote-readable using Python scripts, storing data on a standard PC. See figure 6.7 for typical temperature profiles recorded with the setup during cooling and the subsequent warm-up. For means of humidity suppression a vessel for silica granulate was installed in the box. Observations using the humidity sensor showed that this measure limited relative humidity to $< 10\%$ rH at room temperature. During cooling the value never rose above $\sim 40\%$ rH, thus not indicating the occurrence of condensation. The metal walls of the container were connected to ground potential to provide electromagnetic shielding as the initial wooden setup was found to be prone to interference from switching of the cooling device of the climate chamber as well as the halogen lamps of the lab illumination.

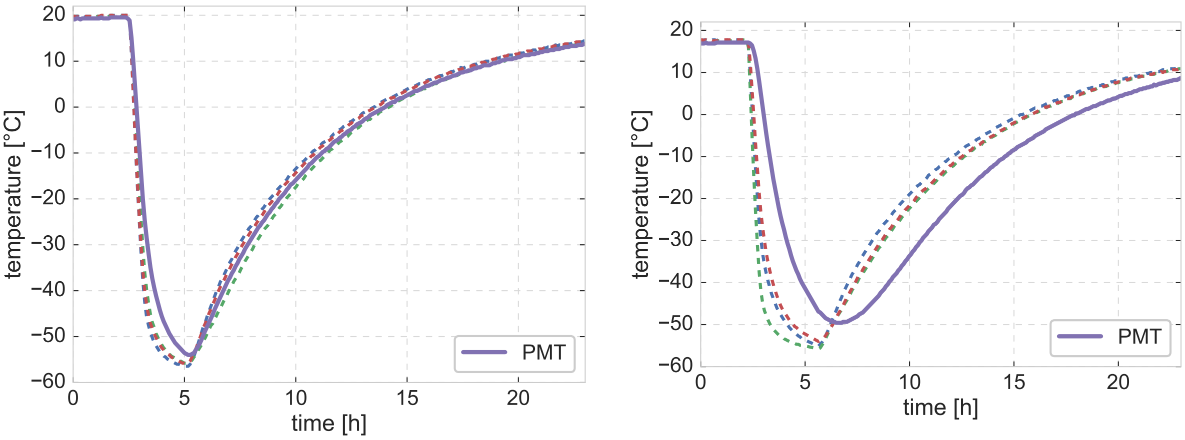

Figure 6.7: Temperatures measured by all four sensors used in the low-temperature performance characterization setup (depicted in figure 6.6), highlighting the PMT temperature (*solid* line), as a function of time during cooling and the subsequent slow warm-up process. Presented is the case of a bare PMT (**left**, see section 6.5) as well as a PMT in contact with a pressure vessel (**right**) discussed in section 6.6.2. Heat capacity of glass and silicon oil introduces a time lag observed in the latter case.

For the quantification of the influence of optical module components on the dark rate[1], a dedicated PMT mount was designed. In the device, the PMT is positioned vertically inside a 3d-printed holder, corresponding to a segment of the holding structure of the mDOM, which also allows to mount a reflector. The device is presented in figure 6.20. The holder, also featuring the possibility to precisely adjust the vertical position of the PMT, is placed inside a Griffin beaker, which can be filled with silicon oil. Thus, samples, of e.g. different glass sorts in question for the production of the pressure vessel, can be positioned at a well defined distance to the PMT, with silicon oil providing optical contact and electric insulation of the cathode[2], emulating the situation in the assembled module. A dedicated mount allows to position one of the temperature sensors in close proximity to the PMT in order to estimate the temperature of the photocathode, which is a crucial parameter for dark rate generation (see section 3.8). It cannot be directly accessed, e.g. via a sensor attached to the surface of the entrance window, as that would affect the dark rate, contaminating the measurement[3].

The combination of climate chamber, maze-equipped container, and PMT mount enabled dark rate measurements in a well defined and controlled environment, eliminating the free parameters present in earlier approaches. Results obtained with this setup are discussed in the following sections.

---

[1] This measurement was the initial reason for the determination the of a dark rate baseline.

[2] Which is a prerequisite for dark rate stability if negative voltage is supplied to the PMT.

[3] As discussed earlier, if operated at a negative potential a PMT is very sensitive to external electric fields, which e.g. arise from objects at ground or undefined potential placed near the cathode.

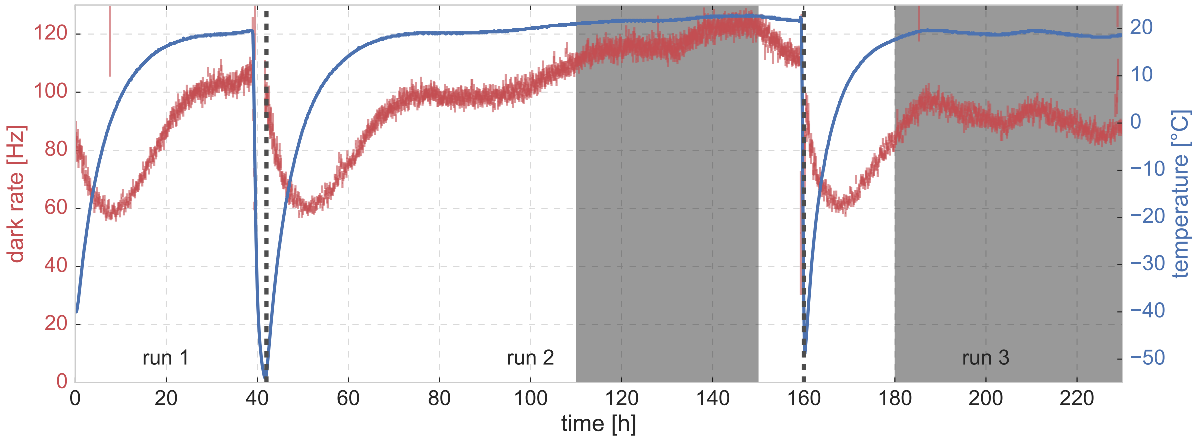

Figure 6.8: Dark rate and temperature of a bare Hamamatsu R12199-02 HA PMT recorded as a function of time. Subdivided into individual "runs", the data was used to derive the rate as a function of temperature (see figure 6.10) as discussed in the text. Errorbars are based on statistical standard errors. *Gray* shade marks regions of pronounced dark rate variations caused by small scale changes in temperature, easily mistaken for instabilities without environmental monitoring. A close-up view of the right region is presented in figure 6.9. The observed outliers, were found to coincide with powering up/down of halogen room illumination.

6.5 Temperature dependence

The "controlled environment" setup introduced above was used to assess the temperature dependence of the dark rate of R12199-02 HA PMTs. In addition, the photocathode was covered by a black polyethylene cap for improved insulation and shielding against photons. Dark count values were retrieved by means of a remote-controlled oscilloscope, as discussed in section 6.1. The provided (negative) PMT voltage resulted in a gain of $4.1 \cdot 10^6$. Signal amplification[1] by a factor of ~ 10 and a low level of electronic noise permitted data taking at a threshold of ~ 0.1 photoelectrons.

In spite of the Faraday cage role of the aluminum box, it was found not possible to perform rate measurements during active cooling of the climate chamber, due to noise generated by the switching of the cooling system. A strategy was adopted to cool down the setup, switch off the climate chamber and measure the dark rate during the slow warming-up of the device. Dark rate and temperature values were logged as a function of time (see figure 6.8). This timing information was used to link both measurements, thus allowing to deduce the dark rate as a function of temperature.

As introduced in section 3.8 (see in particular figure 3.15), at room temperature, thermionic emission of electrons from the photocathode should be the dominant mechanism for the generation of dark rate. Featuring the $T^2 \exp\left(T^{-1}\right)$ dependence of Richardson's law (see equation 3.25), a pronounced drop of the rate is expected with cooling of the PMT. Yet, on the other hand, cooling has also been reported [169, 170] to produce increased rates, following the initial reduction. No general consensus so far exists on the physics reason for this increase in literature, with different mechanisms being suggested, among them:

---

[1] The amplifier was located outside the climate chamber to ensure stable conditions.

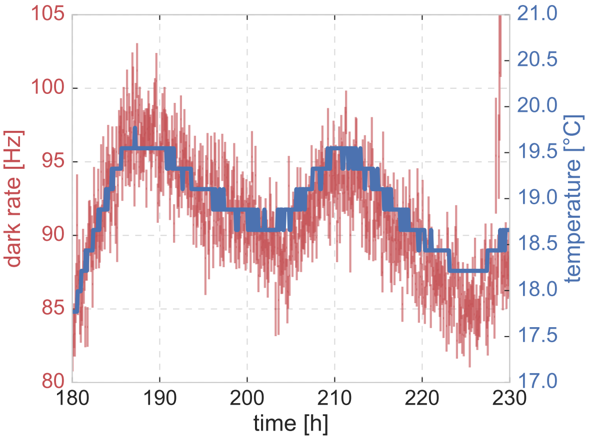

Figure 6.9: Illustration of dark rate temperature dependence: Zoom-in on shaded region of figure 6.8. Discrete steps of temperature measurement represent the 0.2°C-resolution of the sensor. Corresponding uncertainties (∼ 0.5°C) are omitted for the sake of clarity.

- **Scintillation** efficiency of trace elements in the glass envelope of a PMT, such as cerium, increasing with lower temperatures [171]. In this model, the constant rate of radioactive decays in the glass is assumed to translate into an increasing number of scintillation photons, when cooling the PMT.

- Generic **electron trap** mechanisms, featuring the ability to emit or recombine electrons. Assuming an exponential temperature dependence of the recombination, this model will produce increasing emission with declining temperature [169, 170] (and references therein).

- Temperature variability of **PMT sensitivity parameters**. Cooling is reported to impact the quantum and collection efficiencies, as well as the gain and output linearity of a tube [158, 159]. A more detailed overview of the predictions is given in the dedicated section 5.3. Being ambiguous on respective trends of the individual parameters the considered sources agree on a resulting rise of the dark rate.

The latter statement was assessed in the scope of testing the low-temperature performance of the PMT, reported in section 5.3. No indication was found for a variation of the quantum efficiency, but an increase of the gain by some 15% was measured when cooling the PMT to ∼ −45°C. Effectively lowering the applied amplitude threshold, this effect should account for a part of an increased dark rate.

Both former models were derived phenomenologically from experimental data, and agree not only a general increase of the mean rate at low temperatures, but also on an increasing correlation of the dark rate signals: At low temperatures pulses are reported to not occur randomly, but come in “bursts”, with the rate of bursts, as well as the number of events per burst increasing with further cooling. The remaining question is whether these bursts are caused by emptying an electron trap or by scintillation photons.

Based on the information presented above, apart from an initial reduction of the rate due to cooling, the temperature behavior of the R12199-02 HA PMT was a-priori not clear.

The measurement results, presented in figure 6.10, feature the expected initial decline of the count with temperature. A minimum plateau around ∼ 0°C is followed by an increase towards lower temperatures. This temperature behavior was found to be reproducible[1]

---

[1] Which can not be taken for granted in the case of dark rate, as discussed earlier.

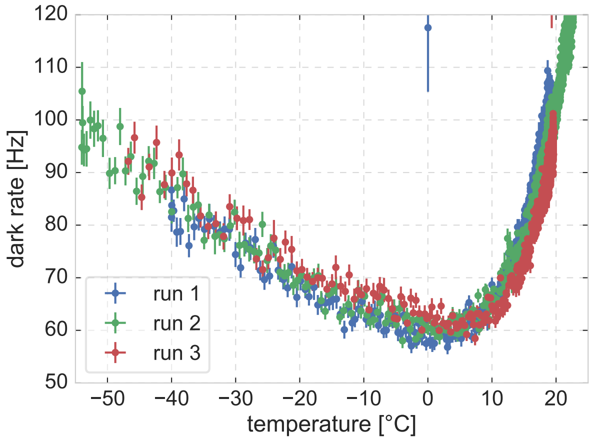

Figure 6.10: Temperature dependence of the dark rate. Curves are based on the data presented in figure 6.8, also defining the runs. Errorbars are based on statistical standard errors of the rate measurement.

in subsequent cooling cycles. Consequently, at temperatures from −20°C to −60°C, as expected in Antarctic ice, the tested PMT features a dark count ranging from ∼ 70 Hz to ∼ 100 Hz. The determination of these values was the main motivation for the measurement.

In addition, the setup allowed to assess the impact of temperature on the charge spectrum of the dark rate, which was derived integrating self-triggered signal waveforms, as introduced e.g. in sections 3.6 or 5.1.1. A trigger level corresponding to ∼ 0.3 photoelectrons was applied[1]. A selection of the spectra, obtained for PMT temperatures ranging from room temperature (18°C) to −42°C, is presented in figure 6.11.

Well in agreement with literature (see section 3.8, in particular figure 3.16), the distributions are dominated by a pronounced SPE peak, featuring a tail of larger charge values, mainly originating from (late) afterpulses [126]. Apart from an overall shift towards larger charges with decreasing temperature, no crucial impact of cooling was identified. The observed shift was attributed to the increase of the PMT's gain (see section 5.3): For instance, the SPE peak position found in the −42°C spectrum, corresponding to 1.14 ± 0.02 "room temperature photoelectrons"[2], is in good agreement with the increase of the gain ∼ 15% measured at this temperature.

The singular pedestal bin observed in the room temperature spectrum (figure 6.11, *blue* curve) is caused by electronic noise. Not featuring the characteristic pulse shape of PMT signals, sharp noise "spikes", sporting only little charge, can exceed the threshold, contaminating the sample. In case of the ∼ 0.1 photoelectron level, used in the current dark rate temperature dependence study, this contamination (at room temperature) amounted to well below ∼ 1% of the overall event count. No pedestal pulses[3] were found at lower temperatures as cooling decreases the noise level and the effective lowering of the trigger threshold (in terms of photoelectrons) only applies to PMT pulses. Consequently, an increasing contribution of pedestal events, caused e.g. by a systematic shift of the signal baseline with temperature, could be safely ruled out as a reason for the enhanced dark

---

[1] Spectra featuring lower threshold settings, including the ∼ 0.1 photoelectron level used in the dark rate study, were also examined yielding equivalent results. The latter spectra are not shown as, due to the dynamic range of the oscilloscope, the "zoom-in" required to apply low threshold levels also resulted in large pulses being cropped, distorting the characteristic shape of the spectrum.

[2] Value and error are based on a Gaussian fit of the SPE peak.

[3] Even for threshold levels as low as ∼ 0.03 photoelectrons.

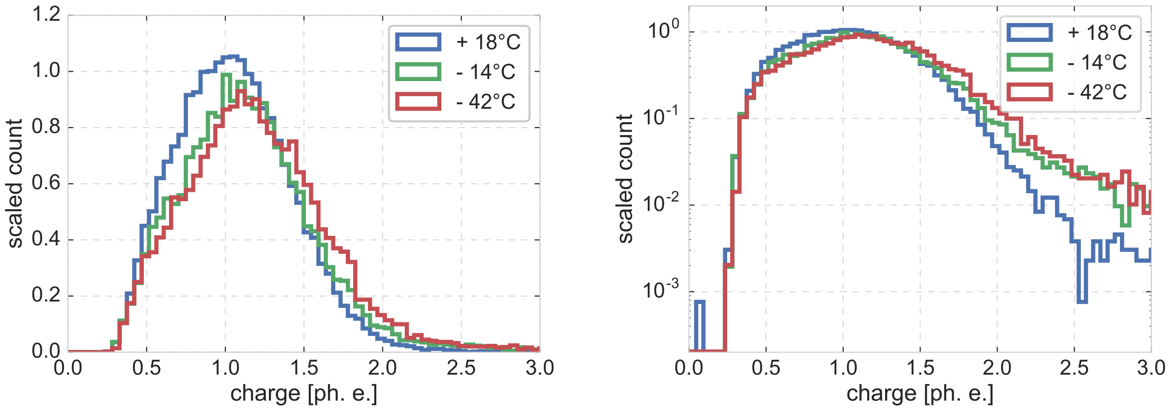

Figure 6.11: Dark pulse charge spectra of a Hamamatsu R12199-02 HA PMT, shown in linear (**left**) and logarithmic scale (**right**) for different temperatures. For the sake of clarity, only a subset of the acquired spectra[a] is presented. The photoelectron scaling, applied to the charge axis, was derived from the room temperature data set[b]. The observable shift towards larger charge values with decreasing temperature is in agreement with the increase of the gain, reported in section 5.3. Remaining spectra were found to follow this trend. The position of the left hand slope of the distribution defines the applied trigger level in terms of equivalent charge. The count was scaled based on the total number of recorded signals which was ∼ 50 000 for all spectra.

---

[a] In total, spectra for seven temperatures values, ranging from 18°C to −42°C, were derived.

[b] See text for a discussion of the “sub-threshold” pedestal entry at room temperature.

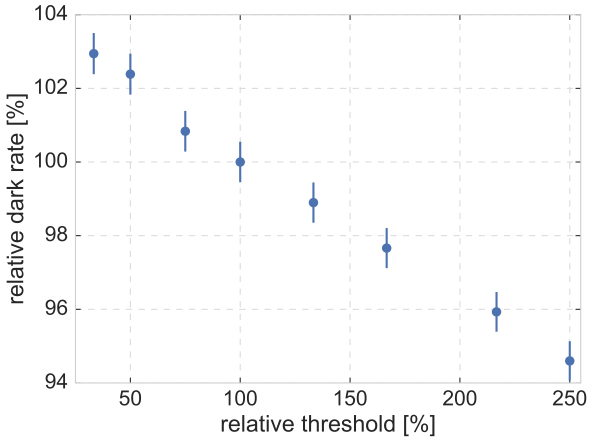

Figure 6.12: Dark rate as a function of the applied trigger threshold. The values were derived off-line from stored dark pulse waveforms (see text for a discussion of the method). Both quantities are given relative to a trigger level of ∼ 0.1 photoelectrons. The linear shape is in good agreement with literature expectations[a] [123, 126].

[a] See also in integral curve in figure 3.16.

rates below ∼ 0°C.

The acquisition of dark rate spectra also allowed to address the question, whether the increased gain is accountable for the observed rise of the dark rate with low temperatures. This study was based on a dark pulse charge spectrum obtained at a temperature of 10°C using a particularly low trigger level, equivalent to ∼ 0.03 photoelectrons[4]. Thresholds ranging from ∼ 0.03 to ∼ 0.25 photoelectrons were applied off-line to the recorded waveforms, using the number of pulses passing the respective condition as a proxy for the expected dark rate. The outcome, presented in figure 6.12, indicates a significant, but minor, influence of the trigger level on the dark rate, inside the considered threshold region. Most notably, the (maximum) observed enhancement of the gain due to PMT cooling of ∼ 15%, which translates to an effective reduction of the threshold by the same magnitude assuming a constant shape of the pulses, induces a dark rate increase on the sub-percentage level only. Consequently this effect cannot account for the behavior presented in figure 6.10.

Comparison of the obtained dark rate dependence on PMT temperature with the experimentally derived rate-temperature relation for cryogenic temperatures, associated with the electron-trap mechanism [170]

$$R_{\text{cryo}}(T) = G \cdot A \cdot e^{-T/T_{\text{ref}}} \tag{6.3}$$

where A is the cathode area, $G = 5\,\text{cm}^{-2}\text{s}^{-1}$ is the specific emission rate found for bialkali photocathodes, and $T_{\text{ref}} = 100\,\text{K}$ is an empiric reference temperature, presented in figure 6.13, exhibits a good agreement, however only if unrealistic assumptions on the cathode area are made, i.e. $\sim 180\,\text{cm}^2$. The actual area of the cathode is $\sim 100\,\text{cm}^2$, with typical tube-by-tube variations on the $1\,\text{cm}^2$ scale.

This observation indicates that the expression is not applicable[5] in the studied case, in contrast to the claimed universal validity for bialkali PMTs. Based on the above-mentioned relation between dark rate and amplitude threshold, the utilization of different threshold levels (∼ 0.3 photoelectrons in the investigations by Meyer, in contrast to ∼ 0.1 in the current study) can be ruled out as an explanation for the discrepancy.

---

[4] Which was the lowermost possible setting, still exceeding the electronic noise.

[5] However, with the discussed study covering a relatively small temperature range in comparison to [170], the possibility remains that a potential validity of the model only becomes apparent at lower temperatures.

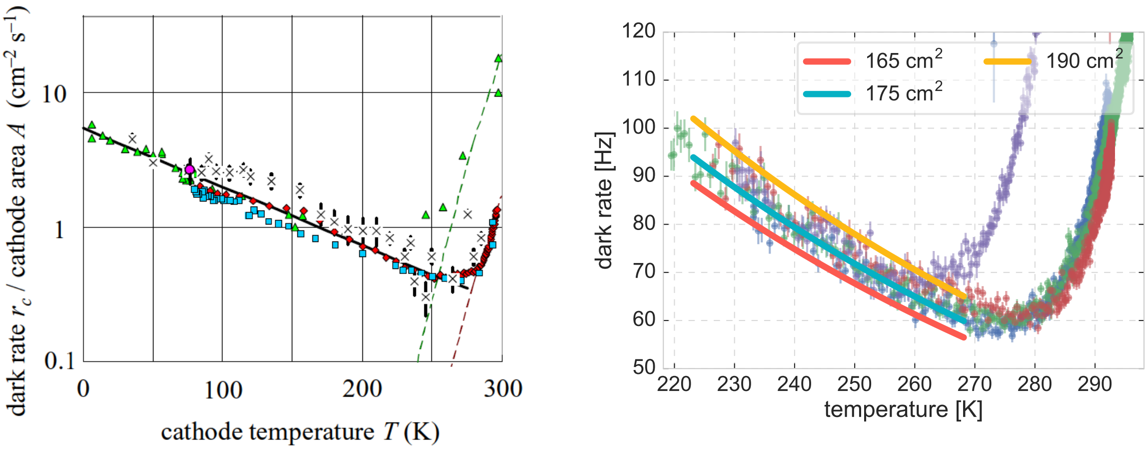

Figure 6.13: **Left**: Dark rate per photocathode area as a function of temperature, shown for several bialkali PMTs (featuring different gains and amounts of initial illumination). An empirically found functional description of the low temperature trend, depending on the cathode area (see equation 6.3), is marked by a solid black line. Figure taken from [170]. **Right**: Application of equation 6.3 to the data of the current study, using different assumptions on the cathode area. A further run, taken after in-situ illumination at low temperatures (*violet* markers), was added featuring a behavior in good agreement with the observations by [170] discussed in the text.

It is worth noting, that a similar measurement, conducted by our colleagues in Mainz on a R12199-02 PMT, produced contradicting results, failing to reproduce the rate enhancement at low temperatures after the initial drop [172]. Consequently there is still room, and need, for further investigations, in particular for tests including a larger, representative, sample of PMTs, as only two specimen have been measured so far.

More detailed measurements, including e.g. the burst fraction[1], and inter-pulse timing, along the layout of the testing campaign by Meyer [169, 170], might also contribute to a better understanding of this “cryogenic emission”, which is of interest in its own right[2]. In the light of (short-term) module development, however, most pressing questions are the true dark rate of the PMTs at low temperatures and its modulation by the surrounding module. The latter is addressed in section 6.6.2.

In the long run, a real understanding of the cryogenic component of the dark rate might also become beneficial for module development, allowing to improve potential reduction and stabilization measures.

6.6 Influence of module components

As mentioned earlier, the original main drive behind the close examination of the dark rate was the idea to quantify its expected increase due to module components. A corresponding

---

[1] This term is used in [169, 170] referring to the fraction of correlated events.

[2] A low-temperature setup of two PMTs facing each other inside a medium allowing photon but not electron travel, such as silicon gel, might be used to distinguish between the above mentioned generation mechanisms.

testing campaign is the subject of the current section. First attempts at measuring the effect will be introduced as well as results of the final measurement presented.

6.6.1 Initial tests

The initial setup design and measurements were done in collaboration with M. Ivren, who also compiled her Bachelor's thesis on this topic [160]. Problems encountered with the setup provided input for the later "controlled environment" approach.

Experimental setup

The experiment was set up to reproduce, as close as possible, the situation of a PMT in actual operation inside an optical module, using one of the cylindrical half-vessels available at that point. A PMT, equipped with a holder segment (see also section 6.4) featuring the possibility to mount a reflector, was positioned vertically, facing the ground, into the spherical part of the glass vessel. The glass vessel was in its turn nested inside a dark waterproof volume (a black bucket customized with a module mount).

The design of the setup itself was not optimized to be light-tight as it was intended to be used inside a walk-in dark chamber, already available in Erlangen.

This setup allowed to test the PMT in various configurations, to asses their impact on the dark rate and test initial expectations:

- Placing the **reflector** was expected to enhance the dark rate, increasing the effective area of the PMT. Moreover, the reflector should also increase the dark rate by being a conductive object at undefined potential in close proximity to the photocathode (see section 3.8)
- Adding a **silicon oil** layer between PMT and the inner surface of the vessel provided electric insulation of the photocathode as well as optical contact between the PMT and the glass. While the insulation should stabilize the dark rate, the improved contact, with relatively small differences of the refractive index, was anticipated to increase it, allowing a larger fraction of photons originating in the vessel glass to reach the cathode.
- From filling the volume surrounding the vessel with **water** an effect similar to the one discussed above for gel was expected, however with the opposite impact on the measurable dark rate: Matching the refractive indices of the vessel environment to that of the glass should suppresses the probability for internal reflection at the glass-environment barrier, allowing more photons to escape the bulk glass and consequently decreasing the number of those reaching the PMT.

Observations

A major limitation of the setup was again the before-mentioned lack of environmental control. Although a general trend, consistent with the expectations, could be observed, e.g. the optical connection of a reflector-equipped PMT to the pressure vessel increased the dark count by $\sim 900\,\mathrm{Hz}$ and the initial addition of water resulted in a drop of the dark rate of approximately 30%, the measurement suffered from a lack of reproducibility and therefore conclusiveness. It was a priori not clear whether the improvement was due to escaping photons or due to cooling by the surrounding water volume. This experience contributed to the development of the fully monitored climate chamber setup introduced in section 6.4.

6.6.2 Glass at low temperatures

A modified version of the measurement was done after the availability of the climate chamber as well as the delivery of the first vessel of the new mDOM design (see figures 4.5 and 8.8). The main goal was to determine the dark rate of a PMT inside the mDOM at low temperatures characteristic for Antarctica.

Experimental setup

The testing was done using the setup introduced in section 6.4, comprising the ventilated, lightproof, sensor-equipped aluminum box inside the climate chamber. One half of the mDOM pressure vessel was positioned inside the box. A reflector-equipped PMT, facing downwards and surrounded by silicon oil, was placed vertically into the glass sphere. To access the temperature of the PMT, one of the sensors was immersed into the oil while the rest was used to monitor the cooling of the setup volume at different locations (for example temperature profiles, see figure 6.7).

All other setup parameters (including supply voltage, amplification factor and trigger level) were identical to the bare PMT study (see section 6.5). Noise generated by the climate chamber during operation again prohibited reliable measurements during cooling, confining the data-taking to the slow heating-up of the setup. Temperature and dark rate were logged independently, linked by the internal clock of the controlling PC.

Results

From initial expectations, as well as from observations with the "bucket setup" (see section 6.6.1), it was clear that the connection to the pressure vessel would increase the dark count of the PMT. For the low-temperature behavior however, based on the mechanisms discussed in section 6.5, there were different possibilities:

- Assuming increasing scintillation efficiency of borosilicate glass, put forward in [171][1], as the main reason for the rise of the dark rate at low temperatures, a trend, similar to the one found for the PMT itself, was to be expected. In fact, the low-temperature part of the curve should have the same shape, scaled up linearly with the total contributing glass mass, while at higher temperatures, where the rate of a stand-alone PMT is dominated by thermionic emission from the photocathode (see section 3.8), a roughly constant offset could be expected.

---

[1] The underlying study is actually based on the observation of such an increase in an AMANDA module, not a bare PMT.

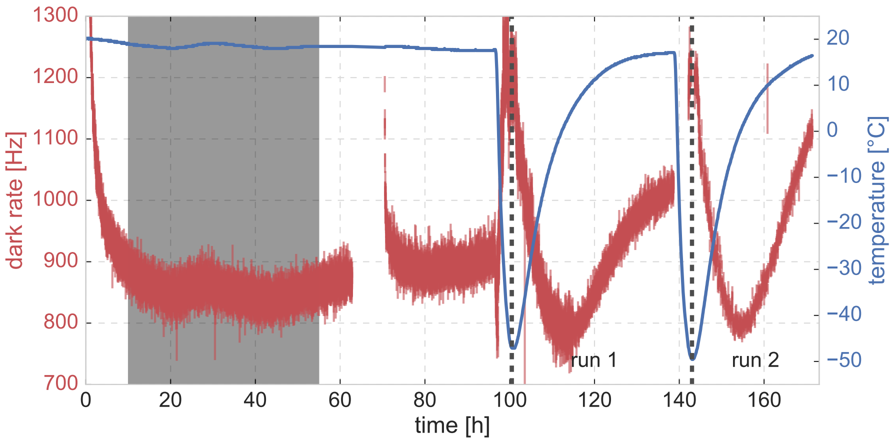

Figure 6.14: Dark rate and temperature of a reflector-equipped PMT in contact with silicon oil and pressure vessel as a function of time. The data, partitioned in "runs", was used to derive the rate as a function of temperature (see figure 6.16). The more pronounced spread of the values in run 1 (and prior to it) is due to the averaging over a smaller number of triggered events. Errorbars are based on statistical standard errors. Shaded area marks the location of pronounced dark rate variations caused by small scale changes in temperature. See figure 6.15 for a detailed view of this region.

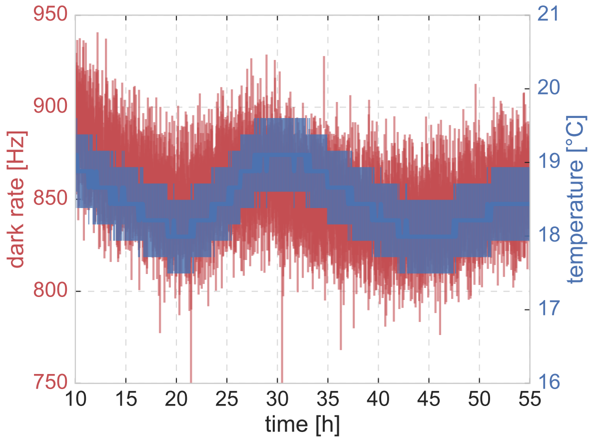

Figure 6.15: Illustration of dark rate temperature dependence: Zoom-in to shaded region of figure 6.14. Discrete steps of temperature measurement represent the 0.2°C-resolution of the sensor. In case of the dark rate errorbars refer to statistical uncertainties while for the temperature they refer to the precision limits as stated by the manufacturer [167].

- If, on the other hand, a temperature-affected electron trap inside the PMT (see [169, 170]) is responsible for the bare PMT behavior, adding glass should result in a constant offset throughout the temperature range.

Evaluation of the data (see figures 6.14 and 6.16) only partially agreed with these considerations: As expected, the dark rate was, in general, higher than that of a bare PMT by ∼ 700 Hz and ∼ 1100 Hz, depending on the temperature. A direct comparison of the dark rate exhibited by PMTs in both setups is presented in figure 6.19. In the low-temperature region (below −10°C) the curve resembles that of the stand-alone PMT scaled up by a factor of ∼ 11, thus favoring the "scintillation theory" (see figure 6.17). However, this is true for the entire temperature range of the measurement. The observed rate appears to only scale with the total mass of the glass. As was the case for the bare PMT, the found temperature dependence proved to be reproducible in consecutive cooling cycles. Both of the above-considered mechanisms do not explain such a trend.

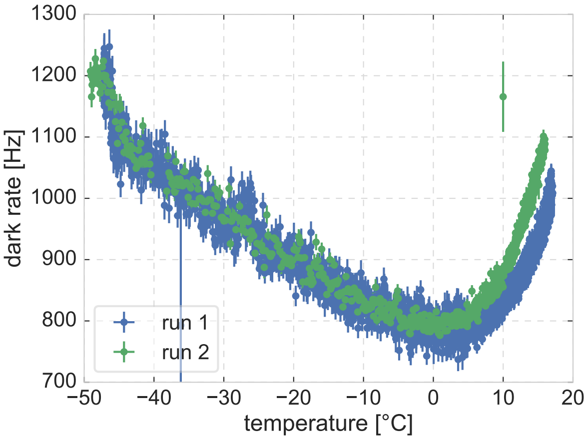

Figure 6.16: Temperature dependence of the dark rate for a PMT in optical contact with an mDOM pressure vessel. Curves are based on, sequenced, data presented in figure 6.14. Errorbars are based on statistical standard errors of the rate measurement.

Figure 6.17: Collective distribution of all dark rate measurement runs, presented individually in figures 6.10 (bare PMT) and 6.16 (reflector-equipped PMT in optical contact with a glass vessel). Bare PMT values were scaled by a factor of 11.5.

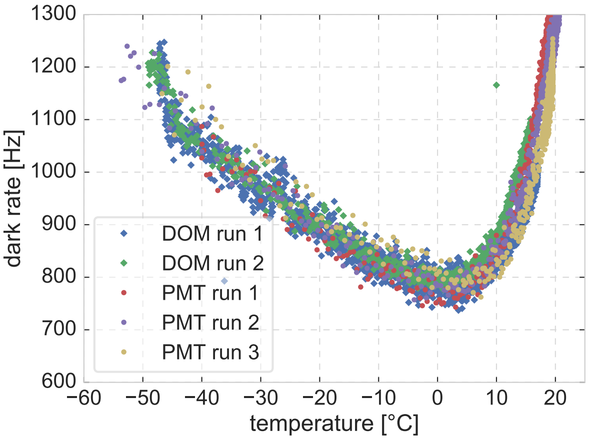

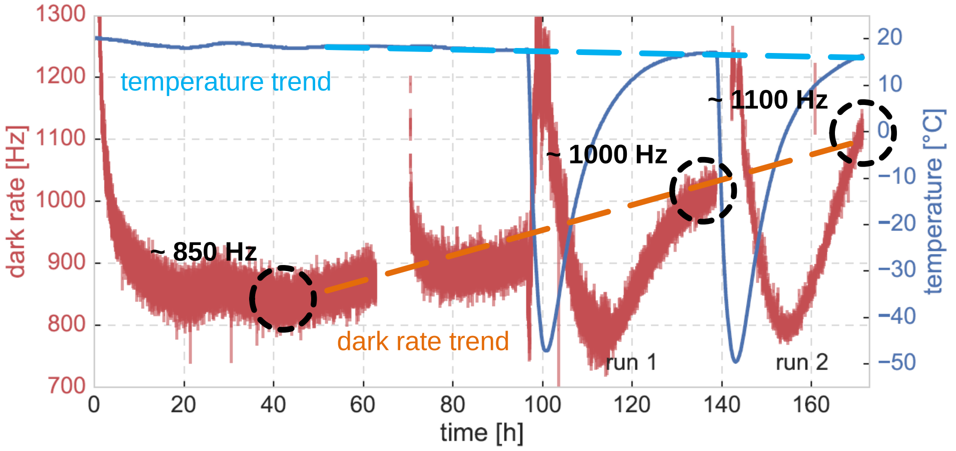

Figure 6.18: Long term trend (*orange*) in dark rate behavior observed in the measurement of a reflector-equipped tube in contact with a glass vessel (see also figures 6.14 and 6.16 for details and explanations). The highlighted values indicate the dark rate at "room temperature"[a].

---

[a] As indicated by the *light blue* line, the room temperature tended to slightly decrease with time, a trend expected to entail a corresponding decrease of the dark rate.

Possible reasons for the observed behavior range from overlooked systematics of the setup[2] to the dark rate actually being totally dominated by the influence of the glass or some unlikely superposition of mechanisms mimicking this effect. In any case, the results call to be cross-checked using a different setup, to eliminate systematic effects. A corresponding study is currently under way in the scope of a Master's thesis in the IceCube group in Münster co-supervised by the author [173].

The time development of the dark rate curve also exhibited an indication for a slow increase of the dark rate, highlighted in figure 6.18. Being most prominent at high temperatures and apparently vanishing for low ones, this subtle increase accounts for the discrepancy observed between the runs at high temperatures in figure 6.16. This trend, potentially indicating a charge-up of the electrically conductive reflector (located at a floating potential), triggered a dedicated study in collaboration with J. Bloms (who also compiled a Bachelor's thesis [161] on the subject) presented in the following section.

Actually, this effect has the potential to account for the peculiar behavior presented in figure 6.17: If the dark rate of the "in-DOM" PMT is in fact $\sim 850\,\mathrm{Hz}$, as indicted by the curve prior to the onset of the trend, rather than the $\sim 1000\,\mathrm{Hz}$ or $\sim 1100\,\mathrm{Hz}$ obtained in the subsequent cooling runs (see figure 6.18), and the low temperature values are indeed not affected[3], the high temperature ($\gtrsim 0°\mathrm{C}$) section of the dark rate curve would become flatter (*red* datapoint in figure 6.19, **right**), resulting in the (almost) constant contribution

---

[2] Such as the influence of non-constant electric properties of base components, condensation of residual humidity, or a potential time lag between the recorded and the actual PMT temperature. The latter seems unlikely however, taking in consideration the pronounced correlation between dark rate and small variations of the room temperature (highlighted in figures 6.9 and 6.15).

[3] Such a behavior would be in line with observations that cryogenic dark rate does not depend on electric field effects [170], see also figure 6.13.

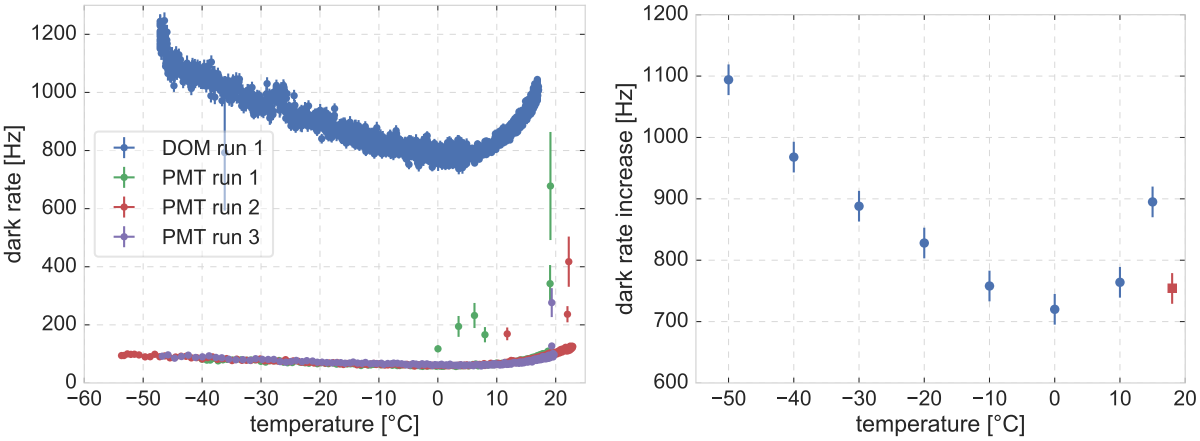

Figure 6.19: **Left**: Direct comparison between the dark rate of a bare PMT (dubbed “PMT”, see also figure 6.10) and a reflector-equipped PMT in contact with a pressure vessel (dubbed “DOM”, see figure 6.16 for details) as a function of temperature. Errorbars are based on statistical standard errors of the rate measurement. **Right**: Increase in dark rate caused by the module components. Values were retrieved comparing the first run to the PMT equipped with module components (found to be least affected by the reflector-related “increasing rate trend”, see figure 6.18) to the average of all bare PMT runs. Errorbars indicate the typical scattering range of the equipped PMT datapoints, being the main source of uncertainty. For a discussion of the *red* data point see text.

from the vessel glass predicted by the scintillation photon scenario[1].

In spite of the open questions, the results of the study provide a first benchmark on the dark rate to be expected from a reflector-equipped three-inch PMT inside the mDOM at Antarctic temperatures.

6.6.3 Reflector potential

In the scope of a Bachelor’s thesis [161] co-supervised by the author, dark rate reduction measures (for negatively fed PMTs) were revisited in more detail. The goals of the study were

- the quantification of the impact of insulation, concerning a potential benefit from **increasing the gel layer**, as well as
- an investigation of the impact of the **reflector potential** on the dark rate, triggered by the observed increase of the dark rate of a reflector-equipped PMT with time (reported in the previous section) as well as predictions from literature (discussed in section 3.8).

The tests were done using the above-introduced Griffin beaker setup (see figure 6.20) and silicon oil as gel substitute in combination with full environmental control (including temperature and humidity). Main results of the study can be summarized as follows:

---

[1] With the reflector potential study (see section 6.6.3) resulting in a viable way to eliminate the observed reflector-induced rise of the dark rate, this question will also be addressed in dedicated measurements in Münster.

Figure 6.20: Griffin beaker setup used for the reflector potential investigations.

- Within a realistic gel layer thickness range (i.e. $\lesssim 1\,\mathrm{cm}$) no significant improvement of the dark rate was observed.
- A reflector at floating potential promotes a slow increase of dark rate, even in a HA-coated PMT insulated by silicone oil. This was interpreted as a steady adjustment of the reflector potential to that of the photocathode via weak electric currents, entailing electric field variations across the cathode which, in turn, increase the rate, as suggested in literature (see section 3.8).
- Placing the reflector at a defined potential, e.g. grounding it, causes, as was expected from earlier results by M. Ivren [160] and the author, a high and unstable dark rate. This peculiar behavior was found to roughly scale with the difference between cathode and reflector potential, a trend also implied in figure 3.18.
- Stable operation is achievable if the reflector (along the PMT surface) is placed at cathode potential.

In general the study was a, more elaborate, confirmation of the lesson learned earlier: Conductive objects in close proximity to the cathode of a negative-fed PMT should always be at cathode potential to prevent unstable behavior of the dark rate.

6.7 Resulting design choices

The study results and rationales, laid out in this chapter, lead to the following design decisions concerning the further development of the mDOM:

- PMTs in the mDOM will be operated with **negative high-voltage**, mainly due to easier read-out enabled by it.
- The gel layer thickness of 2 mm introduced in the baseline design will be kept.
- The (stem) surface of PMTs will feature **conductive coating**, connected to **cathode potential** in order to reduce and stabilize dark rate, surrounded by an insulating sleeve (i.e. “HA coating” by Hamamatsu or equivalent solutions from other manufacturers).

- **Reflectors** will also be connected to **cathode potential** for the same reason.

This configuration will be used in the construction of first prototypes. Final design tuning will then, if needed, be done following extensive (in-situ) testing of the device's performance.

7 Active PMT base

Apart from the main board, which is in earlier stages of development so far[1], the active low-power base, presented in figure 7.2, is the most crucial read-out device. Based on the KM3NeT design developed at Nikhef (a functional block representation is shown in figure 7.1), it inherits several components from the original device:

- On-board **high-voltage generation** is done by means of a Cockcroft-Walton multiplier (see section 3.4). While state of the art commercially available circuits dissipate ~ 50 mW, the Nikhef design was optimized to require 3.3 mW only [140].
- The CoCo is a custom ASIC used for **high-voltage control** and production of the pulses needed to drive the Cockcroft-Walton chain [174].

Also adopted was the general trace pitch layout and component positioning scheme. Optimized for noise reduction, it – for instance – prevents coupling of the Cockcroft-Walton driver frequency into the signal output.

Changes specific to the mDOM base include:

- The **base shape** is defined by space conditions in the most current vessel design. Initially, versions featuring a central hole for the glass process at the rear surface of the PMTs were considered, allowing mounting the base closer to the tube in order to gain space. This approach was vetoed by the manufacturers, based on the fear that soldering that close to the tube might destroy the glass. A compromise using receptacles instead of direct soldering, employed in the resistive bases used for PMT testing (see figure 6.4), was ruled out for cost reasons, but also because an opening in the base would deteriorate the decoupling between high-voltage generation and signal acquisition[2] and potentially entail noise. The most recent layout together with a first prototype of the dedicated mDOM base is presented in figure 7.2.
- A dedicated **pre-amplifier** is under development.
- A **multi-comparator system**, featuring either four or 63 levels (see section 4.3) replaces the original ASIC producing single ToT information (PROMiS [174], see figure 7.1).

7.1 General functionality

In integrated electronics, even minor changes in circuitry can have major impacts on performance, due to e.g. introduction of parasitic capacities or resistances. Crucial for event reconstruction efforts[3] is a precise understanding of properties, as well as limitations, of the base in general, and of its output in particular. Thus, after the redesign, performance

---

[1] The general plan is to use the default IceCube-Gen2 hardware and reprogram the FPGA, see section 4.3.

[2] In the current design respective components are located on opposite sides of the base.

[3] For details on neutrino interaction signatures see section 2.1.1.

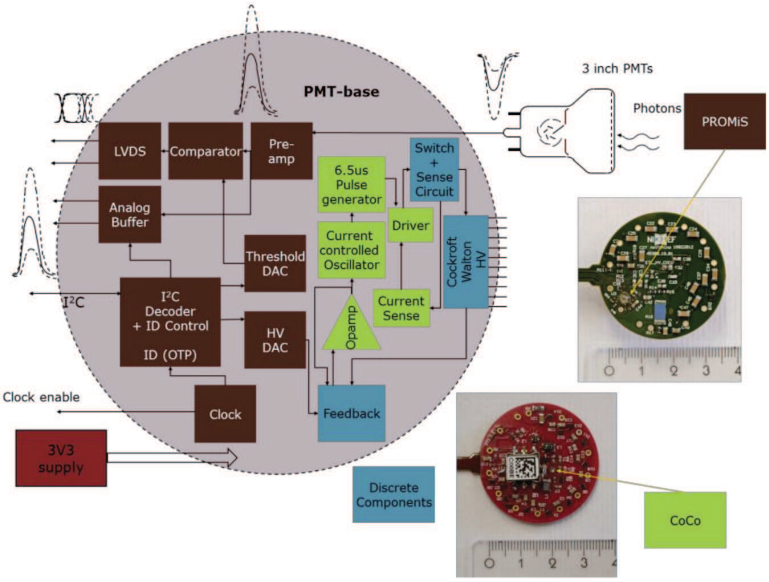

Figure 7.1: Block diagram of the KM3NeT project active base (developed at Nikhef, Amsterdam), featuring main components and functionality principle. Figure taken from [174].

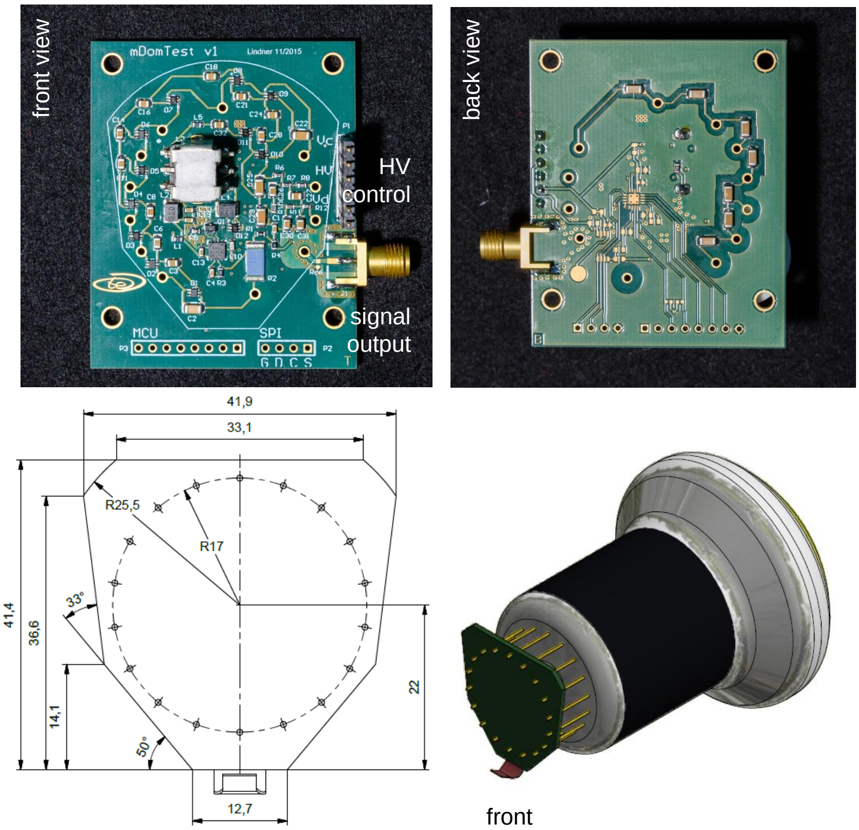

Figure 7.2: Prototype of the active Cockcroft-Walton PMT base for the mDOM. The depicted specimen was used in the tests discussed in this chapter. The technical drawing and stated dimensions refer to the second generation of the base currently under development. Figures courtesy of the IceCube Münster group.

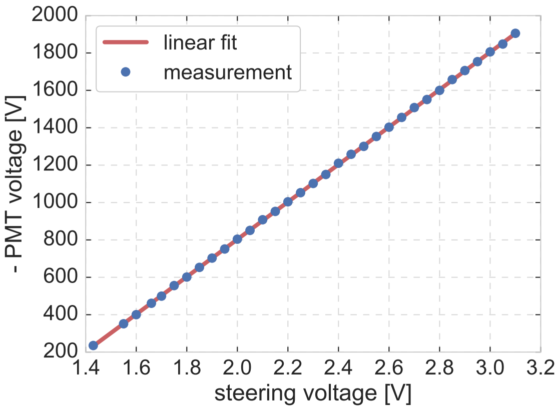

Figure 7.3: Functionality test and calibration of the active base high voltage production: PMT voltage as a function of the applied steering voltage, featuring a linear fit. Fluctuations were measured to be on the order of 0.001 V for the steering voltage and 0.1 V in case of the PMT voltage, i.e. smaller than data point markers. Relative fit-to-data deviation is below 1% in all cases.

needed to be tested and characterized, not relying on previous efforts by the KM3NeT collaboration. As at the time of writing the newly designed base was not finalized and fully operational, only a part of potentially interesting properties could be tested. Nevertheless these initial tests, actually mainly debugging so far, already provided insight and valuable feed-back for the development process:

- General operability of the **high-voltage** generation was assessed at room temperature. Setting the supply voltage via a reference value worked, allowing to determine a (linear) calibration function (see figure 7.3). Voltage increments between individual dynodes were found to be equal and stable on a 1% level[1].
- The newly designed **pre-amplifier** was tested, but found to be noisy and exhibit intense output oscillation after the initial pulse ("ringing").
- Although **stable performance** of base circuitry was simulated down to temperatures as low as −40°C [175], when mounted on a PMT and cooled below ~ -10°C, the base produced a huge excess in dark rate of several 10 kHz. Notably, the shape of the signal waveform was also strongly distorted. This effect was traced back to a coupling of the voltage multiplier supply frequency into the signal output. The base features a low-pass filter to prevent that. It was found that capacitors included in this filter were not stable **under cooling**.

All in all, the main conclusion was that the base still needed revision. Our engineer colleagues at the Institute for Electronics Engineering of the University of Erlangen are currently working on that.

7.2 Output linearity

A test that already worked rather well was the determination of the output linearity. As discussed in section 3.4, linearity is usually limited by choice of the base, and not the PMT itself, which is why it is discussed in the scope of this chapter.

---

[1] The measurement was performed using a high-voltage volt-meter featuring an internal resistance of 1 GΩ, which is still rather low for the task. A custom high-impedance device for more precision is under development at the Institute for Electronics Engineering in Erlangen.

In the given case, the figure of merit was linearity of the output pulse of the base-equipped PMT (prior to shaping and/or amplification) evoked by a short burst, with photons arriving simultaneously[1]. Knowledge of this feature is important, as it defines the maximum achievable dynamic range of the PMT-base compound and consequently the optical module. Also, it provides input for the design of the pre-amplifier/pulse shaper and read-out. In the particular case of the multi-threshold scheme of the mDOM, it is needed to guide the decision on threshold levels.

7.2.1 KM3NeT base

An initial linearity test was done using a KM3NeT base. The results provide input for corresponding mDOM development as well as a benchmark for the performance of the mDOM base prototype.

Experimental approach

The device was mounted on a Hamamatsu R12199-02 PMT operated[2] at a gain of $5 \cdot 10^6$. The "raw" pulse, prior to amplification and shaping by the on-base electronics[3], was fed into a digital oscilloscope[4]. Ideally, the input signal for the envisaged linearity measurement would be provided by a fast linear light source[5], producing pulses of sub-nanosecond duration featuring a linearly adjustable amplitude (number of photons per pulse). As no such device was available, the pulsed LED source[6], introduced in section 5.1.1, was used. Its output, which can be tuned in a non-linear manner, was calibrated using a photodiode featuring linear acceptance[7]. During calibration a high pulse rate was beneficial to produce measurable output on the photodiode. On the other hand, the rate was confined to a range where pulse shape is not affected by a change in frequency, i.e. $f_{\mathrm{pulse}} \leq 2.5\,\mathrm{MHz}$, according to the manufacturer. The final calibration, presented in figure 7.5, was done using frequencies of 1 kHz and 10 kHz, producing measurable light levels placing the light source in close proximity to the photodiode. In this frequency range the amplitude and shape of the light pulse are specified to be constant, which was confirmed by the good agreement of the datasets after scaling the one-kHz values by a factor of ten. A polynomial fit of the obtained curves was used to calibrate the light output level for the subsequent linearity measurement. A prerequisite for this approach is LED source stability on a run-to-run basis, which was found to be the case[8]. The method allowed to

---

[1] Or at least inside a time window significantly shorter than the transit-time spread of the PMT, i.e. some nanoseconds in the case of designated three-inch tubes (see chapter 5).

[2] A dedicated stand-alone test-board was used to control the base via a PC.

[3] Accessed cutting the connection of the anode pin to the base and attaching a coaxial signal cable.

[4] See chapter 5 for details on the device.

[5] Several standard approaches to assess output linearity are suggested in literature [123, 124]. Featuring the use of double pulses of known amplitude relation or radioactive sources. None of them was really applicable in our case.

[6] Featuring a pulse length of $\sim 800\,\mathrm{ps}$ and a wavelength of $(460 \pm 10)\,\mathrm{nm}$.

[7] The employment of a combination of an LED with and an arbitrary pulse generator was also investigated. However, the minimum pulse width of 15 ns, achievable in this approach, was found too long for the purpose, as it did not ensure quasi-simultaneous photon arrival. This resulted in a strongly enhanced apparent dynamic range.

[8] As discussed in sections 5.2 and 7.2.2 this was not the case any more approximately one year later.

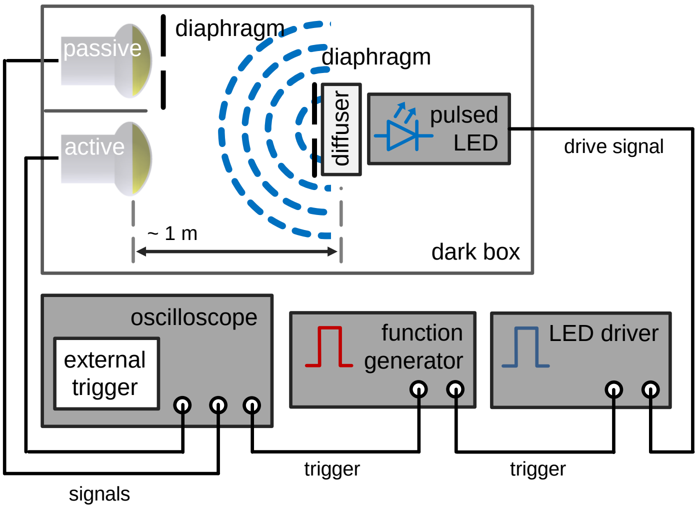

Figure 7.4: Output linearity measurement setup. The depicted passive-base reference PMT was used for mDOM-base characterization only (see discussion in text).

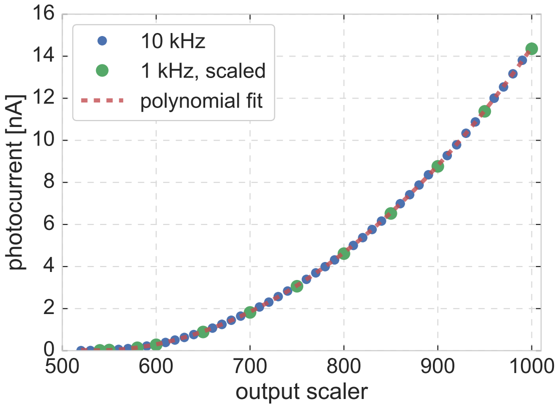

Figure 7.5: Pulsed diode output calibration. The photodiode current as a function of the pulsed light source output tune is shown for different pulse frequencies, with one-kHz data scaled by a factor of ten. Ten-kHz data is fit by a 5th order polynomial function (see discussion in text). Statistical standard errors, measured to be below the ‰-level, are hidden by data markers. Relative deviation between data and fit is below 1% for all data points.

use the once-derived calibration curve on different levels of attenuation of the light source, if needed.

For an illustration of the final setup see figure 7.4.

For the PMT output measurement, a low pulse frequency of $f_{\text{pulse}} = 1\,\text{kHz}$ was chosen based on the known recharge frequency of the high-voltage generator of the base ($f = 15\,\text{kHz}$), in order to prevent pile-up effects (e.g. from afterpulses , see section 3.7). The setup featured a diffusor mounted on the light source to ensure homogeneous illumination of the photocathode and an attenuation device (a diaphragm mounted on the diffusor output). Data taking was done in externally triggered pulse mode, recording PMT signal waveforms by means of an oscilloscope for offline analysis. The amplitude of the output signal was given by the charge derived integrating pulse waveforms.

Results

Results of the test are presented in figure 7.6. The Cockcroft-Walton base of KM3NeT features linearity, in terms of a 10% deviation[1] from an extrapolated linear fit to signal

---

[1] Which is a typical benchmark used in literature. See e.g. [123]

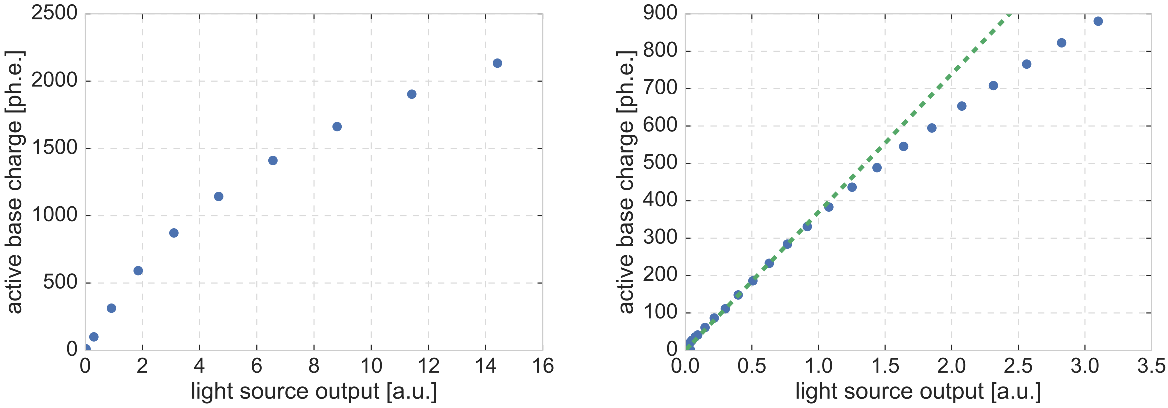

Figure 7.6: KM3NeT base linearity results. **Left**: Output pulse charge of the KM3NeT base as a function of the normalized light source output. **Right**: Detailed scan of the region of interest around a signal level of $\lesssim 500$ photoelectrons, featuring the onset of non-linear behavior. The *green dashed* line indicates a linear fit of the lower output region (charge below 300 photoelectrons). Statistical error bars are hidden by data markers.

amplitudes below 300 photoelectrons, for sub-nanosecond bursts up to ~ 500 photoelectrons. Taking into account the quantum efficiency at the given wavelength, this roughly translates to ~ 2000 photons arriving at the PMT simultaneously.

7.2.2 mDOM base

After completion of the first mDOM base prototype, its output linearity was also to be assessed using the above-introduced setup. Due to a problem concerning the light source calibration[1], another PMT (of the same type, but equipped with a passive resistor base and featuring stronger input attenuation) was used as a reference, simultaneously observing the light output. Both PMTs were operated in pulse mode and read out by means of a digital oscilloscope without amplification. A comparison of the respective output amplitudes (given by the integrated charge of the pules) allowed to identify the occurrence of non-linearity on part of the PMT equipped with the mDOM base, as presented in figure 7.7. Further, both output amplitudes were re-scaled to average numbers of photoelectrons, based on measurements of the respective gain at single photon illumination level, as introduced in section 5.1.1.

As presented in figure 7.8, the new base provides good output linearity, with deviations from the linear behavior, fitted in the low-input region (output charge < 300 photoelectrons), found to exceed 10% only at illumination levels larger than ~ 500 photoelectrons.

As was to be expected, the performance is comparable to that of the KM3NeT design,

---

[1] In an initial test, the calibration derived earlier was found to be not valid any more due to a general decrease of the output level of the pulsed LED. For instance, the output deteriorated to an extent that a new calibration using the photodiode could not be performed in the low-frequency regime of constant pulse shape. According to the manufacturer that kind of aging is to be expected from one year of regular operation having passed between the two measurements.

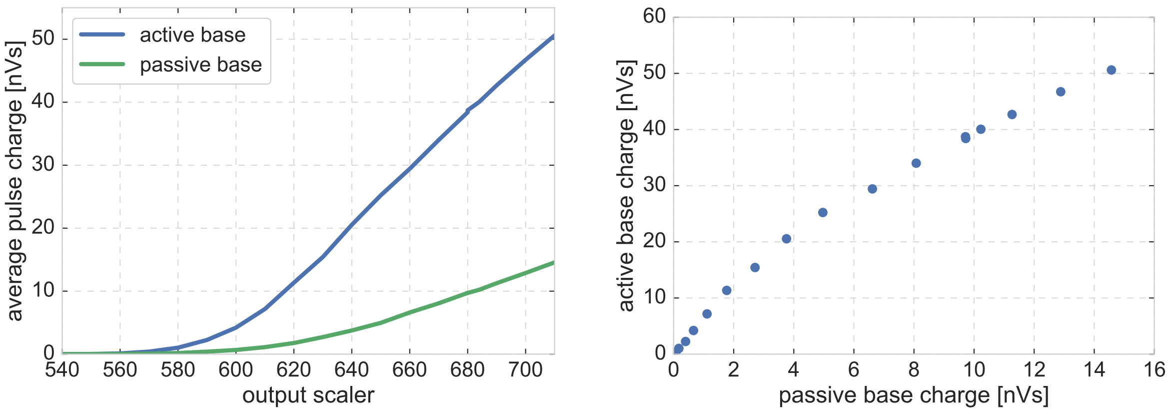

Figure 7.7: mDOM active base linearity evaluation principle. **Left**: Signal amplitudes (pulse charges) of a PMT equipped with the probed active base and a passive base reference PMT, as a function of the (non-linear) light source output tune. **Right**: Active base output as a function of the corresponding output of the passive base, exhibiting non-linearity. Recorded statistical standard errors are smaller than linewidth and markersize, respectively.

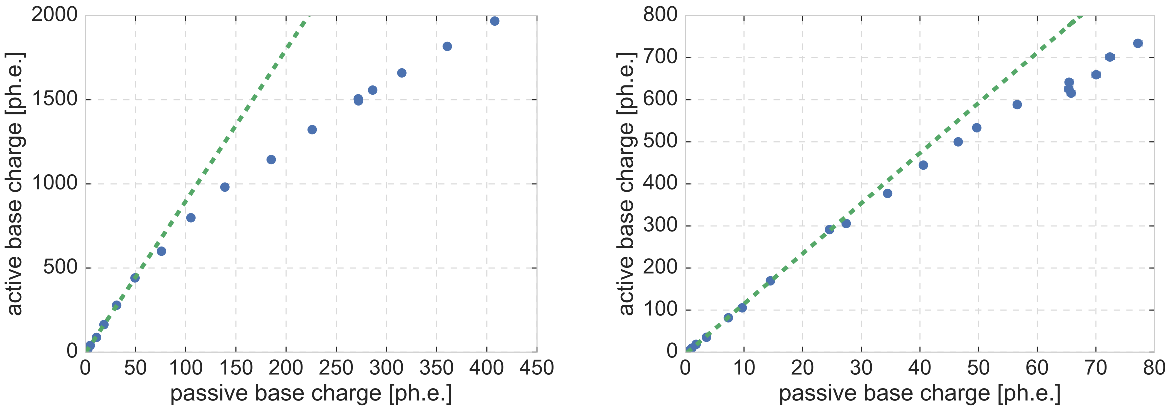

Figure 7.8: mDOM active base linearity results. **Left**: Respective charge outputs of active and passive bases[a] (*blue*), given in terms of the average number of photoelectrons per pulse. The *dashed green* line indicates a linear fit based on datapoints with the active base charge not exceeding a limit of 300 photoelectrons. **Right**: Detailed scan of the region of interest, containing the onset of deviation from active base output linearity (determined to be located around a signal level of $\sim$ 300 photoelectrons). Featuring a linear fit (*dashed green* line) of the lower output region (active base charge below 300 photoelectrons). Statistical error bars (propagated from signal standard errors and gain derivation) hidden by data markers. Scattering of the data points (e.g. in the $\sim$ 65 photoelectron region of the passive base) can be attributed to (potential) fluctuations of the light source output on the timescale of the readout lag between active and passive PMT, and the (actually observed) fluctuations of the active base steering voltage, affecting its gain.

---

[a] The passive-base PMT was used as a reference detector, equipped with a diaphragm to prevent saturation as illustrated in figure 7.4.

demonstrating that no errors, such as of parasitic resistances and capacities, were introduced during the adaptation of the circuitry to the new board shape.

This result (linearity up to 500 photoelectrons produced in less than one nanosecond) is particularly competitive when compared to the standard ten-inch IceCube PMT, featuring a linear output[1] up 31 photoelectrons per nanosecond [111]. Assuming uniform spacial distribution of the arriving photons, the potential overall output linearity of the mDOM can roughly be estimated to be on the order 5000 simultaneous photoelectrons[2]. The finally achieved linearity will however be limited by the setting of readout threshold levels, which still need to be decided upon.

---

[1] Defined as in the current study by a 10% deviation from linearity

[2] This rough estimation is based on the assumption of an equivalent of ten PMTs facing each direction (see discussion of the angular acceptance uniformity is section 10.4.2), and the arriving photons homogeneously illuminating one hemisphere of the module, effectively neglecting scattering. If strong scattering is considered, allowing the distribution of incident photons over the entire surface of the module, the total linearity will rise up to ~ 12000 photoelectrons.

8 Mechanical components

As introduced in section 4.1, the multi-PMT module for IceCube-Gen2 was subject to a number of requirements, imposed by the Antarctic environment as well as the IceCube infrastructure framework, ultimately resulting in the mDOM layout presented in sections 4.2 and 4.3.

The current chapter is dedicated to a detailed coverage of the work that lead to the decisions on the mechanical part of the layout (section 4.2), that is to say the shape and dimensions of the pressure vessel as well as the design and production method of the PMT mounting structure.

8.1 Pressure vessel stability

At the time of initiation of the multi-PMT module development for IceCube-Gen2[1], spherical pressure vessels, originally developed for marine applications, were commercially available in several standard sizes and pressure ratings. Cylindrical vessels were also existent, however none of them matched the initial design specification of $\sim 13\,\text{inch}$ in diameter and a pressure rating of $\sim 700\,\text{bar}$ (see section 4.1).

As the dimensions, in particular the length, of the PMTs[2] intended for the application in the module was pretty much fixed, with only minor changes to be expected without a substantial redesign of the dynode structure, the thickness of the glass was a crucial parameter. It limited the number of PMTs that could be fit into one horizontal layer, thus defining the homogeneity of the solid angle coverage and the total effective area of the module. With the outer diameter considered to be predefined, glass thickness and cylinder height remained the only free parameters.

Before engaging in negotiations with potential manufactures, pressure stability simulations were performed in order to get an estimation of the general viability of the envisaged design and the maximum number of PMTs it could house.

8.1.1 Evaluation strategy

To predict the pressure stability, a strategy based on the so-called maximum stress criterion[3] [176] for the failure of brittle materials was adopted (for illustration see figure 8.3). This approach was deemed applicable, as it was used earlier by KM3NeT colleagues in collaboration with the R&D department of a glass manufacturer to perform a very similar task [177]. According to this criterion, a component will fail if one of the principal stresses[4] σ_i either exceeds the tensile strength σ_t or falls below the compression strength

---

[1] Actually originally for the PINGU project.

[2] See chapter 5 for details on the available PMTs.

[3] Also known as Coulomb, Rankine, or normal stress criterion.

[4] Principal stresses are the eigenvalues of the stress tensor. Usual numbering convention follows ascending strength. From a more practical point of view: In any material subject to a superposition of forces producing normal and shear stresses, which are the entries of the stress tensor, a coordinate system can be chosen, such that all shear stress components disappear, leaving only normal stresses which are

σ_c of the material (negative in the convention used here), which can be formulated in as:

$$\sigma_c < \{\sigma_1, \sigma_2, \sigma_3\} < \sigma_t \tag{8.1}$$

However, the actual values of tension and compression strength for the particular borosilicate glass used for pressure housings, as well as applicable safety margins, were not known to the author[1]. In order to yet be able to make a statement on vessel stability, principal stresses occurring in commercially available geometries when submitted to their respective nominal pressures, were used as a proxy (supposedly with safety margins already included). Dimensions were taken from the websites of the respective manufacturers [178, 179]. These principal stresses were retrieved independently using two analytic models, as well as a fully-fledged finite-element simulation, which is presented in more detail in the following section, allowing to cross-check the respective results.

Two sets of formulae where used for the analytic calculation:

- The most simple approach is referred to as **Barlow's** or **kettle formulae**[2] which can be used to calculate the axial and tangential stresses, σ_a and σ_t, occurring in the material (for meaning of "axial" and "tangential" in this case, see figure 8.1) of a thin-walled cylindrical pressure vessel:

  $$\sigma_a = -\frac{R \cdot p}{2d}, \qquad \sigma_t = -\frac{R \cdot p}{d} \tag{8.2}$$

  where R is the radius of a cylindrical or spherical pressure vessel submitted to a hydrostatic pressure p, and d the thickness of its walls. In case of spherical vessels the axial component applies. Defined e.g. in the industrial standard DIN 2413 [180] it is originally intended for (internal) pressure vessels and limited to cases where the ratio between outer and inner diameter is below 1.2 (or as low as 1.05, depending on the source[3]). As the assumptions used in the derivation of equation 8.2 are agnostic of the sign of the applied pressure, it was included in the study. Due to the fact that $\sigma_a < \sigma_t$, the minimum principal stress is given by σ_a for spheres, while for cylinders it equals σ_t. This also reflects the common knowledge, that spherical vessels are always more stable than cylindrical ones featuring the same wall thickness.

- For a more sophisticated assessment a solution of the **Lamé equations** for the case of thick-walled vessels was used [181]. Relevant for the current application[5] are the expressions for the minimum tangential stress in capped cylinders $\sigma_{\mathrm{t\,min}}$ as well as the

---

called the principal ones.

[1] From online resources, such as

- `http://www.makeitfrom.com/material-properties/Borosilicate-Glass` or
- `http://www.qvf.com/glass-equipment/borosilicate-glass/physical-properties.html`

the values could be estimated to be $\sigma_c \propto -1000\,\mathrm{MPa}$ and $\sigma_t \propto 100\,\mathrm{MPa}$. The reliability of those values and their applicability in the studied case were not clear, however.

[2] Notably in Germany, it is also known as the "sausage-formula", as it vividly reflects the familiar fact, that an overcooked sausage will always rip lengthways.

[3] The latter, more conservative, prerequisite was not met by the geometries under investigation.

[5] The full set of formulae also includes axial, tangential and radial stresses as a function of inner and outer radius as well as inner and outer pressure which can be evaluated at any radial position inside the vessel wall.

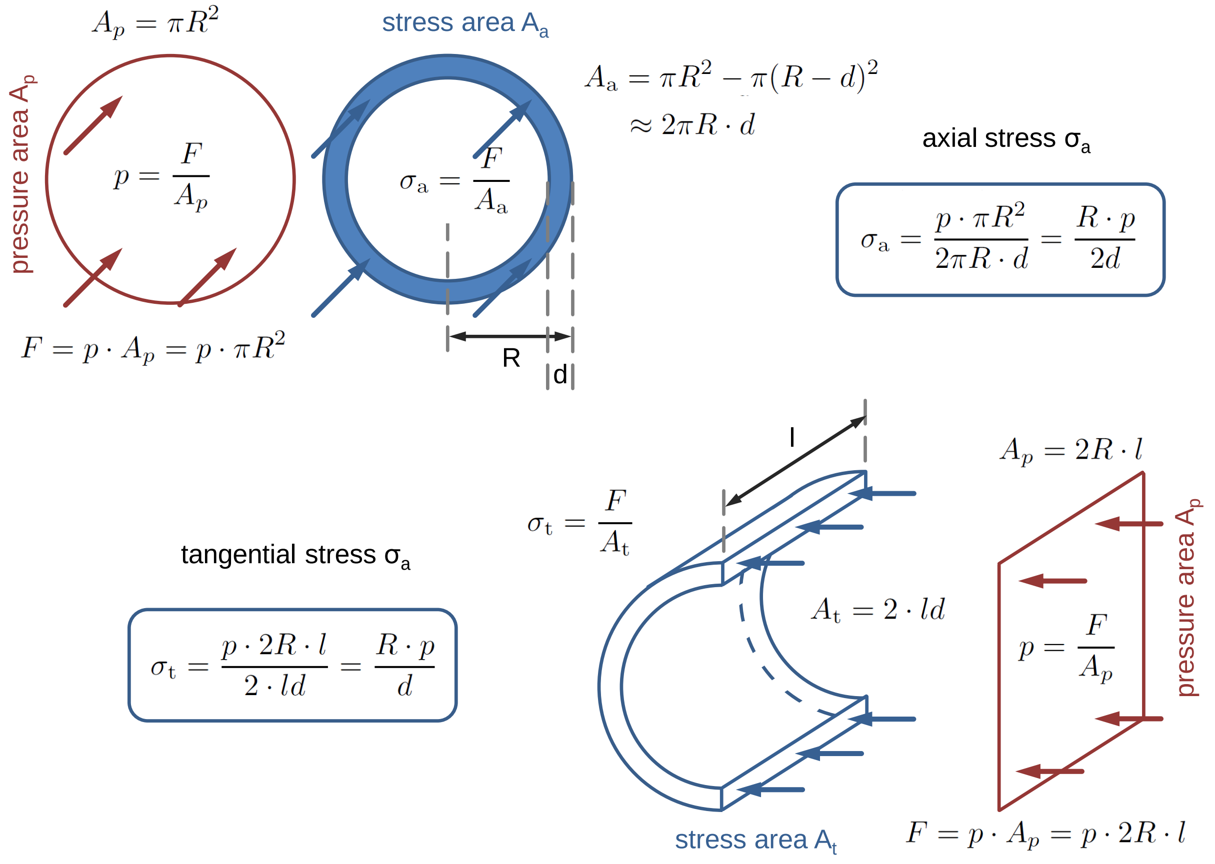

Figure 8.1: Barlow's formulae for axial and tangential stress occurring in a thin-walled[4] vessel subjected to hydro-static pressure.

minimum axial stress for spheres $\sigma_{\mathrm{a\,min}}$ which occur at the inner surface of the pressure vessel:

$$\sigma_{\mathrm{a\,min}} = -\frac{3R_{\mathrm{out}}^3 \cdot p_{\mathrm{out}}}{2(R_{\mathrm{out}}^3 - R_{\mathrm{in}}^3)}, \qquad \sigma_{\mathrm{t\,min}} = -\frac{2R_{\mathrm{out}}^2 \cdot p_{\mathrm{out}}}{R_{\mathrm{out}}^2 - R_{\mathrm{in}}^2} \tag{8.3}$$

where R_{out} and R_{in} are the outer and inner radii of the vessel and p_{out} the pressure at the outer surface.

Furthermore, Lamé equations also allow to derive the contractions of the inner and outer radius of a cylindrical vessel under pressure (ΔR_{in} and ΔR_{out}), as well as the shortening of its length Δl:

$$\Delta R_{\mathrm{out}} = -\frac{R_{\mathrm{out}} p_{\mathrm{out}}}{E} \cdot \frac{R_{\mathrm{out}}^2(1-2\gamma) + R_{\mathrm{in}}^2(1+\gamma)}{R_{\mathrm{out}}^2 - R_{\mathrm{in}}^2} \tag{8.4}$$

$$\Delta R_{\mathrm{in}} = -\frac{R_{\mathrm{in}} p_{\mathrm{out}}}{E} \cdot \frac{R_{\mathrm{out}}^2(2-\gamma)}{R_{\mathrm{out}}^2 - R_{\mathrm{in}}^2} \tag{8.5}$$

$$\Delta l = -\frac{l p_{\mathrm{out}}}{E} \cdot \frac{R_{\mathrm{out}}^2(1-2\gamma)}{R_{\mathrm{out}}^2 - R_{\mathrm{in}}^2} \tag{8.6}$$

where E is Young's modulus and γ refers to Poisson's ratio.

In the case of spherical vessels the following expressions are used, featuring the same naming convention:

$$\Delta R_{\mathrm{out}} = -\frac{R_{\mathrm{out}} p_{\mathrm{out}}}{E} \left(\frac{(R_{\mathrm{in}}^3 + 2R_{\mathrm{out}}^3) \cdot (1-\gamma)}{2(R_{\mathrm{out}}^3 - R_{\mathrm{in}}^3)} - \gamma \right) \tag{8.7}$$

$$\Delta R_{\mathrm{in}} = -\frac{R_{\mathrm{in}} p_{\mathrm{out}}}{E} \cdot \frac{3R_{\mathrm{out}}^3(1-\gamma)}{2(R_{\mathrm{out}}^3 - R_{\mathrm{in}}^3)} \tag{8.8}$$

A discussion of the results, including a comparison between the stress values retrieved with both analytic techniques, as well as the simulation approach, is given in section 8.1.3.

8.1.2 Finite element pressure simulation

A more detailed prediction of the physical behavior can be achieved from a simulation using the Finite Element Method (FEM)[1]. In general, FEM is a numerical technique for finding approximate solutions to boundary value problems for partial differential equations. Characteristic for the approach is the subdivision of large domains, e.g. a complex geometry, into smaller (and simpler) segments, the finite elements, where the underlying differential equation can be evaluated. In the scope of this work an integrated finite-element suite, called COMSOL Multiphysics™[182], was used[2]. The work-flow of a simulation study using this software consists of:

---

[1] Also referred to as Finite Element Analysis (FEA).

[2] Actually an older version still named FEMLab.

- Choice of appropriate **physics**. A feature of the software is the possibility to study the impact and interplay of numerous physics effects simultaneously. Hence, the "multiphysics" included in the name. At this step the user also has the choice of dimension of the simulation.

- Modeling the **geometry** of the workpiece to be investigated. A (limited) tool for the construction of geometries from several primitives, such as spheres, cubes, or ellipsoids, using boolean operations is part of the software. An alternative is the import of geometry data from a CAD file.

- Definition of **material parameters** to go into the differential equations, e.g. Young's modulus, in the case of a pressure stability simulation, As well as **boundary conditions**, such as pressure load.

- Generation of a **mesh grid**. The positions of grid points define the corners of the finite elements.

- **Evaluation** of the differential equations on the grid and extraction of desired physics parameters from the results.

- If needed, **refinement** of mesh at locations of interest. These usually are areas where steep gradients of a property of interest are found. At locations with little or no variation the grid can in turn be thinned out to reduce calculation time.

The last two steps can be (re-)iterated several times until a satisfactory solution, that is to say one stable against re-meshing, is found.

Main common features of the simulated setups were:

- axially symmetric two-dimensional model: reflecting the symmetry of the investigated vessel and allowing a substantial speed-up of the calculation

- no initial stress in the material

- homogeneous material, in particular no defects, such as trapped air bubbles, which are common in real glass vessels

- Young's modulus: $E = 63\,\mathrm{GPa}$

- Poisson's ratio: $\gamma = 0.2$

- density: $\rho = 2230\,\mathrm{kg\,m^{-3}}$

The listed material parameters are characteristic of Vitrovex[1], a borosilicate glass used by Nautilus GmbH for the production of pressure housings, and were retrieved from the company's website [178]. A schematic of the mDOM simulation model is shown in figure 8.2.

---

[1] For an investigation of the optical properties of this glass, see section 9.1.

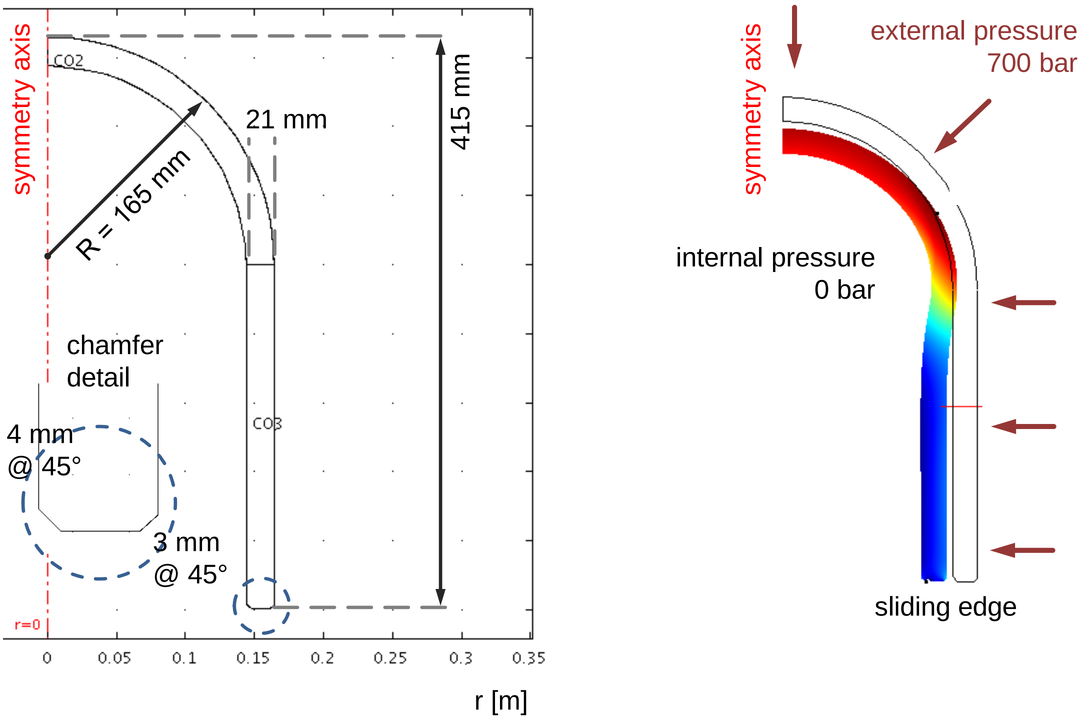

Figure 8.2: FEA model details. **Left**: Geometry details and dimensions. **Right**: Simulation of pressure load. Pressure-induced deformation shown qualitatively, i.e. strongly exaggerated. Maximum displacement was found to be 1.6 mm. Color code represents third principal stress, see figure 8.3 for details.

name	D [in]	d [mm]	p [bar]	$\sigma_{\mathrm{a,B}}$ [MPa]	$\sigma_{\mathrm{a,L}}$ [MPa]	$\sigma_{\mathrm{min,sim}}$ [MPa]	$\sigma_{\mathrm{max,sim}}$ [MPa]
Benthos 2040 13V	13	12.5	900	-594	-642	-641	71
Nautilus IS-7000	13	12.0	700	-482	-518	-517	57
Nautilus IS-9000	17	18.0	900	-540	-587	-587	66
Nautilus IS-12000	17	21.0	1200	-617	-680	-681	77

Table 8.1: Principal stress results for commercially available spherical pressure vessels together with dimensions and pressure ratings used in the calculation and simulation. Abbreviations denote: D the vessel diameter, d the wall thickness, and p the pressure rating. Presented are the analytically calculated axial stresses $\sigma_{\mathrm{a,i}}$, where "B" refers to Barlow's formula, and "L" indicates values derived using Lamé equations, together with the FEM-simulated minimum principal stress $\sigma_{\mathrm{min,sim}}$ as well as the maximum principal stress $\sigma_{\mathrm{max,sim}}$.

8.1.3 Cylindrical pressure vessel

As presented above, principal stresses were deduced using an analytic (equations 8.2 and 8.3) as well as a numerical simulation approach. Values for the benchmark geometries resulting from both techniques are presented in table 8.1. While underestimated by the simplified expressions by Barlow, simulated values were found to agree remarkably well (maximum deviation $< 0.2\%$) with those derived using the Lamé set of equations.

A noteworthy initial observation was a large excess of stress in the joint region between the semi-vessels resulting from the simulation. This is a true effect of the load distribution inside the glass volume and is the reason for the use of chamfers. After introducing chamfers to the model, the effect was strongly reduced.

A semi-cylindrical mDOM vessel was assessed in the same manner. The height of its cylindrical section was given by the desire to house at least five horizontal layers of PMTs inside the module. While the outer diameter of the vessel was taken to be fixed by the borehole diameter to 13 inch, the wall thickness was left as a free parameter. Here the figure of merit was the number of PMTs placeable per layer. Given the then-current dimensions of PMTs and bases, as well as the initial intention to use PMMA lenses in front of the cathode, relevant wall thicknesses were found to be:

- < 30.2 mm for three PMTs per layer,
- < 21.5 mm to house four PMTs, which was considered a realistic goal, and
- < 13.6 mm in the case of five tubes.

Geometric details of the simulation model are shown in figure 8.2. Resulting extremal principal stress values are presented in table 8.2 together with the numbers derived analytically. As in the case of the reference geometries, there is good agreement between simulation and the calculation using Lamé's equations (see equation 8.3). Considering the semi-cylindrical shape of the vessel, the minimum tangential stress was expected to be the quantity limiting pressure stability (see equation 8.2 and discussion) which is confirmed by the simulation (see also figure 8.3). Comparison of results in tables 8.1 and 8.2 indicate

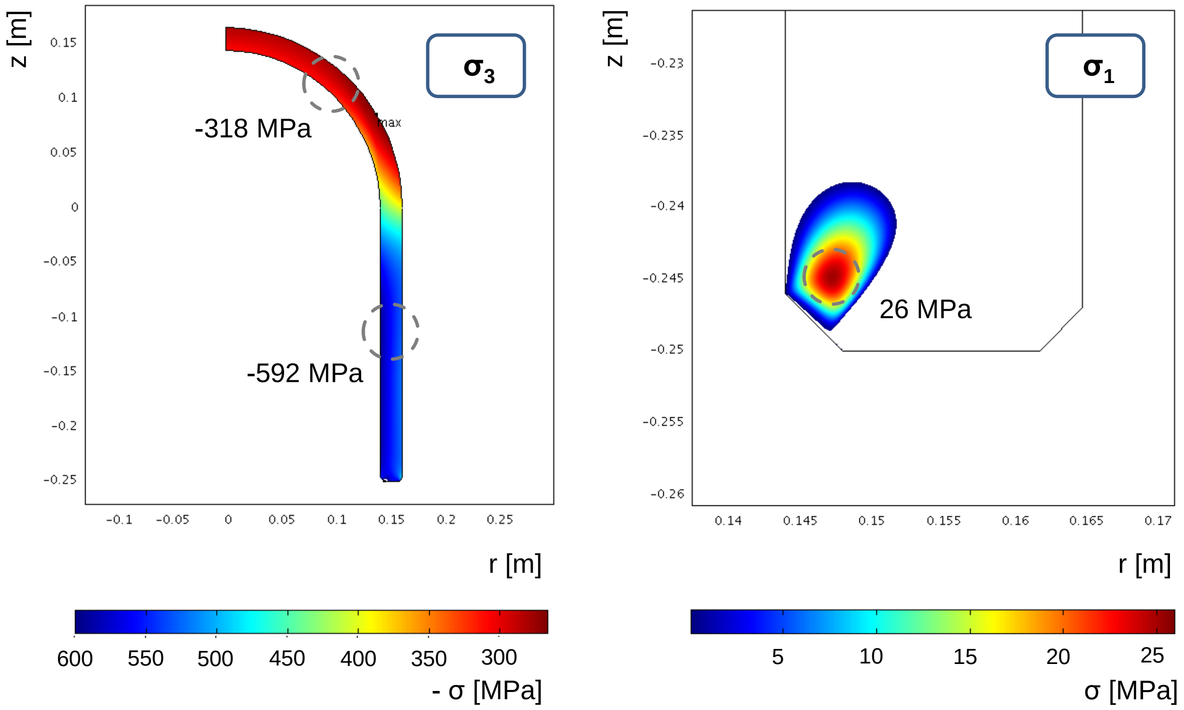

Figure 8.3: Principle of stress derivation from simulation results shown for the mDOM model. Figures feature the smallest and the largest of the three principal stresses occurring in the glass: σ_3 is a measure of the overall compression, corresponding to the axial stress in the spherical and the tangential stress in the cylindrical section, whereas corner traction gives rise to σ_1. To ensure structural stability under the normal stress criterion, the maximum of σ_1 needs to be smaller than the tensile strength of the material, while the minimum of σ_3 is required to be larger than its compressive strength[a]. The distribution of σ_3 demonstrates that overall stability is limited by the cylindrical section.

---

[a] In the COMSOL numbering convention σ_1 indicates the largest principal stress.

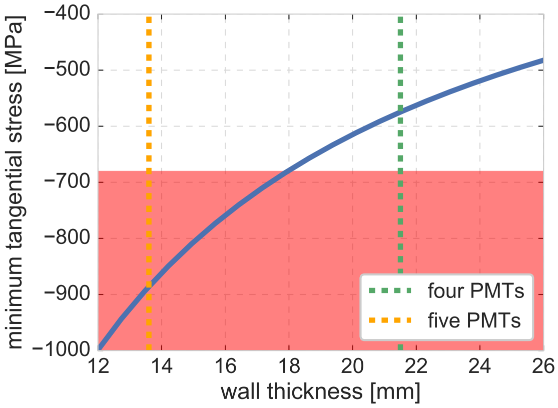

Figure 8.4: Limitation of the mDOM wall thickness by the minimum tangential Lamé stress. *Red*-shaded area marks the region excluded by the stress value of Nautilus IS-12000, representing the lowermost limit from the benchmark geometries. Vertical lines mark the maximum wall thicknesses allowing the placement of the respective number of PMTs per layer.

$\boldsymbol{D}$ [in]	$\boldsymbol{d}$ [mm]	$\boldsymbol{p}$ [bar]	$\boldsymbol{\sigma_{aB}}$ [MPa]	$\boldsymbol{\sigma_{t,B}}$ [MPa]	$\boldsymbol{\sigma_{a,L}}$ [MPa]	$\boldsymbol{\sigma_{t,L}}$ [MPa]	$\boldsymbol{\sigma_{a,sim}}$ [MPa]	$\boldsymbol{\sigma_{t,sim}}$ [MPa]	$\boldsymbol{\sigma_{max,sim}}$ [MPa]
13.0	21.0	700	-275	-550	-313	-588	-318	-592	26

Table 8.2: Stress values obtained for a cylindrical mDOM vessel as shown in figure 8.3. Naming convention for dimensions and pressure identical to table 8.1. The listed stresses comprise: the calculated axial and tangential stresses $\sigma_{\mathrm{a,i}}$ and $\sigma_{\mathrm{t,i}}$, respectively, as well as the simulated values for the axial stress $\sigma_{\mathrm{a,sim}}$, the tangential stress $\sigma_{\mathrm{t,sim}}$ (which in this case corresponds to the minimum compressive stress), and the simulated maximum (tensile) stress $\sigma_{\mathrm{max,sim}}$.

structural stability of the considered mDOM geometry as the maximum and minimum stresses are contained inside the allowed range retrieved from the benchmark vessels. A significant reduction of the wall thickness, enabling the positioning of five PMTs per layer, was ruled out based on the analytic expression for $\sigma_{\mathrm{t,L}}$ as illustrated in figure 8.4. The minimum wall thickness for a cylindrical pressure vessel stable at 700 bar was determined to be $\sim$ 18 mm.

The deformation of the vessel by the ambient pressure was also derived from the simulation and is presented qualitatively in figure 8.2. The overall maximum displacement was found to be 1.29 mm (radial shrinkage of the cylindrical section), defining the elasticity range required from the PMT holding structure (see also section 8.2). This value again agreed well with analytic Lamé expectations ($\mathit{\Delta} R_{\mathrm{in}} = -1.21\,\mathrm{mm}$, $\mathit{\Delta} R_{\mathrm{out}} = -1.10\,\mathrm{mm}$, $\mathit{\Delta} l = -0.70\,\mathrm{mm}$).

In general, the obtained results demonstrated, in principle, the feasibility of a semi-cylindrical pressure housing featuring the desired dimensions as well as a pressure rating of 700 bar, and were used as input for the subsequent initial consultations with Nautilus GmbH, who confirmed the validity of the approach. Further negotiations, in combination with additional simulations and tests by the company, finally resulted in the production of a cylindrical mDOM vessel presented in figure 8.8. Notably, the manufactured vessel features a wall thickness of 18 mm, the very limit of structural stability as defined in figure 8.4. Changes in the module design, such as the omission of PMMA lenses, allowed to increase the number of PMTs to five per layer with the given inner diameter.

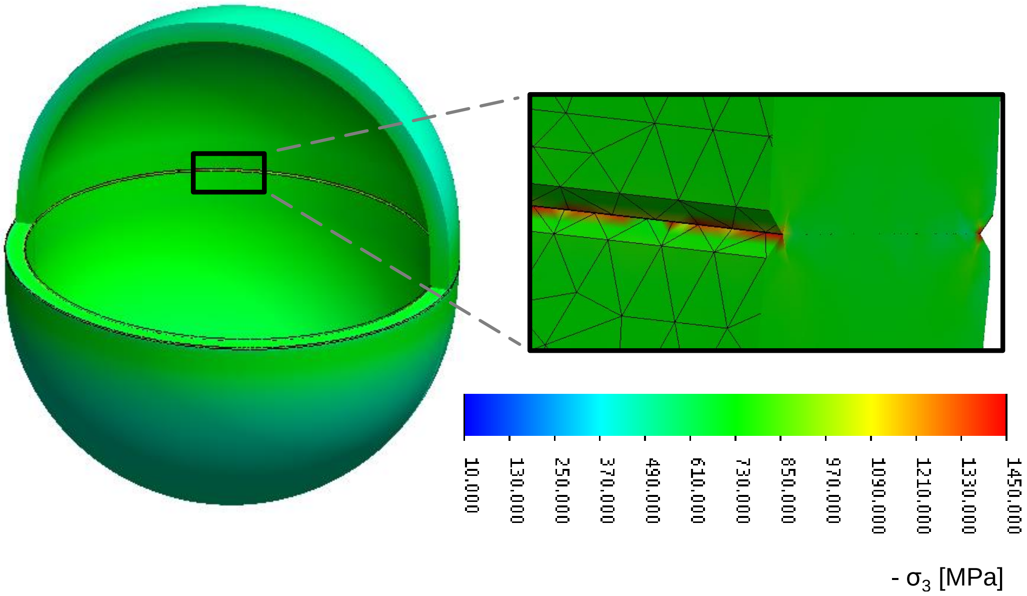

Figure 8.5: Compressive stress distribution expected in the current (quasi-spherical) mDOM pressure vessel geometry when subjected to 1050 bar (corresponding to 700 bar including a safety factor of 1.5). Presented for a wall thickness 16 mm. Stress spikes at the contact surfaces are believed to be due to a combination of meshing artifacts and unphysically sharp edges. Figures courtesy of Steffen Pausch (Nautilus Marine Service GmbH), modified.

8.1.4 Quasi-spherical vessel design

As discussed in section 4.2 the vessel design featuring a large cylindrical central section was ultimately abandoned. Structural stability simulations for the new, more spherical, 14-inch module were done by Nautilus GmbH for a pressure rating of 700 bar using a three-dimensional model. In addition, the company approach included a safety factor of 1.5, resulting in an actually simulated pressure of 1050 bar. An example of the minimum stress distribution is presented in figure 8.5. Table 8.3 features a comparison of the provided results to corresponding analytic calculations, showing that the new, more sphere-like, geometry strongly differs from a pure cylinder expectation, exhibiting minimum stresses deviating from a pure spherical model by only 10%. Based on the simulation results, as well as production procedure considerations, the actual vessels have a wall thickness of 13 mm.

The company also provided information on the compressive ($\sigma_\mathrm{c} = -1448\,\mathrm{MPa}$) and tensile ($\sigma_\mathrm{t} = 41.4\,\mathrm{MPa}$) strength of Vitrovex from their database. These values must be considered excluding a safety margin. Unfortunately it was not possible for the company to actually trace the source of the information or comment on its reliability. For instance, it is notable that all maximum tensile stresses found in our simulation, including those for reference geometries, exceed the provided limit.

d [mm]	$\sigma_{\mathrm{t,L}}$ [MPa]	$\sigma_{\mathrm{a,L}}$ [MPa]	$\sigma_{\mathrm{min,sim}}$ [MPa]
12	-1612 (-1074)	-834 (-556)	~ -920
13	-1492 (-995)	-774 (-516)	–
16	-1223 (-815)	-640 (-427)	~ -710

Table 8.3: Principal stress results for the quasi-spherical mDOM geometry featuring wall thicknesses d at a hydrostatic pressure of 1050 bar. FEM-simulated minimum stresses $\sigma_{\mathrm{min,sim}}$ provided by the company are compared to minimum analytic Lamé stresses for a sphere $\sigma_{\mathrm{a,L}}$ as well as a cylinder $\sigma_{\mathrm{t,L}}$. Brackets indicate respective values for the nominal pressure of 700 bar.

8.2 PMT mounting structure

Initially[1], the holding structure for PMTs inside the KM3NeT multi-PMT optical module prototypes was produced from bulk foam, a technique initially also envisaged for the mDOM. Due to the complex manufacturing process and the large amount of gel needed to fill the module, caused by the coarse surface structure of the material, the technique was abandoned for mass production. An even more crucial flaw was the susceptibility to the occurrence of air bubbles, deteriorating the optical properties of the module. Emergence of these bubbles was traced back to small volumes of residual air trapped by the gel expanding during vacuum treatment[2]. An alternative method was found in rapid prototyping, also known as three-dimensional printing, particularly the laser-sintering of polyamide[3]. Although not being distinctly cheap, this approach allows the realization of delicate and complicated structures, at the same time featuring flexibility to ad-hoc changes of the layout if required, as no casting mold or similar costly devices are needed. Originally planned to be applied during module prototyping, three-dimensional printing has continued to be used for the production of KM3NeT modules up to the present moment.

Consequently, rapid prototyping was (and still is) the method of choice for the production of the mounting structure of the mDOM. Holding structures have been designed[4] and ordered from a commercial company for the initial cylindrical module layout, as shown in figure 8.6, with structures for each half vessel consisting of one hemispherical and one cylindrical part, to be glued together during assembly. This bipartite layout was chosen to facilitate the mounting, and more important, the connection of PMTs to the central logic board in the very space-limited environment of the mDOM. The assembly procedure envisaged, comprised, as a first step, mounting and connecting the PMTs in the cylinder to an elongated electronics board while this part is still accessible from both sides, followed by the equipment of the spherical part, and gluing of the segments after connection of the remaining electronics. PMTs are fixed by supporting their cylindrical part ("stem") and sealed with o-rings against the leakage of gel. As a precaution against air trapping, which would result in bubbles and detachment of gel from the inner surface of the glass vessel,

---

[1] That is to say before late 2012.

[2] The modules are sealed by connecting the halves of the vessel in a low-pressure environment.

[3] Type PA 2200 [183].

[4] Design choices were made by the author in cooperation with O. Kalekin. Production of corresponding CAD models was performed by K. Kärcher, the ECAP resident mechanical engineer.

Figure 8.6: PMT and reflector mounting structure for the initial cylindrical mDOM layout. The bi-partite structure was designed to support Hamamatsu R12199-02 PMTs. Note the peculiar reflector shapes in the cylinder section. Courtesy of the IceCube Münster group

it was decided to fill the optical gel beginning from the lowest point[1], via a dedicated tube included in the holder, instead of pouring the gel from above, as was done with first KM3NeT prototypes.

As mentioned earlier (see section 4.2), the cylindrical pressure vessel was ultimately abandoned due to cost and weight issues, in favor of near-spherical design. With the changed shape of the vessel an appropriate holding structure became necessary. Based largely on the initial cylindrical version, the new layout also incorporates experience gained in the meantime from PMT testing, namely the monitoring of dark rate behavior (discussed in section 6.6.1), as well as from reports on the KM3NeT design: Attempting to economize optical gel, plastic clamps were added to the KM3NeT holder. Providing stable positioning of the PMT by clenching its hemispherical part, it eliminated the need for a support of the stem, reducing the volume filled with gel. After issues with high and unstable dark rate arose from the new KM3NeT design, and based on the observation that any object at a different electric potential close to the photocathode will enhance the dark rate[2], it was decided for the mDOM to stick with the initial “stem support” layout, which provides better insulation of the cathode area with gel. For the same reason – improvement of cathode insulation – the reflector holder was modified. In the current layout the reflector rests on three sockets (see figure 8.7, b), creating additional gel volumes behind it. This change is also expected to diminish the probability for the occurrence of air bubbles after degassing by reducing the amount of narrow gaps not filled with gel due to its large viscosity. Infilling of gel is again supposed to start at the lowest point via a tube positioned at the pole of the structure. Should these measures prove not effective enough, connections of PMT nests by printed tubes is considered.

8.3 Design conclusions

With the custom-developed quasi-spherical design a precise and cost-effective solution suitable for mass production was found for the shape of the pressure vessel. According to finite element simulations by the manufacturer, in agreement with analytic estimations, the vessel features the required pressure rating of 700 bar. Several specimen of the new vessel were acquired and will be used for prototyping.

---

[1] This refers to a half-vessel in vertical position, with the opening on top.

[2] Which is in agreement with literature, as discussed in section 3.8.

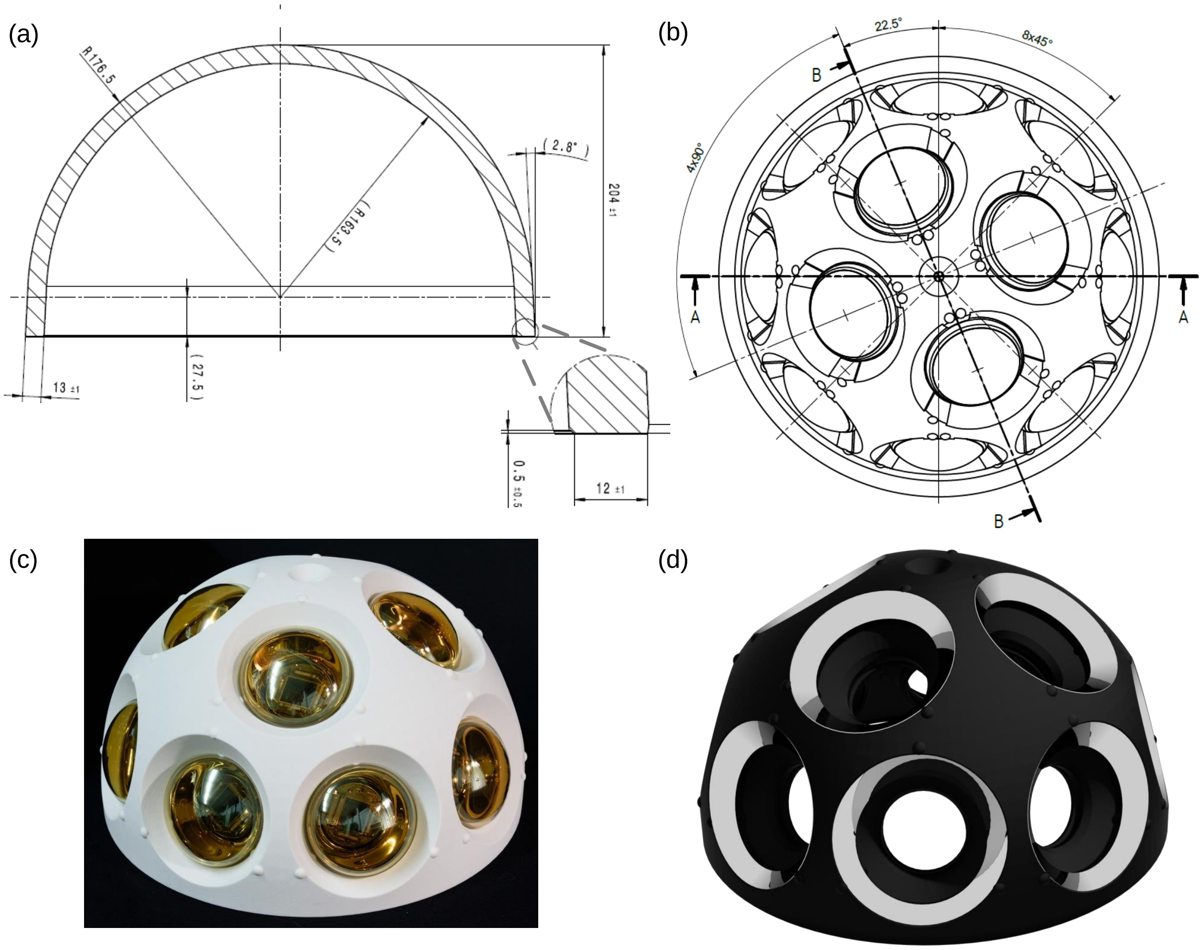

Figure 8.7: Spherical mounting structure of the current mDOM design. Featuring technical drawings of the pressure vessel (*a*, figure provided by Nautilus GmbH, modified), and the mounting structure (*b*), as well as a photograph of the actual (unpainted) device (*c*) and an artist's impression (*d*) of the final configuration (latter figures courtesy of the IceCube Münster group). Depicted is the structure for the default PMT model (Hamamatsu R12199-02).

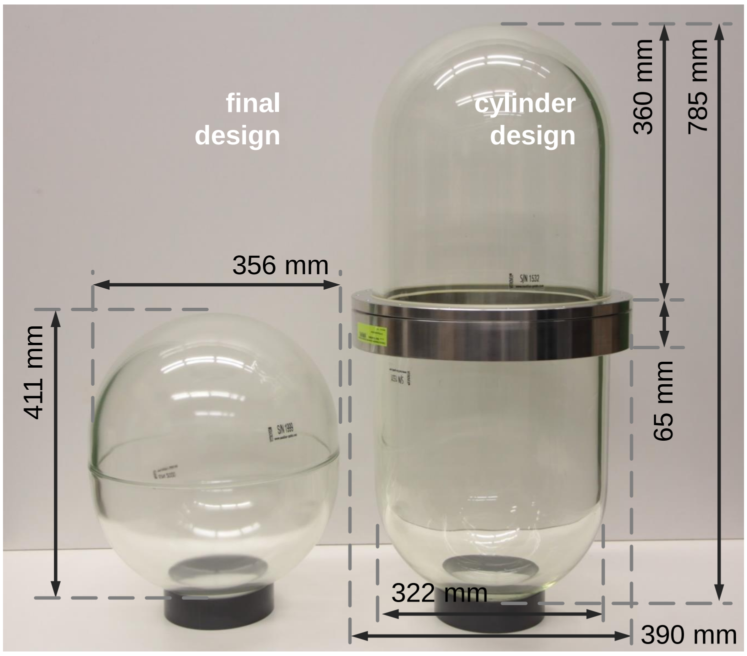

Figure 8.8: Pressure vessel dimensions of the current (**left**) and the discarded cylindrical mDOM design (**right**).

However, reliable failure prediction for brittle materials is in general challenging. See e.g. [184] for a comprehensive discussion of this topic. Even though the maximum stress criterion is a standard approach[1], it should not be trusted blindly. Consequently, only hyperbaric qualification tests can provide the necessary proof of stability.

Such tests are scheduled for early 2017 (not part of this work). Apart from examining stability the tests will also address pressure-induced shrinking. From Lamé equations it is expected to range from -2.3 mm in the cylindrical and -1.0 mm in the spherical section. In cooperation with DESY-Zeuthen a device based on remotely controlled high-precision linear resistors was developed to measure the actual deformation to a precision of 10 µm (see figure 8.9).

Distinct support structures were designed to house three-inch PMTs of type R12199-02 by Hamamatsu and the ET Enterprises 9320KFL type, together with corresponding reflectors to be produced from polyamide using rapid prototyping. The Hamamatsu version of the mount is presented in figure 8.7.

For mass production, alternative, more cost-effective production methods are also taken into consideration.

---

[1] There are yet also more conservative criteria, such as Mohr's theory, or the latest and more sophisticated criterion by Christiansen [184]. Their usage however requires knowledge of tensile and compressive strength of the material.

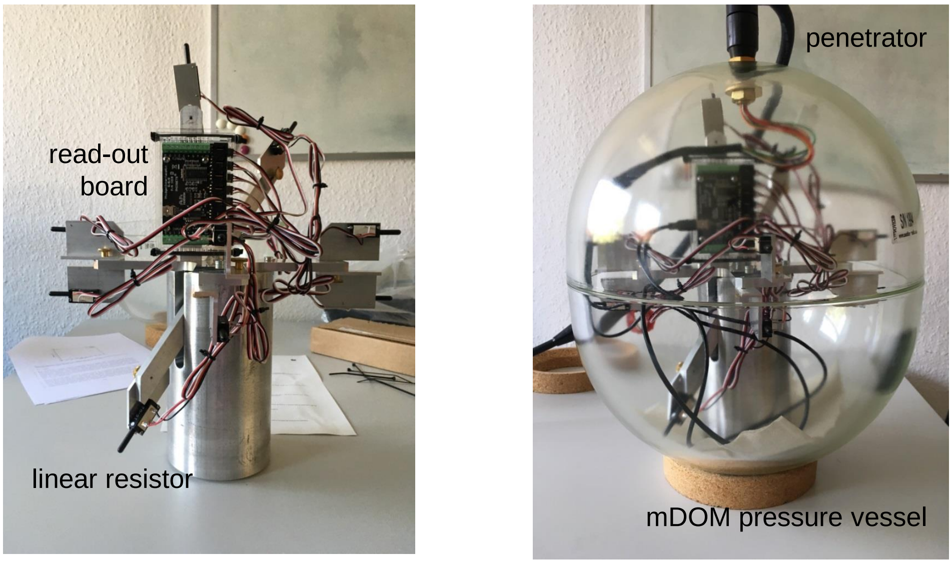

Figure 8.9: Pressure vessel deformation measurement device, featuring main components. Photos courtesy of DESY-Zeuthen.

9 Passive optical components

The sensitivity of an optical module is defined by the respective properties of its optical components, for instance the glass, gel, reflective cones and of course the PMTs. Good knowledge of these properties is thus needed for reconstruction as well as simulation purposes. While PMT characteristics have been discussed earlier (see chapters 5 and 6), this chapter is dedicated to the examination of the remaining (passive) optical components.

9.1 Glass and gel

Ideally, from an optical point of view, the glass of the pressure vessel should be totally transparent for all relevant wavelengths, feature no scattering and match the refractive index of the surrounding medium in order to minimize refraction and reflective losses at its outer surface. In practice however, there is also the need of stability against ambient pressure and good processibility of the material. The latter also reflects on the mass-producibility and price of the vessel. Currently operating neutrino telescopes use pressure vessels from borosilicate glass (see chapter 2). The amount of good experience made with the material as well as its generally good availability at low prices from various manufacturers world-wide makes it a natural candidate for the current development. There is however a drawback, in particular for the use in ice: The transmission spectrum of borosilicate glass, while being transparent well into the infrared region, features a low-wavelength cut-off[1] around 300 nm, with the exact position varying from manufacturer to manufacturer but also on a batch-to-batch basis. The cut-off roughly coincides with that of the quantum efficiency of typical bialkali PMTs (see section 3.1, in particular figure 3.5) due to the fact that those are produced from borosilicate glass as well[2]. This feature plays a minor to no role if the detector is constructed in sea water, which is opaque to UV light[3], but becomes important in the clear glacial ice of the IceCube site (see discussion in section 2.1.2). An alternative is the use of quartz glass, as intended by the group developing the WOM (see section 2.4, figure 2.16). The downside here is the high cost, in particular in case of the mDOM with its larger diameter. A further alternative was presented by the IceCube group at Chiba university developing the D-Egg (see section 2.4, figure 2.17). Depleting contamination by iron-oxide, they claim to have extended the UV transparency range by some 10 to 20 nanometers.

The same considerations apply to the silicon-based optical gel, coupling the PMTs to the inner surface of the pressure vessel. However, gel tends to feature higher levels of UV transparency, not limiting the overall performance of the optical module.

In the scope of the work reported in this section the optical transmission of several materials was assessed:

---

[1] In the given context the term “cut-off” will indicate the position of the transmittance surpassing 50% of the maximum or typical value.

[2] The quantum efficiency of bialkali PMTs usually ranges further into the ultraviolet than the transmission of a pressure vessel due to the lower material thickness.

[3] Convolution of the emitted Cherenkov spectrum with sea water transparency results in maximum flux around 470 nm. Therefore most measurements of PMT properties refer to this wavelength as the standard.

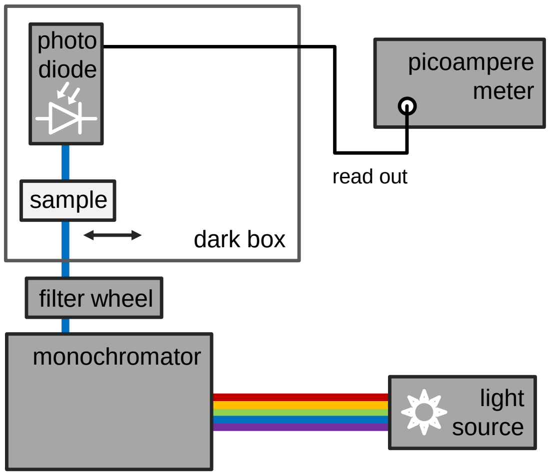

Figure 9.1: Schematic sketch of the transmission measurement setup. For reference measurements the sample is removed from the light beam. Monochromator, filter wheel and picoampere meter are remotely controlled by a PC (not shown).

- **Vitrovex** is the standard borosilicate glass used by Nautilus GmbH. Prototype vessels for the mDOM ordered from this manufacturer featuring a wall thickness of 18 mm, as well as KM3NeT vessels available at ECAP (wall thickness of 15 mm), were used to measure the transmission of this material.
- A sample of the UV-enhanced borosilicate, dubbed **"Chiba glass"**, was provided by the Chiba group. Its wall thickness was measured to be 18 mm.
- The group also did some optimization work on the optical properties of the gel. This **"Chiba gel"** was also tested.

Transmission measurements were performed using a modified version of the monochromator setup for PMT quantum efficiency testing shown in figure 9.1 (for a comprehensive description of the devices employed, see section 5.1.5). In order to be able to measure in the ultraviolet region the xenon lamp of the original setup, featuring only little flux below 290 nm (see figure 9.3), was replaced by a combined tungsten-halogen and deuterium light source[1]. Band-pass color filters were added at the aperture of the monochromator in order to suppress contamination of the visual range output by higher order contributions of ultraviolet light which could be safely neglected in the original xenon lamp setup. The material samples were positioned in the light beam in front of a photodiode. Transmission $T(\lambda)$ was derived as

$$T(\lambda) = \frac{I_{\text{sample}}(\lambda)}{I_0(\lambda)} \tag{9.1}$$

where $I_0(\lambda)$ and I_{sample} are the currents generated by the bare and the sample-equipped photodiode, respectively. Both values were corrected for dark rate contributions subtracting the mean value of currents measured before and after the main data taking with the shutter closed. Statistical uncertainties, in terms of standard errors of the current measurement, were found to be on the low ‰-level. A systematic limitation of the setup was the availability of curved glass samples only, potentially introducing uncertainties due to refraction. While not an option for the large Vitrovex vessels, it was possible to measure the transmission of the Chiba glass sample with light passing in both directions,

---

[1] Type L10290 UV-VIS by Hamamatsu. A data sheet highlighting main features is available from the manufacturer online [185]. Special thanks to M. Sondermann for generously providing the device.

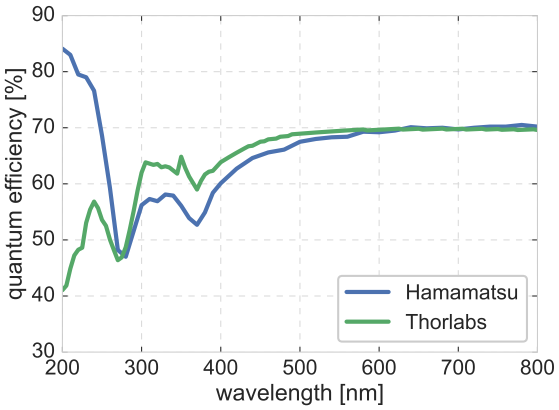

Figure 9.2: Quantum efficiency spectra of calibrated photodiodes available at ECAP. Values taken from tables provided by the manufacturers. Based on its superior sensitivity in the ultraviolet region the Hamamatsu model was chosen for transmission characterization.

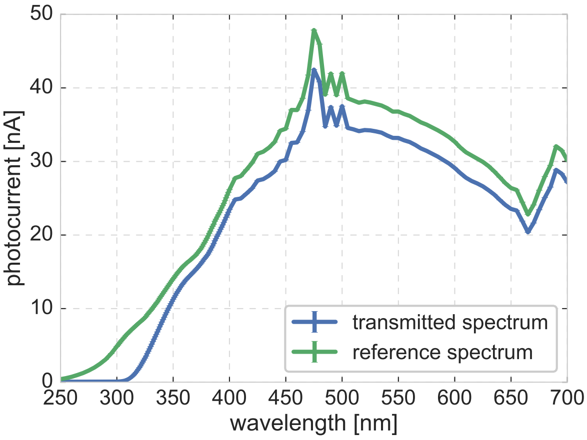

Figure 9.3: Example xenon lamp spectra used for the determination of material transmittance. Errorbars (smaller than line width) indicate statistical standard errors.

showing no significant impact on the results, as long as the photodiode was positioned as close as possible to the sample. The glass results were also found not to be affected by the distance to the light source, as long as the light spot was fully contained by the diode input window, while a corresponding effect was found for the tested (flat) sample of Chiba gel, preventing a conclusive result. The latter finding is interpreted as an impact of light scattering, which is negligible in glass but not in the case of gel. Therefore, no attempt was made to measure transmission properties of the default Wacker 612 gel with the available setup.

Figure 9.5 features the final results of the glass transmission study. Featuring identical sample material thicknesses, the measured spectra of Vitrovex and Chiba glass allowed a direct comparison. In addition, the Chiba group provided transmittance data obtained from the glass manufacturer, also included in the figure. The latter spectra were recalculated from the original values $T(x_0)$ using

$$T(x_{\text{new}}) = \exp\left(\ln T(x_0) \cdot \frac{x_{\text{new}}}{x_0}\right) \tag{9.2}$$

where x_{new} and x_0 are the original and new wall thickness, respectively, neglecting, for the time being, losses at glass-air interfaces.

Chiba glass has indeed shown a better performance compared to Vitrovex in terms of the position of the UV cut-off as well as the overall transmittance, albeit not to the extent of shifting the UV cut-off by several 10 nm. In particular it was not quite possible to reproduce the more optimistic values provided by the manufacturer: While transmittance of the measured samples drops below 45% at 332 nm (Vitrovex) and 328 nm (Chiba glass), respectively, the company data indicates a cut-off located[1] at 315 nm.

A possible explanation is that, according to experts from Nautilus GmbH [186], the exact position of the cut-off is strongly influenced not only by the density of iron-oxide, but by many other small-scale contaminations in the glass. The source of these can be the various raw materials, but also the walls of the heated volume where the glass melt is produced and stored (which therefore has to be replaced on a regular basis). As, at least in the case of Vitrovex, the optical properties are not part of the material's official specification, these contaminations are not prevented or monitored during production. Consequently, the actual UV transmittance of borosilicate glass can vary from one production cycle to another, but also depend on the age of the molten mass at the moment of extraction of a batch.

The large amount of Vitrovex spheres available in Erlangen for the construction of KM3NeT allowed for an attempt to monitor this behavior: Transmission spectra were measured[2] for ten spheres, randomly chosen from a total number of 100. As shown in figure 9.6, no variation exceeding the 2%-level was found between the tested vessels, allowing to assume optical transmission homogeneity on this level[3].

Apart from merely determining the position of the UV cut-off, the transmission data was also used to derive the wavelength-dependent absorption length $\alpha(\lambda)$ of the material, which is a crucial input parameter for any simulation of the optical properties of the module. In the convention used in the scope of this work, the absorption length is defined as indicated by

$$I(x,\lambda) = I_0(\lambda) \cdot e^{-x/\alpha(\lambda)} \tag{9.3}$$

where I_0 is the initial light intensity and $I(x)$ is the value after the passage through a layer of material featuring a thickness of x. In a simplified approach, the absorption length thus can easily be extracted from the transmission T using $T(\lambda) = \exp\left(-x/\alpha(\lambda)\right)$. To be more precise, however, reflection occurring at interfaces between media with different refractive indices n_1 and n_2 has to be taken into account. The fraction of reflected light R (for normal incidence) is given by Snell's law

$$R = \left(\frac{n_1 - n_2}{n_1 + n_2}\right)^2 . \tag{9.4}$$

as a function of the refractive indices n_i on both sides of the interface [187]. Inserting typical values for glass ($n = 1.5$) and air ($n = 1$) results in a reflective loss of $\sim 4\,\%$, which can not be safely neglected. Refractive index spectra for the glasses under investigation were provided by the respective manufacturers [186, 188] (however values for Vitrovex covered only wavelengths larger than 335 nm). To be applicable throughout the considered

---

[1] Originally, Chiba glass transmittance was claimed to range as far as 280 nm, which, in particular considering the $1/\lambda^2$-dependence of the Cherenkov spectrum and the weak absorption in ice, would have been very beneficial. In fact, it was this optimistic value that triggered the study reported in the current section and also implied the need to assemble a UV-sensitive experimental setup. After presenting the manufacturer with the obtained spectra this claim was found to be accidentally based on specially treated test samples and not valid for mass-produced vessels.

[2] By J. Reubelt.

[3] At least for the tested batch.

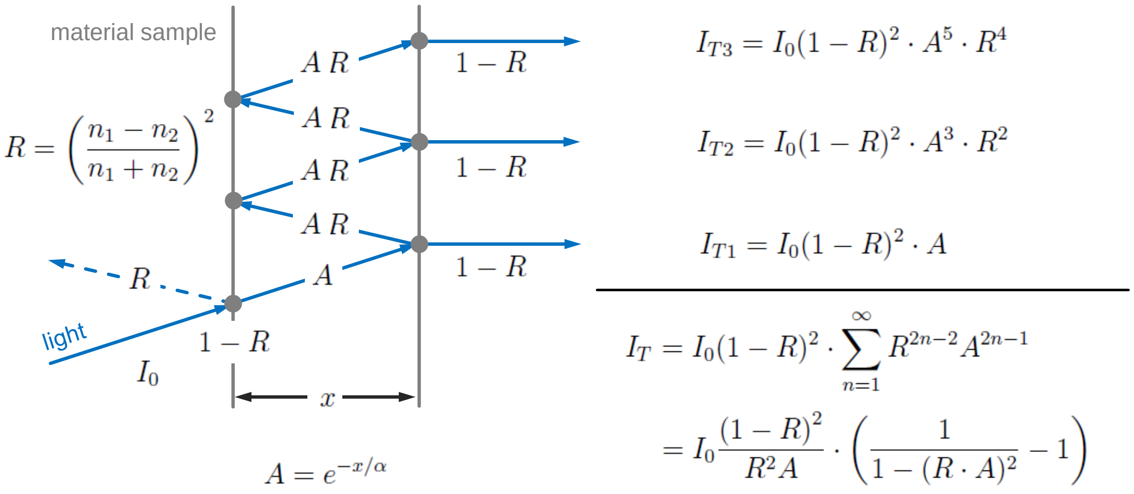

Figure 9.4: Derivation of equation 9.6 for the optical transmittance of a flat material sample. The expression is valid for vertical photon incidence (photon trajectories pictured inclined for the sake of clarity), taking into account the contributions from all reflections at inner and outer sample surfaces, as well as absorption along the path through the material. Subsequent order contributions I_{Tn} are derived by multiplying all factors along the corresponding photon paths. Final expression for the transmitted light intensity I_T emerges by means of a geometric series. Based on sample thickness interference effects were not included.

wavelength region (250 nm to 700 nm) the datasets were fit using the Sellmeier equation [189]:

$$n^2(\lambda) = 1 + \frac{A_1 \lambda^2}{\lambda^2 - B_1} + \frac{A_2 \lambda^2}{\lambda^2 - B_2} + \frac{A_3 \lambda^2}{\lambda^2 - B_3} \tag{9.5}$$

where λ is the wavelength while A_i and B_i are material constants, referred to as Sellmeier coefficients. The obtained coefficients where used in further calculations. Taking into account the contribution from multiple reflections at the inner and outer surfaces of a flat sample, as illustrated in figure 9.4, the final expression for the light intensity transmitted by a material sample is given by

$$T = \frac{(1-R)^2}{R^2 A} \cdot \left(\frac{1}{1-(R \cdot A)^2} - 1\right) \qquad \text{where} \qquad A = e^{-x/\alpha} \tag{9.6}$$

with T denoting transmission and R reflection at an interface, as defined above (equations 9.1 and 9.4, respectively). Not marked explicitly is the dependence on the wavelength of the incident light, which applies to all above-mentioned quantities. Absorption length spectra derived from the measured transmittance using equation 9.6 are presented in figure 9.7.

There was however a problem with deriving the absorption length from the transmittance measured on a sample of fixed thickness: Even though the uncertainties of the photocurrent measurement are small, and in fact negligible considering the transmission, they start having an impact regarding the absorption length:

- In the case where the absorption length is much smaller than the available material sample, it becomes impossible to arrive at the actual value as the small amount of transmitted light falls below the sensitivity of the photodiode and becomes indistinguishable from the dark current and stray light background.

- Also problematic is the reverse situation where the absorption length is much larger than the sample thickness, illustrated in figure 9.8. In this case the calculated absorption length reaches unrealistically large values, as the small amount of attenuation by the sample can not be discriminated from no attenuation at all. Small errors introduced by the dark rate subtraction (which is measured before and after the run and linearly interpolated), minor light output variations, which are not monitored in real-time during a run, or the deviation of the refractive index from the value provided by the manufacturer can result in a situation where the measured transmission is surpassed the maximum value allowed by reflection losses. In this case the absorption length becomes negative, effectively describing the production of the “surplus” photons inside the medium.

The above mentioned caveats introduce errors in any potential simulation based on them. Those are not very prominent if the thickness of the material in the final setup is comparable to the sample dimensions, as it is the case for the glass of the pressure vessel. For instance, for vertical impact of photons a simulation will simply reproduce the sample behavior serving as input. But angled incidence is already prone to deviations, as is the transmission of components thinner than the available sample. An example for the latter is the optical gel featuring a minimum layer thickness of only two millimeters. Simulation of ^{40}K decays originating inside the glass will suffer most from incorrect values for the UV cut-off, underestimating the amount of Cherenkov photons detected by the PMTs.

A solution can be the testing of several samples of each material featuring different thicknesses covering the entire spectrum of dimensions relevant in the final device. Precision of the measurement can also benefit from a dedicated setup using an Ulbricht sphere[1] to minimize stray losses and a spectrometer instantly recording the entire spectrum to prevent errors from dark current correction and light source drift.

In spite of the above-mentioned drawbacks, the absorption length provides valuable input for the Geant4-based optical module simulation described in more detail in chapter 10. In addition to the absorption length spectra of Vitrovex and Chiba glass, corresponding properties were included for different gels as well as further glass types. Not being readily available the absorption lengths were derived from respective transmittance spectra using the approach introduced above.

9.2 Reflectors

Reflective cones around the photocathode are used to increase the effective area of the PMTs (see e.g. figure 4.5). Actually, due to etendue conservation [191], the devices merely redistribute photon sensitivity from larger to smaller incidence angles resulting in an

---

[1] The term Ulbricht sphere [190] refers to a hollow sphere featuring a highly diffuse reflective coating with well-known properties on the inner surface. Via apertures, light can be fed in and guided out of the sphere. No matter under which angle the light enters the device, it will contribute to the output.

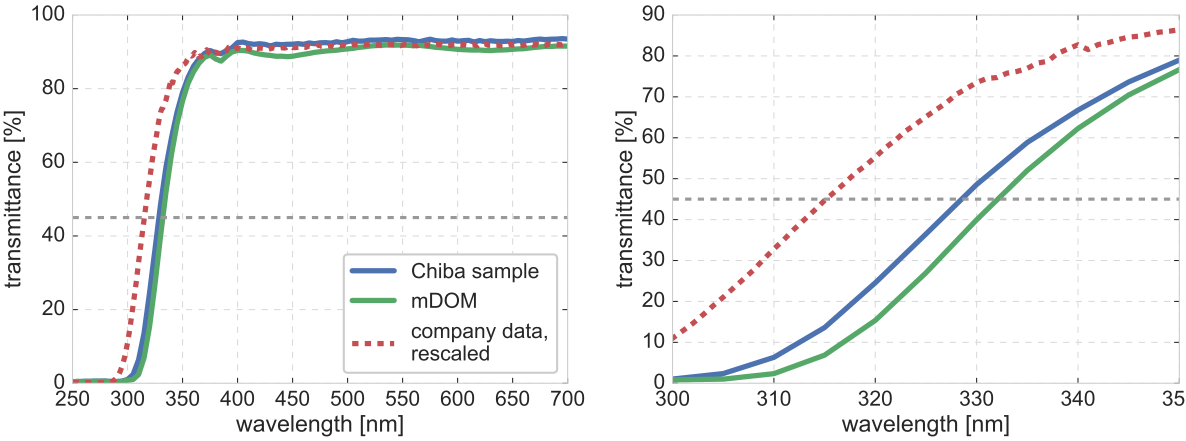

Figure 9.5: Transmittance of Vitrovex and Chiba glass: Presented spectra (**left**) were acquired using the UV light source discussed in the text (*solid* lines). Featuring identical material thicknesses (18 mm) the values are directly comparable. Data provided by the glass manufacturer (*dashed*) was rescaled for this purpose (using equation 9.2). **Right** subfigure features zoom to UV cut-off region. The horizontal *dashed* line marks the approximate position of "half-maximum" transmittace ($T = 45\%$) defining the cut-off location. Statistical errors were found to be smaller than linewidth.

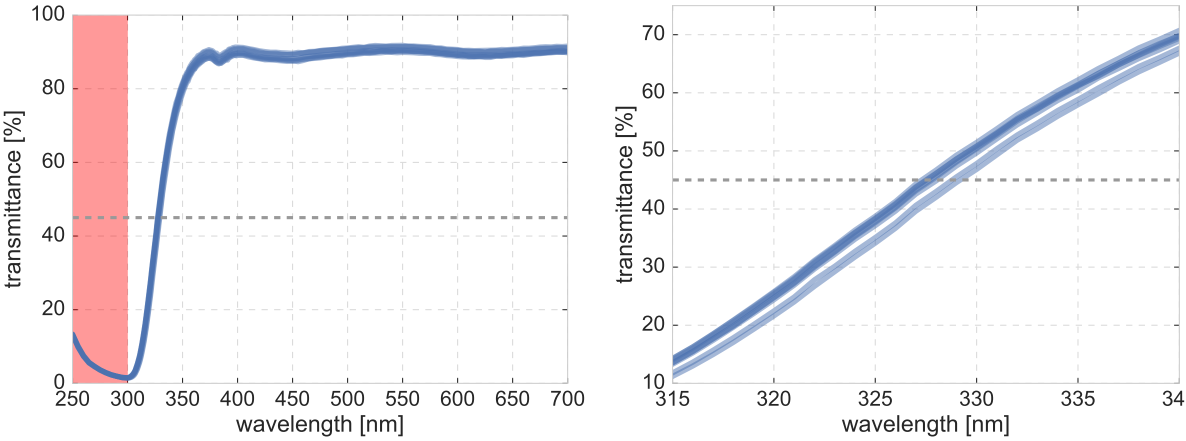

Figure 9.6: Transmittance characterization of KM3NeT pressure vessels: Cumulative data obtained from ten semi-vessels randomly chosen from a batch of 100 (**left**). In the optical range ($\lambda > 300$ nm) relative differences between individual spectra are below 2%. The position of the UV cut-off is stable up to few nanometers, ranging from ~ 326 nm to ~ 329 nm for all tested vessels. See zoom to relevant wavelength region (**right**). A horizontal *dashed* line marks approximate position of "half-maximum" transmittace ($T = 45\%$) used to derive the UV cut-off position. Due to the weak flux of the xenon light source at respective wavelengths, results below 300 nm (*red* shaded area) are considered not reliable. Statistical errors, on the ‰-level, invisible in the plot.

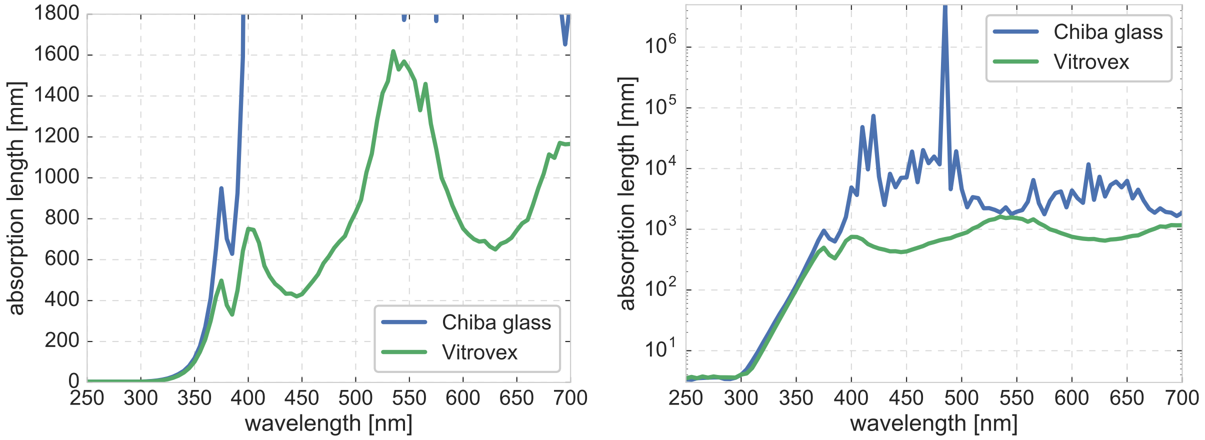

Figure 9.7: Absorption length spectra of Vitrovex and Chiba glass, in linear (**left**) and logarithmic representation (**right**). The values were derived from the transmittances presented in figure 9.5 numerically solving equation 9.6. For discussion of uncertainties see figure 9.8.

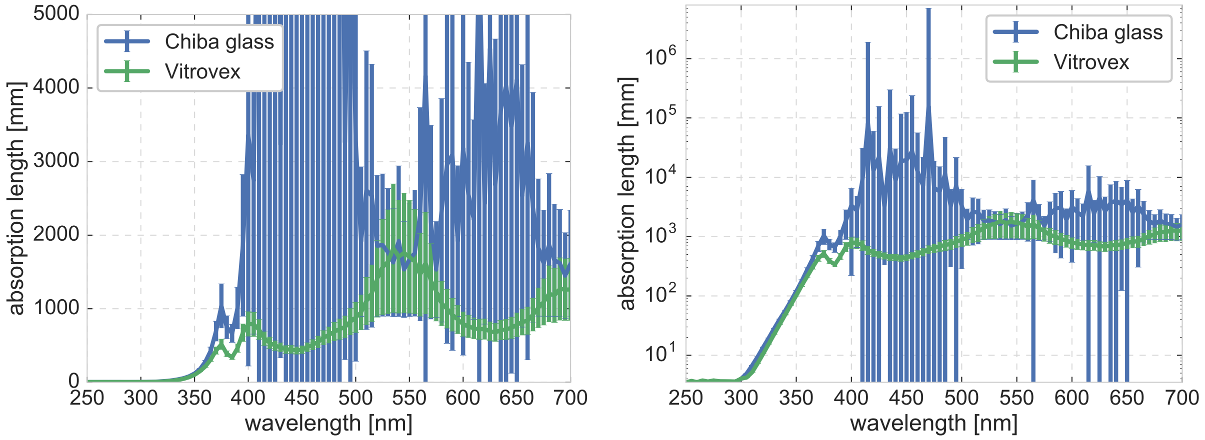

Figure 9.8: Impact of transmittance uncertainties on determination of the absorption length, presented on linear (**left**) and logarithmic scale (**right**). For both materials a relative transmittance error of 0.5% was assumed, representing the upper bound of uncertainty expected from observed run-to-run variability of the light source output. As discussed in the text, the impact is more pronounced for Chiba glass, featuring a superior transparency. Absorption lengths were derived from transmittance values using the first order expression from figure 9.4 allowing to analytically handle error propagation.

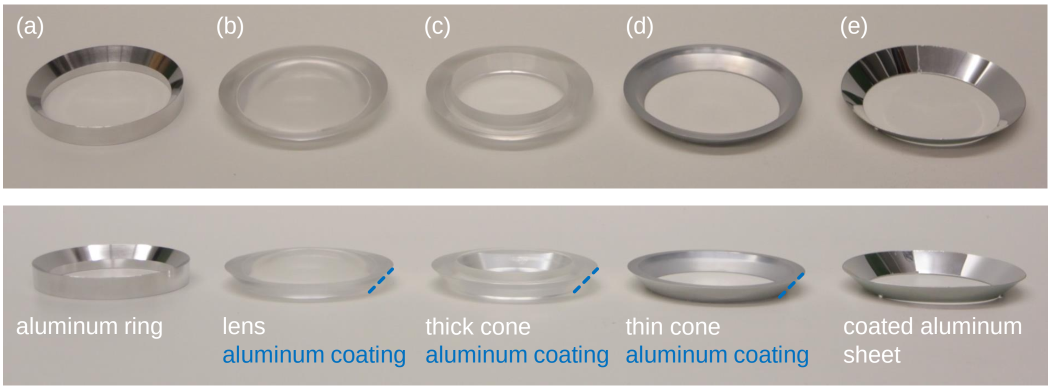

Figure 9.9: Evolution of reflector concepts, featuring KM3NeT reflector prototypes in chronological order of issue ((a) to (e)). Pictured specimen of types (b) and (c) lack reflective coating finish. The pre-production module, actually operated in the Mediterranean, was equipped with type-(d) reflectors. Type (e) represents the current default for the KM3NeT module as well as the mDOM.

effective "beaming" of the acceptance profile. This enables to reclaim photons that would otherwise be lost due to shadowing of the holding structure and/or neighboring PMTs or absorption occurring along the longer path trough glass and gel.

First reflector prototypes for KM3NeT where milled from massive aluminum blocks. In an attempt to reduce cost (and to fit the shape of the new hemispherical PMTs), it was replaced by a (likewise milled) PMMA lens with aluminum- or silver-coated edges. Casting the lenses from a more UV-transparent material, such as Zeonex, was also considered, but vetoed by potential manufacturers, expecting problems with the very thin material layer located at the tip of the cathode. Finally the development arrived, via thin metallized PMMA cones, at conical reflectors produced from aluminum sheets, featuring reflectance-enhancing coating. This solution came with a reduction of cost and production time as well as a minimization of photon losses in the UV region. Measurements of reflectivity spectra of available cone materials, which contributed to finalizing the choice, are presented in the following section. The evolution of reflector production concepts is illustrated in figure 9.9.

The benefit from the use of reflectors can be assessed measuring their effect on the angular acceptance. A further possibility is scanning the aperture using a pencil beam[1]. Corresponding measurements have been undertaken e.g. in an extensive campaign at Nikhef, when first introducing the idea to use such devices in the KM3NeT optical module [192], and by J. Reubelt at ECAP testing the, then-current, PMMA lens version. As these earlier layouts were finally discarded, measurements using the aluminum sheet version of the KM3NeT cone were performed by the author in collaboration with R. Frytz, and are documented in his Bachelor's thesis [193]. A further update was needed after production of first dedicated mDOM reflectors. Corresponding results are presented in section 9.2.2.

Initially, the opening semi-angle of the KM3NeT cone was 45°. This value, optimized in ray-tracing simulations for vertical photon incidence [192], was also used in the baseline

---

[1] Narrow beam scans of reflector-equipped PMTs were performed by the author in the scope of measuring the output uniformity. Results are presented in section 5.2.

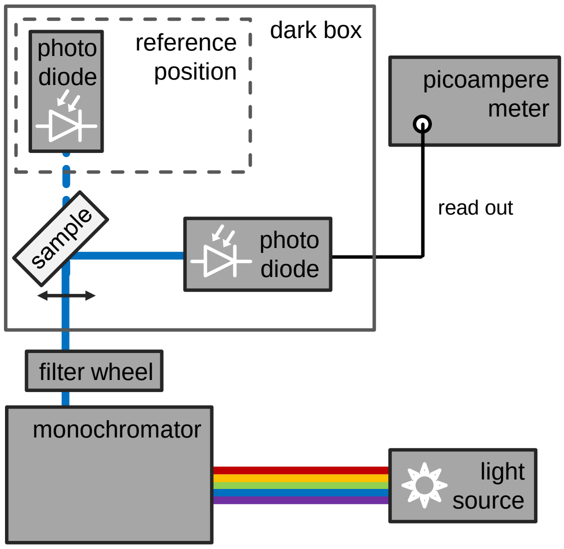

Figure 9.10: Experimental setup for material reflectance characterization. Reference measurements are performed placing the photodiode in the marked position after removal of the material sample. PC controlling monochromator, filter wheel and picoampere meter via Python scripts omitted.

design of the mDOM. A dedicated study revisiting the effect of the opening angle is presented in section 10.4.1.

9.2.1 Material reflectivity

Following the decision in favor of thin metal cones, an assessment of the reflective properties of the materials in question became necessary. Coated aluminum sheets as well as adhesive metal foils were scrutinized in collaboration with J. Reubelt.

Setup

The tests were performed using components of the quantum efficiency test stand introduced in section 5.1.5. The actual setup is shown in figure 9.10. Material samples were placed into the output light beam of the monochromator at an inclination of 45° with respect to the light incidence direction[1]. The photodiode was located at the emergent angle of the light to measure the photocurrent I_{ref} induced by the reflected fraction. A reference measurement placing the photodiode inside the beam provided a measure of the incident light intensity I_0. The reflectivity spectrum was then derived using

$$R(\lambda) = \frac{I_{\mathrm{ref}}(\lambda)}{I_0(\lambda)} \tag{9.7}$$

Both currents were corrected for dark current contributions, subtracting an average of current values taken before and after the main measurement with the shutter closed.

Results and conclusions

Figure 9.11 features the obtained reflectivity spectra for all materials under investigation, while average (weighted) reflectances are presented in table 9.1. The latter were derived

---

[1] As a cone angle of 45° was considered the baseline value at that time based on simulation studies.

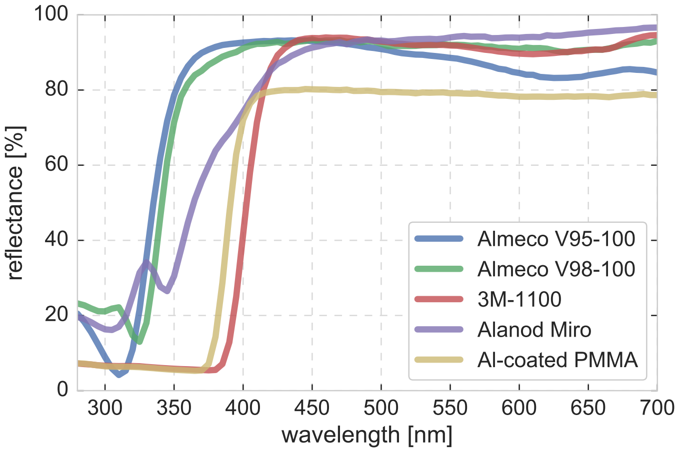

Figure 9.11: Measured reflectance spectra of potential reflector materials. Statistical errors, on the ‰-level, are smaller than the linewidth.

reflector material	average weighted reflectance [%]			
	uniform	quantum efficiency	Cherenkov spectrum	Cherenkov spectrum & quantum efficiency
Almeco V95-100	78	11	67	12
Almeco V98-100	80	11	68	12
3M-1100	67	8	48	7
Alanod Miro	77	10	62	10
Al-coated PMMA	60	8	45	7

Table 9.1: Average reflectances of the tested materials. For details on the applied weighting factors, see discussion in text.

integrating (and normalizing) the measured spectra in a wavelength range between 280 nm and 700 nm, after application of quantum efficiency $QE(\lambda)$ and/or uniform or Cherenkov-based spectral weighting $w(\lambda)$:

$$R_{\text{mean}} = \frac{1}{N} \int_{280\,\text{nm}}^{700\,\text{nm}} [QE(\lambda)] \cdot R(\lambda) \cdot w(\lambda)\, d\lambda, \quad N = \int_{280\,\text{nm}}^{700\,\text{nm}} w(\lambda)\, d\lambda \tag{9.8}$$

For quantum efficiency scaling the property of the KM3NeT default PMT (Hamamatsu R12199-02) was used, while Cherenkov-weighting was based on an approximate radiation spectrum:

$$w_{\text{Cherenkov}}(\lambda) = \frac{1}{\lambda^2} \cdot \left(1 - \frac{1}{n(\lambda)}\right) \tag{9.9}$$

where $n(\lambda)$ is the refractive index of the deep clear ice.

Based on these figures of merit Vega95-100 by Almeco, a 0.5 mm enhanced-reflectivity aluminum sheet, was chosen for reflector production in KM3NeT. While the KM3NeT decision was based upon the results of quantum efficiency scaling, additional Cherenkov-weighting also favors the same material. Moreover, it is also cheaper than the second best candidate, Vega98-100.

Comparing the obtained results to data provided by the manufacturer [194], see figure 9.12, a good reproduction of the position of the short-wavelength cut-off (within ∼ 5 nm) is

Figure 9.12: Reflectance of Alemco materials: Comparison of measured spectra (*solid*) to data provided by the company (*dashed*). Horizontal *dashed* line marks approximate position of "half-maximum" reflectance ($R = 48\%$) used to derive the UV cut-off position. Values in the wavelength range marked *red* are considered preliminary by company engineers and can be subject to further optimization in the future [194].

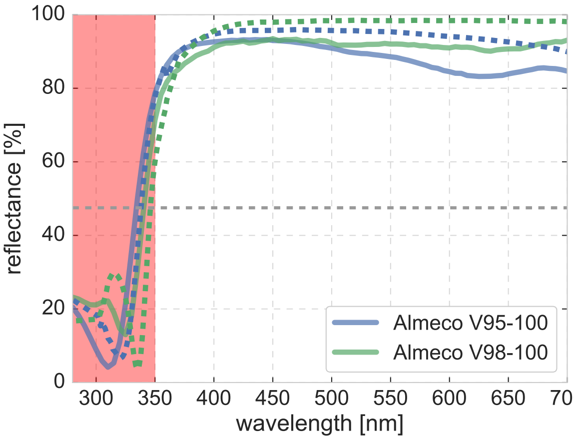

observed, while reflection values in the optical range are lower in general, featuring relative deviations up to $\sim 10\%$. This can be attributed to a systematic effect: The reference measurement by the manufacturer was done using a professional Ulbricht sphere setup. This results in the diffuse component of the reflection, although supposedly small, being included in the reported overall reflectivity. In our setup this was not the case. Another potential source of the deviation was the sample preparation: Being cut manually the material specimen may not have been perfectly flat, thus increasing the amount of diffuse reflection.

The reflectivity spectra of available cone materials were also important input parameters for the Geant4 module simulation introduced in chapter 10. Values provided by the manufacturer[1], deemed more reliable, were used for this purpose. Including all relevant optical properties and interfaces, the simulation was also used to revisit the choice of reflector materials in terms of the performance of a complete optical module in ice (see section 10.4.1).

9.2.2 Angular acceptance

The shape of the angular acceptance of a PMT is of interest in its own right but was also used e.g. as input for detector simulations using IceTray (see section 10.5) and to assess validity of the Geant4 module simulation, as discussed in section 10.3. The topic is addressed in the scope of this chapter as the angular acceptance is strongly modified by the utilization of reflectors.

Setup

Measurement of the angular acceptance (given e.g. in terms of an angle-dependent effective area or relative sensitivity) requires a plane wave illuminating the PMT at different incidence angles. In practice, this condition was met positioning a diffusor-equipped LED

---

[1] In addition to the reflective spectra measured in air (presented in figure 9.12) the manufacturer was also so kind as to provide modified spectra assuming a gel environment based on the refractive index of the Chiba gel (see section 9.1).

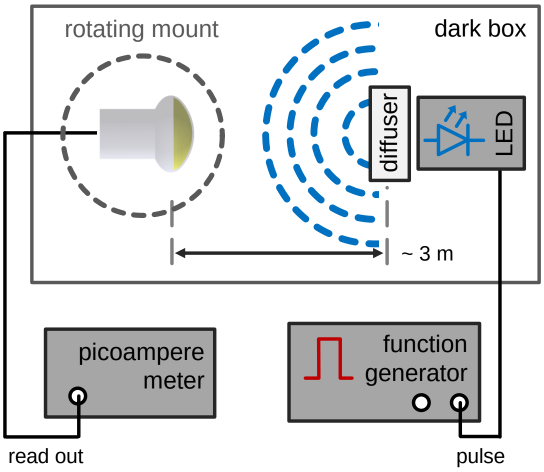

Figure 9.13: Setup of the angular acceptance measurement in current mode. The rotating mount was operated via Python scripts by a PC (not shown) also logging picoampere meter data. In pulse mode an oscilloscope was used for waveform acquisition, triggered externally by the function generator. For a photograph of the actual setup see figure 9.14.

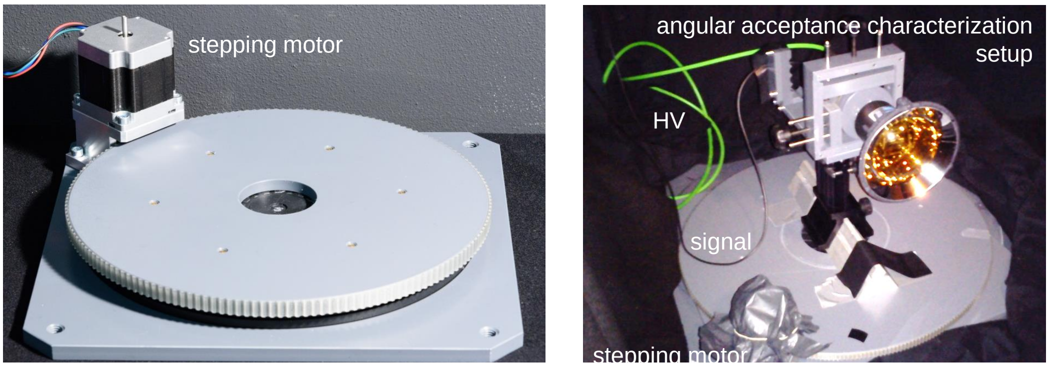

Figure 9.14: Remote controlled rotator used in the angular acceptance characterization. In operation the motor was covered to prevent reflections.

(featuring a wavelength of $\lambda_{\text{LED}} \approx 470\,\text{nm}$ [1]) at a sufficiently large distance from the PMT. A distance of approximately three meters, available in the largest of the light-proof chambers at ECAP, was found to satisfy the far field approximation. The LED was driven using a function generator. The PMT was placed on a horizontally rotatable mount, thus allowing to measure the angular dependence of the effective area. In addition, the PMT could be equipped with a reflector mount. This device, identical to a section/cut-out of the PMT mounting structure of the module, was produced from polyamide using rapid prototyping (see section 8.2). The angular acceptance measurement was carried out for PMTs of type **R12199-02** by Hamamatsu and **9320KFL** by ET Enterprises in three configurations:

- Using a **bare PMT**,
- a PMT provided with a reflector **mounting structure**, as well as
- a fully equipped PMT with **mount and reflector**.

---

[1] Marking the maximum of the Cherenkov emission spectrum after convolution with the transmission of sea water, this wavelength is used as a standard reference when stating PMT performance by the KM3NeT and ANTARES collaborations.

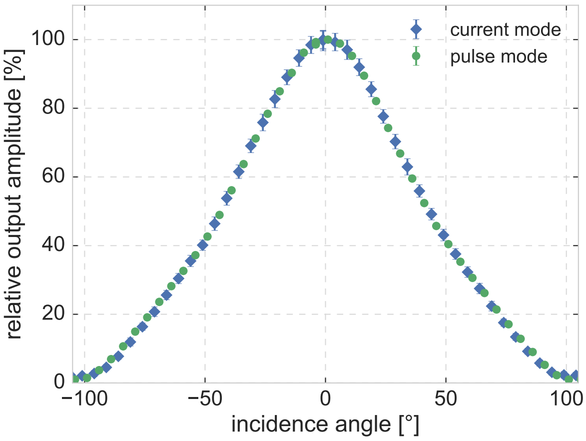

Figure 9.15: Relative angular acceptance of a reflector-equipped PMT (Hamamatsu R12199-02) determined independently in a pulse mode and a current mode measurement. Errorbars indicate statistical uncertainties based on fit uncertainties of the mean photoelectron level or current standard errors, respectively.

While in case of the ETEL tube only one custom-designed and custom-made mDOM reflector was investigated, three reflector models, with corresponding mounts, were available for the Hamamatsu PMT:

- A preliminary **hand-made** reflector (originally intended as a test for KM3NeT),
- a dedicated **mDOM design**, as well as
- the current **KM3NeT reflector**, featuring an opening angle of 48°.

A resistive base was used to supply negative polarity[1] voltage to the PMT, which allowed the usage of both read-out modes[2] for data acquisition:

- In **pulse mode** waveforms were recorded using an oscilloscope, externally triggered by the reference signal of the function generator. The signal amplitude corresponded to the mean charge of the waveform, which was retrieved as in section 5.1.1.
- When operated in **current mode**, the signal of the PMT was read out by means of a picoampere meter, with the current value taking the role of the amplitude (see figure 9.15).

While the signal is recorded background-free in pulse mode, due to external triggering, the dark current contribution has in principle to be measured and subtracted in current mode. On the other hand, current mode allows to speed up the measurement process significantly, as the current output can be monitored and evaluated “on the fly”, with no need of off-line data extraction from stored waveforms. In both cases the respective signal amplitude was recorded as a function of the incidence angle.

In principle, pulse mode is closer to the final use-case in the module, extracting charge amplitudes from digitized waveforms. However, as both approaches were found to deliver identical results (in terms of the shape of the angular acceptance curve as demonstrated in figure 9.15), the current mode measurement became the method of choice. A schematic overview of the setup in the latter configuration is presented in figure 9.13.

---

[1] See section 3.4 on PMT voltage polarities.

[2] Find PMT operation modes explained in detail in section 3.3.

A moderate illumination level of < 10 photoelectrons with an LED pulse length of 20 ns was used so that saturation of the PMT was not an issue[1]. To marginalize the contribution of dark current in DC mode the LED was operated at a rather high pulse frequency of 5 MHz. This way, the relative dark current was on the order of ‰ allowing to be neglected safely. A potential contribution of afterpulses (see section 3.7) being on the low % level and moreover proportional to the signal amplitude, was deemed unproblematic.

Initial measurements were performed making use of an already available mount, originally designed for angular scans of ANTARES optical modules. Apart from being stationary (built into a table), this setup features some drawbacks, among them the limited angular range and the impossibility to correct angular errors[2]. To cope with this problem a compact mobile revolvable mount, depicted in figure 9.14, was produced customizing a commercially available screen pedestal. To enable unlimited rotation an inverted closed-loop tooth-belt was attached to the outer rim. A powerful motor was used to minimize step missing, equipped with an optical encoder on the rotation axis. The latter device allows to measure the actual rotation of the motor and correct for missing steps.

Evaluation

The experimental setup laid out above allowed to measure the angular dependence of the PMT's output amplitude, either as an average pulse charge or in terms of a mean current value. Due to the significant reduction in testing time, all results discussed below were obtained in current mode. As mentioned earlier, dark current contributions could be safely neglected.

A non-vanishing amplitude measured in positions facing away from the light source was interpreted as the impact of stray light reflected from the (black) walls of the dark room as well as other components of the setup. Its contribution was found to be significantly larger than that of the dark current (ca. 50 times larger), still amounting to only 0.5% of the amplitude measured at perpendicular illumination. It was eliminated subtracting a constant value derived averaging the amplitudes of the maximum and minimum incidence angles[3]. Typically on the 0.1% level, statistical uncertainties (propagated from standard errors of the current measurement) were much smaller than amplitude differences between positive and negative versions of the same incidence angle, which could be up to 18% (in the most extreme case, see figure 9.17). These discrepancies are supposed to be a cumulative result of potential systematic uncertainties, such as a non-constant (in particular angle dependent) stray light field not covered by the correction measures, problems with cable contacts during PMT rotation, poor alignment of reflector mount and the reflector itself, or, last but not least, an actual asymmetry of the PMT's angular acceptance.

---

[1] As discussed in section 7.2, the PMT output is linear up to at least ~ 500 photoelectrons per pulse in these conditions.

[2] The setup features a pivoted cog-equipped PMMA disc actuated via a stepping motor. As the cogs are not carved into the disc material, but added by gluing an open tooth-belt to the outer rim, there is a joint which prevents a full revolution. Due to friction in the system the relatively weak motor misses some steps from time to time on a random basis. It is not possible to predict, monitor or correct this effect as only the "ordered" number of steps is available to the remote-control script, resulting in a distorted measurement.

[3] In the applied convention vertical photon incidence corresponds to $\theta = 0°$ while rotated positions were assigned positive or negative values, depending on the direction.

Stepping errors of the motor, observed in earlier versions of the setup, could be excluded from the error budget.

As the design of the experiment did not include precise alignment with the light source, the position of vertical light incidence ($\theta = 0°$) had to be derived from data. This was achieved fitting a parabola to a range of $\pm 15°$ around the observed amplitude maximum. Based on the fit parameter errors ($< 0.1°$), the approach is not believed to significantly degrade the overall angular positioning precision of 0.2°.

An unpleasant feature of the setup was the observed (long-term) instability of the LED prohibiting a direct comparison of measurements. With the picoampere meter featuring a single input channel, a simultaneous reference measurement (using a photodiode or another PMT) of the light-field was not viable[1]. To yet enable comparison, a scaling factor was derived, a-posteriori, form measurement data on the same PMTs in different setups as follows:

- The measurement of the **bare PMT** was used as a **reference template**. Normalization to the amplitudes to the vertical incidence value also allowed inter-PMT comparisons.
- Featuring an acceptance curve identical to that of a bare PMT for small photon incidence angles, while behaving like a reflector-equipped tube at large angles, dominated by shadowing of the mounting structure (see e.g. figure 9.16 for an illustration of this behavior), the measurement of the **holder-equipped PMT** provided a natural **link** between the respective setups. It was scaled using a factor derived in the central angle region.
- Results of the **reflector-equipped PMT** were then **scaled** to coincide with the curve of the holder-equipped tube at large angles.

After this data treatment procedure the measurements could be translated to a relative angular acceptance $A_{\mathrm{rel}}(\theta)$ of the corresponding PMT setup:

$$A_{\mathrm{rel}}(\theta) = \frac{I(\theta)}{I_{\mathrm{bare\,PMT}}(0°)} \tag{9.10}$$

where θ is the (corrected) photon incidence angle, $I_{\mathrm{bare\,PMT}}(0°)$ the (stray-light subtracted) amplitude at frontal illumination, and $I(\theta)$ the output amplitude at the particular angle, after stray light subtraction and scaling.

Relative acceptance results for the ETEL PMT are presented in figures 9.16 and 9.17, while figures 9.18 and 9.19 feature the curves for the Hamamatsu tube outfitted with various reflectors. Showing the acceptance as a function of the absolute value of the photon incidence angle, the respective latter plots allow to assess acceptance symmetry (and also the quality of the applied zero-point correction).

In order to obtain an independent cross-check of the results, as well as the data processing approach, the relative acceptance obtained for head-on illumination of reflector-equipped PMTs was compared to the corresponding value derived from the anode output scans, introduced in section 5.2. Respective results are summarized in table 9.2. The values agree

---

[1] The setup constructed in Münster, featuring such a monitoring possibility, will allow to revisit the angular acceptance more precisely.

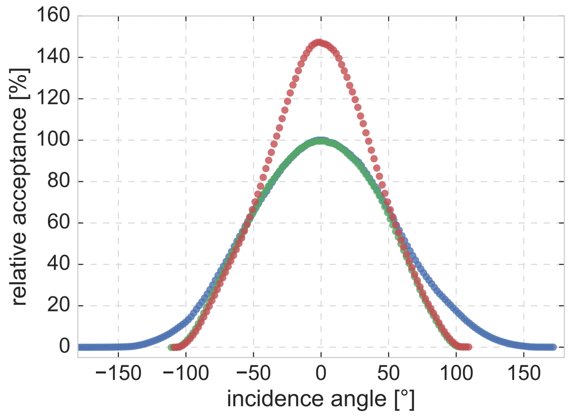

Figure 9.16: **ETEL 9320KFL**: Relative angular acceptance of the bare PMT (*blue*), a PMT inserted in the mounting structure (*green*), as well as a reflector-equipped PMT (*red*). Values are normalized to the acceptance of the bare PMT for vertical photon incidence. Statistical uncertainties were measured to be smaller than data markers.

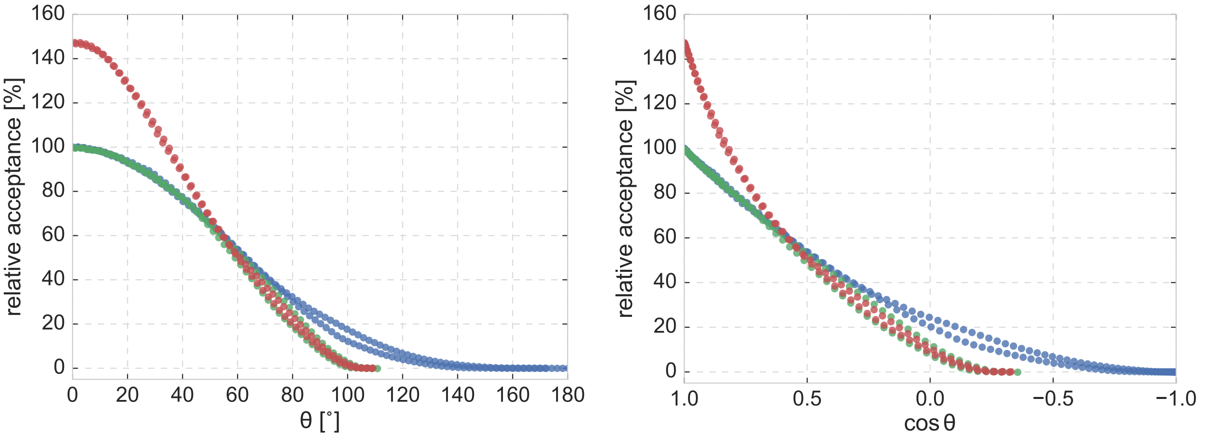

Figure 9.17: **ETEL 9320KFL**: Relative angular acceptance in different configurations (for nomenclature see figure 9.16) shown as a function of the absolute values[a] of the photon incidence angle θ (**left**) as well as its cosine (**right**).

---

[a] The observable acceptance discrepancy between the positive and the negative version of the same incidence angle is treated in the text in the wake of a discussion of setup uncertainties.

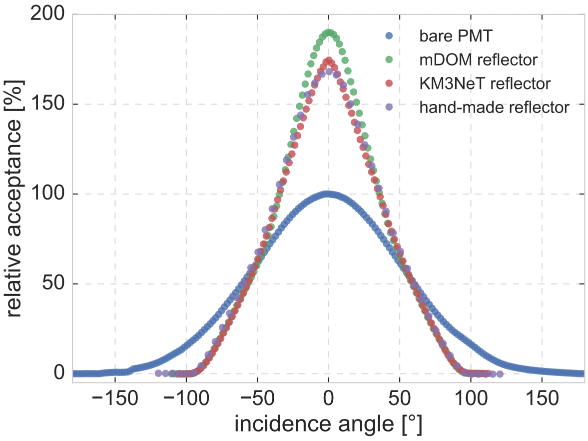

Figure 9.18: **Hamamatsu R12199-02**: Relative angular acceptance of the bare PMT compared to the tube equipped with different reflector models (see text for details). For the sake of clarity, setups featuring the respective reflector mounts only (see e.g. figure 9.16) are omitted. Acceptances are normalized to the bare-PMT value for vertical photon incidence. Statistical uncertainties were measured to be smaller than data markers.

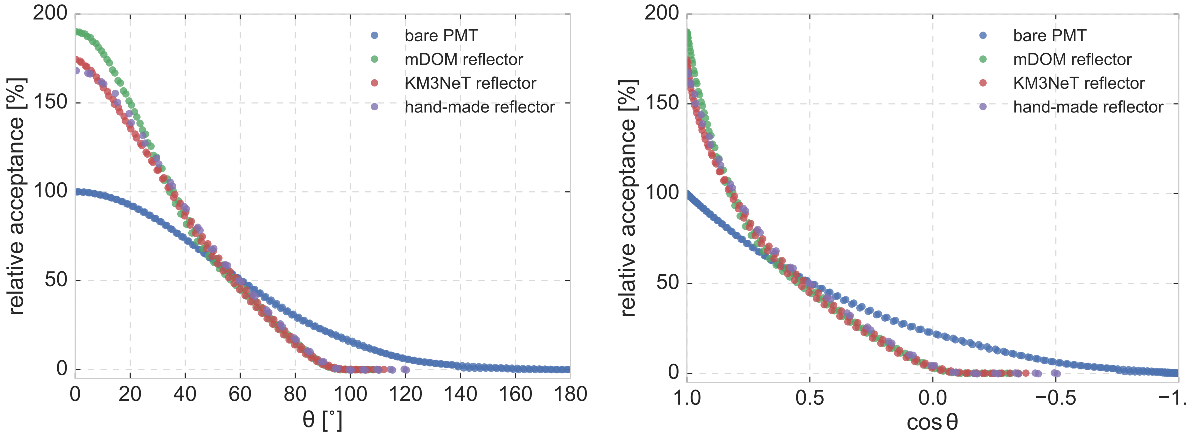

Figure 9.19: **Hamamatsu R12199-02**: Relative angular acceptance in different configurations shown as a function of the absolute values of the photon incidence angle θ (**left**) as well as its cosine (**right**).

PMT type	reflector	$A_{\mathrm{rel}}(0°)$ [%] x/y scan	$A_{\mathrm{rel}}(0°)$ [%] angular scan	relative deviation [%]
Hamatsu R12199-02	hand-made	-	168	-
	KM3NeT	177	175	1
	mDOM	186 [191]	190	2 [1]
ETEL 9320KFL	mDOM	146	147	1

Table 9.2: Sensitivities of reflector-equipped PMTs for vertical illumination, normalized to the values for the respective bare tubes. Featuring a comparison between figures of merit derived form a pencil beam x/y scan of the anode output (values in brackets were derived using the “pinhole” setup, deemed less reliable, see section 5.2 for a detailed discussion) and the angular acceptance scan, object to the current section. Deviations are given relative to the angular scan results.

PMT type	reflector	average sensitivity [%], relative to **bare PMT**	 **holder mounted**
Hamamatsu R12199-02	hand-made	96	118
	KM3NeT	92	119
	mDOM	94	121
ETEL 9320KFL	mDOM	95	114

Table 9.3: Impact of the utilization of reflectors on the average PMT sensitivity, shown for different PMT and reflector models. Average sensitivities of reflector-equipped PMTs are set in relation to values obtained for bare tubes as well as PMTs featuring a reflector mounting structure (see respective columns). For a review of the numbers see discussion in text.

remarkably well within few percent. Remaining minor discrepancies can be attributed to systematic effects, such as slight differences in PMT pointing between the setups[1] and the bending precision of the reflectors, but also small uncertainties inherent to the scaling technique applied to the angular data.

Solid-angle averaging of the relative angular acceptance $A_{\mathrm{rel}}(\theta)$ using

$$A_{\mathrm{mean}} = \frac{1}{N} \int\limits_{|\theta|=0}^{|\theta|_{\mathrm{max}}} A_{\mathrm{rel}}(\theta) \cdot |\sin\theta| \; d\theta, \qquad N = \int\limits_{0}^{2\pi} |\sin\theta| \; d\theta \tag{9.11}$$

allowed to assess the impact of reflector utilization on the (overall) sensitivity of the PMT in a more comprehensive manner: Table 9.3 features a comparison of the average relative acceptance between bare, holder-mounted and reflector-equipped PMTs for both tube models. As mentioned earlier, no net gain is to be expected from the use of reflectors if the total solid angle is considered as these devices, in the most ideal loss-less case, merely redistribute the sensitivity of the sensor. This expectation is very well met by the comparison between reflector-equipped and bare PMTs. The major part of the observable losses, amounting to 4% to 8%, depending on reflector and PMT model, can be traced back to the reflectivity of the cone material which is $\sim 95\%$ at the wavelength used in the study, and non-reflecting parts of the mounting structures.

However, the term “sensitivity loss” might be misleading, as in practice, referring to a PMT built into an optical module, only a part of its overall angular sensitivity is available. Incidence angles larger than $\sim 100°$ would be shadowed by the PMT mounting structure even in the most optimistic design, while, in a more realistic approach, the need to economize the costly optical gel would lead to a further reduction of sensitivity. Reflectors effectively reclaim this, otherwise lost, sensitivity. The situation can be approximated comparing the results obtained for a reflector-equipped PMT to the average sensitivity of a tube featuring a mounting structure only. Utilization of reflectors in this case yields an enhancement of the overall sensitivity by $\sim 20\%$ (see table 9.3).

Out of curiosity, the use of a matte white (unpainted) mounting structure was also in-

---

[1] Based on the relative acceptance curves e.g. a misalignment of 5° will reduce the output amplitude by $\sim 3\%$.

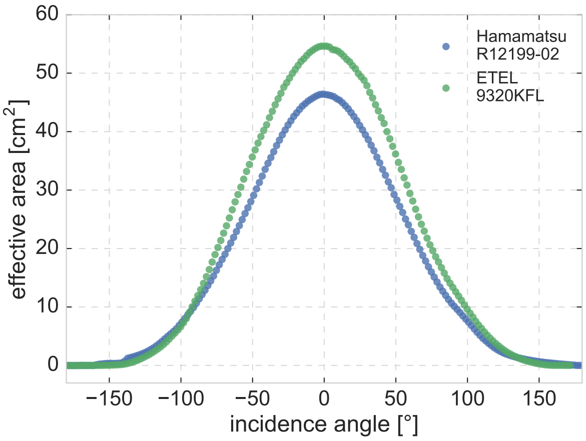

Figure 9.20: Angular dependence of the effective area shown for both PMT models under investigation. Values are based on respective relative acceptance curves (see figures 9.16 and 9.18) weighted by the effective areas for vertical photon incidence (derived from x/y scans of the anode output, see section 5.2). Statistical uncertainties are smaller than data markers.

vestigated. It results in an increase of vertical incidence sensitivity by 3% but an overall sensitivity enhancement (compared to a black version of the mount) of only 1% (see also discussion on mounting structure colors in section 10.4.2).

A comparison between the average relative sensitivities of both PMT models indicates that the ETEL tube has a slightly more favorable shape (or collection efficiency profile), resulting in a gain of 2% with respect to the Hamamatsu model. For a more profound comparison of the models, the relative acceptance was weighted with the frontal effective area of the respective PMTs[1] resulting in the angle dependent effective areas presented in figure 9.20. Based on these numbers, the employment of the larger ETEL tube yields an increase of the solid-angle averaged effective area, equivalent to the overall sensitivity, of 20% with respect to the default Hamamatsu PMT.

The three experimental setups (bare PMT and PMT inside a holder, with and without reflective cone) were also reproduced in Geant4, to validate the simulation approach[2] (see section 10.3). For the same purpose, study results were shared with C. Hugon, who is in charge of KM3NeT optical module simulations.

9.3 Conclusions

The characterization of passive optical components reported in the scope of the current chapter yielded valuable information on key properties of respective materials.

The investigation of potential reflector materials contributed to the decision in favor of Vega95-100, an enhanced-reflectivity aluminum sheet, for the KM3NeT optical module based on its quantum efficiency weighted average reflectivity, also indicting its suitability for the mDOM project. For a more profound final choice, taking into account the collective impact of all mDOM components, the reflectivity spectra of relevant materials were also incorporated in a detailed Geant4-based simulation model of the mDOM, introduced in the following chapter.

---

[1] derived from x/y scans of the anode output (see section 5.2)

[2] In case of the Hamamatsu PMT the dedicated mDOM reflector was produced too large, based on a misunderstanding with the colleagues from the mechanics workshop. For the verification of the simulation a measurement of the old hand-made reflector was used, as its dimensions were found to be more realistic.

The obtained absorption length spectra for potential pressure vessel glasses provided further input for the simulation, ultimately leading to decisions in concerning the mDOM design elaborated on in section 10.4.

10 Optical module simulations

As introduced in chapter 4, the development of the mDOM began with the idea to take advantage of the features of the multi-PMT concept in IceCube-Gen2. Before constructing the module however, some elaboration on the impact of those features was needed. In particular, a quantification of the

- overall gain from increased **effective area**,
- the homogeneity of the **angular acceptance** of the new module, and
- a demonstration of **directionality**

were of interest.

Also optimization studies were required to make final design decisions, e.g. concerning the opening angle of the reflective cones. Another topic of interest was the impact of using glasses and gels other than the KM3NeT defaults[1].

As a straight-forward simulation of optical processes using COMSOL Multiphysics$^{\mathrm{TM}}$(used to assess pressure vessel stability, see section 8.1) was not possible at the beginning of the work[2], Geant4[3] was chosen, after some research. This Monte-Carlo toolkit, introduced in more detail in the following section, apart from being (unlike COMSOL) free of charge, comprehensive, and widespread in the particle physics community, was already in use at ECAP, developing a simulation of ^{40}K optical background in the KM3NeT module [195]. The attractiveness of choosing a fully-fledged physics Monte-Carlo instead of some specialized optics code, such as e.g. SLitrani [196], lay in the possibility to enhance the simulation, adding further particles, processes and functionality, to cover other physics problems in the future.

The mDOM simulation began as a purely optical spin-off from the ^{40}K simulation, borrowing applicable code from this project[4]. In its final stage, it lead to the creation of an interactive multi-purpose simulation tool, capable of assessing optical properties of the module(s)[5] in various setups as well as study the **impact of radioactive decays** in the glass of the vessel.

---

[1] Which for instance are Vitrovex and Wacker 612 A/B, see chapter 9.

[2] Eventually, a ray-optics module was added to COMSOL in mid-2014.

[3] GEometry ANd Tracking

[4] Special thanks to B. Herold for providing the code as well as substantial support and counsel.

[5] In the course of the development, simulations have been performed for the mDOM in its initial cylindrical configuration as well as in the final spherical version (see chapter 4). For comparison purposes the standard single-PMT IceCube module (see section 2.2.3), was also modeled. With the ultimate obsolescence of the cylinder, only results concerning the latest mDOM version and the IceCube module will be presented in the scope of this chapter. Intermediate results on the cylindrical layout can be found in dedicated publications [135, 24].)

10.1 Simulating with Geant4

Geant4 is an extensive software toolkit for the simulation of virtually all physics aspects of the passage of particles through matter. Originally developed for CERN and KEK, the tool is currently used in a variety of scientific fields, spanning from high energy particle physics over nuclear and accelerator physics to medical and space applications. The object oriented C++ code is freely available under the GPL license and continuously developed by a dedicated collaboration [197, 198]. The software was designed to cover all aspects relevant for a particle physics simulation, such as

- geometrical layout of the **experiment**,
- properties of the used **materials**,
- injection of **particles**,
- **interactions**, including secondary particle production,
- extraction of **results**, and
- **visualization** of the detector setup and particle trajectories.

A comprehensive set of physics models, ranging from simple optical to electromagnetic to complex baryonic interaction processes, compiled from various sources, and valid for a wide range of particle energies, is included in the Geant4 core. The driving idea is to relieve the user from the need to implement the details of a physical process, allowing to concentrate on detector design and physics. The user is required to define the detector layout, the particles to be taken into account together with applicable physics processes, define the manner of the read-out and finally provide the initial particles, which can be done either using a dedicated primary generator class or using the scripting language of the so-called “general particle source”, which is the method of choice for a straightforward creation of sophisticated beam profiles.

10.1.1 Detector construction

Geometry definition in Geant4 is a three-steps process. In the beginning a so-called **solid** volume needs to be defined, defining the geometrical form and dimensions of a detector element. The user has the choice between a sample of primitive volumes, such as cubes, spheres, cylinders, and cones but also more sophisticated ones like e.g. twisted trapezoids. The primitives can be manipulated using a set of boolean operations (union, intersection, subtraction) in order to create more complicated geometries. As an alternative, importing volumes generated with CAD software is also possible.

In the next step a **logical** volume is created assigning physical properties, such as chemical composition, density, or refractive index, to a solid. Several logical volumes can be derived from the same solid.

The final step is the placement of the logical volume into the simulated “world”, defining the position and orientation with respect to a reference frame as well as its “mother volume" (see below for explanation). Again it is possible to place one logical volume multiple times, creating several identical **physical** objects at different positions.

There is, however, one restriction concerning the positioning: Newly placed volumes (**"daugthers"** in Geant terminology) are required to be fully contained inside already existing ones (their **"mothers"**). It is in particular not possible for a volume to protrude from one volume into another and share boundary surfaces with more than one volume in Geant4, a behavior still allowed in earlier versions of the software. As a result, the final setup is a hierarchical sequence of daughter volumes nested inside their respective mother volumes, much like a matryoshka doll. The "mother of all volumes", comprising the entire setup to be simulated, is referred to as the **world volume**. It is the only volume that is placed without any further information.

10.1.2 From primary particles to detector response

Although the implementation of the physics models is taken care of by Geant4, the user is required to compile a so-called **physics list** including all processes/interactions relevant for the particular simulation, as well as all potential sorts of particles, be it primaries or secondaries. This approach is very versatile, allowing the user to e.g. define energy cuts on particular interactions or limit the production of secondary particles to the most interesting ones. Geant4 does not provide any "default" physics behavior intentionally forcing the user to make an explicit decision on this topic. Nevertheless, there is a number of standard pre-compiled physics lists, optimized for certain applications, which can be included without further modifications.

Processes taking place in the detector are simulated in a hierarchically segmented approach: On the highest level a **run** can consist of a number of events. An **event** object comprises time-stamped information, such as trajectory and total energy development, on all primary emitted particles as well as those generated in interactions. Trajectories and supplement information for an individual particle are contained in a **track** object. Each track is again subdivided into so-called **steps**. The impacts of physics processes, such as energy loss, change of direction, emission of new particles, or the decay of the primary, are usually evaluated at the step level, with the length of a step being given by the shortest of the interaction lengths of all applicable processes. There are however exceptions from this general rule: steps, for example, always end at optical border surfaces in the case of optical photons, enabling the proper simulation of refraction, reflection, and scattering. By means of dedicated classes (SteppingAction, TrackingAction etc.) the user is given the opportunity to interfere with the processes or to extract information on each particle, such as position, direction, or energy. An event comes to its end with the destruction of the last constituent particle, primary or secondary. Destruction of particles occurs either in physics interactions, by a particle parameter (e.g. energy) falling below a predefined threshold, resulting in cease of tracking, or by departure of the particle from the world volume.

The high level of detail results in long calculation times, which can be counter-acted using parallel computing, on a high-performance grid.

For a software toolkit, being free of charge and at the same time very versatile comes at a cost: Geant4 is far less user-friendly and not that well documented compared to a commercial product, such as COMSOL. The user can also expect to run into some bugs along the way, but the online user forum is very helpful and developers are grateful for reports helping to improve the code.

10.2 Gen2 module simulation tool

In its (currently) final configuration the module simulation toolkit, developed in the scope of this thesis, consists of three sub-programs, each dedicated to a specific task:

- **mdom_scan_angular** is used to assess the angular acceptance of the module, in terms of an effective detector area as a function of the angle of incidence of a plane wave front. For this purpose a disc, emitting mono-energetic photons perpendicular to its surface with a constant density profile across the plane, is used to emulate a plane wave illuminating the module. The effective area A_{eff} is derived from the stored number of detected photons N_{det} as

  $$A_{\text{eff}}(\theta, \varphi) = \frac{N_{\text{det}}(\theta, \varphi)}{N_{\text{emit}}} \cdot A_{\text{rad}} \tag{10.1}$$

  where the number of emitted photons is N_{emit} and A_{rad} is the area of the radiating plane. The user provides the number of emitted photons, together with their wavelength, the diameter of the source and its distance from the center of the module, as well as the incidence direction of the plane wave in terms of θ (zenith) and φ (azimuth). The approach is illustrated in figure 10.1.

- **mdom_scan_xyz** provides a "pencil beam", that is to say, a small-diameter monochromatic source of parallel photons, mimicking a laser. In addition to defining color, diameter, direction and intensity (number of photons), the user can place the beam at an arbitrary position, providing its x-, y- and z-coordinate. From the registered fraction of the emitted photons a local detection efficiency can be derived. The utilization of the tool to simulate a linear scan of a PMT the is illustrated in figure 10.2.

- **mdom_scan_K40** is used to study the impact and signatures of a user-defined number of ^{40}K decays. Unlike the situation in KM3NeT studies, the decay locations are confined to the glass vessel as no contribution is expected from the ancient glacial ice. Inside the glass volume the positions are randomly distributed. For an illustration see figure 10.3.

All input parameters mentioned above are supplied by the user via command-line arguments, permitting to change the setup on a run-to-run basis without the need of recompiling the code. In addition to the parameters specific to a task, there are also a number of common ones to choose from:

- **module type**: The final version of the mDOM as well as a single-PMT IceCube module can be simulated[1]

---

[1] The initial version of the code included the cylindrical mDOM layout. As it was finally discontinued, this model was also dropped from the simulation.

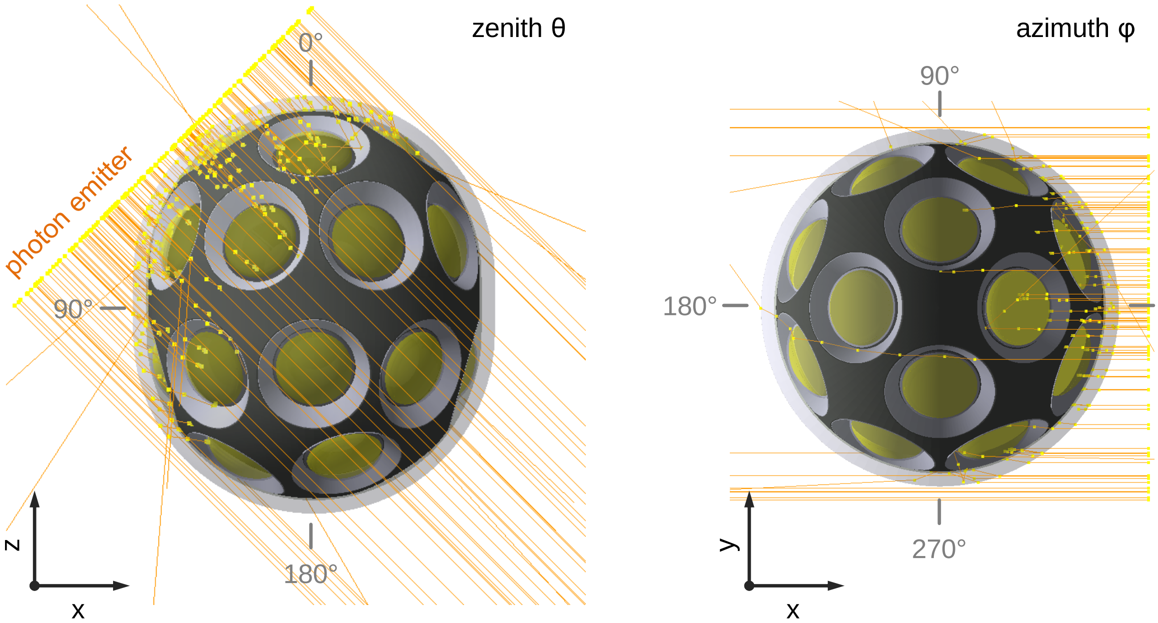

Figure 10.1: Principle of the angular acceptance simulation approach: A flat emitter of parallel monochromatic photons, modeling the incidence of a plane wave, is rotated around the optical module, scanning the solid angle in zenith and azimuth. Depicted are the cases of a R12199-equipped mDOM in ice, illuminated from $(\theta, \varphi) = (45°, 0°)$ (**left**) and $(\theta, \varphi) = (90°, 0°)$ (**right**). *Yellow* dots mark the occurrence of physics interactions, which, in the scope of the model, can be emission, reflection, refraction, or absorption of photons. For further details see section 10.2.

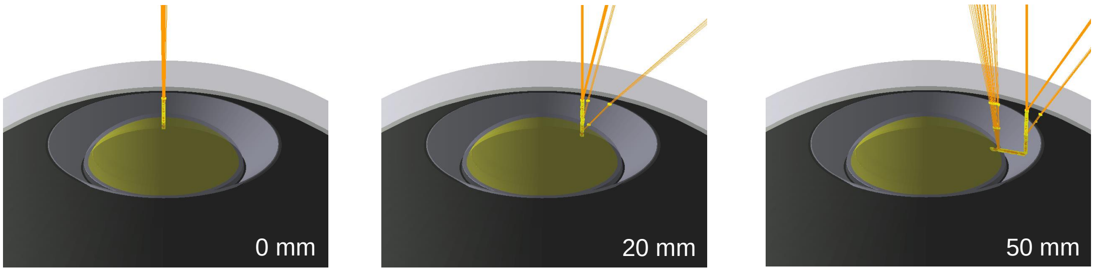

Figure 10.2: Illustration of a linear pencil-beam scan. The setup features a Hamamatsu R12199-02 PMT inside an mDOM located in ice. As introduced in more detail in figure 10.1, the occurrence of interactions is marked by *yellow* dots. Numbers indicate radial positions of the beam.

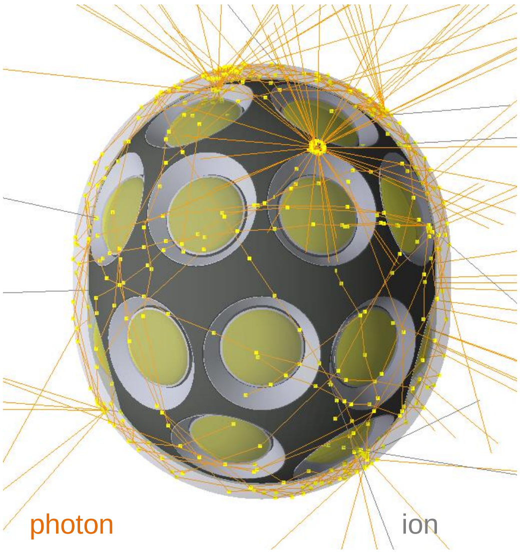

Figure 10.3: Simulated ^{40}K decays occurring in the glass envelope of an mDOM placed in ice. The locations of physics interactions, comprising radioactive decays and optical photon processes (see table 10.1 for details), are marked by *yellow* dots. The figure shows the cumulative particle output of ten ^{40}K decays.

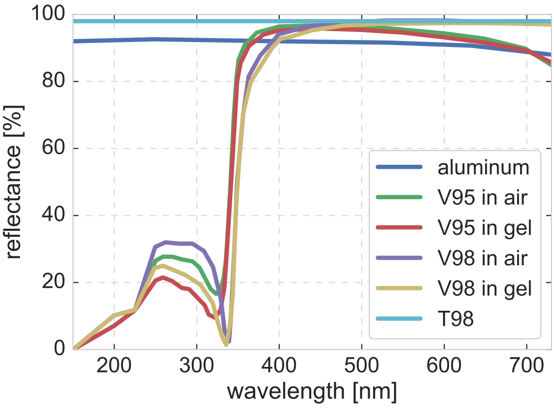

Figure 10.4: Reflectance spectra of materials available for PMT reflector construction in the module simulation toolkit.

- **PMT**: If the IceCube module is simulated the PMT type is fixed to a model of the Hamamatsu R7081 tube (see figure 10.8 for model details). The mDOM, however, can either be equipped with Hamamatsu R12199-02 PMTs, or ones of the type 9320KFL by ET Enterprises. Dimensions and implementation details are presented in figures 10.9 and 10.10, respectively. Characteristics of both three-inch tubes are discussed in section 5.1.

- **reflector angle**: Reflective cone geometry is defined providing the opening semi-angle of the device (only applicable to mDOM simulations).

- **reflector material**: In addition its reflectivity spectrum can be tuned, choosing one of four potential materials: The user can decide between Almeco's **V95** and **V98**, featuring reflectivity provided by the manufacturer[1] [194], (non-oxidized) **aluminum**, assigned a generic reflectivity spectrum [199], and a hypothetical[2] enhanced material featuring a constant reflectivity of 98 % for all wavelengths, dubbed **T98** in the scope of the toolkit. The respective reflectance spectra implemented in the simulation model are presented in figure 10.4.

---

[1] For an actual measurements of the reflectivity of a variety of potential materials, see section 9.

[2] The implementation of this material was motivated by efforts of the CTA collaboration to enhance the UV-reflectivity of metal sheets applying additional coating [200].

- **holder color**: The laser-sintered PMT support structure (see section 8.2) is produced from a **white** material. In the case of the KM3NeT module it is painted using a matte **black** color. Both configurations can be simulated for the mDOM. In addition a hypothetical **reflective** aluminum coating can be applied to the structure.
- **world size**: The world volume (see section 10.1.1) is a sphere with a radius tunable by the user. Reducing the world size will result in faster calculation.
- **environment**: Three "environments" (materials of the world volume) can be used to place the module in. The user can choose from **air** (constant refractive index $n = 1$, no absorption) and two sorts of **ice**, both featuring the appropriate refractive index spectrum, but only in one case also including corresponding absorption and Mie scattering. The implemented optical properties, taken from [77] and [78] represent the situation in the clearest part of the ice, at a depth of 2278.2 m.
- **interactive & visual**: Upon completing a run and saving the output, the simulation can either quit, or open an interface, either a command line-based or graphical, allowing the user to interact with the simulation. The latter tool is not only useful for visualization of the setup, but also essential for debugging the code.

Furthermore, the material of the **pressure vessel** can be selected from a variety of glasses. The choice defines the wavelength-dependent absorption length (see figure 10.6 for an overview) and refractive index (presented in figure 10.5):

- **Vitrovex** is the default (borosilicate) glass by Nautilus GmbH. The implemented refractive index spectrum was provided by the manufacturer [186]. Concerning absorption there is a choice between **official** KM3NeT data [79] as well as the more pessimistic values **measured** in the scope of this thesis, reported in section 9.1.
- **Chiba glass** refers to the enhanced borosilicate used for the construction of the D-Egg optical module (see section 2.4). The absorption length was derived from transmission data **provided** by the Chiba group [188], as well as **own measurements** (see section 9.1, referred to as "Chiba glass, measured"). Both versions share the refractive index spectrum provided by our colleagues [188].
- The absorption spectrum of **IceCube glass**, the default material of the current IceCube optical module, was taken from IceCube simulation packages [201, 202]. As no dedicated data was available the refractive index of Chiba glass was used.
- **WOM glass** is the quartz-based glass used for the UV-transparent pressure vessel of the WOM (see section 2.4). The implemented absorption lengths are based on a transmission measurement performed by our colleagues [203]. Lacking original data, a generic refractive index spectrum of fused quartz glass was used [204].
- To assess the impact of maximum UV-transparency also enhanced **fused silica** was included. It shares the refractive index spectrum with WOM glass, while information on absorption length was taken from [205].

The **optical gel** infill of the module can also be constructed from different materials:

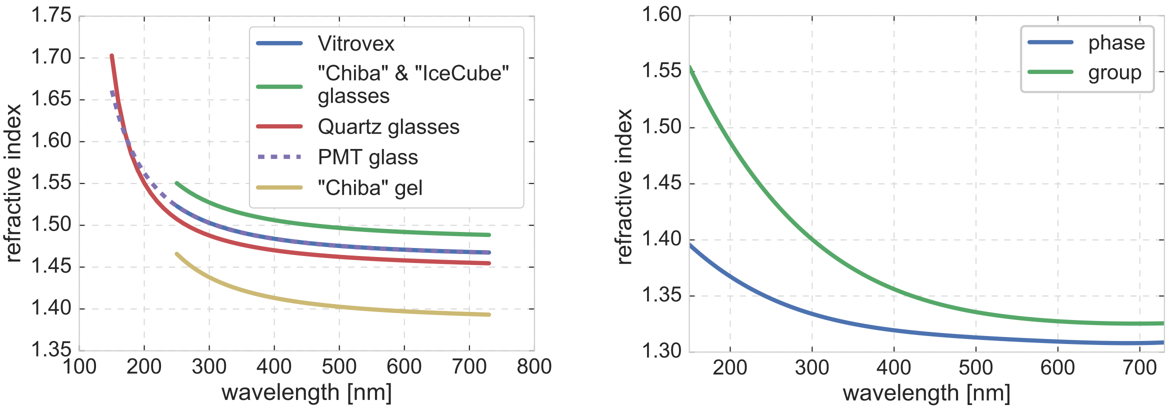

Figure 10.5: **Left**: Refractive indices of optical component materials defined in the module simulation shown for respective ranges of definition. The “Quartz glasses” values are used for the WOM glass and fused Silica. Due to the lack of appropriate data Chiba gel properties were applied to all available gels. **Right**: Refractive index of the glacial ice. Function taken from [77].

- Two versions of **Wacker** SilGel 612 are available. The absorption length spectrum is either based on KM3NeT data [79] or includes, in the UV cut-off region, data points derived from a thin-sample[1] transmission measurement by the company [136]. The latter is dubbed “ Wacker C(ompany)” in some plots. Chiba gel data was used for the refractive index.

- Properties of **Chiba** gel (used in the D-Egg module), both transmission and refractive index, were provided by the Chiba group [122].

- Standard **IceCube** gel was modeled using absorption length data available from simulation packages [201, 202] in combination with the refractive index of Chiba gel.

As unknown to the author, scattering properties of the gel, even though potentially not negligible as discussed in section 9.1, are so far not included in the model. An overview of all implemented absorption lengths are presented in figure 10.7. For refractive indices see figure 10.5.

Simulation **results** are provided in the form of output text files, containing columns for each input parameter and the number of hits on each of the PMTs, allowing simple access for processing and plotting using e.g. Python’s Pandas package. This output style is the default choice for optical simulations. Alternatively, the user can choose (again via command-line parameter) to retrieve detailed information on individual photons, featuring one line per recorded photon, which contains properties such as arrival time, energy, position and direction. The latter option is mainly intended for the ^{40}K branch, but is also useful for e.g. debugging. The decision in favor of ASCII files over more sophisticated formats (and memory saving), such as HDF5 files or root trees, was driven by the desire to maximize compatibility and to prevent output corruption: if a run crashes on a high-performance computing cluster, the result file will not be complete, but still usable[2].

---

[1] For the impact of sample thickness on absorption length results see section 9.1.

[2] Consultations with B. Herold contributed to this decision.

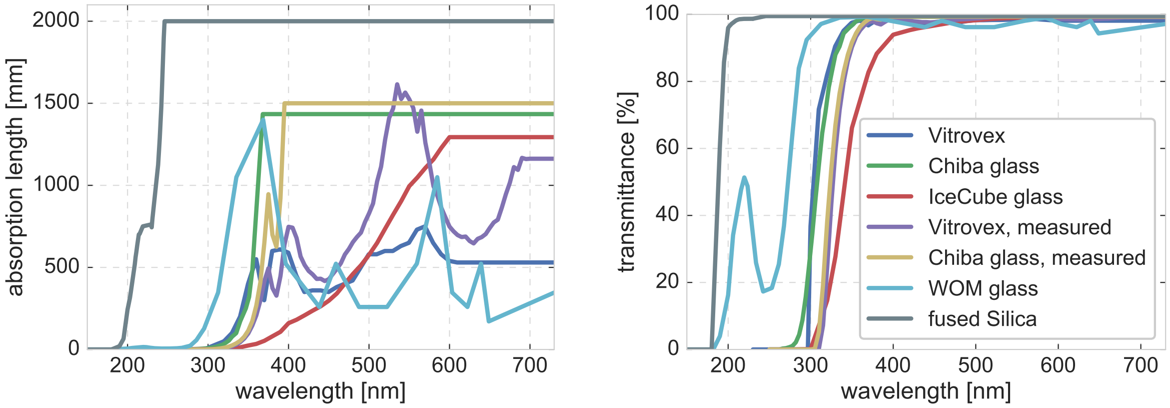

Figure 10.6: **Left**: Absorption lengths values for all glass sorts available for the pressure vessel Geant4 model. **Right**: Transmittance exhibited by respective glasses featuring a material thickness of 12 mm, corresponding to the actual wall thickness of the IceCube DOM.

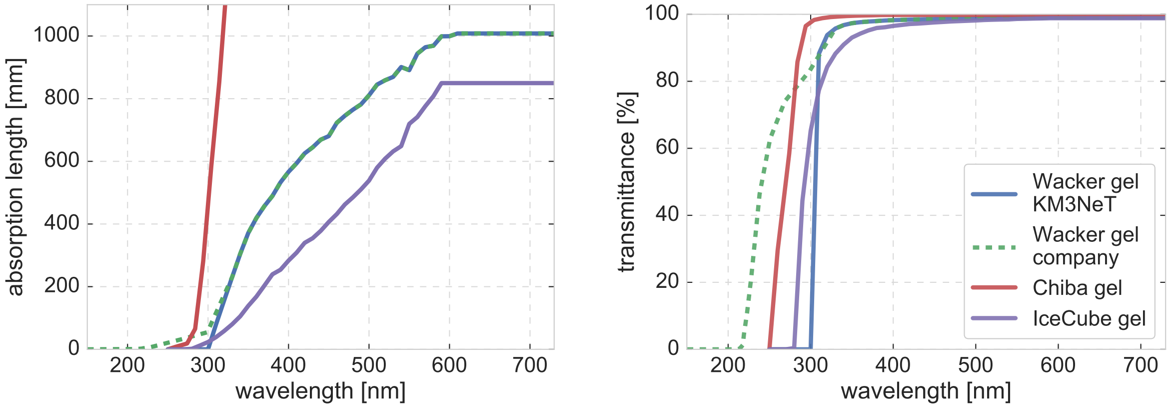

Figure 10.7: **Left**: Absorption lengths for different gel versions implemented in the Geant4 model. For wavelengths exceeding 350 nm Chiba gel values were set to 5000 mm [a]. **Right**: Corresponding transmittances resulting from a 10 mm gel layer.

---

[a] While not significantly affecting the transmission of the material for typical photon path lengths (∼ 1 cm) this measure was beneficial to program stability preventing run duration excesses by trapped (multi-reflected) photons.

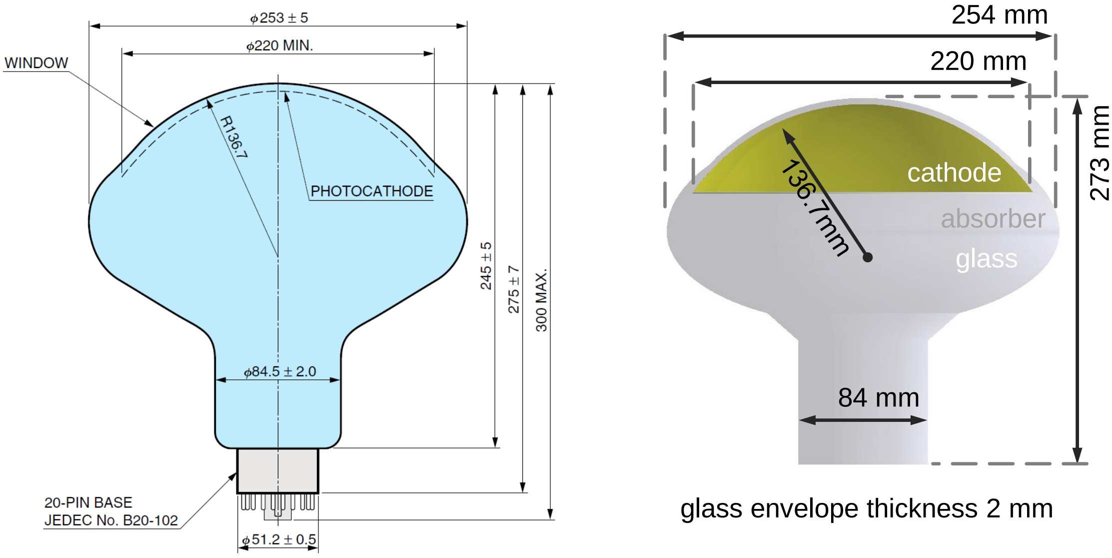

Figure 10.8: **Left**: Technical drawing of a type R7081 ten-inch PMT by Hamamatsu Photonics used in the standard IceCube single-PMT optical module (see sections 2.2.3 and 4.1). Dimensions are given in millimeters. Taken from [206], modified. **Right**: Corresponding model in Geant4.

The centerpiece of the simulation is a detailed hierarchic model of the respective optical module illustrated in figure 10.11. Its core component, in turn, is a model of the PMT. This model consists of a solid glass "bulb" containing a volume representing the cathode. Depending on the selected PMT type the glass volume is either a union of a tube and an ellipsoid, or features an additional sphere (see figures 10.8, 10.9, and 10.10 for details and dimensions of respective PMTs). Accordingly, the photocathode is either an ellipsoid or a sphere-ellipsoid union. The particular dimensions were chosen to fit information from technical drawings, available from the respective manufacturers. The rear of the photocathode is shielded by a disc against incident photons which would be unphysical, slightly larger in diameter than the cathode and, consisting of the same material as the holding structure, fully absorbing. Hit generation is done at step level: If a photon makes a step inside the photocathode volume it is destroyed ("StopAndKill" in Geant4 slang) and its properties, such as position, direction and energy, are registered. Consequently, no effects of the electron multiplier system or the cathode quantum efficiency[1] are included in the model. The PMT glass features a wavelength-dependent refractive index, typical for borosilicate[2] glass but no absorption. The idea behind this approach, was the possibility

---

[1] Actually, the cathode material was also assigned a constant refractive index of $n_{\mathrm{cathode}} = 2.0$ (based on [151]), in principle allowing for a situation where photons are reflected at the glass-cathode interface. It does not happen though, as, in the world of Geant4, even those photons ultimately reflected, take one step into the material and are subsequently killed. Experimental runs explicitly including a thin layer of identical material covering the photocathode, did not produce a significant impact on the overall results of the simulation, giving no reason to include this feature in the final design.

[2] Namely, the one of Chiba glass.

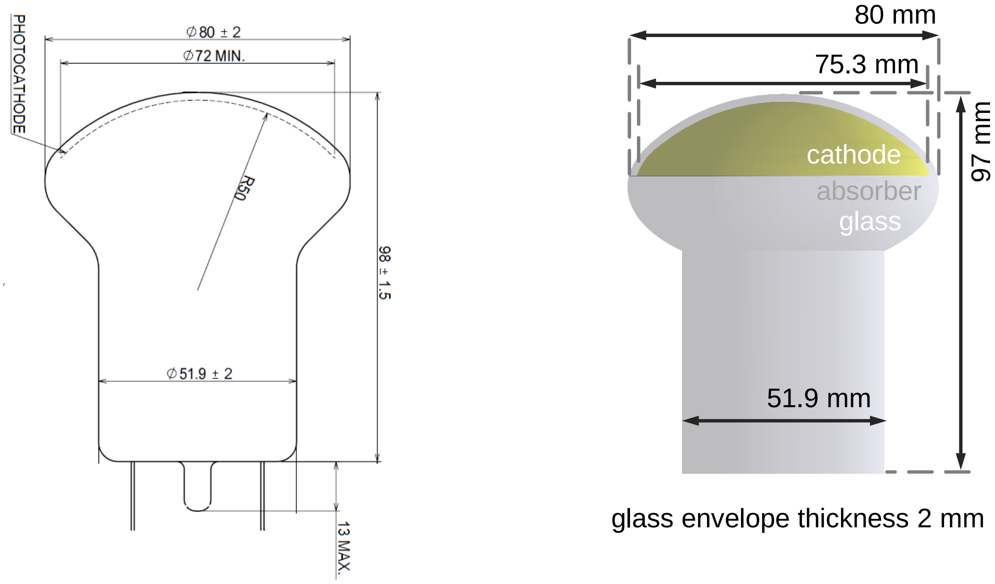

Figure 10.9: **Left**: Technical drawing of a Hamamatsu Photonics R12199-02 three-inch PMT. The model will feature as default for the construction of an mDOM prototype. Dimensions given in millimeters. Figure taken from [207], modified. **Right**: Details of the implementation in Geant4.

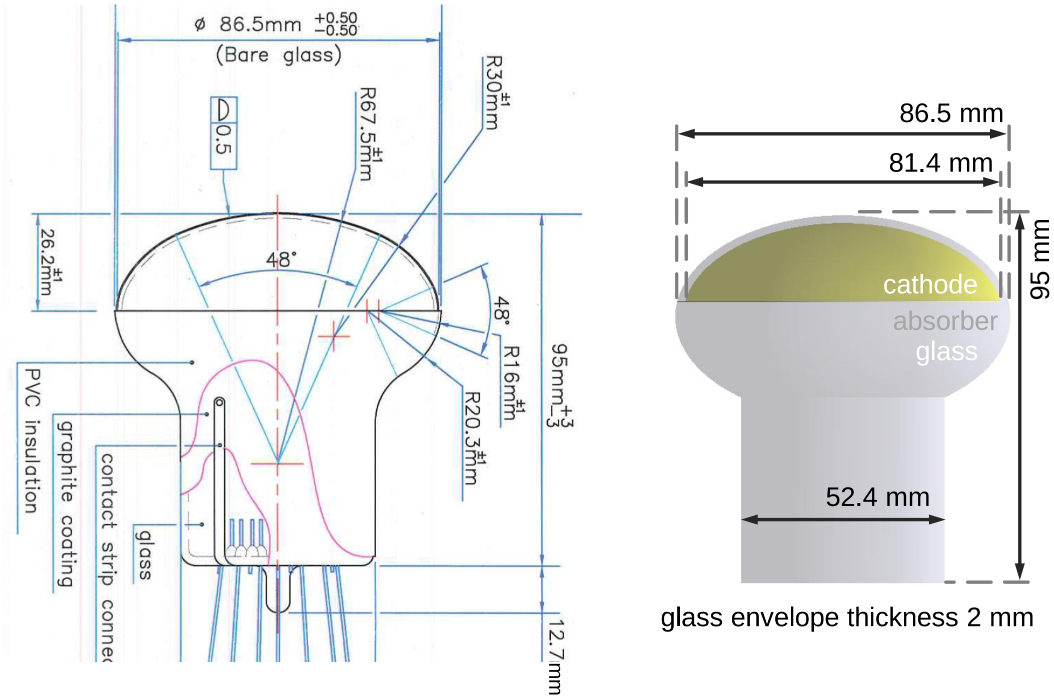

Figure 10.10: **Left**: Technical drawing of a type 9320KFL three-inch PMT by ET Enterprises Limited (ETEL). Figure taken from [208], modified. **Right**: Geant4 implementation details.

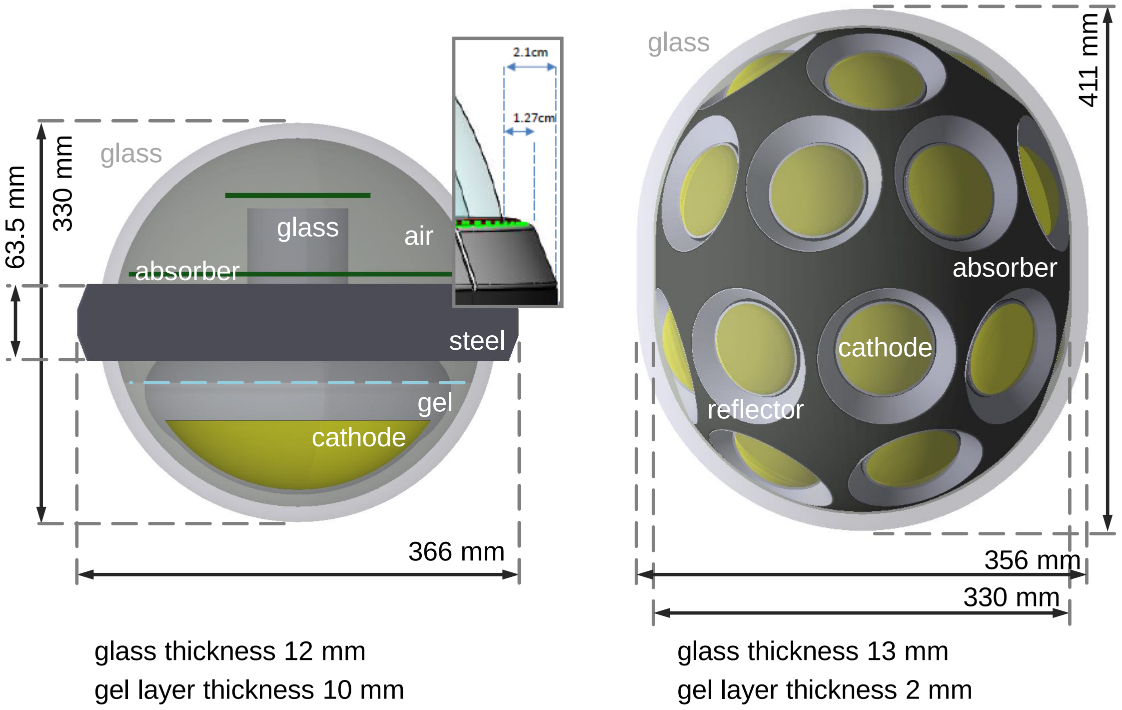

Figure 10.11: Models of the IceCube DOM (**left**) and mDOM (**right**) as implemented in Geant4. For PMT modeling and dimensions see figures 10.8, 10.9, and 10.10. Information on the optical properties of applicable materials is given in figures 10.4 to 10.7. Also see section 10.2 for further details on the simulation approach.

to check the impact of different cathode materials by applying their quantum efficiency spectra to simulation results[1] off-line, with no need to re-run the simulation. Compared to the real device, featuring a semi-transparent, nanometer-scale semiconductor layer and a metallic internal structure defining the collection efficiency but also able to reflect photons[2], this model is strongly simplified. An assessment of the validity, together with resulting limits of this approach, is given in section 10.3.

Further components of the simulation setup depend on the optical module type: In case of the **IceCube DOM** the PMT is placed into a gel volume which fills the lower part of the spherical pressure vessel. The upper part of the vessel is taken up by a volume of air. Optically absorbing discs, located in the air volume around the "stem" of the PMT, represent the electronics boards and PMT base. The model is completed by a representation of the stainless steel[3] harness, located in the equatorial plane of the module.

The pressure vessel of the **mDOM** (see figure 10.11), is a composite of a cylinder and two spherical caps[4]. Nested into the glass is a gel volume defined in the same manner. The gel is the mother volume to 24 PMTs, their associated reflectors as well as a holding structure featuring appropriate recesses.

---

[1] As discussed in section 3.1, the short-wavelength cut-off of the quantum efficiency spectrum is an effect of the transparency of the entrance window material.

[2] See section 5.2 for a demonstration of this effect.

[3] Featuring a diffuse reflectance of 80 %.

[4] For bug-susceptibility reasons the spheres are actually cropped ellipsoids with identical semi-axes.

particle	physics process	Geant4 class
optical photon	bulk absorption	G4OpAbsorption
	optical interface processes (reflection, refraction, absorption)	G4OpBoundaryProcess
	Mie scattering	G4OpMieHG
gamma	pair production	G4LivermoreGammaConversionModel
	Compton effect	G4LivermoreComptonModel
	photo-electric effect	G4LivermorePhotoElectricModel
electron	scattering	G4eMultipleScattering
	ionization	G4LivermoreIonisationModel
	Bremsstrahlung	G4eBremsstrahlung
	Cherenkov radiation	G4Cerenkov
positron	scattering	G4eMultipleScattering
	ionization	G4eIonisation
	Bremsstrahlung	G4eBremsstrahlung
	bulk annihilation	G4eplusAnnihilation
	Cherenkov radiation	G4Cerenkov
ion	radioactive decay	G4RadioactiveDecay
	Cherenkov radiation	G4Cerenkov

Table 10.1: Particles and applicable physics processes in included in the module simulation toolkit, together with the names of corresponding Geant4 classes. Note that optical photons and high energy gammas are considered distinct particles in the scope of Geant4. For details please refer to the Geant4 documentation at `http://geant4.cern.ch/`.

In both cases the modules are located at the center of a world volume filled with the medium of the user's choice. Module orientation is identical to the actual in-situ situation: In the IceCube module the PMT is oriented along the z-axis facing downwards. For the mDOM the z-axis coincides with the symmetry axis of the module.

An overview of the particles included in the simulation, together with corresponding physics processes, is presented in table 10.1.

The modular structure of Geant4 allows for straight-forward expansions of the simulation adding particles and appropriate processes to the model. For example, a modified version has been used for a study of the detectability of supernova neutrinos in the scope of a Master's thesis [209].

10.3 Model validation

As with all simulations, it is important to check its output against real-world results. In case of the mDOM dedicated angular and pencil beam scanner simulations have been created for this purpose, in analogy to the full module setups introduced above. The reduced model consists of only one (three-inch) PMT oriented along the z-axis. In addition to the parameters introduced above, the user can choose (again via command line arguments)

- between reflectors parametrized by the angle, fixed layouts based on the properties

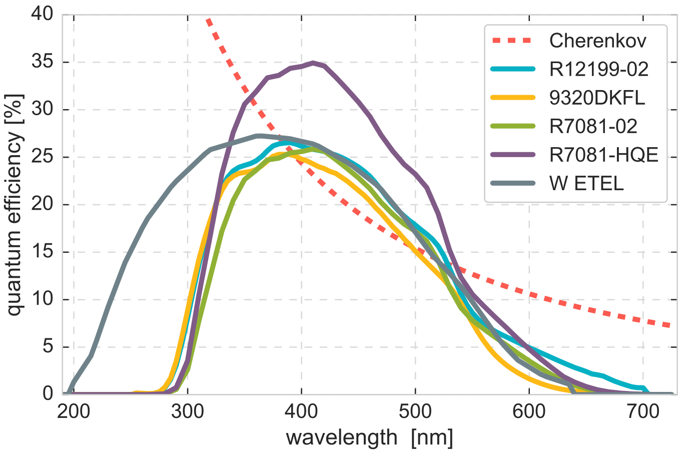

Figure 10.12: Quantum efficiency spectra for various IceCube-Gen2-related PMTs. A Cherenkov emission spectrum is shown in arbitrary units to emphasize the benefit of UV sensitivity. Types R12199-02 and 9320KFL are considered for the mDOM. Types R7081-02 and R7081-HQE were used in IceCube and DeepCore, respectively. The curve for a UV-enhanced PMT (W ETEL) is reproduced from [126].

of the real devices used in angular acceptance and homogeneity measurements[1], or to place no reflectors at all;

- whether the PMT is situated inside a module or directly in the world volume,
- whether to place a holding structure.

The above-mentioned parameters allowed (among others) to reproduce the setups of the angular acceptance measurements for a single, bare or reflector-equipped, PMT (see section 9.2.2) in air as well as the output homogeneity scans across the photocathode, discussed in section 5.2. Results are presented in the following section.

To ensure consistency with available IceCube data, the results obtained for the ten-inch PMT module were cross-checked with the output from standard IceCube simulation tools reported in section 10.3.2.

10.3.1 Three-inch PMT models

Simulation results for the angular acceptance of mDOM three-inch PMTs, presented in figures 10.13 and 10.14, agree well with corresponding measurements, featuring overall discrepancies (in terms of solid angle integrated sensitivity) well below 5% in all cases (see table 10.2). These are, on the one hand, expected to result from small inconsistencies in geometry and optical properties. On the other hand, they reflect intrinsic limitations of the simulation setup: After all, the photocathode is modeled as an opaque object of uniform sensitivity, with photons being stopped and recorded when impinging upon it, no matter at which position and under which angle they arrive. Its actual semi-transparency, allowing photons to hit the cathode again if reflected inside the PMT (discussed in more detail in section 5.2), might account for the major part of the observed deviations.

This simplification is also responsible for the much larger discrepancies in case of pencil-beam data (see figures 10.15 and 10.16). In particular, the case of the output from

---

[1] These were used in the validation.

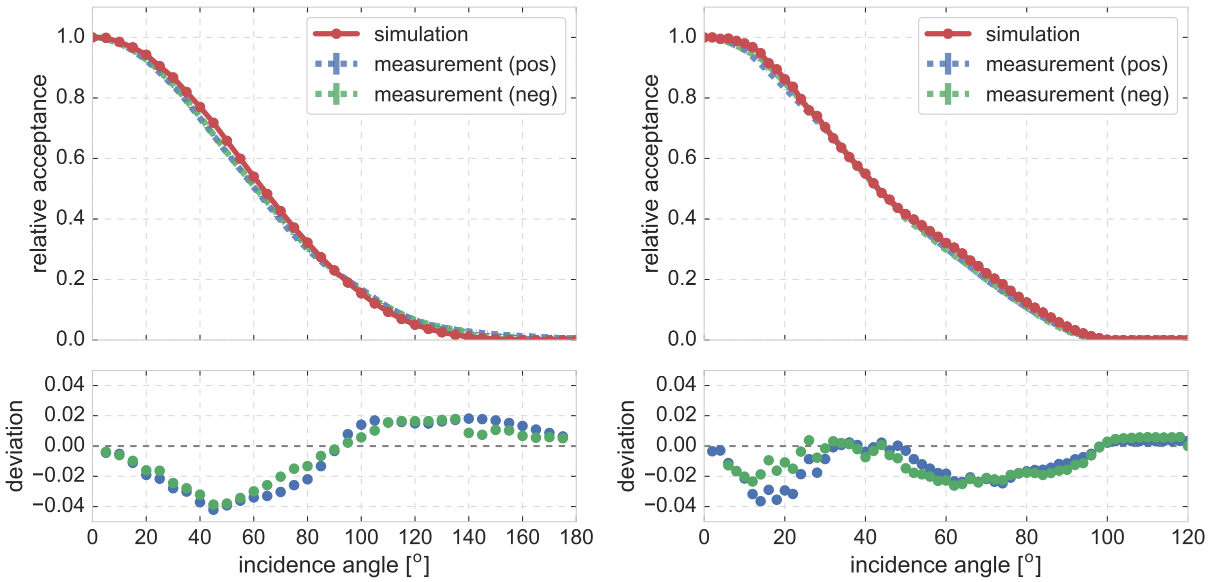

Figure 10.13: **Hamamatsu R12199-02** simulation model verification via angular acceptance: Simulations of a the angular acceptance of a bare PMT (**left**), as well as of a PMT equipped with a reflective cone (**right**), are compared to measurements of the respective setups. Acceptances are normalized to the value for vertical light incidence. Errorbars indicate statistical uncertainties. In case of the simulation errorbars are smaller than data markers. Lower subplots show the absolute difference between measured and simulated data in respective colors.

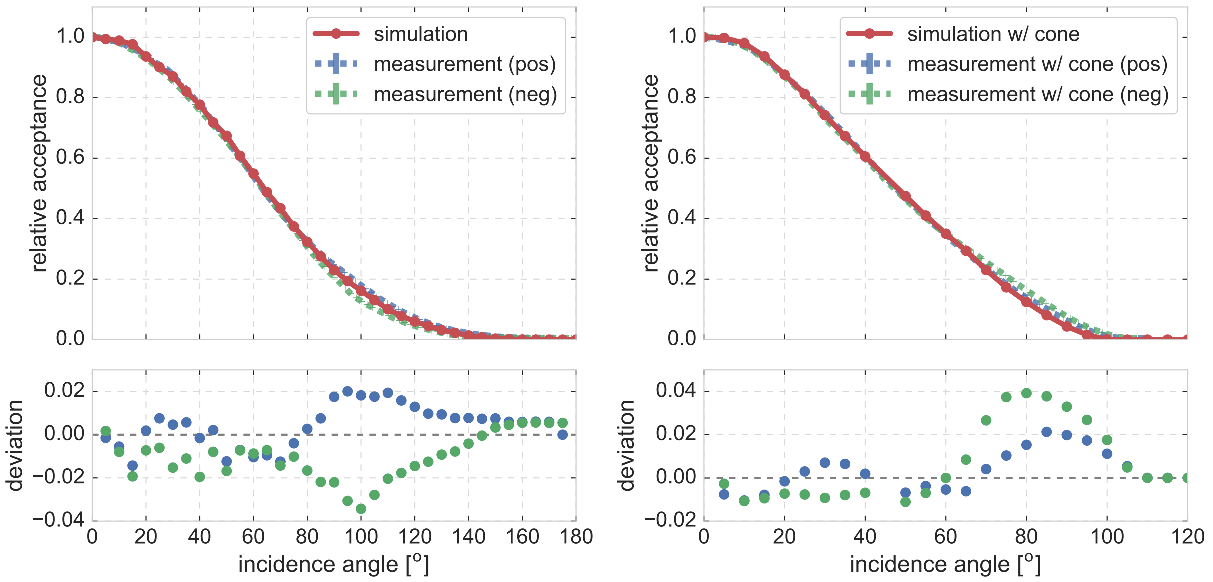

Figure 10.14: **ET Enterprises 9320KFL** simulation model verification via angular acceptance: Simulations of a the angular acceptance of a bare PMT (**left**), as well as of a PMT equipped with a reflective cone (**right**), are compared to measurements of the respective setups. Acceptances are normalized to the value for vertical light incidence. Errorbars indicate statistical uncertainties. In case of the simulation errorbars are smaller than data markers. Lower subplots show the absolute difference between measured and simulated data in respective colors.

PMT type	**bare tube**	**reflector-equipped**
Hamamatsu R12199-02	2.0%	2.5%
ET Enterprises 9320KFL	3.1%	3.2%

Table 10.2: Solid-angle averaged deviations between measurement[1] and simulation of the angular acceptance of a single three-inch PMTs in air. The values correspond to an averaged deviation in effective area. As the measurement features small scale asymmetries between positive and negative incidence angles, values were derived for both directions and averaged. Relative asymmetries of the measurement were found to be on a comparable scale ($< 5\%$ for all setups).

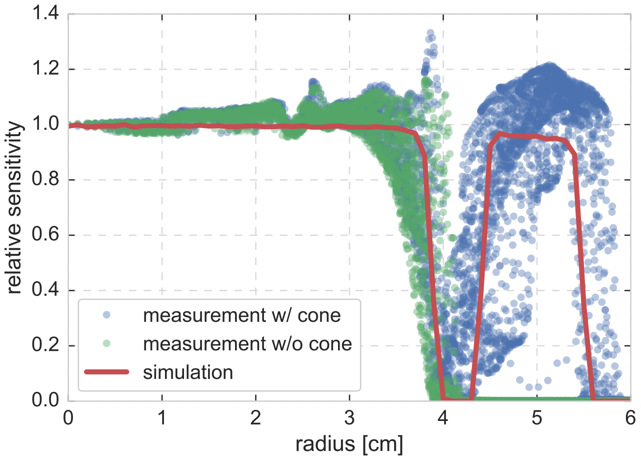

Figure 10.15: Comparison between a vertical pencil-beam scan of the photocathode (see section 5.2.1 for measurement details.) and a corresponding simulation for a **Hamamatsu R12199-02** PMT. Datapoints of the original x/y scan (performed with and without reflector) were mapped on the respective distance to the PMT center (radius). Statistical errors of the measurement and simulation were found to be negligible (smaller than markersize or line width, respectively). The simulation featured a reflector-equipped PMT scanned using a 2 mm diameter parallel light beam at a wavelength of 470 nm. Sensitivities are given relative to the center value.

photons impinging on the reflector exceeding the output caused by direct hits on the cathode, as observed for the Hamamatsu PMT[2], is, by design of the model (introduced in the previous section), impossible to reproduce in the simulation. The same applies to the large increase of sensitivity of the ETEL PMT at a radius of ~ 3 cm which could be traced back to reflections at a metal-coated area surrounding the first dynode. Consequently, the main goal of this cross-check, comparing simulation data to the the respective anode response results obtained using the collimator-terminated fiber setup (see section 5.2 for details on the experimental methods), was to merely verify the cathode and reflector dimensions. In this respect, in particular taking into account the large spread exhibited by the experimental data, the comparison indicates a good reproduction of the dimensions by the simulation model.

---

[2] This feature is attributed to the chance of photons, reflected under specific angles, the to cross the photocathode twice, as discussed in the dedicated section 5.2.

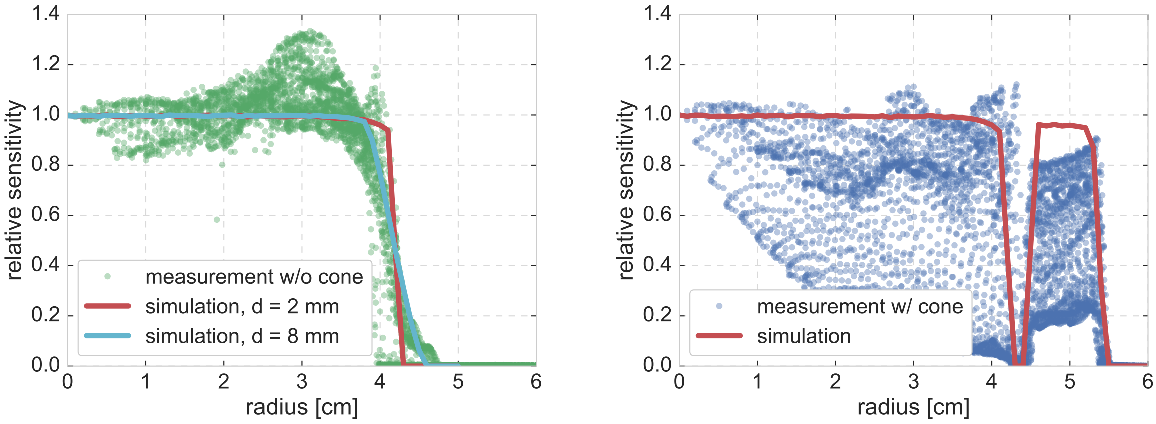

Figure 10.16: Results of a vertical pencil-beam scan of the photocathode of an **ET Enterprises 9320KFL** PMT compared to a simulation of the setup. Measured data was mapped as introduced in figure 10.15. In the case of a bare PMT (**left**) the slope of the measured data can be reproduced increasing the beam diameter d indicating a potential problem in the measurement setup. The “excess” measured at a radius of $\sim 3\,\mathrm{cm}$ is a real effect of internal reflections (see section 5.2.1) not reproducible in the simulation model. Comparison of the data of a reflector-equipped PMT to a corresponding simulation (**right**) reveals a good match of PMT radius and reflector dimensions. Datapoints below the simulated curve are an artifact of a measurement problem (discussed in more detail in section 5.2.1).

In general, the simulation underestimates the frontal effective area of the PMTs (derived from the anode response scans, see section 5.2) which is enhanced by reflections and multiple cathode crossings: The relative discrepancy amounts to $\sim 3\%$ for the Hamamatsu model[1] and $\sim 4\%$ for the ETEL PMT[2]. The impact of this deviation, however, is expected to be most pronounced in the case of near-frontal illumination, which has only little phase space. Concerning the contributions at larger angles there is room for further investigation[3]. But the rather good match of the measured angular acceptance to the simulated curve limits the overall impact of the effect to the order of the observed deviations, i.e. to $< 5\%$.

To conclude, the comparison between measurement and simulation confirms the validity of the chosen PMT simulation approach as well as the implemented dimensions.

10.3.2 IceCube DOM model

Dimensions used to model the R7081 ten-inch tube of the single-PMT IceCube DOM were obtained from a Hamamatsu data sheet [206]. As a result, the implemented photocathode diameter represents only a lower limit guaranteed by the manufacturer. Therefore, a factor was presumably needed to scale up its sensitivity to more realistic values, which

---

[1] Measured to be $46.4\,\mathrm{cm}^2$, compared to the simulation outcome of $44.9\,\mathrm{cm}^2$.

[2] Measured $54.6\,\mathrm{cm}^2$ vs. $52.6\,\mathrm{cm}^2$ resulting from the simulation.

[3] Preliminary measurements, scanning a PMT rotated by 45° relative to the photon incidence direction, indeed show a small scale internal reflection effect.

is particularly important for the comparison of the effective area of the mDOM to that of a standard single-PMT module. To this end, data retrieved from DOMINANT[1] [202] and clsim [201], the standard IceCube tools for the simulation of the optical module and the entire detector, respectively, was used to normalize Geant4 simulation results. The "official" values are based on measurements of several, so-called "golden", IceCube DOMs performed in water and also verified in-situ during calibration runs [202], representing the currently best knowledge on the performance of a typical IceCube module. The overall efficiency of an IceCube DOM is derived in clsim from two tables:

- **Effective area** of the module as a function of wavelength for the case of frontal plane wave illumination: These values contain all effects linking incident photons to emitted photoelectrons, such as quantum and collection efficiencies, as well as losses due to glass and gel.
- **Relative angular acceptance** normalized to vertical illumination: The relative curve is scaled by the respective frontal effective area depending on the color of the incoming light to obtain the appropriate effective area for a certain angle and wavelength. This information is provided, for the user to choose, in terms of a look-up table as well as parameters of a custom parametrization function.

This approach is justified by the observed shape stability of the relative angular acceptance curve throughout the optical wavelength region. In addition, the quantum efficiency curve of a typical R7081 PMT is provided, which was derived averaging lab measurements of "golden" PMTs. While the original IceCube detector was build using standard bi-alkali PMTs, DeepCore DOMs feature an enhanced, high quantum efficiency (HQE) tube. The standard approach to take this into account in clsim, is the scaling of module efficiency by a factor of 1.35. A relative uncertainty of $\sim 10\%$ is claimed on simulation results with respect to actual measurements. The error budget is dominated by the spread of PMT parameters on a tube-to-tube basis.

In order to normalize IceCube module results obtained with the mDOM simulation toolkit to the "official" data, both cases, that is to say head-on illumination with different wavelengths as well as an angular acceptance scan (see 10.2 for respective methods), were reproduced in the scope of the new simulation.

For the vertical illumination case, the standard quantum efficiency of the R7081 PMT was applied to the effective area before comparing it to the clsim table. The outcome is presented in figure 10.17 (left). Best match between the simulated results and the tabulated values was achieved applying a scaling factor of 1.24 to the simulation data. The difference between the wavelength-integrated effective area was found to be 1.0% mainly due to a discrepancy concerning the position of the UV cut-off. Consequently, the application of Cherenkov weighting (see equation 9.9) increased the overall deviation to 1.6%.

The angular acceptance results (in terms of an effective area as a function of the photon incidence angle) were compared to the corresponding clsim curve weighted by the above-mentioned frontal area divided by the quantum efficiency to obtain a situation defined solely by module geometry and the optical properties of its components. Best agreement

---

[1] Dom Optical-photon to Material INteraction ANd Tracking simulator

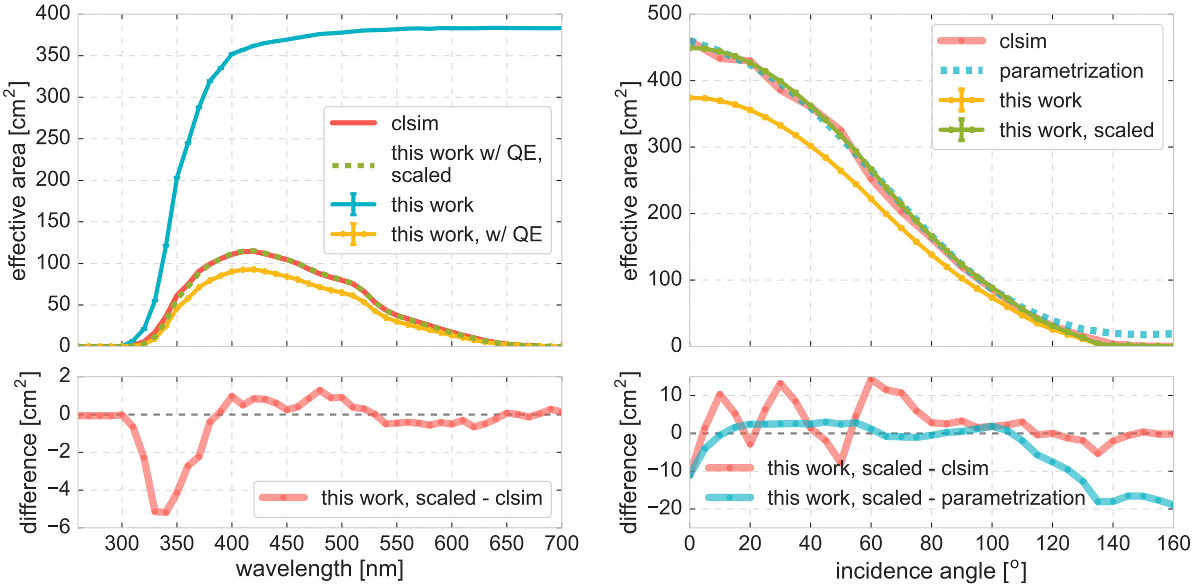

Figure 10.17: Comparison of IceCube DOM effective areas obtained with the current simulation ("this work") to corresponding clsim data. **Left**: Effective area for frontal illumination as a function of photon wavelength. A factor of 1.24 was applied to the scaled curve (*dashed*). Errorbars are based on Monte-Carlo uncertainties ($\sim \sqrt{N}$). **Right**: Effective area as a function of the photon incidence angle. The indicated scaling factor was 1.20. Look-up table data (dubbed "clsim") as well as the corresponding parametrization curve are (see discussion in text) are compared to results from the current simulation.

between both data sets was achieved after scaling the simulation results by 1.2 (see figure 10.17, right). The comparison of solid-angle integrals resulted in relative differences of 1.7% and 1.0% for the look-up table and the parametrized curve, respectively.

To wrap it up, after the application of an overall scaling factor, clsim data could very well be reproduced in the scope of the reported simulation toolkit. For instance, the observed deviations of both approaches are well below the precision claimed by the clsim model. For performance comparisons between mDOM and PDOM, based on the simulation presented in this work, a scaling factor of 1.2 was adopted[1]. As the PDOM is foreseen to contain a DeepCore-style enhanced quantum efficiency PMT, an additional factor of 1.35 is used in comparisons to the mDOM.

10.4 Simulation studies

The module simulation tool introduced above was used to perform a number of studies, presented in the current section. The focus will be on results relevant for the current mDOM design. Results of initial studies concerning the early cylindrical mDOM design can be found in a dedicated publication [135].

---

[1] Choosing the factor from the angular acceptance shape over the one from frontal illumination out of phase space considerations.

10.4.1 Reflector angle optimization

The initial 45° opening semi-angle of the KM3NeT reflectors was the result of a ray tracing optimization study, with the goal to maximize the collection of photons arriving perpendicular to the entrance window, as those were considered most essential for directional reconstruction [192]. However, this study was done with the original, later discontinued, KM3NeT PMT (Photonis XP53B20) in mind, and also did not take into account the optical boundary between pressure vessel and the environment. Also the limitation to vertical photons is only one possible optimization (and not a-priori guaranteed to be the best choice)[1]. So eventually there was a need for a dedicated mDOM study.

It was carried out using the single-PMT version of the angular acceptance scanner, introduced in the previous section. For a range of potential cone angles the effective areas of both PMT types, R12199-02 by Hamamatsu as well as 9320KFL by ETEL, were derived as a function of the incidence angle of a plane wave in ice. The wavelength of the photons was varied between 350 and 700 nanometers, covering the range of non-zero quantum efficiency for both PMT candidates. Vitrovex glass and Wacker gel were modeled according to KM3NeT standards (see figures 10.5, 10.6, and 10.7). Reflectors were modeled from V95 and V98. Several conflicting effects were found to contribute to the overall sensitivity of the PMT for a particular direction:

- Wider opening angles increase the projected frontal area of the cone.
- Yet, if the angle is too large, reflected photons will miss the cathode.
- In addition, refraction and reflection at various interfaces may change the overall picture.
- At a certain point, large-angle reflectors will overlap in the real module, reducing their effective area and demanding more complicated reflector shapes which was deemed undesirable[2]. This limited possible opening angels to $\lesssim 56°$ if using the Hamamatsu PMT and $\lesssim 45°$ in case of the ETEL tube.

Following the argument of the earlier KM3NeT study concerning the supreme importance of vertical photons, an opening angle maximizing the "beaming" effect (also see section 9.2) of the reflector was considered best. In addition, the effective area was integrated over the solid angle to check whether the beaming happened at the cost of overall sensitivity.

Results for a typical case (R12199-02 type PMT illuminated by photons featuring a wavelength of 390 nm, corresponding to the maximum of its quantum efficiency) are presented in figures 10.18 and 10.19. For all simulated wavelengths the angular acceptance beaming of the Hamamatsu PMT was found to peak around a reflector angle of 51°[3]. This circumstance is illustrated in figure 10.20 for selected wavelengths[4]. As shown in figure 10.18 in this region the overall effective area is actually increasing with the opening angle, resulting in a slight gain of $\sim 1\%$ relative to the original default value of 45°. Qualitatively

---

[1] In fact, the cone angle of KM3NeT was also recently changed to 48° as a result of new simulations [210].

[2] Another problem with overlapping or touching is introduced by the idea to put the reflectors at photocathode potential in order to stabilize the dark rate, discussed in section 6.6.3.

[3] Which was expected given the very similar refractive index and transparency of the glass throughout

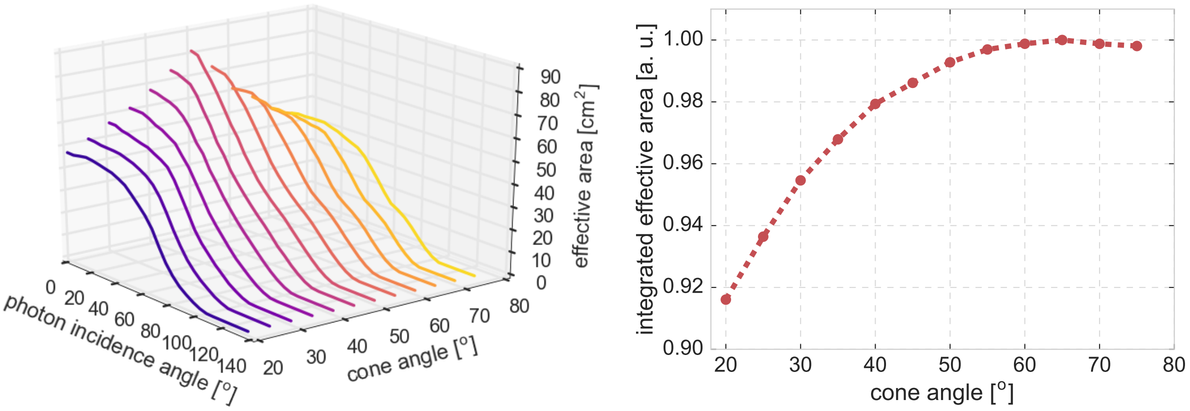

Figure 10.18: Reflector angle optimization results overview for the Hamamatsu R12199-02 PMT. Values are shown for the wavelength of maximum quantum efficiency at 390 nm. **Left**: Effective area as a function of photon incidence and reflector opening angle, featuring a pronounced maximum. Quantum efficiency scaling is not included. **Right**: Solid angle-integrated effective area (in arbitrary units). Statistical errors are smaller than markersize.

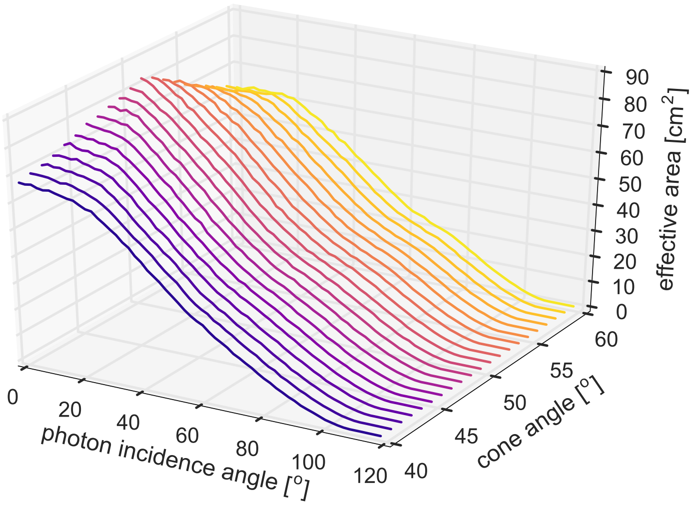

Figure 10.19: Effective area as a function of photon incidence and reflector opening angle. Close-up on the region of interest around the frontal effective area peak from figure 10.18.

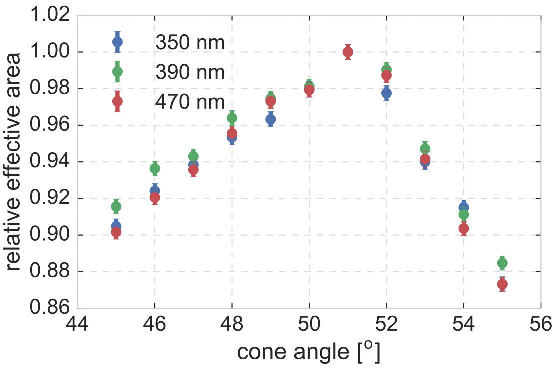

Figure 10.20: Relative effective area for frontal illumination of a R12199-02 PMT, shown for selected wavelengths. Peaking of the distribution at 51° exhibits no dependence on the photon wavelength. Errorbars indicate statistical $\sqrt{N}$ uncertainties. Data sets were normalized by their respective maxima.

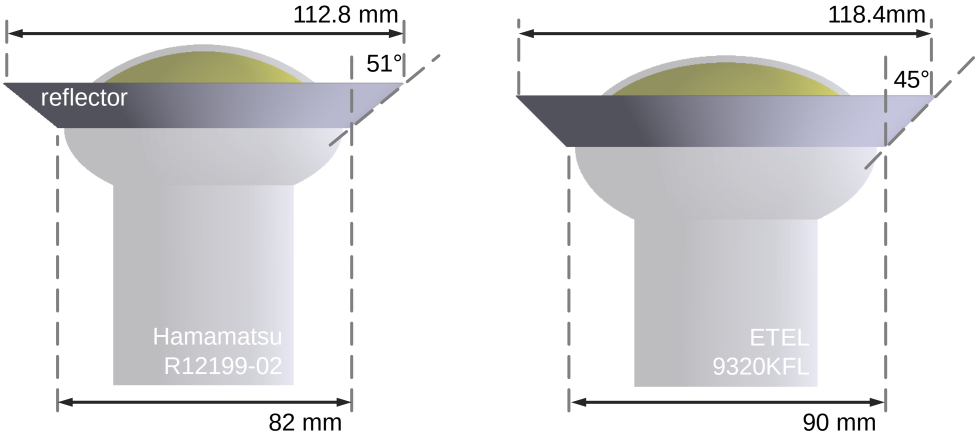

Figure 10.21: Reflector dimensions for both three-inch PMT models available in the mDOM simulation. The depicted opening angles were used as default values.

similar results were obtained for the 9320KFL tube, with an optimum beaming occurring around 52°. The usage of different reflector materials did not alter the overall picture.

Based on this study the opening angle of the first mDOM prototype constructed from R12199-02 PMTs will be 51°[1]. A potential later 9320KFL-equipped version would feature 45° based on the initial limit. The respective angles were used as defaults in the subsequent angular acceptance study of the complete module (see figure 10.21).

The above-presented study includes optical and geometrical effects. A profound, final decision will in addition take into account PMT performance, namely the transit-time-spread. As discussed in more detail in sections 3.2 and 5.2.3, signal transit time is a function of the radial position of photon incidence. Consequently, if mounted to maximize effective area, the innermost part of the reflector will project photons onto regions with longer transit time, increasing, and thus deteriorating, the TTS. Improvement can be achieved by moving the reflector further out along the PMT's axis of symmetry, albeit also resulting in a loss of effective area. The corresponding trade-off (aperture vs. reflector

---

the considered wavelength region.

[4] Namely the position of maximum quantum efficiency (390 nm), the standard reference wavelength of KM3NeT (470 nm), and 350 nm. The latter was chosen to show the effect of a wavelength affected by absorption in the vessel glass.

[1] An integer value was chosen for practical production reasons.

position vs. TTS) is still to be done for the mDOM once a dedicated limit on acceptable timing precision is defined.

10.4.2 Angular sensitivity characterization

The angular acceptance study was carried out using the “angular scanner” tool introduced above (see section 10.2), using the angle dependent **effective area**, defined in equation 10.1, as a figure of merit. Simulations were performed for the initial cylindrical version[1] of the module as well as for the later developed, near-spherical type. To assess the relative gain in effective area and acceptance homogeneity, the baseline single ten-inch PMT optical module (referred to as “PDOM”, see section 2.4) was also simulated using the toolkit, applying appropriate scaling factors derived in section 10.3.2.

The mDOM study included both three-inch PMT versions, a wavelength range between 200 nm and 600 nm, as well as a variety of optical materials. For means of simplicity, the mDOM model featuring R12199-02 tubes by Hamamatsu will be referred to as “mDOM-HAM”, while the version containing ETEL 9320KFL tubes will go by “mDOM-ET”. Reflector angles were set to the respective optimum values derived in a dedicated study discussed in the previous section, namely 51° for the mDOM-HAM and 45° in case of the mDOM-ET. The simulated environment consisted of non-absorbing ice.

Effective areas were derived applying respective quantum efficiencies presented in figure 10.12.

Solid angle coverage homogeneity

The angular acceptance of the mDOM exhibits good homogeneity over the total solid angle. The uniformity was assessed via the ratio of the largest effective area variation occurring throughout the total solid angle to the maximum value of the effective area A_{max}:

$$I = \frac{A_{\mathrm{max}} - A_{\mathrm{min}}}{A_{\mathrm{max}}} \tag{10.2}$$

where A_{min} is the minimum of the effective area and I is a measure of the inhomogeneity. Solid angle inhomogeneity of the mDOM’s acceptance was found to be below 15% in all considered setups. No strong (exceeding 1%) dependence on the wavelength was found in the region between 200 nm and 600 nm. Typical values, corresponding to the cases illustrated in figure 10.22, are summarized in table 10.3. These numbers have to be considered in the light of the conventional, single-PMT, optical module, which features virtually no sensitivity to photons from the upper hemisphere[2] (see figure 10.23). In particular the HESE analysis approach [66, 67] did demonstrate the importance of photons from vertical directions.

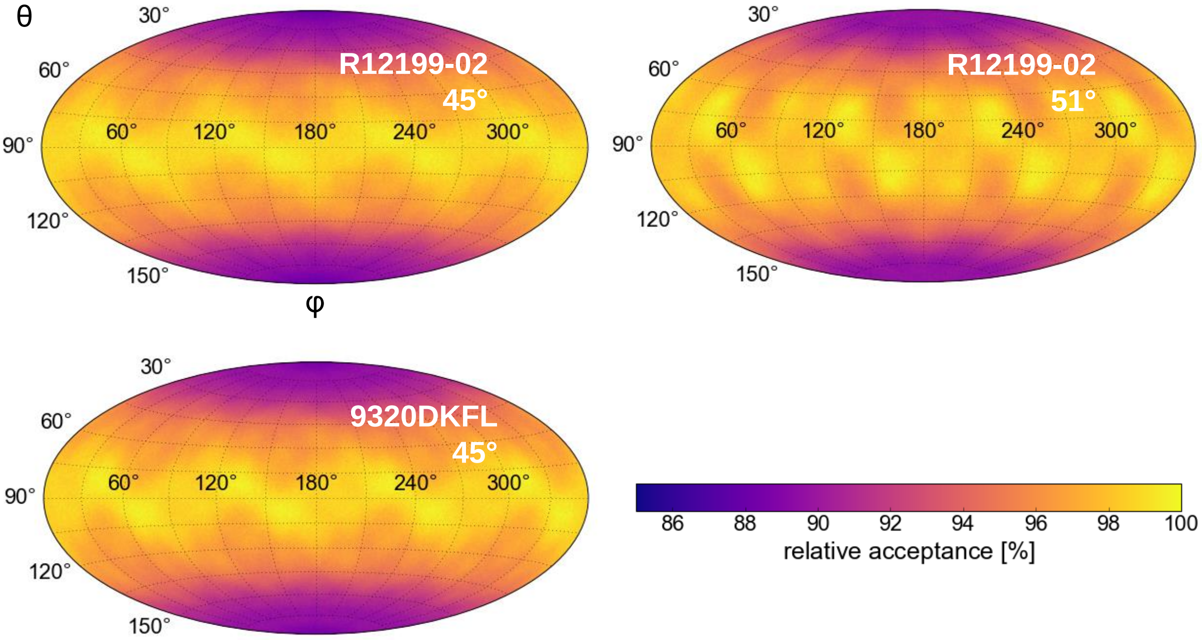

Figure 10.22: Angular acceptance homogeneity of the mDOM, shown for different combinations of PMT type and reflector opening angle and an incident photon wavelength of 390 nm[a]. Effective areas were normalized to respective maximum values. Top right configuration (Hamamatsu R12199-20 PMT equipped with a 51° reflector) represents the current default.

---

[a] Corresponding to the approximate location of maximum quantum efficiency.

configuration	**R12199-02**(51°)	**R12199-02** (45°)	**9320KFL** (45°)
I [%]	10.9 ± 0.2	12.4 ± 0.2	11.9 ± 0.2

Table 10.3: Typical mDOM angular acceptance inhomogeneities I, as defined in equation 10.2, for different mDOM configurations (PMT types and reflector angles). Simulated at the wavelength of maximum quantum efficiency (390 nm). Error margins are based on Monte-Carlo uncertainties ($\sqrt{N}$).

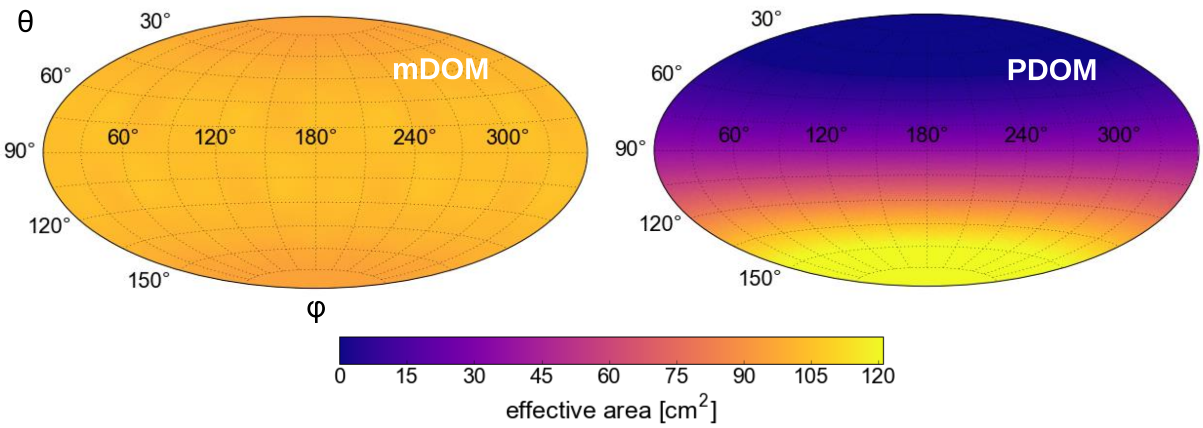

Figure 10.23: Effective areas of mDOM and PDOM as a function of the incidence angle of a plane wave. Values are shown for a wavelength of 390 nm. Effects of respective quantum efficiencies are included. The default configuration was used for the mDOM.

Overall sensitivity comparison

An important goal of this work was to quantify the benefit of using mDOMs with respect to single ten-inch PMT modules (PDOMs) in terms of sensitivity, as this number has a direct impact on the decision on detector layout, such as the number of modules per string and the inter-string spacing. Equally important, for instance to convince the collaboration of the validity of the comparison, was an understanding of the factors influencing the claimed sensitivity gain.

A simple comparison of projected frontal areas of the involved PMTs yields the often-quoted "ten three-inch PMTs make one ten-inch tube" estimation. Being valid in case of identical shape of the angular acceptance (as well as all other PMT properties, such as detection efficiency) it results in a PDOM-to-mDOM sensitivity ratio[1] of 2.4. Results of angular effective area simulations of individual ten-inch and and three-inch PMTs in air, averaged over the photon incidence angle, agreed with the initial rough estimation within[2] 2%, as did the comparison of a PDOM to a single reflector-equipped three-inch PMT inside a pressure vessel in ice. In both cases identical glass and gel properties were assumed and no quantum efficiency included.

For a more sophisticated evaluation, the solid-angle- and wavelength-averaged effective area $\bar{A}$, defined as

$$\bar{A} = \frac{1}{N} \int\limits_{200\,\mathrm{nm}}^{600\,\mathrm{nm}} \int\limits_{\theta=0}^{\theta_{\mathrm{end}}} \int\limits_{\varphi=0}^{\varphi_{\mathrm{end}}} A(\lambda, \theta, \varphi) \cdot \sin\theta \, d\theta \, d\varphi \, d\lambda, \quad N = \int\limits_{200\,\mathrm{nm}}^{600\,\mathrm{nm}} \int\limits_{\theta=0}^{\theta_{\mathrm{end}}} \int\limits_{\varphi=0}^{\varphi_{\mathrm{end}}} \sin\theta \, d\theta \, d\varphi \, d\lambda \quad (10.3)$$

where θ and φ refer to zenith and azimuth[3] while λ is the photon wavelength, was used as the figure of merit. The default mDOM was compared to the PDOM model (including the

---

[1] Not discussed in the scope of this work as only of "historical" interest. See [135] for results.

[2] Which would, applying equation 10.2, correspond to an inhomogeneity of 100%.

[1] Values discussed here apply to the default version of the mDOM, namely the mDOM-HAM.

[2] After application of a scaling factor of 1.2 to the PDOM results. See section 10.3.2.

[3] For symmetry reasons the only one eighth of the total solid angle needed to be simulated for the

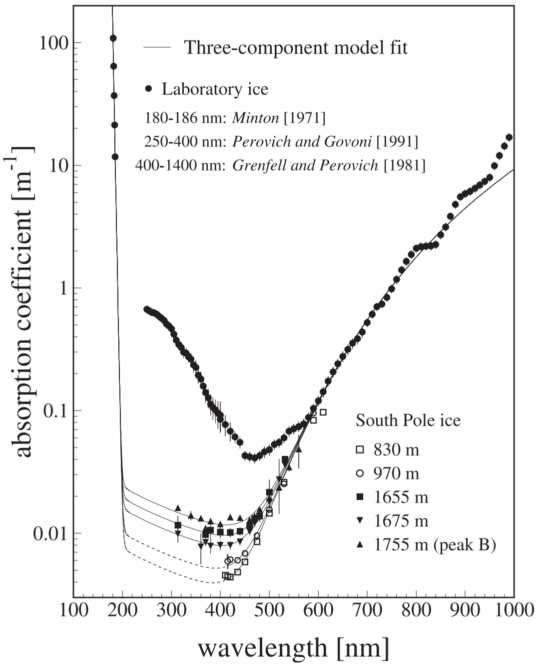

Figure 10.24: Wavelength dependence of the absorption coefficient in (glacial and laboratory) ice. Figure taken from [77]. Featuring best transparency, the region between 200 nm and 600 nm was considered in the current study.

factor of 1.2, see section 10.3.2), both located in non-absorbing ice, including appropriate optical properties of the respective module components. Solid-angle averaged effective areas for the simulated modules, prior to wavelength averaging, are presented in figure 10.25. The subsequent wavelength averaging was done inside the "transparency window" ranging from 200 nm to 600 nm, a choice based on ice absorptivity, illustrated in figure 10.24.

The ratio obtained from these average effective areas, namely ~ 2.7 in the case of the default mDOM, corresponds to the case of identical quantum efficiencies for PDOM and mDOM, and might become relevant if a decision towards enhanced quantum efficiency, so-called "ultra-bialakali", PMTs, which became available recently, is taken in the mDOM project.

Folding actual quantum efficiency spectra $QE(\lambda)$ (presented in figure 10.12) of the respective tubes into the wavelength averaging, results in a ratio valid for incident photons featuring a flat spectrum (~ 2.2 considering the default mDOM configuration). Due to the more pronounced scattering of ultraviolet photons in the ice with respect to visual light this is approximately the case for remote sources[1]. The resulting mDOM/PDOM sensitivity ratio is thus relevant for the sparsely instrumented high-energy part of IceCube-Gen2.

To assess the case of close sources, targeted by the PINGU array, an additional weighting factor, based on the Cherenkov emission spectrum (see equation 2.2), was introduced.

An overview of the resulting average effective areas for all investigated optical module configurations is presented in table 10.4, corresponding sensitivity ratios are given in table 10.5. Values stated for the mDOMs were derived using a conservative assumption[2] on the glass properties and default V95 reflectors. While, in the un-weighted case, the ratio is increased with respect to the initial simple approximation due to superior UV

---

mDOM while the acceptance of the PDOM featured rotational symmetry concerning the azimuth.

[1] For a corresponding study see e.g. [211].

[2] Vitrovex absorption length based on own lab measurement, see figure 3.3.

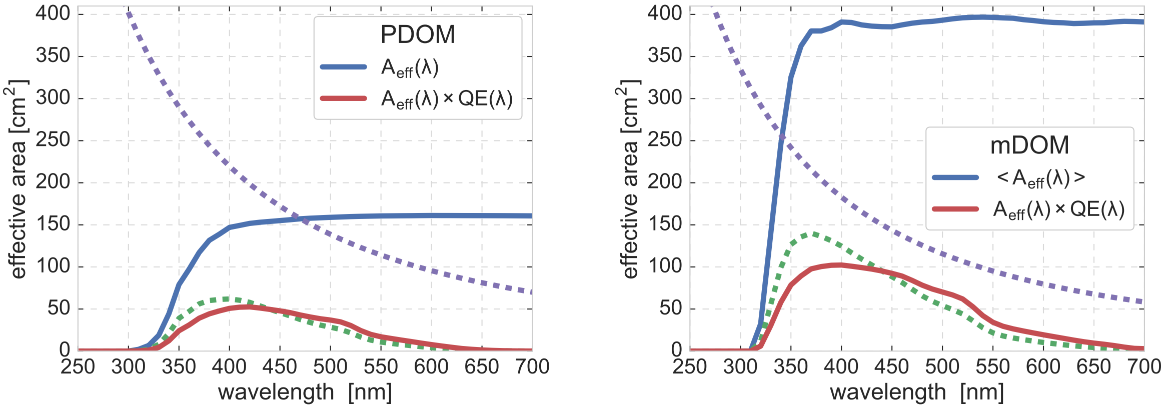

Figure 10.25: Solid angle averaged effective areas for PDOM and mDOM. Values are shown before ($A_{\text{eff}}(\lambda)$) and after scaling by applicable quantum efficiencies. In case of the PDOM, the enhanced HQE spectrum was used (see figure 10.12). The mDOM simulation features the default three-inch PMT (R12199-02) and measured, more conservative, glass properties (see section 10.2) together with the scaling factor of 1.2 (see section 10.3). Statistical errors were calculated to be smaller than linewidth. Cherenkov radiation spectrum (*purple*) and Cherenkov-weighted effective areas (*green*) shown in arbitrary units, illustrating the benefit of increased UV transparency.

module	$\overline{A}$[cm^2]	$\overline{A(\lambda)\cdot QE(\lambda)}$[cm^2]	$\overline{A(\lambda)\cdot QE(\lambda)\cdot w_{\mathrm{Cher}}(\lambda)}$[cm^2]
PDOM	96.4	22.3	13.6
mDOM-HAM	257.2	47.9	30.6
mDOM-ET	305.6	56.9	36.3

Table 10.4: Mean effective areas for the PDOM and two possible mDOM configurations[1]. Quantum efficiencies $QE(\lambda)$ of respective PMTs and the PDOM scaling factor of 1.2 applied, as well as a weighting based on the spectrum of Cherenkov radiation ($w_{\text{Cher}}(\lambda)$). Values for the mDOM represent a lower limit of module performance, simulated using the more conservative assumption on Vitrovex absorption length. Being at sub-percent level, for instance, much smaller than systematic effects, statistical uncertainties are omitted.

transparency of the Vitrovex pressure housing, it falls short of it after quantum efficiency folding. The latter is an effect of the enhanced quantum efficiency of the PDOM tube. Emphasizing UV transparency, Cherenkov weighting slightly changes the value in favor of the mDOM. While in case of the default mDOM-HAM, which corresponds to the currently developed prototype, the final sensitivity ratio was found to be 2.24, the potential use of the larger diameter ETEL PMTs (mDOM-ET) in later models will increase the number to 2.66.

Lacking reliable information from the manufacturers, the collection efficiency of the three-inch tubes was not taken into account in the study. Earlier tests of the Hamamatsu PMT at ECAP [154] indicate a potential sensitivity loss between 5% and 10%, resulting in a proportional correction of the above-stated numbers.

Simulation statistics were chosen such that relative statistical errors, as well as systematics introduced by e.g. the choice of solid angle sampling, were always negligible (i.e. well below

sensitivity ratio	$\overline{A}$	$\overline{A(\lambda)\cdot QE(\lambda)}$	$\overline{A(\lambda)\cdot QE(\lambda)\cdot w_{\mathrm{Cher}}(\lambda)}$
mDOM-HAM / PDOM	2.67	2.15	2.24
mDOM-ET / PDOM	3.17	2.55	2.66
mDOM-ET / mDOM-HAM	1.19	1.19	1.19

Table 10.5: Sensitivity ratios between mDOM-HAM, mDOM-ET and PDOM. Based on (weighted) average effective area values presented in table 10.4.

0.5% in all cases). Therefore, from a simulation perspective, the above-stated results can be considered exact, or rather featuring an uncertainty on the level of the deviations between the "official" PDOM data and the according model in the current simulation, that is to say $\sim 1\%$ (see section 10.3.2).

Concerning a statement on the actual devices, once the mDOM is produced, some additional uncertainties need to be taken into account: A relative uncertainty of $\sim 10\%$ is usually claimed on sensitivities employed in clsim [202]. The overall error budget is dominated by the DOM-by-DOM variations observed in the "golden DOM" sample used to derive the properties.

In the case of the mDOM the overall discrepancy between the tested PMTs and the simulation was found to be $< 5\%$, reported in section 10.3. For the time being we shall assume this value to be a characteristic of the statistical spread, and not e.g. a systematic error. Angular acceptance tests on larger quantities of PMTs will help to clarify this. Also information on the distribution of collection efficiency would be helpful. Mass data is however available, as reported in chapter 5, on other PMT properties potentially affecting the sensitivity, namely the gain and the quantum efficiency. As the gains of individual PMTs will be adjusted to the same value, no significant contribution to the error budget is to be expected. The typical (absolute) variations of the quantum efficiency of up to 2 percentage points, however, translate to integrated overall relative deviations of $\lesssim 10\%$[1]. Using Gaussian propagation of these relative errors $u_{\mathrm{rel}\,i}$, in the particular case using

$$U_{\mathrm{rel}} = \sqrt{\sum_i u^2_{\mathrm{rel}\,i}} \tag{10.4}$$

results in an overall relative uncertainty of $U_{\mathrm{rel}} \sim 10\%$ for the sensitivity of a single PMT. The corresponding uncertainty for the sensitivity of a complete module, featuring 24 PMTs, is consequently given by

$$U_{\mathrm{rel\,mDOM}} = \frac{\sqrt{24}}{24} \cdot u_{\mathrm{rel\,PMT}} \tag{10.5}$$

resulting in $\sim 2\%$.

Here shows another benefit of the multi-PMT concept: While the spread in performance of individual three-inch PMTs is comparable to that of their ten-inch counterparts, the overall sensitivity of mDOMs will be much more uniform than that of conventional single-PMT modules.

---

[1] This value is comparable to the spread observed in the ten-inch IceCube PMTs, which makes sense given the fact that a standard bialkali cathode is used in both models.

The propagation of the relative uncertainties for the sensitivities of mDOM and PDOM introduced above, by means of equation 10.4, results in an accuracy of the stated sensitivity ratios of $\sim 10\%$.

Impact of optical components

The choice of different combinations of optical components (glass, gel and reflector material) and the potential use of enhanced quantum efficiency PMTs allow in principle to further modulate the sensitivity of the mDOM. For the purpose of exploring the potential gain, effective areas for all possible combinations[1] were simulated in the wavelength range of interest[2]. The figure of merit for the comparison was, as introduced in the previous section, the wavelength- and solid-angle-averaged effective area, which also included weighting by quantum efficiency and, when stated, the Cherenkov spectrum.

As Geant4 simulations are rather time-consuming, the study was done for a single reflector-equipped three-inch PMT inside the module. Comparison of a single PMT average effective area, scaled by a factor of 24, to the simulation of the full module (done for ten glass-gel-reflector combinations) reveal only minor deviations (below 0.8% for all cases), justifying this approach[3]. Monte-Carlo statistics and the step size of the angular and chromatic scan were chosen such as to limit relative uncertainties of the average sensitivities to $< 0.2\%$, i.e. being negligible.

The goal of the study was to assess enhancement potentials for the final mDOM[4], testing realistic alternatives to Vitrovex and Wacker gel, but also to show what could be gained by such exotic (and expensive) materials as quartz glass. In addition, it was important to quantify the sensitivity loss resulting from the use of standard IceCube glass and gel. Those are considered a back-up solution should the currently used glass prove too noisy and the gel not temperature resistant enough[5]. Furthermore the impact of a diffuse white[6] as well as a reflective, aluminum-coated, mounting structure, instead of the default matte black one, was examined.

A graphic overview of the achievable gain in average effective area compared to the default mDOM-HAM configuration is given in figures 10.26 and 10.27. Figures 10.28 and 10.29 put the sensitivities of different setups in relation to the PDOM. Main findings concerning further mDOM developments were:

- As expected (see sections 5.2.1 and 9.2.2), relative gains between setups (combinations of glass, gel and reflector materials) did not depend on the choice of the PMT model. Corresponding differences were found to be below 0.6 percentage points in all cases. The usage of the ETEL tube always yielded a $\sim 19\%$ increase in sensitivity over the corresponding Hamamatsu tube setup.

---

[1] For an overview of all material properties see section 10.2.

[2] That is to say 200 nm to 600 nm.

[3] The remaining small deviation is attributed to the non-spherical shape of the pressure vessel and the tilt of the PMTs located at the equator.

[4] The mDOM-HAM mentioned above being only the current prototype.

[5] According to the manufacturer, Wacker gel tends to crystallize below $-50\,^{\circ}\mathrm{C}$ [136, 137]

[6] Which is actually the original state of the structures prior to painting.

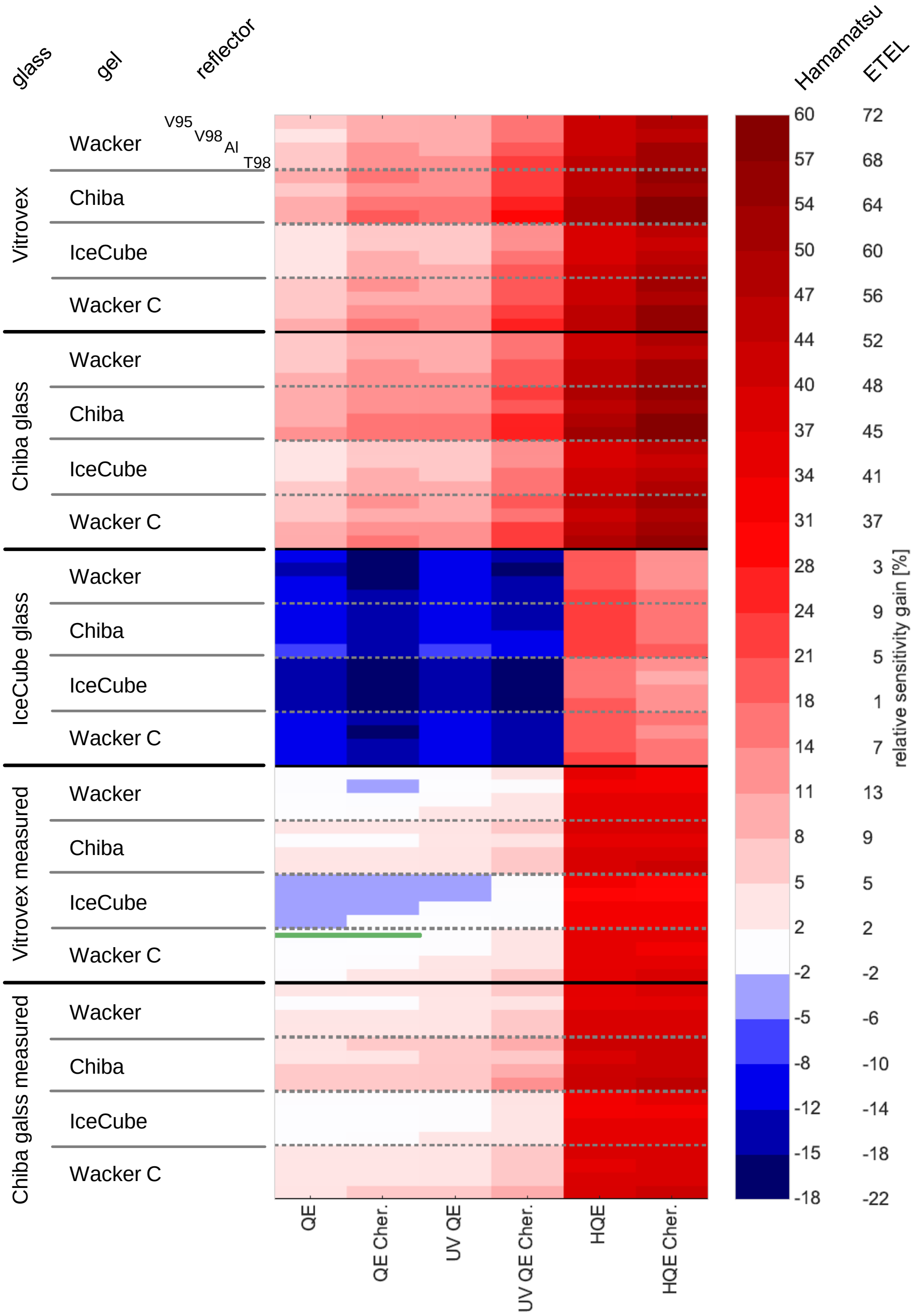

Figure 10.26: Sensitivity gain relative to default the mDOM-HAM configuration (marked *green*) achievable by the use of alternative optical components. Each cell represents a particular combination of glass, gel and reflector material. The material naming convention introduced in section 10.2 is used. UV-transparent glasses are presented in a dedicated figure (10.27). Values are given for a Hamamatsu R12199-02 mDOM as well as for the case of a module equipped with 9320KFL tubes by ETEL, both featuring respective default reflector angles (see section 10.4.1). Monte-Carlo hits were evaluated using different assumptions on quantum efficiency: "QE" represents the actual (measured) quantum efficiency of respective PMTs, "UV QE" refers to the spectrum of an UV-enhanced window tube, and "HQE" denotes a high quantum efficiency cathode, which, in analogy to the standard IceCube approach, was implemented as an overall scaling factor of 1.35. "Cher." indicates Cherenkov spectrum weighting.

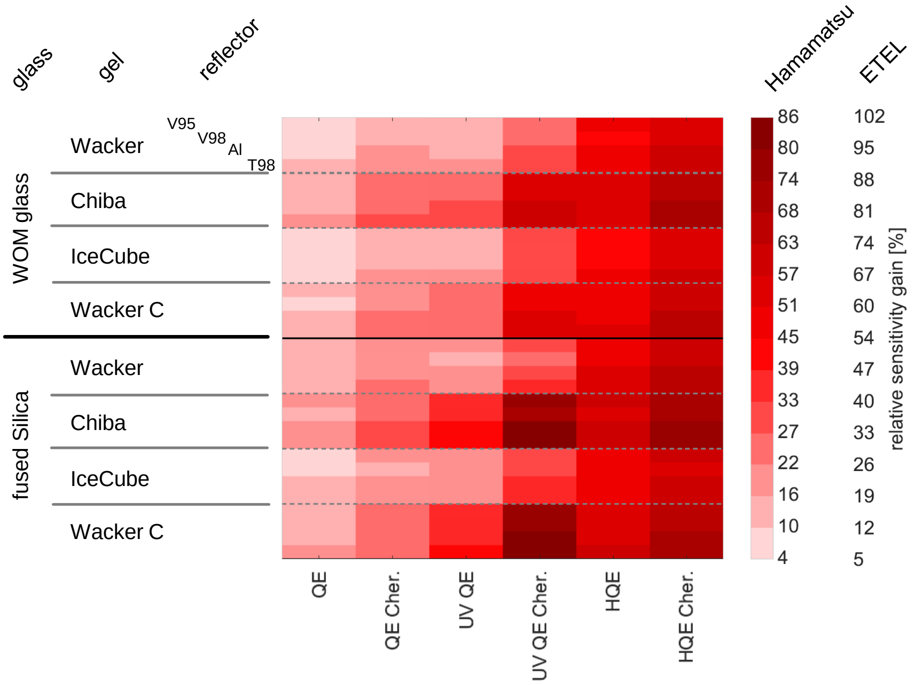

Figure 10.27: Sensitivity gain relative to default mDOM-HAM for the case of UV-transparent pressure vessel glasses. See figure 10.26 for explanations.

- Using a non-black, that is to say either white or reflective, mounting structure did not result in a significant increase of effective area. The marginal gain (∼ 0.5%) in sensitivity came along with the ejection of unabsorbed photons into the ice. Leading to an effective increase of scattering, thus increasing the amount of photons with poor timing and directional information, this behavior was deemed undesirable.

- For realistic glasses, Chiba gel is always the best choice, outperforming Wacker gel due to better transparency in the visual wavelength regime. The superior UV-transparency of Wacker gel, based on measurements by the manufacturer, only becomes important if combined with UV-transparent glasses.

- For all simulated setups reflector materials were found to perform in the following order (following increasing overall sensitivity): V98, V95, polished aluminum, T98, leading to the conclusion that, apart from the more hypothetical materials, the initially used V95 is indeed the best choice for mass production[1].

- The relative sensitivity gain from using potential UV-enhanced PMTs (see section 10.2 in particular figure 10.12) compared to standard bialkali cathodes was found to be up to ∼ 4% (∼ 8% if Cherenkov weighted) for realistic optical component combinations[2]. Only if used in combination with highly UV transparent glasses and UV reflective cones, such as quartz and T98, the yield rises to ∼ 21% (∼ 46% after Cherenkov weighting). Upgrading the PMTs with high quantum efficiency cathodes increasing the sensitivity of a tube by a factor of 1.35 throughout the spectrum, as used in DeepCore and the

---

[1] This is a nice coincidence as this material also happens to be the cheapest.

[2] Excluding UV-transparent glasses as well as polished aluminum and T98 reflectors.

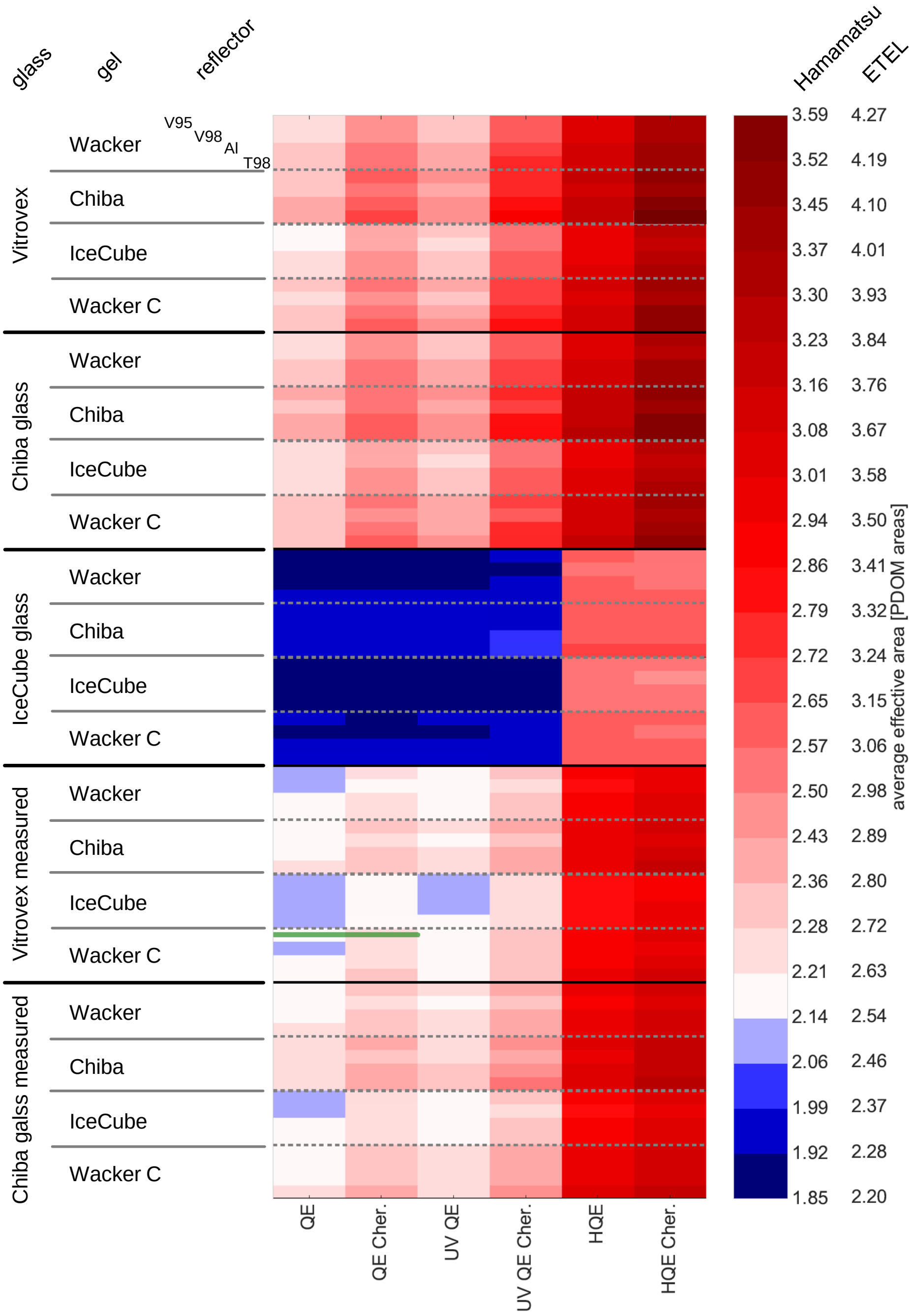

Figure 10.28: Sensitivity of “realistic” mDOM versions. The average effective areas are scaled by the effective area of the PDOM. Default conservative mDOM-HAM configuration marked *green*. See figure 10.26 for further details.

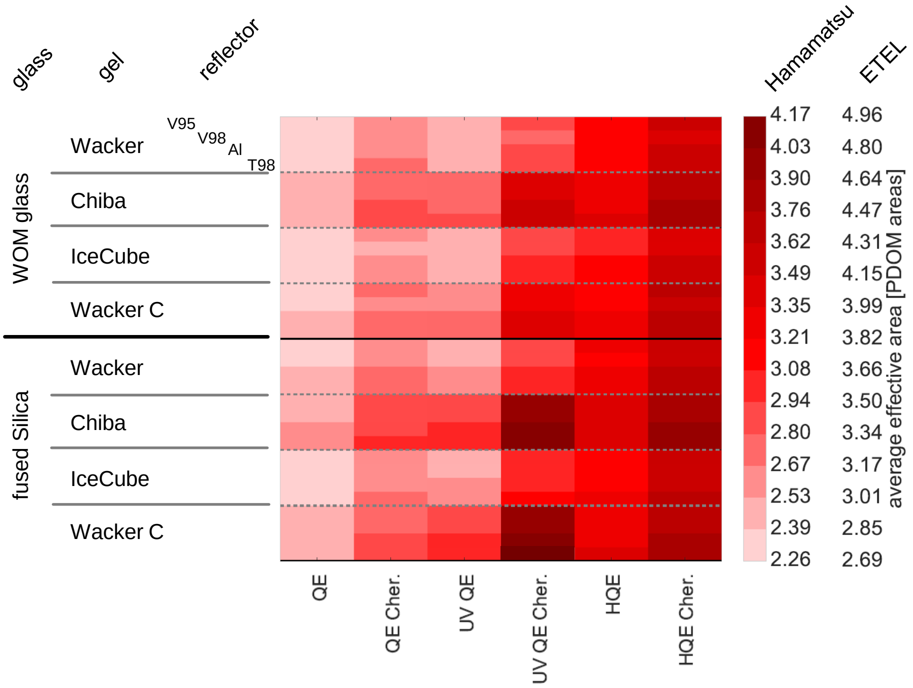

Figure 10.29: Sensitivity of UV-transparent mDOM versions, given as average effective area scaled by the corresponding PDOM value. See figure 10.26 for further details.

PDOM, is thus a more promising path to enhance mDOM performance (if the expected increase in dark rate is deemed acceptable).

- Relative to the conservative mDOM-HAM model introduced in the previous paragraph, the maximum achievable sensitivity increase, if using the Hamamatsu PMT at nominal quantum efficiency and realistic optical components, was found to be ~ 10%, equaling 2.4 PDOM sensitivities (assuming a flat photon spectrum) and ~ 15% applying Cherenkov weight, corresponding to 2.6 PDOMs.

  In the most extreme case, i.e. using the combination of quartz glass, Chiba gel and an enhanced quantum efficiency[1] ETEL tubes equipped with the most optimistic reflectors (T98) the Cherenkov-corrected mDOM sensitivity can be pushed to the equivalent of ~ 5 PDOMs.

- The lack of precise knowledge on absorption lengths for Vitrovex and Chiba glass, in particular concerning the position of the UV cut-off, results in relative sensitivity deviations[2] of up to ~ 7% (~ 12% if Cherenkov-corrected) if only realistic reflectors from V95 and V98 are taken into account. Until the availability of more reliable data, this systematic uncertainty dominates the error budget of the simulation.

- The use of low-background optical components from the original IceCube module results in an efficiency loss of ~ 13% (~ 18% including the Cherenkov factor) with respect

---

[1] Either by using a UV-enhanced or a high quantum efficiency photocathode.

[2] Between setups simulated with "official" properties and such using the results of own measurements. See figure 10.6 for details.

to the default mDOM-HAM. This loss can be balanced using the ETEL tube[1].

As a result of the study, the mDOM project group will examine the suitability of Chiba gel for the employment in the mDOM, in particular concerning its flow properties. Also a dedicated glass characterization campaign will be initiated to obtain a better knowledge of optical glass and gel properties. The default black color of the PMT mounting structure will be kept as will the currently used reflector material (V95).

As of now, the use of quartz glass is vetoed for pricing reasons, however it might become interesting given the possible gain, in particular if the strategy is taken to concentrate sensitive area on a small number of strings in order to economize drilling costs and speed-up deployment. Apart from being expensive and, according to manufacturer information, prone to damage by humidity, UV-enhanced PMTs[2] offer no substantial gain in sensitivity. High quantum efficiency ("ultra-bialkali") PMTs, on the other hand, are an interesting alternative to the current tubes.

10.4.3 Directional reconstruction

One of the main advantages of the multi-PMT concept is its intrinsic directionality (see also section 4). A photon hitting a certain PMT automatically includes information of its direction of origin. It is the aim of this section to elaborate on this claim. A dedicated calibration module, named POCAM[3], is developed in for IceCube-Gen2 (see figure 10.30). The goal is to provide a truly isotropic point photon source in the ice [212, 24]. This objective is more complex to realize using the standard approach, by means of an array of several LEDs mounted inside an optical module alongside the PMT, requiring a precise cross-calibration of the individual outputs that is also stable after cooling and throughout the operation period of the detector[4]. In principle, the POCAM features an Ulbricht sphere, that is to say a hollow sphere featuring a highly diffusive white coating on the inner surface, furbished with outlet openings, located inside a glass pressure vessel. Merely redistributing the flux of a single light emitter it, by design, ensures identical output intensity at all openings. The device is supposed to harbor an array of fast-pulsed LEDs of several wavelengths ranging from 350 nm to 500 nm (with the current prototype operating at 405 nm), featuring a total flux of $\sim 10^{10}$ to $\sim 10^{11}$ photons per pulse.

Simulation and optimization studies, concerning e.g. the coating material as well as light source and opening positions, of the device are currently ongoing. Preliminary results indicate that output isotropy is achieved beginning with distances larger than 20 m from the module [212].

This calibration module will allow, among other tasks, such as assessment of timing and energy resolution, to determine in-situ the actual orientation of the mDOM after refreezing, which is crucial for precise neutrino event reconstruction. One rather natural possibility to achieve this goal is to utilize the information available from the angular

---

[1] Net gain of 3% in the un-weighted case, loss of 2% after Cherenkov weighting.

[2] Equipped with e.g. with W-glass style entrance windows [126] (see also figure 3.5.

[3] Precision Optical CAlibration Module

[4] As discussed e.g. in sections 5.2 and 7.2, the output levels of LEDs tend to drift with time.

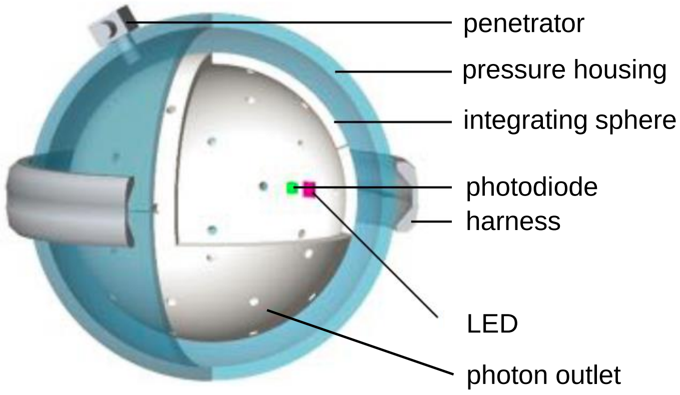

Figure 10.30: A potential POCAM configuration, featuring main components. Figure taken from [212], modified.

acceptance scans for each of the PMTs of the module. This angular sensitivity, given e.g. in terms of an angular effective area (see figure 10.31) can be interpreted as the field of view of a particular PMT. Derived simulating the incidence of a plane wave (see equation 10.1), it is expected to be valid for distant sources where this assumption is applicable[1]. Weighted by the number of photoelectrons N_i recorded by the respective PMT i, the sum of the angular sensitivities

$$A_{\text{event}}(\theta, \varphi) = \sum_{i=0}^{23} N_i \cdot A_i(\theta, \varphi) \tag{10.6}$$

results in a characteristic signature $A_{\text{event}}(\theta, \varphi)$ of the event. This distribution, which can be interpreted as a proxy for a probability map, features a pronounced maximum, located at the light source direction.

An example signature resulting from this approach, for a point source located at a distance of 50 m from the module (in the direction of $\theta = 90°$ and $\varphi = 180°$), is presented in figure 10.32 (left). Using e.g. a two-dimensional Gaussian function of the azimuth φ and zenith θ angles, given by

$$G(\theta, \varphi) = A \cdot \exp\left\{-a(\varphi - \varphi_0)^2 + 2b(\varphi - \varphi_0)(\theta - \theta_0) - c(\theta - \theta_0)^2\right\} + t \tag{10.7}$$

where A is the amplitude of the peak, t an offset, and the parameters a, b and c contain information on the width of the the peak and its rotation in the φ, θ plane, the direction of the light source with respect to the module, θ_0 and φ_0, can be reconstructed as illustrated in 10.32 (right).

The current study is based on the simulation of an mDOM, equipped with the default Hamamatsu model PMTs and 51°-reflectors, located in clear ice. A point source, isotropically emitting photons featuring a wavelength of 400 nm, was placed at distances of 20 m, 50 m and 100 m from the center of the module and a direction of $\theta = 90°$ and $\varphi = 180°$. 400 independent runs à $2 \cdot 10^9$ photons were simulated[2], allowing to obtain larger photon

---

[1] As discussed in section 9.2.2 in case of a single PMT in air, the plane wave assumption is valid for a diffuse point source located ~ 3 meters from the sensor.

[2] Limited by the permitted maximum job duration of the computing cluster.

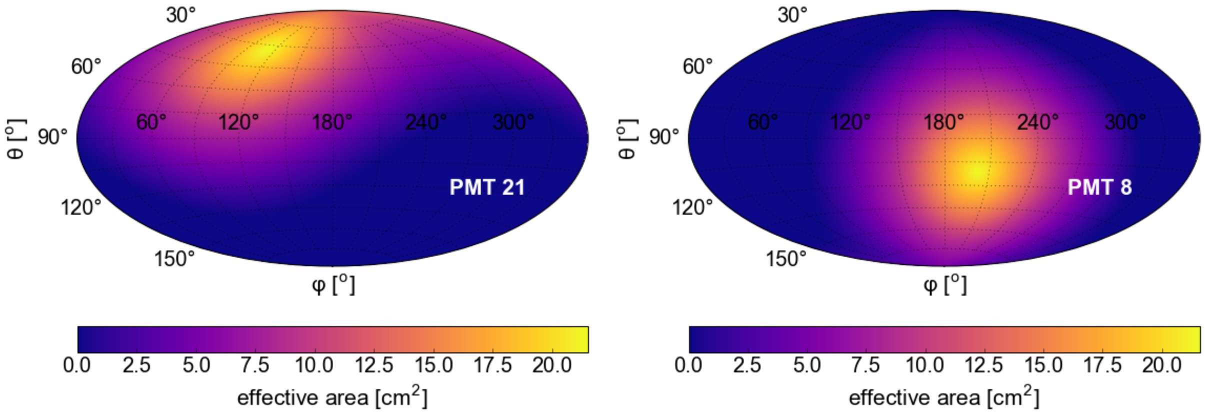

Figure 10.31: Angular effective areas shown for two individual PMTs of the mDOM.

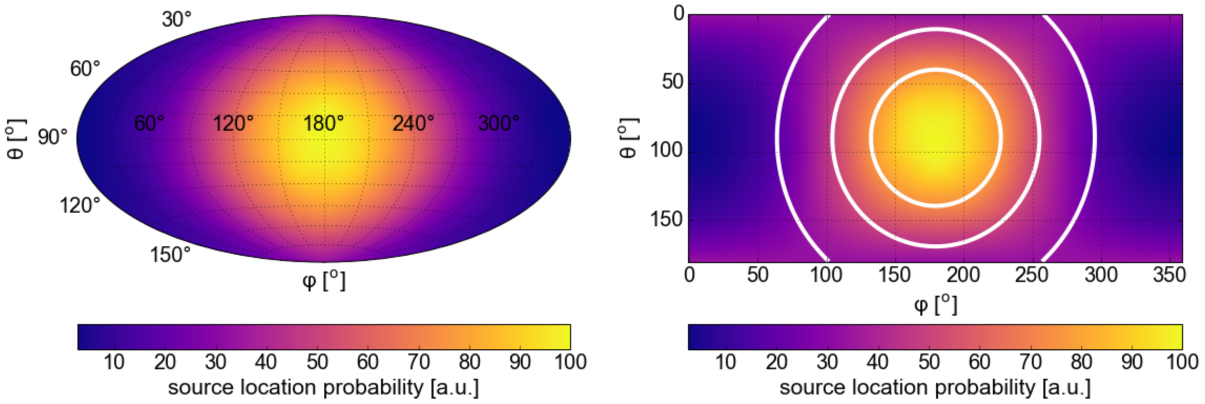

Figure 10.32: Principle of directional reconstruction. **Left**: Amplitude-weighted sum of the effective areas of all PMTs (see equation 10.6) used as a measure for the most probable source location. **Right**: Determination of the source direction, actually located at $(\theta, \varphi) = (90^\circ, 180^\circ)$, fitting a two-dimensional Gaussian (see equation 10.7), indicated by *white* iso-contours, to the distribution.

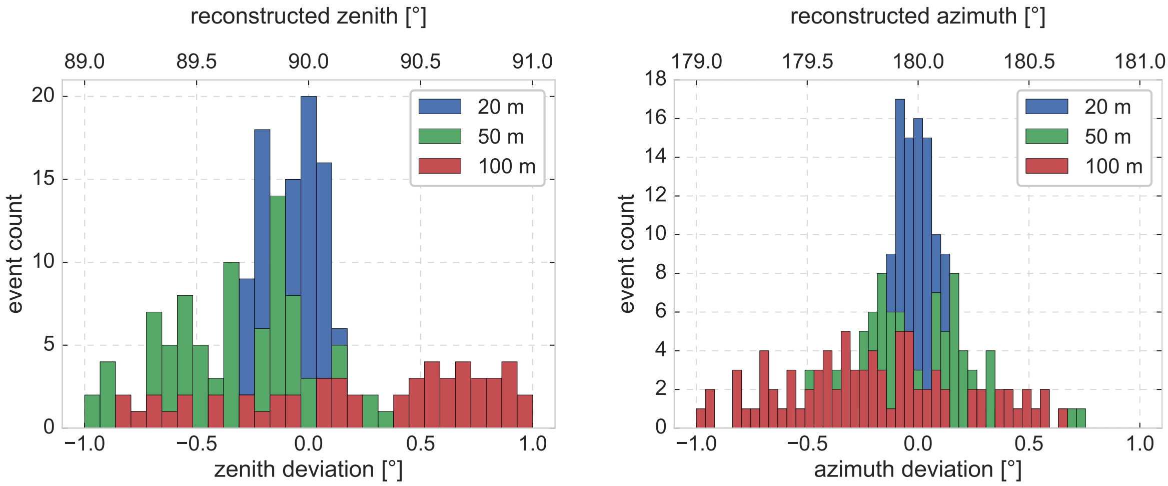

Figure 10.33: Distributions of reconstructed zenith θ (**left**) and azimuth angles φ (**right**) and respective deviations from the true source direction $(\theta, \varphi) = (90°, 180°)$, for different source distances. Each distribution is based on a sample of 100 simulated events à $1 \cdot 10^{11}$ emitted photons.

statistics stacking randomly chosen data sets. In order to obtain an estimate on the precision of the reconstruction technique, 100 random samples were drawn[1] (with refilling) from the grand total of $8 \cdot 10^{11}$ simulated photons, emulating POCAM pulses of different output intensities ($1 \cdot 10^{10}$, $5 \cdot 10^{10}$ and $1 \cdot 10^{11}$ photons). The number of photoelectrons (actual hits) was derived from the amount of photons arrived at a PMT using the appropriate quantum efficiency in combination with binomial statistics, introducing some additional randomness to the results. For all samples a fit of the source direction by means of a two-dimensional Gaussian function was performed.

Example distributions of reconstructed directions for a flux of $1 \cdot 10^{11}$ photons per pulse and different source distances are shown in figure 10.33. The total angular deviation (δ) was derived from the average values of the reconstructed direction distributions θ_{mean} and φ_{mean} as

$$\delta = \sqrt{(\theta_{\text{mean}} - 90°)^2 + (\varphi_{\text{mean}} - 180°)^2} \tag{10.8}$$

with uncertainties based on the respective standard deviations in the same manner. Figure 10.34 summarizes the final results, indicating a precision of the reconstruction technique on the order of few degrees. This outcome is encouraging, as the simulation, in principle, corresponds to the attempt to reconstruct the POCAM direction with only 100 pulses. In practice statistics will be considerable larger.

Simulated for a single source direction[2] it gives a first estimate of the precision achievable for the determination of the module orientation, in ice, by means of the POCAM calibration module. Corresponding studies for further directions are needed for a more profound statement on the overall behavior. However, given the uniformity of the module

---

[1] This approach was motivated by bootstrapping re-sampling [213] used to e.g. estimate the uncertainty of a distribution based on a limited statistical sample.

[2] Chosen as it was least distorted when projected on a flat φ, θ plane enabling the Gaussian fit. An algorithm for arbitrary angles will have to include either coordinate transformations or the use of e.g. the Kent distribution for fitting of the maximum.

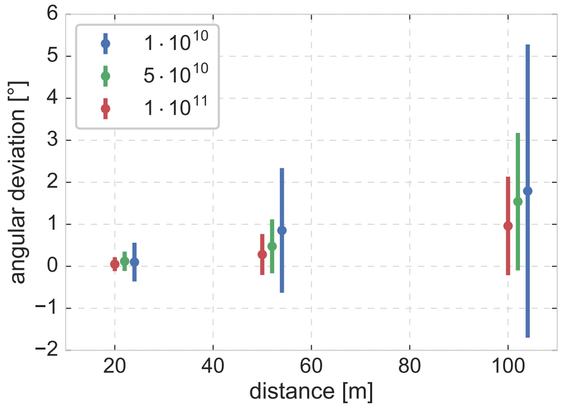

Figure 10.34: Angular deviations between simulated and reconstructed direction of the POCAM as a function of the distance. Values are shown for different numbers of photons per pulse N_γ. The depicted situation corresponds to the precision achievable using the data of 100 pulses. Errorbars are based on the standard deviations of reconstructed angle distributions (see figure 10.33). To allow for a better comparison, the data sets for $N_\gamma = 5 \cdot 10^{10}$ and $N_\gamma = 1 \cdot 10^{10}$ were shifted in distance by 2 m and 4 m, respectively.

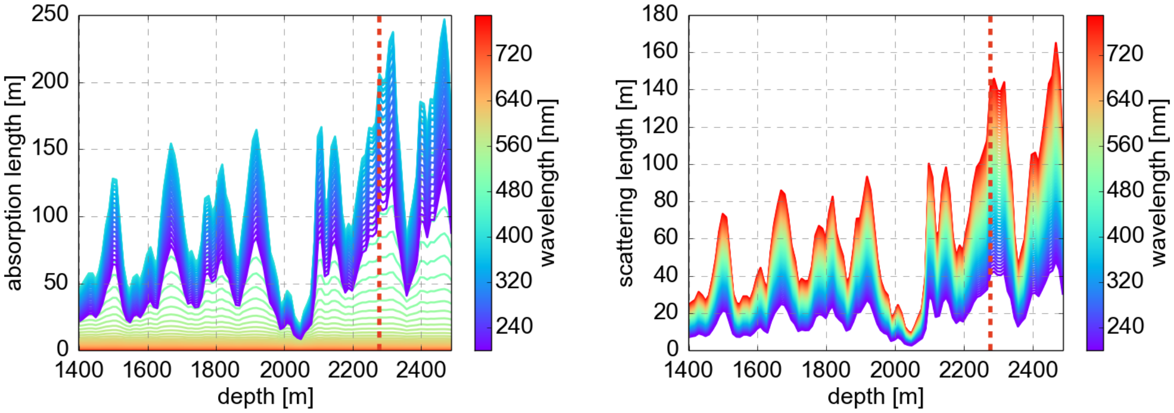

Figure 10.35: Average Mie scattering (**left**) and absorption (**right**) lengths of Antarctic ice implemented in the optical module simulation tool, as a function of depth and photon wavelength. The depth used in the current study is marked by a *dashed* line. Figures, taken from [209] (and modified), are based on [77].

sensitivity (see section 10.4.2) any angle is considered to be representative and no major deviations are expected.

In addition, the properties of the ice used in the study, corresponding to a depth of 2278.2 m, represent a rather ideal case, with the environment at other depths featuring higher levels of scattering and absorption (see figure 10.35). As the corresponding scattering length data is included in the model, its impact also can, and will, be studied in the scope of the module simulation tool. In real application conditions, additional uncertainties will be introduced by dirt and air enclosures in the re-frozen ice column. For zenith angles deviating from the equator the passage of light through different layers will further complicate the reconstruction.

On the other hand, the precision can also be improved using a fully-fledged log-likelihood approach and including timing information which will be available in a real-life calibration run, and as mentioned earlier, increased photon statistics.

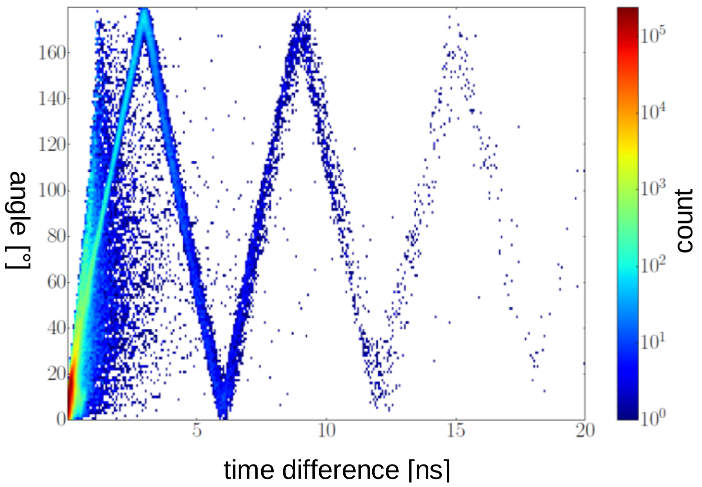

Figure 10.36: Angles between decay location and the directions of the hit PMTs as a function of photon arrival time (relative the occurrence of the associated decay). Figure taken from [214].

10.4.4 Background studies

With no luminescent wildlife, in contrast to the situation in the water based telescopes, such as Antares and the lake Baikal arrays, as well as no background from radioactive decays in the ancient glacial ice of Antarctica, the module components, in particular the glass of the pressure vessel, are the main source for optical background, apart from atmospheric muons. In general ^{40}K accounts for a large fraction of the natural background in glass, with its charged decay products generating photons by the emission of Cherenkov radiation as well as scintillation [171].

It is important to know the background and, if possible, find ways to suppress it. One step in this direction was the dark rate study, reported in section 6, delivering the additional hit rate expected from the glass ($\sim 1000\,$Hz).

With the inclusion of ^{40}K decays in the mDOM simulation tool it was also possible to approach the topic from a simulation perspective.

Background suppression

In the scope of a Bachelor's thesis [214], a first study of the ^{40}K background in the mDOM was performed. The work included an upgrade and functionality tests of the module simulation tool, assisted by the author, as well as a general characterization of hit signatures, local and temporal. Main findings of the work were:

- 94% of all detectable decays produce hits in a single PMT only.
- A vast majority of all hits, namely 99.55%, occurs inside a time-window of 2 ns after the decay. With times exceeding that limit distributed according to an exponential.
- The angular distribution of coincident events does not follow a simple exponential relation.
- The distribution of the angles between the decay location and the directions of the

hit PMTs features as a function of the hit time[1] a characteristic “zig-zag” structure[2] presented in figure 10.36. Being more pronounced if the module is placed in air, it was attributed to Cherenkov photons traveling around the module due to internal reflection.

- The hit distribution across all PMTs was found to be isotropic.
- Coincidences from independent events are negligible[3].

It was also found, hereby confirming the statements of [171], that Cherenkov radiation from ^{40}K alone can not be responsible for the dark rate observed by a PMT when in contact with glass: While a value of $\sim 1000\,\mathrm{Hz}$ is indicted by a measurement, the hit rate retrieved from a simulation of the experimental setup, based on the known ^{40}K activity in the glass, amounted to only $< 20\,\mathrm{Hz}$.

Self-calibration

However, correlated optical background is not only a nuisance, as demonstrated by our colleagues from the KM3NeT collaboration [106]: Two-fold coincidences between PMTs, induced by photons from individual decays, can be used to calibrate the module, determining, in-situ, timing offsets between individual PMTs, introduced e.g. by faulty signal cables[4].

The information needed to perform such a calibration are a large sample of hit times for all PMTs, produced by ^{40}K decay photons. In practice, this is achieved acquiring data in dedicated runs[5]. The next step is to define all unique combinations between two PMTs possible in the module. As the hit order is not important no distinction is made between e.g. combination 21 and 12. Subsequently, two-fold coincidences between those PMT pairs, produced by the same decay, are extracted, which in the case of real data, is ensured using a corresponding time window. While, due to the high ^{40}K decay rate in sea water, coincidences produced by photons originating from different decays are indeed an issue [195], they can be safely neglected considering the mDOM in ice, as discussed in the previous sub-section. After identification of the coincidences the relative arrival times between the hits on both PMTs are determined. The distribution of these times is expected to be Gaussian. If timing between the PMTs is synchronized, this Gaussian function should be located around zero. Any deviation from this behavior indicates a timing offset between the involved PMTs. Which PMT is “off” is a-priori not clear from the information on a single pair. But, as an offset will affect all pairs including the faulty PMT, the availability of the corresponding data for the full module allows to derive

---

[1] Referring to the time passed between the occurrence of a decay and the registration of associated photons at a photocathode.

[2] With no knowledge on the location of a decay this feature unfortunately can not be used for background suppression in actual operation.

[3] This statement is based on the mean background rate (reported in section 6.6.2) resulting in a typical time separation of $\sim 40\,\mu\mathrm{s}$ between events, which is much larger than the $2\,\mathrm{ns}$ including the majority of hits from a decay.

[4] This option is very attractive as such faults can also develop after the freeze-in, and be overlooked in lab tests prior to deployment.

[5] While in sea water, with its high background rate, a typical run duration is ~ 10 minutes, runs on the order of several hours will be needed in IceCube-Gen2.

individual timing offsets for all PMTs[1]. As a result of the calibration the respective hit timing can be correspondingly corrected using these values.

There are two ways to determine those corrections:

- Solving the (over-determined) **linear equation** given by
$$A \cdot \vec{t}_{\mathrm{PMT}} = \vec{t}_{\mathrm{combi}} \tag{10.9}$$
where A is a matrix defining the respective pairs, $\vec{t}_{\mathrm{combi}}$ consists of the center positions of the (Gaussian) relative hit time distributions and the vector $\vec{t}_{\mathrm{PMT}}$ features the desired corrections.
- A **simultaneous fit** of all relative offsets distributions using a global function, depending on the individual PMT offsets. This approach corresponds to a fit of the "landscape" (see figure 10.37) of the relative rate as a function of the PMT combination and the time offset.

The KM3NeT collaboration settled for the latter method, which also has the nice feature to depend on the relative detection efficiencies of the PMTs[2], thus allowing, in addition to timing information, to derive a corresponding correction factor for each of the PMTs.

However there is an important difference between the situations in IceCube-Gen2 and KM3NeT: In water, with decays occurring inside a relatively large volume (several m^3) around the module contributing to the background, the source distribution of the light is much more uniform, and thus less affected by small-scale geometric effects of the module, than is the case in the mDOM. Also, all PMTs of the KM3NeT module are oriented perpendicular to the glass surface and there is no cylindrical section modulating photon trajectories (see figures 4.5, and 4.1).

A corresponding dedicated calibration algorithm for the mDOM is currently under development in cooperation with J. Reubelt. For this purpose detailed hit data, based on $24 \cdot 10^6$ $^{40}\mathrm{K}$ decays in the glass envelope of the mDOM, was produced. The module was located in ice and equipped with Hamamatsu PMTs featuring standard 51°-reflectors. The simulation was modified to include the quantum efficiency of the PMTs. Gaussian smearing, featuring a standard deviation of 2.5 ns, was applied to the photon arrival times to account for the transit-time spread of the PMTs.

and 10.38). The angular distribution of the relative coincidence rate, presented in figure 10.39, however does not follow the function empirically found to work best in the KM3NeT case, with an attempt to fit the distribution returning unsatisfactory results. This discrepancy between the two multi-PMT modules is considered mostly the impact of the different geometries.

Preliminary results, indicate that the general prerequisites for $^{40}\mathrm{K}$-based timing calibration are met: No systematic shifts introduced by the peculiarities of the geometric PMT arrangement are observed and the distribution of the relative arrival times feature the expected Gaussian shape (see figures 10.37

---

[1] In practice either the timing offset of one of the PMTs or e.g. the average time offset is set to zero providing the absolute reference.

[2] The occurrence rate of coincidences including an "underperforming" PMT will be lower compared to others featuring the same angular separation.

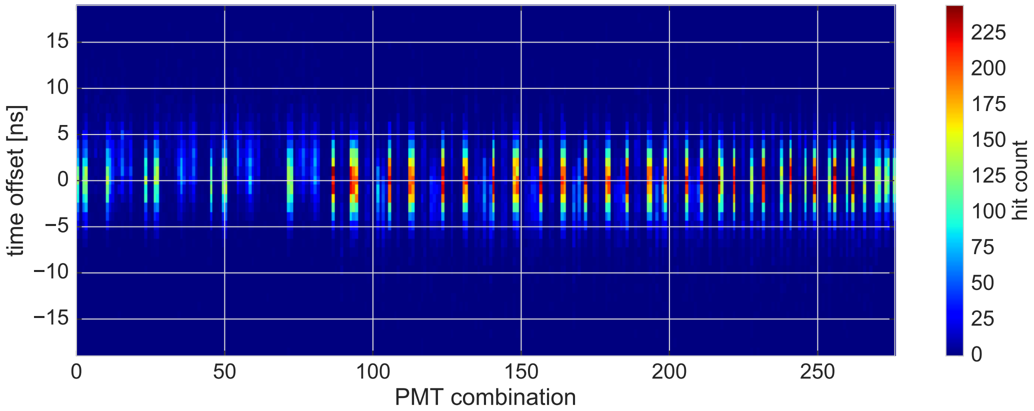

Figure 10.37: Photon arrival time differences for PMTs involved in a two-fold coincident event invoked by a ^{40}K decay. The data is presented for all combinations of two PMTs[a] possible in the mDOM, which were assigned unique identifiers.

---

[a] Without consideration of the order.

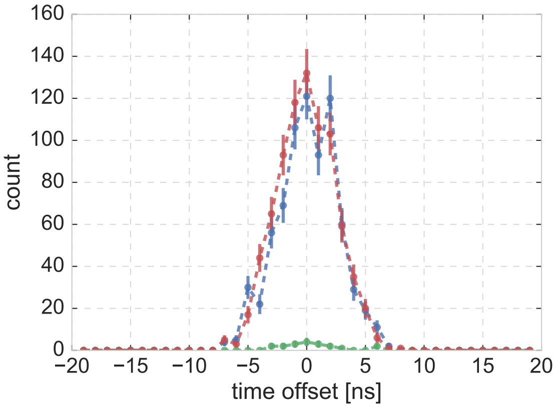

Figure 10.38: Differences between photon arrival times at PMTs involved in ^{40}K-induced a two-fold coincident event, shown for selected PMT combinations. Errorbars indicate statistical uncertainties (based on $\sqrt{N}$ errors).

Figure 10.39: Number of two-fold coincidences as a function of the angle between the involved PMTs. Fitted by means of a custom expression[a] used in the KM3NeT calibration algorithm, which obviously is not a satisfying choice in case of the mDOM.

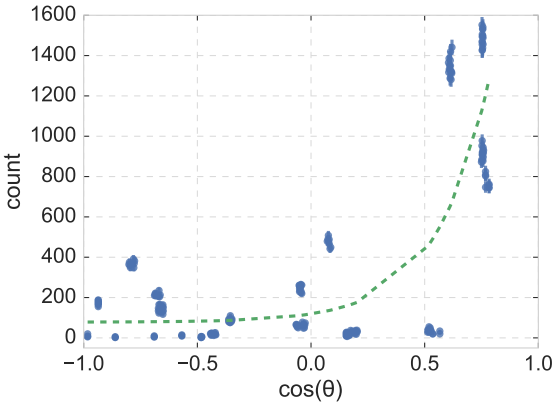

---

[a] An exponential function of a 3rd degree polynomial, which was found to provide a robust fit.

Figure 10.40: Angular acceptance look-up table for a reflector-equipped Hamamatsu R12199-02 PMT inside the mDOM located in ice. A incident photon wavelength of 400 nm was used in the simulation.

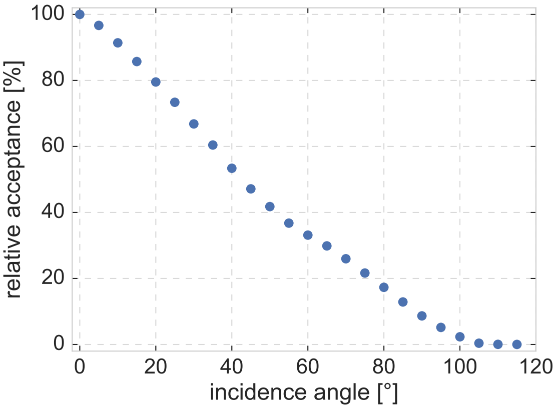

10.5 Look-up table generation

Detector simulations for IceCube rely on a set of standard tools integrated in a framework named IceTray [215]. In the scope of this framework photons are propagated through the ice using the clsim code [201]. Upon reaching the surface of an optical module the wavelength, position, and direction of travel of a photon are stored and passed on to a dedicated module, in which individual PMTs are represented by flat discs with a diameter corresponding to the outer diameter of the reflector. Based on the information in store, the trajectory of the photon is continued using simple ray-tracing, including potential absorption in flat layers of glass and gel. If crossing a PMT disc, the photon is registered and weighted with the quantum efficiency of the PMT.

This approach strongly simplifies the actual geometrical situation where a mushroom-shaped PMT is connected to the spherical surface of the glass vessel by a layer of optical gel featuring variable thickness (from 2 mm to $\sim$ 1 cm depending on the radial position) surrounded by a reflective cone. In particular the real effective area does not follow the $\cos\theta$ dependence of flat objects.

A first upgrade consisted of including a realistic angular acceptance, weighting the hit probability with a tabulated acceptance value after having divided it by $\cos\theta$ in order to account for the intrinsic acceptance of the flat geometry. The required angular acceptance table for a single PMT inside an mDOM located in ice (presented in figure 10.40) was simulated by the author and provided to T. Kittler, who performed the clsim implementation.

This approach is still not accurate on a single photon basis (consider photons impinging under the same angle at different positions, as illustrated in figure 10.42) but produces reasonable results for distant sources, and large numbers of photons[1].

As photons are tracked in clsim on an individual basis an idea for the natural next step to bring the simulation closer to the real situation was the generation of a more detailed look-up table. The intention was to replace the simple ray tracing step by a table of probabilities for being registered by a PMT, depending on the stored arrival position on the surface of the module and the angles of incidence with respect to the normal direction at this point. A corresponding table was generated using an optical module

---

[1] In other words, if a plane wave approximation is applicable.

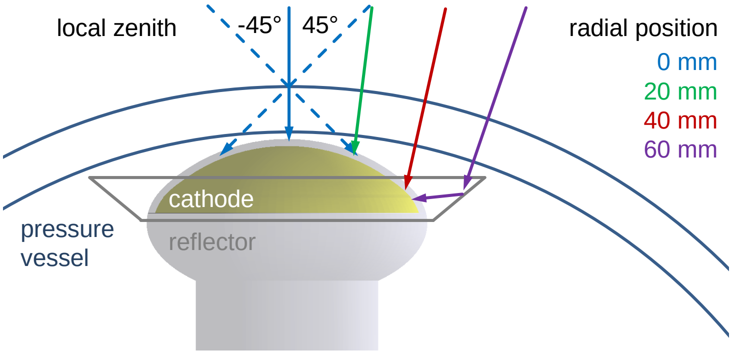

Figure 10.41: Setup for the simulation of the local photon acceptance. A pencil beam was "moved" along the surface of the module, probing the acceptance for vertical as well as inclined[a] photon incidence. Results are presented in figure 10.42.

[a] With respect to the local surface normal.

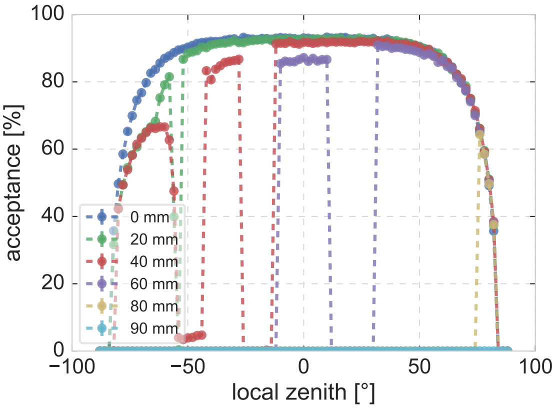

Figure 10.42: Photon acceptance as a function of the incidence angle (in terms of the local zenith, see text), shown for a variety of radial distances from the PMT center. Statistical errors are hidden by datapoint markers.

model featuring a single reflector-equipped PMT inside the pressure vessel[2] (described earlier in section 10.2). A pencil beam of zero diameter, emitting 10^5 photons per position, was moved perpendicularly along the surface as illustrated in figure 10.41. At each radial position[3] the beam was also inclined in "local" (that is to say, with respect to the surface normal) zenith θ_{loc} and azimuth φ_{loc} direction. Hits stored for each combination of position and direction allowed to derive a corresponding hit acceptance $A(\vec{X}, \theta_{\text{loc}}, \varphi_{\text{loc}})$ of the PMT as

$$A(\vec{X}, \theta_{\text{loc}}, \varphi_{\text{loc}}) = \frac{N_{\text{det}}(\vec{X}, \theta_{\text{loc}}, \varphi_{\text{loc}})}{N_{\text{emit}}} \tag{10.10}$$

where $\vec{X}$ is the position of photon incidence, and the variables θ_{loc} and φ_{loc} refer to the angles of incidence relative to the local normal direction. N_{emit} and N_{det} represent the numbers of emitted photons and of those detected by the PMT.

The data set (see figure 10.42 for an example) was provided to the detector simulation group. Its integration into clsim is currently work in progress.

---

[2] Originally, a complete module was simulated, but the huge amount of memory vetoed its practical use. The current idea is to transform each arriving photon into the reference frame of the closest PMTs and derive the respective hit probabilities.

[3] Defined as the distance relative to the center of the PMT.

10.6 Conclusions and further development

The simulation developed in the scope of this thesis proved to be a valuable tool to assess the performance of the mDOM, in particular concerning the gain with respect to the single-PMT baseline design. Demonstrating

- a significant **increase of effective area** per module,
- the **uniform coverage** of the solid angle, as well as
- the utilization of intrinsic **directional sensitivity**

it allowed to elaborate on key advantages, claimed to result from the multi-PMT concept. In addition, the outcome of the reflector angle study also had a direct impact on the further mechanical design of the mDOM, while the studies of the ^{40}K background indicated the potential of the new module to be a "self-calibrating" device.

Nevertheless, there is always room for improvement of the simulation itself, e.g. with the implementation of a more realistic cathode model and of additional physics capabilities, as well as for further studies. The following projects are currently under consideration:

- The accurate treatment of the optical background from **radioactive decays**, including, in addition to ^{40}K, all relevant radioactive contaminations (based on a gamma-spectroscopy analysis of the glass by the group of C. Kopper) and scintillation (based on [171]). Currently a dedicated test bed is set up at the IceCube Münster site to experimentally determine the relevant timing parameters and photon yield of the glass in the scope of a Master's thesis [173].
- A more detailed modeling of the **cathode** and the inner (reflective) structures of the PMT[1] based on the approach currently used in KM3NeT [152, 153].
- Development of detailed **calibration procedures**. This can include an extensive study of the calibration potential of the POCAM as well as the implementation of LED pulsers, intended to be incorporated in the final version of the module, into the simulation and study their impact on (self-) calibration.

---

[1] This effort will benefit from the results of the output uniformity study (see section 5.2) as well as a detailed investigation of photocathode properties currently under way in Münster in the scope of a Master's thesis [156].

11 Towards a first prototype

Since the initiation in early 2012 the mDOM project, based on work by the author but also thanks to essential contributions by colleagues from ECAP and DESY, has come a long way:

Main passive hardware components, that is to say, a pressure vessel, light concentration cones and a mounting structure for those devices as well as the PMTs have been designed and are readily available.

Three-inch PMTs of type R12199-02 HA were tested, including low-temperature performance, and found to be suitable for the application in the mDOM. Specimen of this model, now considered the default sensor for the mDOM, were acquired and will be used for prototyping[1]. In addition alternative PMT models, most of them featuring larger cathode diameters, but still complying with the tight space constraints of the mDOM, allowing the easy enhancement of the overall module sensitivity by $\sim 20\%$, are available form various manufacturers. Their key parameters, currently tested by the KM3NeT collaboration, look promising. The low-temperature capability remains to be tested explicitly.

The superior performance with respect to the single-PMT baseline module has been demonstrated in simulation studies

Yet, some more work needs to be accomplished for the construction of a first prototype:

- **electronics**: The low-power base needs to be finalized, in particular concerning stable low-temperature operation. The four-stage comparator digitization, which will be used in the prototyping phase, is currently in its final stages of development. The central electronics board develped for the PDOM needs adaptation including the incorporation of mDOM-specific components such as an interface to the base.

- **mechanic components**: The PMT mounting structure design will experience last adaptations. In its final version it will feature, in addition to the available PMT and reflector holders, mounts for the main electronics board (located at the center of the module) and calibration devices (see below). A module harness, most likely manufactured from stainless steel following the delicate design used in KM3NeT (see figure 4.1), minimizing the shadowing of PMTs, is under development[2]. The last steps towards a prototype also include the adaptation of the penetrator as well as pressure stability tests of the glass vessel and the assessment of its deformation as discussed in section 8.1.

- **calibration devices**: In-DOM calibration devices, such as fast LED pulsers and cameras, are being developed in the collaboration[3]. Originally intended for the single-PMT baseline module design these will also be applicable in the mDOM as it will be based on the same main board layout. Apart from specific space constraints, no additional input is needed from the mDOM. Not being crucial for prototype production, calibration

---

[1] Further investigations of the dark rate are ongoing but not a show-stopper concerning prototype construction.

[2] Although actually not essential for the first prototype.

[3] Actually a process independent from the mDOM project.

devices will be included depending on their respective status[1].

- **assembly procedure**: A construction procedure, comprising the steps for an efficient assembly of the individual components of the module is in preparation. Apart from the mere assembly of the components it needs also to include techniques for the mixing, degassing and pouring of the optical gel. Moreover, the final sealing of the pressure vessel, held together by underpressure, demands the availability of dedicated vacuum devices. Fortunately, the KM3NeT collaboration has sorted out (most of) the pitfalls and peculiarities of the process. With the final near-spherical mDOM design it is now possible to adapt this solution with minor changes.
- **read-out**: For the read-out of the prototype output during testing a dedicated stand-alone board currently under development at DESY.

Upon the construction of the first prototype, scheduled for late 2017, it will be subjected to intensive scrutinizing to verify its performance. In addition to tests in the lab it is also planned to install the module inside the NEVOD[2] detector [132]. Negotiations to that effect with colleagues from the Moscow Engineering Physics Institute are under way.

---

[1] Rapid prototyping used to produce the mounting structure of the module fortunately enables flexibility regarding ad-hoc design changes.

[2] НЕйтринный ВОдный Детектор (Neutrino Water Detector)

12 Summary and outlook

The mDOM project was initiated with the goal to adapt the novel multi-PMT technology to the IceCube-Gen2 framework allowing the detector sensitivity and precision to benefit from its advantages. In the scope of this thesis major development steps towards a dedicated IceCube-Gen2 multi-PMT optical module have been taken:

- A custom moderate-cost borosilicate glass pressure vessel was designed in cooperation with a manufacturer, featuring the appropriate pressure rating for the deployment in ice and allowing to house 24 three-inch photomultipliers. Several specimen of the new vessel were ordered and will be subjected to hyperbaric stability tests in the lab.

- Suitable PMT candidates were tested and their performance characterized in detail[1]. In the case of the Hamamatsu model R12199-02 HA the low-temperature operability was explicitly demonstrated. In the wake of PMT characterization, also new test beds to assess output uniformity and performance in well-defined environmental conditions were designed.

- Internal module hardware, including a polyamide mounting structure manufactured by means of rapid prototyping and reflectors produced from enhanced-reflectance coated aluminum sheets, was designed and tested in custom setups.

- The general operability, output linearity and low-temperature performance of a first prototype of the dedicated Cockcroft-Walton low-power base was investigated.

- To evaluate key performance parameters of the module prior to the construction of a full prototype, a Geant4-based simulation tool was implemented. Results of detailed PMT testing and the measured optical properties of glass and reflector materials were included the simulation. Its output was cross-checked with lab measurements as well as data from standard IceCube simulation framework to ensure consistency. The simulation tool was applied to studies concerning module sensitivity allowing to compare its performance to the original baseline design and elaborate on the claimed advantages of the new layout.

- In addition, first studies aiming to evaluate the potential for directional reconstruction and pointing calibration using the POCAM calibration module were performed. Furthermore relative PMT timing calibration taking advantage of the optical background from radioactive decays of the natural potassium isotopes in vessel glass was investigated.

In the scope of this work vital development steps towards a multi-PMT optical module for IceCube-Gen2 were made. Demonstrating the feasibility of such a module in compliance with the limitations of the IceCube infrastructure, as well as the benefits entailed by its use, enabled the mDOM to become a well-established concept within the collaboration with an increasing number of colleagues joining the effort.

---

[1] Feed-back to the manufacturers contributed to PMT design improvement.

At present the realization of IceCube-Gen2 is supposed[1] to be pioneered by the so-called "Phase 1" array. Consisting of six to seven strings, featuring 125 optical modules each, effectively a PINGU precursor array, it is expected to be able to reach some of the envisaged PINGU physics goals, most notably a precision measurement of τ-neutrino appearance in the atmospheric neutrino flux and probing the unitarity of the PMNS matrix in the τ-sector. With the adoption of the new scheme the weights have shifted towards reduction of the number of boreholes, in order to speed up and cheapen deployment, and the enhancement of the sensitive area of individual strings. Featuring the largest effective area in the field and adding further benefits, such as intrinsic directionality, the mDOM is now considered the baseline module technology for this project.

Based on its newly gained prominent status, the mDOM is also in a good position to be selected as a major module for the entire IceCube-Gen2 array. It is thus the hope of the author that, in the near future, the mDOM will help paving the way for the determination of neutrino mass hierarchy and unraveling the mysteries on the origin of ultra-high energy cosmic rays.

---

[1] A corresponding NSF proposal is currently under way.

13 Zusammenfassung und Ausblick

Grundlage für das mDOM-Projekt was das Bestreben die Vorteile des neuartigen Modulkonzepts, u.a. in Bezug auf Detektorsensitivität und Präzision der Ereignisrekonstruktion, für IceCube-Gen2 zugänglich zu machen. Im Rahmen der vorliegenden Arbeit wurden wichtige Entwicklungsschritte auf dem Weg eines multi-PMT Moduls für IceCube-Gen2 unternommen:

- In Zusammenarbeit mit einem Hersteller wurde ein maßgeschneiderter Druckbehälter aus Borosilikatglas mit entsprechender Druckfestigkeit entwickelt der 24 3-Zoll PMTs Platz bietet. Mehrere Exemplare des neuen Druckkörpers wurden erworben und sollen in naher Zukunft einem Drucktest unterzogen werden.
- Die Eigenschaften mehrerer PMT-Kandidaten wurden im Detail charakterisiert. Für das Modell R12199-02 HA von Hamamatsu wurde dabei auch explizit das Verhalten bei niedrigen Temperaturen getestet. Im Rahmen der PMT-Charakterisierung wurden neue Teststände zur Untersuchung der örtlichen Homogenität des Ansprecherhaltes und von PMT-Eigenschaften bei wohldefinierten Umweltbedingungen implementiert.
- Passive Modulhardware, bestehend aus einer Haltestruktur[1] und Reflektoren[2], wurden entworfen und getestet.
- Sowohl die generelle Funktionsfähigkeit eins ersten Prototypen der PMT-Base, als auch die Linearität des Ausgabesignals und das Niedrigtemperaturverhalten wurden untersucht.
- Um im Vorfeld die Vorteile demonstrieren zu können wurde ein Simulationsmodell des optischen Moduls in Geant4 implementiert. Ergebnisse, sowohl der detaillierten PMT-Charakterisierung als auch der Messung der optischen Eigenschaften verschiedener Gläser und Reflektormaterialien, flossen in die Entwicklung ein. Simulationsergebnisse wurden durch den Vergleich mit Labormessungen verifiziert. Das Simulationsmodell fand in Studien zum Vergleich der Modulsensitivität zwischen dem mDOM und dem herkömmlichen IceCube-Modul (bestehend aus einem einzelnen großen PMT) Verwendung.
- Darüber hinaus wurden erste Studien zur Richtungsrekonstruktion und zur Bestimmung der relativen Differenzen von Signallaufzeiten unter Verwendung des natürlichen ^{40}K Untergrunds durchgeführt.

Die Ergebnisse dieser Arbeit stellen wesentliche Schritte auf dem Weg zu einem multi-PMT Modul für IceCube-Gen2 dar. Sowohl die Machbarkeit eines derartigen Moduls unter den gegebenen Rahmenbedingungen, als auch die Vorteile des Konzepts konnten aufgezeigt werden und trugen maßgeblich zur Etablierung der Technologie in der IceCube-Gen2 Kollaboration bei, was sich auch in einer wachsenden Beteiligung von Kollegen an dem Projekt niederschlägt.

---

[1] Hergestellt durch selektives Sintern ("3D-Druck") aus Polyamid.

[2] Aus beschichtetem Aluminiumblech.

Nach dem aktuellen Stand der Planungen soll dem eigentlichen Bau von IceCube-Gen2 ein "Phase 1" genannter Detektor vorangehen. Mit sechs bis sieben Strings zu je 125 optischen Modulen stellt dieser einen Vorläufer von PINGU dar und soll einen Teil der Physikziele, darunter eine Präzisionsmessung der Oszillation von τ-Neutrinos im atmosphärischen Fluss sowie die Bestimmung der Unitarität der PMNS-Matrix im τ-Sektor, abdecken. Mit einer verkleinerten Anzahl an Bohrlöchern die über eine vergrößerte Sensitivität der Module ausgeglichen werden soll wurde bei diesem Projekt großer Wert auf der Möglichkeit eines zügigen Aufbaus gelegt. Mit der, im Vergleich zu den Alternativen, größten effektiven Fläche (und weiteren attraktiven Vorteilen) wird das mDOM inzwischen als Standardmodultechnologie für Phase 1 gehandelt.

Aufgrund dieses prominenten Status ist das mDOM auch in einer guten Ausgangsposition bei der Auswahl der optischen Sensoren für das gesamte IceCube-Gen2 Neutrinoteleskop. Es ist daher die berechtigte Hoffnung des Autors, dass das neu entwickelte optische Modul in naher Zukunft dazu beitragen wird, den Weg zur Bestimmung der Neutrinomassenhierarchie zu ebnen und die Geheimnisse um den Ursprung der kosmischen Strahlung zu lüften.

14 Bibliography

[1] M. G. Aartsen, et al. (IceCube Collaboration), *First Observation of PeV-Energy Neutrinos with IceCube*, Phys. Rev. Lett. 111 (2013) 021103. URL `http://link.aps.org/doi/10.1103/PhysRevLett.111.021103`

[2] J. G. Learned, K. Mannheim, *High-Energy Neutrino Astrophysics*, Ann. Rev. Nucl. Part. Sci. 50 (1) (2000) 679–749. URL `http://dx.doi.org/10.1146/annurev.nucl.50.1.679`

[3] J. K. Becker, *High-energy neutrinos in the context of multimessenger astrophysics*, Phys. Rep. 458 (4–5) (2008) 173 – 246. URL `http://www.sciencedirect.com/science/article/pii/S037015730800029X`

[4] U. F. Katz, C. Spiering, *High-energy neutrino astrophysics: Status and perspectives*, Prog. Part. Nucl. Phys. 67 (3) (2012) 651 – 704. URL `http://www.sciencedirect.com/science/article/pii/S0146641011001189`

[5] A. M. Hillas, *Cosmic Rays: Recent Progress and some Current Questions* Preprint arXiv:astro-ph/0607109.

[6] C. Grupen, Astroparticle Physics, Springer-Verlag Berlin Heidelberg, 2005.

[7] E. Fermi, *Versuch einer Theorie der beta-Strahlen. I*, Zeitschrift für Physik 88 (3-4) (1934) 161–177. URL `http://dx.doi.org/10.1007/BF01351864`

[8] C. Sutton, Spaceship Neutrino, Cambridge University Press, 1992.

[9] C. L. Cowan, Jr., et al., *Detection of the Free Neutrino: A Confirmation*, Science 124 (1956) 103–104. URL `http://science.sciencemag.org/content/124/3212/103`

[10] F. Reines, et al., *Detection of the Free Antineutrino*, Phys. Rev. 117 (1960) 159–173. URL `http://link.aps.org/doi/10.1103/PhysRev.117.159`

[11] MissMJ, Nasfarley88, et al. (2014). URL `https://commons.wikimedia.org/wiki/File:Standard_Model_of_Elementary_Particles_modified_version.svg`

[12] G. Danby, et al., *Observation of High-Energy Neutrino Reactions and the Existence of Two Kinds of Neutrinos*, Phys. Rev. Lett. 9 (1962) 36–44. URL `http://link.aps.org/doi/10.1103/PhysRevLett.9.36`

[13] K. Kodama, et al., *Observation of tau neutrino interactions*, Phys. Lett. B 504 (3) (2001) 218 – 224. URL `http://www.sciencedirect.com/science/article/pii/S0370269301003070`

[14] R. Davis, D. S. Harmer, K. C. Hoffman, *Search for Neutrinos from the Sun*, Phys. Rev. Lett. (1968) 1205–1209. URL `http://link.aps.org/doi/10.1103/PhysRevLett.20.1205`

[15] K. Hirata, et al., *Observation of a small atmospheric ν_μ/ν_e ratio in Kamiokande*, Phys. Lett 280 (1992) 146.

[16] E. Kearns, *Experimental measurements of atmospheric neutrinos*, Nucl. Phys. B - Proc. Suppl. 70 (1–3) (1999) 315 – 323. URL `http://www.sciencedirect.com/science/article/pii/S0920563298004411`

[17] Y. Fukuda, et al. (Super-Kamiokande Collaboration), *Evidence for Oscillation of Atmospheric Neutrinos*, Phys. Rev. Lett. 81 (1998) 1562–1567. URL `http://link.aps.org/doi/10.1103/PhysRevLett.81.1562`

[18] Q. R. Ahmad, et al. (SNO Collaboration), *Measurement of the rate of* $\nu_e + d \rightarrow p + p + e^-$ *interactions produced by* ^8B *solar neutrinos at the Sudbury Neutrino Observatory*, Phys. Rev. Lett. 87 (2001) 071301, Preprint arXiv:nucl-ex/0106015.

[19] S. Mikheyev, A. Smirnov, *Resonant amplification of neutrino oscillations in matter and solar-neutrino spectroscopy*, Il Nuovo Cimento C 9 (1) (1986) 17–26. URL `http://dx.doi.org/10.1007/BF02508049`

[20] L. Wolfenstein, *Neutrino oscillations in matter*, Phys. Rev. D 17 (1978) 2369–2374. URL `http://link.aps.org/doi/10.1103/PhysRevD.17.2369`

[21] E. K. Akhmedov, *Atmospheric neutrinos at Super-Kamiokande and parametric resonance in neutrino oscillations*, Nucl. Phys. B542 (1999) 3–30, Preprint arXiv:hep-ph/9808270.

[22] P. C. de Holanda, A. Yu. Smirnov, *Solar neutrinos: Global analysis with day and night spectra from SNO*, Phys. Rev. D66 (2002) 113005, Preprint arXiv:hep-ph/0205241.

[23] J. L. Hewett, et al., *Introduction*, in: J. L. Hewett, et al. (Eds.), Proceedings of the 2011 workshop on Fundamental Physics at the Intensity Frontier, 2011, pp. 1–5, Preprint arXiv:1205.2671.

[24] M. G. Aartsen, et al. (IceCube PINGU Collaboration), *Letter of Intent: The Precision IceCube Next Generation Upgrade (PINGU)* Preprint arXiv:1401.2046.

[25] K. A. Olive, et al. (Particle Data Group Collaboration), *Review of Particle Physics*, Chin. Phys. C38 (2014) 090001.

[26] K. Abe, et al., *Letter of Intent: The Hyper-Kamiokande Experiment – Detector Design and Physics Potential* Preprint arXiv:1109.3262.

[27] C. Spiering, *Towards high-energy neutrino astronomy. A historical review*, Eur. Phys. J. H 37 (2012) 515–565, Preprint arXiv:1207.4952.

[28] S. Betts, et al., *Development of a Relic Neutrino Detection Experiment at PTOLEMY: Princeton Tritium Observatory for Light, Early-Universe, Massive-Neutrino Yield* Preprint arXiv:1307.4738.

[29] G. Bellini, et al., *Observation of geo-neutrinos*, Phys. Lett. B 687 (4–5) (2010) 299 – 304. URL `http://www.sciencedirect.com/science/article/pii/S0370269310003722`

[30] S.-H. Seo, et al. (RENO Collaboration), *New Results from RENO and The 5 MeV Excess*, AIP Conf. Proc. 1666 (2015) 080002, Preprint arXiv:1410.7987.

[31] X. Guo, et al. (Daya Bay Collaboration), *A Precision measurement of the neutrino mixing angle* θ_{13} *using reactor antineutrinos at Daya-Bay* Preprint arXiv:hep-ex/0701029.

[32] Y. Abe, et al. (Double Chooz Collaboration), *Indication of Reactor* $\overline{\nu}_e$ *Disappearance in the Double Chooz Experiment*, Phys. Rev. Lett. 108 (2012) 131801. URL `http://link.aps.org/doi/10.1103/PhysRevLett.108.131801`

[33] A. Porta, et al., *Reactor Neutrino Detection for Non-Proliferation With the NUCIFER Experiment*, IEEE Trans. Nucl. Sci. 57 (5) (2010) 2732–2739.

[34] C. E. Rolfs, W. S. Rodney, W. A. Fowler, Cauldrons in the cosmos : nuclear astrophysics, Theoretical astrophysics, University of Chicago Press, Chicago, 1988. URL `http://repository.gsi.de/record/66499`

[35] K. Hirata, et al., *Observation of a neutrino burst from the supernova SN1987A*, Phys. Rev. Lett. 58 (1987) 1490–1493. URL `http://link.aps.org/doi/10.1103/PhysRevLett.58.1490`

[36] R. M. Bionta, et al., *Observation of a neutrino burst in coincidence with supernova 1987A in the Large Magellanic Cloud*, Phys. Rev. Lett. 58 (1987) 1494–1496. URL `http://link.aps.org/doi/10.1103/PhysRevLett.58.1494`

[37] I. V. Krivosheina, *Sn 1987A – Historical View about Registration of the Neutrino Signal with Baksan, KAMIOKANDE II and IMB Detectors*, Int. J. Mod. Phys. D 13 (2004) 2085–2105.

[38] V. F. Hess, *Über Beobachtungen der durchdringenden Strahlung bei sieben Freiballonfahrten*, Z. Phys. 13 (1912) 1084. URL `http://cds.cern.ch/record/262750`

[39] V. L. Fitch, *Elementary particle physics: The origins*, Rev. Mod. Phys. 71 (1999) S25–S32. URL `http://link.aps.org/doi/10.1103/RevModPhys.71.S25`

[40] S. H. Neddermeyer, C. D. Anderson, *Note on the Nature of Cosmic-Ray Particles*, Phys. Rev. 51 (1937) 884–886. URL `http://link.aps.org/doi/10.1103/PhysRev.51.884`

[41] W. D. Apel, et al. (KASCADE-Grande Collaboration), *Kneelike Structure in the Spectrum of the Heavy Component of Cosmic Rays Observed with KASCADE-Grande*, Phys. Rev. Lett. 107 (2011) 171104. URL `http://link.aps.org/doi/10.1103/PhysRevLett.107.171104`

[42] K. Greisen, *End to the Cosmic-Ray Spectrum?*, Phys. Rev. Lett. 16 (1966) 748–750. URL `http://link.aps.org/doi/10.1103/PhysRevLett.16.748`

[43] G. T. Zatsepin, V. A. Kuz'min, *Upper Limit of the Spectrum of Cosmic Rays*, Soviet Journal of Experimental and Theoretical Physics Letters 4 (1966) 78.

[44] M. Takeda, et al., *Extension of the Cosmic-Ray Energy Spectrum beyond the Predicted Greisen-Zatsepin-Kuz'min Cutoff*, Phys. Rev. Lett. 81 (1998) 1163–1166. URL `http://link.aps.org/doi/10.1103/PhysRevLett.81.1163`

[45] R. U. Abbasi, et al. (High Resolution Fly's Eye Collaboration), *First Observation of the Greisen-Zatsepin-Kuzmin Suppression*, Phys. Rev. Lett. 100 (2008) 101101. URL `http://link.aps.org/doi/10.1103/PhysRevLett.100.101101`

[46] Pierre Auger Collaboration, *The Pierre Auger Cosmic Ray Observatory*, Nucl. Inst. Meth. A 798 (2015) 172 – 213. URL `http://www.sciencedirect.com/science/article/pii/S0168900215008086`

[47] J. Abraham, et al., *Observation of the Suppression of the Flux of Cosmic Rays above* $4{\times}10^{19}eV$, Phys. Rev. Lett. 101 (6) (2008) 061101, Preprint arXiv:0806.4302.

[48] A. Aab, et al. (Pierre Auger Collaboration), *The Pierre Auger Observatory: Contributions to the 33rd International Cosmic Ray Conference (ICRC 2013)* Preprint arXiv:1307.5059.

[49] V. S. Berezinskii, G. T. Zatsepin, *Cosmic neutrinos of superhigh energy*, Yadern. Fiz. 11 (1970) 200.

[50] R. Engel, D. Seckel, T. Stanev, *Neutrinos from propagation of ultrahigh energy protons*, Phys. Rev. D 64 (2001) 093010. URL `http://link.aps.org/doi/10.1103/PhysRevD.64.093010`

[51] Beetjedwars (2008). URL `https://upload.wikimedia.org/wikipedia/commons/2/2c/AirShower.svg`

[52] M. G. Aartsen, et al. (IceCube Collaboration), *Measurement of the Atmospheric* ν_e *Flux in IceCube*, Phys. Rev. Lett. 110 (2013) 151105. URL `http://link.aps.org/doi/10.1103/PhysRevLett.110.151105`

[53] C. G. S. Costa, *The prompt lepton cookbook*, Astropart. Phys. 16 (2001) 193–204, Preprint arXiv:hep-ph/0010306.

[54] N. Busca, D. Hooper, E. W. Kolb, *Pierre Auger data, photons, and top-down cosmic ray models*, Phys. Rev. D 73 (12) (2006) 123001, Preprint arXiv:astro-ph/0603055.

[55] F. Halzen, *Astroparticle physics with high energy neutrinos: from AMANDA to IceCube*, Eur. Phys. J. C 46 (2006) 669–687, Preprint arXiv:astro-ph/0602132.

[56] D. Semikoz, et al. (Pierre Auger Collaboration), *Constraints on top-down models for the origin of UHECRs from the Pierre Auger Observatory data*, in: R. Caballero, et al. (Eds.), Proceedings, 30th International Cosmic Ray Conference (ICRC 2007), Vol. 4, Yucatan Autonoma Univ., Merida, Mexico, 2008, pp. 433–436, Preprint arXiv:0706.2960.

[57] I. F. Mirabel, *Gamma-ray binaries*, Astrophys. Space Sci. 309 (2007) 267–270, Preprint arXiv:astro-ph/0610707.

[58] V. A. Acciari, *A connection between star formation activity and cosmic rays in the starburst galaxy M82*, Nature 462 (7274) (2009) 770–772. URL `http://dx.doi.org/10.1038/nature08557`

[59] S. R. Kelner, F. A. Aharonian, V. V. Bugayov, *Energy spectra of gamma rays, electrons, and neutrinos produced at proton-proton interactions in the very high energy regime*, Phys. Rev. D74 (3) (2006) 034018, Preprint arXiv:astro-ph/0606058.

[60] E. Fermi, *On the Origin of the Cosmic Radiation*, Phys. Rev. 75 (1949) 1169–1174. URL `http://link.aps.org/doi/10.1103/PhysRev.75.1169`

[61] A. R. Bell, *The acceleration of cosmic rays in shock fronts – I*, Monthly Notices of the Royal Astronomical Society 182 (2) (1978) 147–156. URL `http://mnras.oxfordjournals.org/content/182/2/147.abstract`

[62] A. R. Bell, *The acceleration of cosmic rays in shock fronts – II*, Mon. Not. R. Astron. Soc. 182 (3) (1978) 443–455. URL `http://mnras.oxfordjournals.org/content/182/3/443.abstract`

[63] G. F. Krymskii, *A regular mechanism for the acceleration of charged particles on the front of a shock wave*, Akademiia Nauk SSSR Doklady 234 (1977) 1306–1308.

[64] K. Mannheim, R. J. Protheroe, J. P. Rachen, *Cosmic ray bound for models of extragalactic neutrino production*, Phys. Rev. D63 (2) (2001) 023003, Preprint arXiv:astro-ph/9812398.

[65] E. Waxman, J. Bahcall, *High energy neutrinos from astrophysical sources: An upper bound*, Phys. Rev. D 59 (2) (1999) 023002, Preprint arXiv:hep-ph/9807282.

[66] M. G. Aartsen, et al. (IceCube Collaboration), *Evidence for High-Energy Extraterrestrial Neutrinos at the IceCube Detector*, Science 342 (2013) 1242856, Preprint arXiv:1311.5238.

[67] M. G. Aartsen, et al. (IceCube Collaboration), *Observation of High-Energy Astrophysical Neutrinos in Three Years of IceCube Data*, Phys. Rev. Lett. 113 (2014) 101101, Preprint arXiv:1405.5303.

[68] F. Halzen, *Cosmic neutrinos from the sources of galactic and extragalactic cosmic rays*, Ap&SS 309 (2007) 407–414, Preprint arXiv:astro-ph/0611915.

[69] A. Roberts, *The birth of high-energy neutrino astronomy: A personal history of the DUMAND project*, Rev. Mod. Phys. 64 (1992) 259–312. URL `http://link.aps.org/doi/10.1103/RevModPhys.64.259`

[70] M. A. Markov, *On high-energy neutrino physics*, in: E. C. G. Sudarashan, J. H. Tinlot, A. Melissinos (Eds.), Proceedings of the 1960 Annual International Conference on High Energy Physics, Rochester, University of Rochester/Interscience, Rochester, NY, 1960, p. 578.

[71] F. Halzen, S. R. Klein, *IceCube: An Instrument for Neutrino Astronomy*, Rev. Sci. Instrum. 81 (2010) 081101, Preprint arXiv:1007.1247.

[72] S. Fukuda, et al., *The Super-Kamiokande detector*, Nucl. Inst. Meth. A 501 (2–3) (2003) 418 – 462. URL `http://www.sciencedirect.com/science/article/pii/S016890020300425X`

[73] J. A. Formaggio, G. P. Zeller, *From eV to EeV: Neutrino cross sections across energy scales*, Rev. Mod. Phys. 84 (2012) 1307–1341. URL `http://link.aps.org/doi/10.1103/RevModPhys.84.1307`

[74] P. A. Čerenkov, *Visible Radiation Produced by Electrons Moving in a Medium with Velocities Exceeding that of Light*, Phys. Rev. 52 (1937) 378–379.

[75] И. М. Франк, *Излучение электронов, движущихся в веществе со сверхсветовой скоростью*, Успехи физических наук 30 (11) (1946) 149–183. URL `http://ufn.ru/ru/articles/1946/11/a/`

[76] Baikal Collaboration, *BAIKAL-GVD: Gigaton Volume Detector in Lake Baikal* (2012). URL `http://baikalweb.jinr.ru`

[77] M. Ackermann, et al., *Optical properties of deep glacial ice at the south pole*, Journal of Geophysical Research: Atmospheres 111 (D13) (2006) n/a–n/a, d13203. URL `http://dx.doi.org/10.1029/2005JD006687`

[78] M. Aartsen, et al., *Measurement of South Pole ice transparency with the IceCube LED calibration system*, Nucl. Inst. Meth. A 711 (2013) 73 – 89. URL `http://www.sciencedirect.com/science/article/pii/S0168900213001460`

[79] K. Collaboration, Detector Simulations for KM3NeT, v3.3 Edition (2014). URL `http://www.km3net.org/internal.php`

[80] V. Balkanov, et al. (NEMO Collaboration), *Simultaneous measurements of water optical properties by AC9 transmissometer and ASP-15 Inherent Optical Properties Meter in Lake Baikal*, Nucl. Inst. Meth. A298 (2003) 231–239, Preprint astro-ph/0207553.

[81] R. J. Wilkes, J. G. Learned, P. W. Gorham, *Deep Ocean Neutrino Detector Development: Contributions by The DUMAND Project*, unpublished. URL `http://www.phys.hawaii.edu/~dumand/dumacomp.html`

[82] R. I. Bagduev, et al., *The Optical module of the Baikal deep underwater neutrino telescope*, Nucl. Inst. Meth. A420 (1999) 138–154, Preprint arXiv:astro-ph/9903347.

[83] I. Belolaptikov, et al., *The Baikal underwater neutrino telescope: Design, performance, and first results*, Astropart. Phys. 7 (3) (1997) 263 – 282. URL `http://www.sciencedirect.com/science/article/pii/S0927650597000224`

[84] V. Aynutdinov, et al., *The Baikal neutrino experiment: Status, selected physics results, and perspectives*, Nucl. Inst. Meth. A 588 (1–2) (2008) 99 – 106. URL `http://www.sciencedirect.com/science/article/pii/S016890020800048X`

[85] L. B. Bezrukov, et al., *The Optical Module of the Baikal Neutrino Telescope NT-200*, in: D. V. R.B. Hicks, D.A. Leahy (Ed.), Proceedings, 23rd International Cosmic Ray Conference, Vol. 4, World Scientific, River Edge, 1993, pp. 581–584.

[86] V. Balkanov, et al. (Baikal Collaboration), *Reconstruction of atmospheric neutrinos with the Baikal Neutrino Telescope NT-96*, in: D. v. d. W. M.S. Potgieter,

B.C. Raubenheimer (Ed.), Proceedings, 25th International Cosmic Ray Conference, Vol. 8, World Scientific, Singapore, 1998, pp. 21–24, Preprint arXiv:astro-ph/9705244.

[87] G. Domogatsky, *A new neutrino telescope for Lake Baikal*, CERN Courier 55 (6) (2015) 23. URL `http://cerncourier.com/cws/article/cern/61865`

[88] V. Aynutdinov, et al. (Baikal Collaboration), *The BAIKAL-GVD project of km3-scale neutrino telescope in Lake Baikal*, in: H. Wang, et al. (Eds.), Proceedings, 32nd International Cosmic Ray Conference (ICRC 2011), Vol. 5, The LOC of ICRC 2011, Beijing, 2011, p. 248. URL `https://inspirehep.net/record/1352469/files/v5_0968.pdf`

[89] A. V. Avrorin, et al., *Current status of the BAIKAL-GVD project*, Nucl. Inst. Meth. A 725 (2013) 23 – 26. URL `http://www.sciencedirect.com/science/article/pii/S0168900212014982`

[90] E. Aslanides, et al. (ANTARES Collaboration), *A deep sea telescope for high-energy neutrinos* Preprint arXiv:astro-ph/9907432.

[91] M. Ageron, et al., *ANTARES: The first undersea neutrino telescope*, Nucl. Inst. Meth. A 656 (2011) 11–38, Preprint arXiv:1104.1607.

[92] *NESTOR project homepage.* URL `http://www.nestor.noa.gr/`

[93] E. Anassontzis, et al., *NESTOR: A neutrino particle astrophysics underwater laboratory for the Mediterranean*, Nucl. Phys. B - Proc. Suppl. 35 (1994) 294 – 300. URL `http://www.sciencedirect.com/science/article/pii/0920563294902674`

[94] *NEMO project homepage.* URL `http://nemoweb.lns.infn.it`

[95] A. Capone, et al., *Recent results and perspectives of the NEMO project*, Nucl. Inst. Meth. A 602 (1) (2009) 47 – 53. URL `http://www.sciencedirect.com/science/article/pii/S0168900208018238`

[96] P. Amram, et al. (ANTARES Collaboration), *The ANTARES optical module*, Nucl. Inst. Meth. A484 (2002) 369–383, Preprint arXiv:astro-ph/0112172.

[97] J. A. Aguilar, et al. (ANTARES Collaboration), *The data acquisition system for the ANTARES Neutrino Telescope*, Nucl. Inst. Meth. A570 (2007) 107–116, Preprint arXiv:astro-ph/0610029.

[98] J. d. D. Zornoza, J. Zuniga, *The ANTARES neutrino telescope*, in: J. C. Guirado, et al. (Eds.), 10th Scientific Meeting of the Spanish Astronomical Society (SEA 2012) Valencia Spain, July 9-13, 2012, 2012, Preprint arXiv:1209.6480. URL `http://inspirehep.net/record/1188655/files/arXiv:1209.6480.pdf`

[99] A. M. Brown, et al., *Positioning system of the ANTARES Neutrino Telescope* Preprint arXiv:0908.0814.

[100] J. A. Aguilar, et al., *AMADEUS - The acoustic neutrino detection test system of the ANTARES deep-sea neutrino telescope*, Nucl. Inst. Meth. A 626 (2011) 128–143, Preprint arXiv:1009.4179.

[101] A. Trovato (ANTARES Collaboration), *Recent results from ANTARES*, EPJ Web Conf. 99 (2015) 06003.

[102] P. Bagley, et al. (KM3NeT Collaboration), *Conceptual Design Report* (2008). URL `http://www.km3net.org/CDR/CDR-KM3NeT.pdf`

[103] P. Bagley, et al. (KM3NeT Collaboration), *Technical Design Report* (2011). URL `http://www.km3net.org/TDR/TDRKM3NeT.pdf`

[104] S. Adrián-Martínez, et al. (KM3NeT Collaboration), *Letter of intent for KM3NeT 2.0*, J. Phys. G43 (8) (2016) 084001, Preprint arXiv:1601.07459.

[105] S. Adrian-Martinez, et al. (KM3NeT Collaboration), *Deep sea tests of a prototype of the KM3NeT digital optical module*, Eur. Phys. J. C74 (9) (2014) 3056, Preprint arXiv:1405.0839.

[106] S. Adrián-Martínez, et al. (KM3NeT Collaboration), *The prototype detection unit of the KM3NeT detector*, Eur. Phys. J. C76 (2) (2016) 54, Preprint arXiv:1510.01561.

[107] R. Bruijn, D. Van Eijk (KM3NeT Collaboration), *The KM3NeT Multi-PMT Digital Optical Module*, PoS ICRC2015 (2016) 1157. URL `http://pos.sissa.it/archive/conferences/236/1157/ICRC2015_1157.pdf`

[108] M. G. Aartsen, et al. (IceCube Collaboration), *The IceCube Neutrino Observatory: Instrumentation and Online Systems* Preprint arXiv:1612.05093.

[109] E. Andres, et al., *The AMANDA neutrino telescope: Principle of operation and first results*, Astropart. Phys. 13 (2000) 1–20, Preprint arXiv:astro-ph/9906203.

[110] E. Andres, et al., *Observation of high-energy neutrinos using Cherenkov detectors embedded deep in Antarctic ice*, Nature 410 (6827) (2001) 441–443. URL `http://dx.doi.org/10.1038/35068509`

[111] R. Abbasi, et al., *Calibration and characterization of the IceCube photomultiplier tube*, Nucl. Inst. Meth. A 618 (1–3) (2010) 139 – 152, Preprint arXiv:1002.2442v1. URL `http://www.sciencedirect.com/science/article/pii/S0168900210006662`

[112] R. Abbasi, et al. (IceCube Collaboration), *The IceCube Data Acquisition System: Signal Capture, Digitization, and Timestamping*, Nucl. Inst. Meth. A601 (2009) 294–316, Preprint arXiv:0810.4930.

[113] C. Wiebusch, et al. (IceCube Collaboration), *Physics Capabilities of the IceCube DeepCore Detector* Preprint arXiv:0907.2263.

[114] R. Abbasi, et al. (IceCube Collaboration), *The Design and Performance of IceCube DeepCore*, Astropart. Phys. 35 (2012) 615–624, Preprint arXiv:1109.6096.

[115] T. Waldenmaier, *IceTop – Cosmic Ray Physics with IceCube*, Nucl. Inst. Meth. A588 (2008) 130–134, Preprint arXiv:0802.2540.

[116] J. Ahrens, et al., *IceCube Preliminaty Design Document* (2001). URL `https://icecube.wisc.edu/icecube/static/reports/IceCubeDesignDoc.pdf`

[117] M. Kowalski, *Status of High-Energy Neutrino Astronomy*, Journal of Physics Conference Series 632 (1) (2015) 012039, Preprint arXiv:1411.4385.

[118] C. Spiering, *The Global Neutrno Network* (2014). URL `http://www.globalneutrinonetwork.org/`

[119] M. G. Aartsen, et al. (IceCube Collaboration), *IceCube-Gen2: A Vision for the Future of Neutrino Astronomy in Antarctica* Preprint arXiv:1412.5106.

[120] E. Blaufuss, et al. (IceCube-Gen2 Collaboration), *The IceCube-Gen2 High Energy Array*, PoS ICRC2015 (2016) 1146.

[121] D. Hebecker, et al. (IceCube-Gen2 Collaboration), *Progress on the Development of a Wavelength-shifting Optical Module*, PoS ICRC2015 (2016) 1134. URL `http://pos.sissa.it/archive/conferences/236/1134/ICRC2015_1134.pdf`

[122] L. Lu, et al. (IceCube-Gen2 Collaboration), *A dual-PMT optical module (D-Egg) for IceCube-Gen2*, PoS ICRC2015 (2016) 1137. URL `http://pos.sissa.it/archive/conferences/236/1137/ICRC2015_1137.pdf`

[123] Hamamatsu Photonics K.K., Photomultiplier Tubes – Basics and Applications, 3rd Edition (2007). URL `https://www.hamamatsu.com/resources/pdf/etd/PMT_handbook_v3aE.pdf`

[124] S.-O. Flyckt, C. Marmonier, Photomultiplier Tubes - Principles and Applications (2002). URL `www.pv.infn.it/~debari/doc/Flyckt_Marmonier.pdf`

[125] W. F. Krolikowski, W. E. Spicer, *Photoemission Studies of the Noble Metals. I. Copper*, Phys. Rev. 185 (1969) 882–900.

[126] ET Enterprises Ltd., Understanding Photomultipliers, 1st Edition (2011). URL `http://www.et-enterprises.com/files/file/Understanding-photomultipliers.pdf`

[127] Hamamatsu Photonics K.K., Photomultiplier Tubes – Construction and Operating Charactreistics (1998). URL `https://wwwmu.mpp.mpg.de/docs/pmtconstruct.pdf`

[128] E. H. Bellamy, et al., *Absolute calibration and monitoring of a spectrometric channel using a photomultiplier*, NASA STI/Recon Technical Report N 95 (1993) 24635.

[129] O. Y. Smirnov, P. Lombardi, G. Ranucci, *Precision measurements of time characteristics of etl9351 photomultipliers*, Instruments and Experimental Techniques 47 (1) (2004) 69–80. URL `http://dx.doi.org/10.1023/B%3AINET.0000017255.60520.e0`

[130] B. K. Lubsandorzhiev, et al., *Photoelectron backscattering in vacuum phototubes*, Nucl. Inst. Meth. A 567 (1) (2006) 12 – 16. URL `http://www.sciencedirect.com/science/article/pii/S0168900206008606`

[131] E. de Wolf (Ed.), Proceedings, Workshop on Technical aspects of a Very Large Volume Neutrino Telescope in the Mediterranean Sea, Nikhef, Amsterdam, 2004. URL `http://www.vlvnt.nl/proceedings/`

[132] V. M. Aynutdinov, et al., *Neutrino Water Detector on the Earth's Surface (NEVOD)*, Ap&SS 258 (1) (1997) 105–116. URL `http://dx.doi.org/10.1023/A:1001779122430`

[133] S. Biagi, T. Chiarusi, P. Piattelli, D. Real, *The data acquisition system of the KM3NeT detector*, PoS ICRC2015 (2016) 1172.

[134] P. Sandstrom, *Generation2 Digital Optical Module*, talk at next-generation hardware workshop, Aachen (December 2014).

[135] L. Classen (IceCube PINGU Collaboration), *Development of a multi-PMT optical module prototype for PINGU*, AIP Conf. Proc. 1630 (2014) 176–179.

[136] M. Gippert, private communication.

[137] Wacker Chemie AG, Solutions for the semiconductor and power electronics industries (2011). URL `https://www.wacker.com/cms/media/publications/downloads/6883_EN.pdf`

[138] J. Reubelt, *Detailed in-situ calibration of the KM3NeT Digital Optical Module (working title)*, Ph.D. thesis, Friedrich-Alexander Universität Erlangen-Nürnberg, Erlangen, in preparation.

[139] S. Aiello, et al. (KM3NeT Collaboration), *Characterization of the 80-mm diameter Hamamatsu PMTs for the KM3NeT project*, AIP Conf. Proc. 1630 (1) (2014) 118–121. URL `http://dx.doi.org/10.1063/1.4902786`

[140] P. Timmer, E. Heine, H. Peek, *Very low power, high voltage base for a Photo Multiplier Tube for the KM3NeT deep sea neutrino telescope*, Journal of Instrumentation 5 (12) (2010) C12049. URL `http://stacks.iop.org/1748-0221/5/i=12/a=C12049`

[141] PicoQuant GmbH, PLS series – Sub-nanosecond Pulsed LEDs for PDL 800-B/-D/828 (2017). URL `http://www.picoquant.com/images/uploads/downloads/pls_series.pdf`

[142] PicoQuant GmbH, PDL 800-B – Picosecond Pulsed Diode Laser Driver (2014). URL `https://www.picoquant.com/images/uploads/downloads/pdl800-b.pdf`

[143] Keithley Instruments, Model 486 Picoammeter Model 487 Picoammeter/Votage Source Instruction Manual (2000). URL `http://exodus.poly.edu/~kurt/manuals/manuals/Keithley/KEI%20486,%20487%20Instruction.pdf`

[144] Hamamatsu Photonics K.K., Si photodiode S6337-01 (2004). URL `http://shpat.com/docs/hamamatsu/S6337-01.pdf`

[145] B. Herold, O. Kalekin, J. Reubelt, *PMT characterisation for the KM3NeT project*, Nucl. Inst. Meth. A 639 (1) (2011) 70 – 72. URL `http://www.sciencedirect.com/science/article/pii/S0168900210020115`

[146] B. Herold, O. Kalekin, *PMT characterisation for the KM3NeT project*, Nucl. Inst. Meth. A 626–627, Supplement (2011) S151 – S153. URL `http://www.sciencedirect.com/science/article/pii/S0168900210009836`

[147] B. Herold, *Studien zur Photodetektion im KM3NeT-Projekt*, Diploma Thesis, Friedrich-Alexander Universität Erlangen-Nürnberg, Erlangen (2008).

[148] J. Reubelt, *Messung der spektralen Quanteneffizienz von Photomultipliern*, B.Sc. Thesis, Friedrich-Alexander Universität Erlangen-Nürnberg, Erlangen (2010).

[149] L. Classen, O. Kalekin, (KM3NeT Consortium), *Status of the PMT development for KM3NeT*, Nucl. Inst. Meth. A 725 (2013) 155–157.

[150] R. Bormuth, et al. (KM3NeT Collaboration), *Characterization of the ETEL and HZC 3-inch PMTs for the KM3NeT project*, AIP Conf. Proc. 1630 (2014) 114–117.

[151] D. Motta, S. Schönert, *Optical properties of bialkali photocathodes*, Nucl. Inst. Meth. A 539 (2005) 217–235, Preprint arXiv:physics/0408075.

[152] C. M. F. Hugon (ANTARES, KM3NeT Collaboration), *Step by step simulation of phototubes for the KM3NeT and ANTARES optical modules*, Nucl. Inst. Meth. A787 (2015) 189–192.

[153] C. M. F. Hugon (ANTARES, KM3NeT Collaboration), *GEANT4 simulation of optical modules in neutrino telescopes*, PoS ICRC2015 (2016) 1106. URL `https://pos.sissa.it/archive/conferences/236/1106/ICRC2015_1106.pdf`

[154] J. Reubelt, *Characterisation of photomultiplier tube models to be used in the KM3NeT project*, M.Sc. Thesis, Friedrich-Alexander Universität Erlangen-Nürnberg, Erlangen (2012).

[155] A. Oshima, et al., *Tests of PMT uniformity for the GRAPES-3 experiment*, in: B. S. Acharya, et al. (Eds.), Proceedings, 29th International Cosmic Ray Conference, Vol. 5, Tata Institute of Fundamental Research, Mumbai, 2005, pp. 335–338. URL `http://articles.adsabs.harvard.edu/full/2005ICRC....5..335O`

[156] R. Busse, *Setup and commissioning of a test stand for detailed investigations of quantum efficiency characteristics of photomultiplier tubes, and initial studies for IceCube-Gen2 (working title)*, M.Sc. Thesis, Westfälische Wilhelms-Universität Münster, Münster, in preparation.

[157] Mini-Circuits, Coaxial Amplifier ZX60-43+ (2016). URL `https://www.minicircuits.com/pdfs/ZX60-43+.pdf`

[158] A. Lyashenko, et al., *Measurement of the absolute Quantum Efficiency of Hamamatsu model R11410-10 photomultiplier tubes at low temperatures down to liquid xenon boiling point*, JINST 9 (11) (2014) P11021, Preprint arXiv:1410.3890.

[159] M. Prata, et al., *Performance and behaviour of photomultiplier tubes at cryogenic temperature*, Nucl. Inst. Meth. A 567 (1) (2006) 222 – 225. URL `http://www.sciencedirect.com/science/article/pii/S0168900206009223`

[160] M. Ivren, *Ratenmessungen für das Multi-PMT-Modul für PINGU*, B.Sc. Thesis, Friedrich-Alexander Universität Erlangen-Nürnberg, Erlangen (2014).

[161] J. Bloms, *Kalibration und Dunkelratenmessungen von Photomultipliern für optische Module in IceCube-Gen2*, B.Sc. Thesis, Westfälische Wilhelms-Universität Münster, Münster (2016).

[162] S. Adrian-Martínez, et al. (KM3NeT Collaboration), *A method to stabilise the performance of negatively fed KM3NeT photomultipliers*, JINST 11 (12) (2016) P12014. URL `http://stacks.iop.org/1748-0221/11/i=12/a=P12014`

[163] Wacker AG, Wacker AK 350 Silicone Fluid (2014). URL `https://www.wacker.com/cms/de/products/product/product.jsp?product=13343`

[164] Electrolube, TRV Tropicalized Varnish (2013). URL `http://www.electrolube.com/core/components/products/tds/044/TRV.pdf`

[165] F. Maack, *Detailed study of dark rate mechanisms and counter-measures in three-inch bialkali PMTs (working title)*, M.Sc. Thesis, Westfälische Wilhelms-Universität Münster, Münster, in preparation.

[166] TestEquity LLC, Model 1007C Temperature Chamber – Operation and Service Manual (2013). URL `https://www.testequity.com/documents/chambers/1007C-EZ.pdf`

[167] Phidgets Inc., 1124_0 – Precision Temperature Sensor (2012). URL `http://www.phidgets.com/products.php?product_id=1124`

[168] Phidgets Inc., 1125_0 – Humidity/Temperature Sensor (2012). URL `http://www.phidgets.com/products.php?product_id=1125`

[169] H. O. Meyer, *Dark Rate of a Photomultiplier at Cryogenic Temperatures* Preprint arXiv:0805.0771.

[170] H. O. Meyer, *Spontaneous electron emission from a cold surface*, Europhys. Lett. 89 (5) (2010) 58001. URL `http://stacks.iop.org/0295-5075/89/i=5/a=58001`

[171] K. Helbing, et al., *Light emission in Amanda pressure spherres*, internal review, AMANDA-IR/20030701.

[172] C.-C. Fösig, *A Readout System for the Wavelength-shifting Optical Module*, Diploma Thesis, Johannes Gutenberg-Universität Mainz, Mainz (2016). URL `http://butler.physik.uni-mainz.de/icecube/thesis/dipl_Carl_Foesig.pdf`

[173] M. Unland Elorrieta, *Detailed study of the dark rate impact of radioactive decays in the glass envelope of a multi-PMT optical module (working title)*, M.Sc. Thesis, Westfälische Wilhelms-Universität Münster, Münster, in preparation.

[174] D. Gajanana, V. Gromov, P. Timmer, *ASIC design in the KM3NeT detector*, Journal of Instrumentation 8 (02) (2013) C02030. URL `http://stacks.iop.org/1748-0221/8/i=02/a=C02030`

[175] P. Timmer, private communication (2015).

[176] C. A. Coulomb, *Essai sur une application des regles des maximis et minimis a quelquels problemes de statique relatifs, a la architecture.*, Memoires de l'Academie Royale pres Divers Savants 7 (1776) 343–387.

[177] A. Cosquer, P. Keller, *Studies of an alternative glass pressure housing for optical modules in the KM3NeT neutrino telescope*, Nucl. Inst. Meth. A 626–627, Supplement (2011) S127 – S129. URL `http://www.sciencedirect.com/science/article/pii/S0168900210009927`

[178] Nautilus Marine Service GmbH, VITROVEX – glass instrumentation housings (2014). URL `http://www.nautilus-gmbh.com/fileadmin/images_nautilus/002_VITROVEX/Instruments/Data_sheets/140101_VITROVEX_deep_sea_instrumentation_housings.pdf`

[179] Teledyne Benthos, Flotation Glass Instruments Housings (2013). URL `http://teledynebenthos.com/_doc/main/Brochures_Datasheets/Flotation_Spheres_Data_Sheet_2013_lo_1.pdf`

[180] *Seamless steel tubes for oil- and water-hydraulic systems – Calculation rules for pipes and elbows for dynamic loads*, Norm DIN 2413:2011-06 (2011).

[181] W. C. Young, R. G. Budynas, A. M. Sadegh, Roark's formulas for stress and strain; 8th ed., McGraw Hill, New York, NY, 2012. URL `https://cds.cern.ch/record/1420544`

[182] *COMSOL Multiphysics^{TM}*, COMSOL AB, Stockholm, Sweden. URL `www.comsol.com`

[183] EOS GmbH – Electro Optical Systems, Material data sheet – PA 2200 (2008). URL `https://www.shapeways.com/rrstatic/material_docs/mds-strongflex.pdf`

[184] R. M. Christensen, *A comprehensive theory of yielding and failure for isotropic materials*, Journal of Engineering materials and Technology 129 (2) (2007) 173–181. URL `http://materialstechnology.asmedigitalcollection.asme.org/article.aspx?articleid=1427952`

[185] Hamamatsu Photonics K.K., High power UV-VIS fiber light source L10290 (2011). URL `https://www.hamamatsu.com/resources/pdf/etd/L10290_TLSZ1010E.pdf`

[186] S. Pausch, private communication.

[187] M. Born, E. Wolf, Principles of Optics, 5th Edition, Pergamon Press, Oxford, 1975.

[188] L. Lu, private communication.

[189] D. Poelman, P. F. Smet, *Methods for the determination of the optical constants of thin films from single transmission measurements: a critical review*, J. Phys. D 36 (15) (2003) 1850. URL `http://stacks.iop.org/0022-3727/36/i=15/a=316`

[190] J. A. Jacquez, H. F. Kuppenheim, *Theory of the Integrating Sphere*, J. Opt. Soc. Am. 45 (6) (1955) 460–470. URL `http://www.osapublishing.org/abstract.cfm?URI=josa-45-6-460`

[191] J. Chaves, Introduction to Nonimaging Optics, 2nd Edition, CRC Press, 2015.

[192] S. Adrian-Martinez, et al. (KM3NeT Collaboration), *Expansion cone for the 3-inch PMTs of the KM3NeT optical modules*, JINST 8 (2013) T03006.

[193] R. Frytz, *Messungen für einen Prototypen eines aus mehreren Photomultipliern bestehenden optischen Moduls für PINGU*, B.Sc. Thesis, Friedrich-Alexander Universität Erlangen-Nürnberg, Erlangen (2014).

[194] A. Tassinari, private communication.

[195] B. Herold, *Simulation and measurement of the deep sea Potassium-40 background using multi-PMT optical modules*, Ph.D. thesis, Friedrich-Alexander Universität Erlangen-Nürnberg, Erlangen, in preparation.

[196] F.-X. Gentit, *SLitrani* (2012). URL `https://crystalclear.web.cern.ch/crystalclear/SLitraniX/SLitrani/index.html`

[197] S. Agostinelli, et al., *Geant4 – a simulation toolkit*, Nucl. Inst. Meth. A 506 (3) (2003) 250 – 303. URL `http://www.sciencedirect.com/science/article/pii/S0168900203013688`

[198] J. Allison, et al., *Geant4 developments and applications*, IEEE Trans. Nucl. Sci. 53 (1) (2006) 270–278.

[199] Laser Beam Products, Reflectivity of Aluminium (2014). URL `https://laserbeamproducts.wordpress.com/2014/06/19/reflectivity-of-aluminium-uv-visible-and-infrared/`

[200] A. Okumura, et al., *Prototyping of Hexagonal Light Concentrators for the Large-Sized Telescopes of the Cherenkov Telescope Array*, PoS ICRC2015 (2016) 952, Preprint arXiv:1508.07776. URL `https://pos.sissa.it/archive/conferences/236/952/ICRC2015_952.pdf`

[201] C. Kopper, *clsim* (2011). URL `https://github.com/claudiok/clsim`

[202] IceCube collaboration, *DOMINANT: Dom Optical-photon to Material INteraction ANd Tracking simulator* (2007). URL `http://www.ppl.phys.chiba-u.jp/research/IceCube/DetectorSim/DOMINANT/index.html`

[203] T. Karg, private communication.

[204] I. H. Malitson, *Interspecimen Comparison of the Refractive Index of Fused Silica*, J. Opt. Soc. Am. 55 (10) (1965) 1205–1209. URL `http://www.osapublishing.org/abstract.cfm?URI=josa-55-10-1205`

[205] Thorlabs, Inc., Optical Sustrates – A Comprehensive Guided to Optical Glass used at Thorlabs (2016). URL `https://www.thorlabs.de/newgrouppage9.cfm?objectgroup_id=6973&tabname=UV%20Fused%20Silica`

[206] Hamamatsu Photonics K.K., Large photocathode area photomultiplier tubes (2016). URL `http://www.hamamatsu.com/resources/pdf/etd/LARGE_AREA_PMT_TPMH1286E.pdf`

[207] Hamamatsu Photonics K.K., Photomultiplier tube R12199 (2015). URL `https://www.hamamatsu.com/resources/pdf/etd/R12199_TPMH1356E.pdf`

[208] ET Enterprises Ltd., *9320KFL datasheet* (August 2015).

[209] C. J. Lozano Mariscal, *Studies on the sensitivity of multi-PMT optical modules to supernova neutrinos in the South Pole ice*, M.Sc. Thesis, Westfälische Wilhelms-Universität Münster, Münster (2017).

[210] P. Kooijman, *Reflector Ring*, talk at mPMT/NEUT workshop, Amsterdam (July 2016).

[211] T. A. Fischer, *Simulationen zur Propagation und Detektion von Photonen im tiefen Eis am Südpol für IceCube-Gen2*, B.Sc. Thesis, Friedrich-Alexander Universität Erlangen-Nürnberg, Erlangen (2015).

[212] J. Veenkamp, *A Precision Optical Calibration Module for IceCube-Gen2*, M.Sc. Thesis, University of Amsterdam, Amsterdam (2016).

[213] B. Efron, *Bootstrap methods: Another look at the jackknife*, Ann. Statist. 7 (1) (1979) 1–26. URL `http://dx.doi.org/10.1214/aos/1176344552`

[214] T. Eder, *Simulationsstudien zum Untergrund durch radioaktive Zerfälle in einem optischen Modul mit mehreren Photomultipliern für IceCube-Gen2*, B.Sc. Thesis, Westfälische Wilhelms-Universität Münster, Münster (2016).

[215] T. DeYoung, *IceTray: A software framework for IceCube*, in: A. Aimar, J. Harvey, N. Knoors (Eds.), Computing in high energy physics and nuclear physics. Proceedings, CHEP'04, CERN, 2005, pp. 463–466. URL `http://cds.cern.ch/record/688747/files/CERN-2005-002-V1.pdf?version=2`

List of Figures

List of Tables

Part III

Appendix

A Acknowledgments

First of all, I want to thank my supervisors, Prof. Dr. Uli Katz and Prof. Dr. Alexander Kappes, for giving me the opportunity to do research on this exciting topic and the chance not only to learn about detector hardware and astrophysics but also to get to know the world-wide community on numerous meetings and conferences. Thank you very much for the committed and personal support, your helpful advice, and your never-ending patience.

I also thank Prof. Dr. Gisela Anton for fruitful discussions on PMT properties and for joining the examination board, as well as Prof. Dr. Christopher van Eldik and Prof. Dr. Hanno Sahlmann, for compiling a report on the thesis and agreeing to participate in the exam, respectively.

Furthermore, I owe a lot to Dr. Oleg Kalekin who taught me not only most of what I know about PMTs but also working in a laboratory in general. Thank you for always taking the time to answer all my questions, even the stupid ones...

In addition, I would like to express my gratitude to all the people of ECAP who contributed to the nice and cooperative working atmosphere that I enjoyed a lot.

Thanks to my colleagues Dr. Fred Uhling, Markus Pfaffinger, Dr. Markus Sondermann, Prof. Dr. Stefan Funk and Stefan Eschbach for allowing me to borrow their lab equipment and the helpful advice.

Gratitude to Stefan Lindner, Dr. Jürgen Röber, and Dr. Alexander Kölpin from the Institute for Electronics Engineering in Erlangen, as well as Dr. Timo Karg and Axel Kretzschmann from DESY/Zeuthen for joining “team mDOM” and contributing their electronics expertise.

Particular thanks go to my fellow PhD candidates:

- To Björn Herold, Alexander Enzenhöfer and Tamás Gál, for introducing me to the worlds of Geant4, Comsol and Jupyter, respectively.
- To Maria Tselengidou and Thomas Kittler who helped me understand the IceCube simulation chain and also had an open ear for general questions.
- And, of course, to my office buddies, Dominik Stransky and Jonas Reubelt. Thank you very much for helpful discussions, long, but exciting, hours in the lab as well as the proof-reading of this manuscript. It is always fun working with you guys!

I am also grateful to the members of the Institute for Nuclear Physics in Münster, in general, for welcoming me into the team and the new city, and to the newly formed AG Kappes, in particular, for totally being the most awesome working group in the institute[1]. Special thanks go to Raffaela Busse for proof-reading parts of the text and Cristian Lozano and Martin Unland for making improvements to the simulation code.

Moreover, I thank my parents, my brothers, and also my parents-in-law, for their endorsement and cheering-up, notably in the busy time towards the end.

---

[1] ...everyone is so nice...

And last, but definitely not least, I owe a lot to my wife Regina for understanding, encouraging and supporting me the entire time. None of this would have been possible without you and I do not know how to thank you enough!

B Declaration

Statement of Authorship

I hereby certify that this thesis was composed by me based on my own work, unless stated otherwise, and that I did not use resources other than those listed in the bibliography and identified as references. I further declare that I have not submitted this thesis at any other institution in order to obtain a degree.

Erlangen, February 10, 2017

(Lew Classen)